Perylene–based Metal Complexes: Their Synthesis, Electrochemical, Photovoltaic Properties and Efficient Dye Sensitized Solar Cells

Meltem Dinleyici

Submitted to the
Institute of Graduate Studies and Research
in partial fulfillment of the requirements for the degree of

Doctor of Philosophy
in
Chemistry

Eastern Mediterranean University
September 2021
Gazimağusa, North Cyprus

Approval of the Institute of Graduate Studies and Research

_____

Prof. Dr. Ali Hakan Ulusoy
Director

I certify that this thesis satisfies all the requirements as a thesis for the degree of Doctor of Philosophy in Chemistry.

_____

Prof. Dr. İzzet Sakallı
Chair, Department of Chemistry

We certify that we have read this thesis and that in our opinion it is fully adequate in scope and quality as a thesis for the degree of Doctor of Philosophy in Chemistry.

_____

Prof. Dr. Huriye İcil
Supervisor

Examining Committee

1. Prof. Dr. Huriye İcil   _____

2. Prof. Dr. Sermet Koyuncu   _____

3. Prof. Dr. Mahmut Kuş   _____

4. Assoc. Prof. Dr. Nur Paşaoğluları Aydınlık   _____

5. Asst. Prof. Dr. Süleyman Aşır   _____

ABSTRACT

This thesis approaches the perylene diimide molecules and their metal complexes, their synthesis, properties, and use in organic photovoltaics. Especially, it is focused on the use of perylene diimides as molecular organic semiconductors in dye sensitized solar cells. In the present research work, two novel chromogenic perylene diimides, N,N'−bis(3−amino−5−phenyl− 2,4,6 − triazinyl)perylene − 3, 4, 9, 10− tetracarboxylic diimide and N,N'− bis(2− hydroxy−1− (1−hydroxymethyl) ethyl)perylene− 3, 4, 9, 10−tetracarboxylic diimide were synthesized by condensation of perylene−3,4,9,10−tetracarboxylic dianhydride with hindered aromatic diamine, 2,4−diamino−6−phenyl−1,3, 5−triazine and aliphatic diol, 2−amino−1,3−propanediol, respectively in isoquinoline and *m*−cresol solvents mixture under argon atmosphere. Also a novel naphthalene diimide, N,N'− bis (3− amino−5− phenyl−2,4,6−triazinyl) naphthalene− 1, 4, 5, 8− tetracarboxylic diimide was synthesized by using same method.

In order to improve the optoelectronic and photochemical properties of perylene diimides dyes, three 1,7−symmetrically substituted perylene dyes, N,N'−bis(2−hydroxy−1− (1−hydroxymethyl)ethyl)− 1,7 −di((S)−2−hydroxypropoxy) perylene−3,4,9,10−tetracarboxylic diimide, N,N'− bis (2−hydroxy −1−(1− hydroxyl methyl)ethyl) −1,7−di (3−thiophenemethoxy) perylene−3, 4, 9, 10− tetracarboxylic diimide and N,N'−bis [3− ((2−methyl− 5− pyrimidinyl)methyl) −5− (2− hydroxyethyl) −4− methylthiazolium] − 1, 7 − di(2−hydroxypropoxy) perylene −3, 4, 9, 10 −tetracar boxylic diimide have been synthesized. In order to achieve this aim first we

synthesized 1,7−Dibromoperylene−3,4,9,10−tetracarboxylic dianhydride and then modification of perylene core at bay position was done with the different alcoholic substituents. At the end two different bay substituted perylene dianhydrides, 1,7−di(3−thiophenemethoxy)perylene−3,4,9,10−tetracarboxylic dianhydride and 1,7−di((S)−2−hydroxypropoxy) perylene−3,4,9,10− tetracarboxylic dianhydride were obtained. In order to improve the power conversion efficiencies of the products, metal complexation was studied for perylene diimides.

The chemical structures of products were confirmed by using elemental analysis, IR and NMR spectroscopic measurements. Thermal stabilities of the compounds were studied with TGA and DSC measurements. Electrochemical properties were characterized by cyclic voltammetry technic. Also, photochemical properties of the compound studied by using UV−vis absorption and emission spectroscopic methods and different absorption and emission properties have been observed due to different intermolecular interactions in various solvents. Finally, the power conversion efficiencies of the compounds were successfully determined.

Keywords: perylene diimides, dye sensitized solar cells, metal complex.

ÖZ

Bu tez, perilen diimid moleküllerine ve metal komplekslerine, bunların sentezine, özelliklerine ve organik fotovoltaikteki kullanımına değinmektedir. Özellikle, Boya esaslı güneş pillerinde moleküler organik yarı iletkenler olarak perilen diimitlerin kullanımına odaklanmıştır. Bu araştırmada, iki yeni kromojenik perilen diimit, N,N'−Bis(3 −amino−5−fenil−2,4,6−triazinil)perilen−3,4,9,10−tetrakarboksilik diimit ve N,N'−Bis (2−hidroksi−1−(1−hidroksimetil) etil)perilen−3,4,9,10−tetrakarboksilik diimit, perilen−3,4,9,10−tetrakarboksilik dianhidrit ve engellenmiş aromatic diamin ve alifatik dialkol sırasıyla 2,4− diamino −6−fenil−1, 3, 5− triazin ve 2− amino−1,3 −propandiol kullanarak kondenzasyon yöntemi ile izokinolin ve *m*−krezol çözücü karışımı içinde argon ortamında sentezlenmiştir. Ayrıca aynı yöntem kullanılarak yeni bir naftalin diimit, N,N'−Bis(3−amino−5−fenil− 2,4,6−triazinil)naftalin−1,4,5,8 −tetrakarboksilik diimit sentezlenmiştir.

Perilen diimit boyalarının optoelektronik ve fotokimyasal özellikleri geliştirmek için üç tane simetrik olarak 1,7−pozisyonlarından sübstitüe edilmiş perilen boyaları, N,N'− bis(2 − hidroksi −1 − (1−hidroksimetil) etil)−1, 7−di((S)−2−hidroksipropoksi) perilen−3, 4, 9, 10 −tetrakarboksilik diimit, N,N'− bis (2− hidroksi−1− (1−hidroksimetil) etil)− 1,7− di(3− tiyofenmetoksi) perilen−3, 4, 9, 10− tetrakarboksilik diimit ve *N,N′* −bis− [3−((2−metil−5− pirimidinil)metil) −5− (2−hidroksietil) −4− methyltiazolyum] −1,7 −di(2 −hidroksipropoksi) perilen− 3,4,9,10−tetrakarboksilik diimit sentezlenmiştir. Bu amaca ulaşmak için ilk olarak 1,7−dibromoperilen−3, 4, 9, 10−tetrakarboksilik dianhidrit ve sonra perilen

çekirdeğinin körfez pozisyonundan farklı alkol sübstitüeleri ile yer değiştirilmiş iki farklı körfez sübstütie perilen dianhidrit, 1,7−di(3−tiyofenmetoksi)perilen−3, 4, 9, 10−tetrakarboksilik dianhidrit ve 1,7−di((S)−2−hidroksipropoksi) perilen−3, 4, 9, 10 −tetrakarboksilik dianhidrit elde edilmiştir. Ürünlerin güç dönüşüm verimliliklerini iyileştirmek için, perilen diimidler için metal kompleksleşmesi çalışıldı.

Sentezlenen ürünlerin kimyasal yapıları element analizi, IR ve NMR spektroskopi ölçümleri kullanılarak aydınlatılmıştır. Maddelerin termal kararlılıkları TGA ve DSC ölçümleri ile çalışılmıştır. Elektrokimyasal özellikler dönüşümlü voltametri yöntemi ile karakterize edilmiştir. Ayrıca, maddelerin fotokimyasal özelliklerinin detaylı olarak UV−Vis absorpsiyon ve emisyon spektroskopi metotları kullanılarak çalışılmıştır. Ve moleküller arası etkileşimlerden dolayı farklı absorpsiyon ve emisyon özellikleri gözlenmiştir. Son olarak, bileşiklerin güç dönüşüm verimleri başarıyla belirlendi.

Anahtar kelimeler: perilen diimit, boya esaslı güneş pilleri, metal kompleks.

ACKNOWLEDGEMENT

First and foremost, I would like to express my sincerest appreciation to my supervisor, **Prof. Dr. Huriye İcil**, for her encouragement, continuous supports and trust in me. She has been always very supportive and understanding whenever I need her helps for my research work and academic career. What I have learned from her in these years is not only about science but also about personal life in general.

I would like to thank my jury members **Prof. Dr. Mahmut Kuş, Prof. Dr. Sermet Koyuncu, Assoc. Prof. Dr. Nur P. Aydınlık, Asst. Prof. Dr. Süleyman Aşır**.

I would like to show my deepest gratitude to my best friend, **Dr. Basma Basil Al–Khateeb**. We have shared many smiles and many tears with her, and she became a part of my family. Thank you for your help, support and understanding.

I would like to thank **Dr. Duygu Uzun** for her support and help when I needed it most.

I would like to show my appreciation to all the current and past group members in the **İcil's Organic Chemistry Research Group** for their help during these years.

Lastly, I would like to thank my parents, who have always supported me financially and morally through my life, who have raised me with love, and my dear sister and brother who have always stood by me with their love. Also, I would like to thank with all my heart my husband, who I know has always been there for me, who showed me endless support during my doctoral studies.

TABLE OF CONTENTS

x

LIST OF TABLES

Table 4.49: Maximum wavelength of the absorption λ_{max} (nm), molar extinction coefficient ε_{max} ($M^{-1}cm^{-1}$), oscillator strength f, fluorescence quantum−yield Φ_f (λ_{exc}= 485 nm), radiative life time τ_0 (ns), fluorescence life time τ_f (ns), fluorescence rate constant k_f (s^{-1}), rate−constant of radiationless deactivation k_d (s^{-1}), and singlet−energy

LIST OF FIGURES

LIST OF SYMBOLS AND ABBREVIATIONS

Å	Angstrom
A	Absorption
A	Electron Acceptor
CAN	Acetonitrile
Anal.	Analytical
AU	Arbitrary Unit
Avg.	Average
C	Concentration
calcd.	Calculated
^{13}CNMR	Carbon−13 Nuclear Magnetic Resonance Spectroscopy
Cm	Centimeter
$CDCl_3$	Deutero−Chloroform
$CHCl_3$	Chloroform
CV	Cyclic Voltammetry
^{o}C	Degree Celsius
Co	Cobalt
CE	Counter Electrode
Δ	Chemical Shift (ppm)
D	Electron Donor
DMF	*N,N'*−dimethylformamide
DMSO	Dimethyl Sulfoxide
DSC	Differential Scanning Calorimetry

DSSC	Dye Sensitized Solar Cell
E	Extinction Coefficient
ε_{max}	Maximum Extinction Coefficient (Molar Absorptivity)
eV	Electron Volt
$E_{1/2}$	Half−wave Potential
Eg	Band Gap Energy
Eox	Oxidation Potential
Ep	Separation of Peak Potentials
Epa	Anodic Peak Potential
Epc	Cathodic Peak Potential
Ered	Reduction Potential
Es	Singlet State
F	Oscillator Strength
Fc	Ferrocene
Fig.	Figure
FT−IR	Fourier Transform Infrared Spectroscopy
FTO	Fluorine Doped Tin Oxide
GPC	Gel permeation chromatography
H	Hour
$H\nu$	Irradiation
Hz	Hertz
^{1}H NMR	Proton Nuclear Magnetic Resonance Spectroscopy
HOMO	Highest Occupied Molecular Orbital

HEPDI	N,N'−Bis(2−hydroxy−1−(1−hydroxymethyl)ethyl)perylene−3,4,9 ,10−tetracarboxylic diimide
HP−PDA	1,7−di((S)− 2− hydroxypropoxy)perylene−3,4,9,10−tetracarboxyli c dianhydride
HP−HEPDI	*N,N'*−Bis(2−hydroxy−1−(1−hydroxymethyl)ethyl)−1,7−di((S)−2 −hydroxypropoxy) perylene−3,4,9,10−tetracarboxylic diimide
HP−TCPDI	*N,N'*−bis−[3−((2−methyl−5−pyrimidinyl) methyl) −5− (2−hydro xyethyl)−4−methylthiazolium] 1,7−di(2−hydroxy propoxy) peryl ene−3,4,9,10−tetracarboxylic diimide
Ip	Peak Current
Ipa	Anodic Peak Current
Ipc	Cathodic Peak Current
IR	Infrared Spectrum/Spectroscopy
ITO	Indium Doped Tin Oxide
J	Coupling Constant
J_{SC}	Reduced Cell Photocurrent
Kcal	Kilocalorimetry
K_d	Rate Constant of Radiationless Deactivation
K_f	Fluorescence Rate Constant
L	Path Length
KBr	Potassium Bromide
KOH	Potassium Hydroxide
LUMO	Lowest Unoccupied Molecular Orbital
M	Molar Concentration

M^+	Molecular Ion Peak
Mw	Weight Average Molecular Weight
mHz	Megahertz
Min	Minimum
mmol	Millimole
Mol	Mole
MS	Mass Spectrometry
N	Refractive Index
NIR	Near Infrared Region
NMP	$N-$methylpyrrolidinone
NMR	Nuclear Magnetic Resonance Spectroscopy
Nm	Nanometer
NaBF4	Sodium Tetrafluoroborate
Φ_f	Fluorescence quantum yield
V_{OC}	Open−circuit Voltage
PDA	Perlyene−3,4,9,10−tetracarboxylicdianhydride
PDI	Perlylene Diimide
PEC	Photoelectrochemical
Ppm	Parts Per Million
Pt	Platin
PV	Photovoltaic
Ru	Ruthenium
SS−DSSC	Solid State Dye Sensitized Solar Cell
Std.	Standard
SWV	Square Wave Voltammetry

τ_o	Theoretical Radiative Lifetime
τ_f	Fluorescence Lifetime
t	Time
TANDI	N,N'−Bis(3−amino−5−phenyl−2,4,6−triazinyl)naphthalene−1,4,5, 8− tetracarboxylicdiimide
TAPDI	N,N'−Bis(3−amino−5−phenyl−2,4,6−triazinyl)perylene−3,4,9,10 −tetracarboxylic diimide
$TBAPF_6$	Tetrabutylammoniumhexafluorophosphate
TGA	Thermogravimetric Analysis
TFAc	Trifluoroacetic Acid
TM−PDA	1,7−di(3−thiophenemethoxy) perylene−3,4,9,10−tetracarboxylic dianhydride
TM−HEPDI	*N,N'*−Bis(2−hydroxy−1−(1−hydroxymethyl) ethyl) −1,7−di(3−th iophenemethoxy) perylene−3,4,9,10−tetracarboxylic diimide
μ	Micro
UV	Ultraviolet
UV-vis	Ultraviolet Visible Light Absorption
N	Wavenumber
$\Delta\tilde{\upsilon}_{1/2}$	Half-width of the Selected Absorption
V	Volt
vs.	Versus
WE	Working Electrode
λ	Wavelength
λ_{exc}	Excitation Wavelength

λ_{em}	Emission Wavelength
λ_{max}	Maximum Wavelength
ZnO	Zinc Oxide

Chapter 1

INTRODUCTION

1.1 Solar Cells

Energy has a vital role to reach virtually all of the renewable reconstruction targets, from its position in poverty obliteration to developments in industrialization, instruction, sanitary and aqua resources to change in the climate. Mainly accelerating financial, exhaustible and ecological factors can be attributed to global concern over energy issue. High−speed economic development needs more energy sources; exhaustible fossil fuels that are now commonly used demand sustainable energy sources because ecological destruction induced by the combustion of greenhouse effects and fossil fuel purport people need to make use of environmentally friendly sustainable energy supplies [1]. Studies and production of renewable energy sources have gained significant worldwide attention. Globally, renewable energy (wind, hydro, wave and solar) industries account for an estimated 7.7 million working areas, with solar power the biggest renewable energy employer [2].

Solar power is the best of all sources of renewable and clean energy and the world gets 174 PW of incoming sunlight at the upper atmosphere in one year [3]. The amount of solar power that arrives at the planet's surface is so wide and it is more than what will ever be achieved in one year from a combination of all the non−sustainable energy supplies of coal, oil, natural gas and mined uranium [4]. A photovoltaic cell (PV), commonly identified as a solar cell, is a technological device that converts solar light

1

photons into electrical energy using the photoelectric phenomenon. Photovoltaic technology is considered to be the most encouraging of all sustainable energy technologies. PV has turned into a multi−billion, fast−growing technology and the largest potent of any renewable energy industry [5]. The plentiful, efficient, reliable and affordable PV technology is contemplated to be the most hopeful of all the modern industries in the energy area [6].

1.2 History of Solar Cells

Solar power has always governed life at the ground. The photovoltaic effect was first demonstrated experimentally in 1839 by Edmond Becquerel at age of nineteen. In this study, silver chloride (AgCl) was placed in a solution that has pH of less than 7 and discovered when attached to a Pt electrode, producing current and voltage [7]. The PV effect is therefore denominated the "Becquerel effect". Charles Fritts who is an American inventor succeeded the large area photovoltaic cells firstly from selenium wafers in 1883 [8]. But, since the conversion of all incident sunlight into electric power is less than 1% and distorted so fast when was subject of powerful light by the selenium cells, these pioneers in photoelectricity were not accomplished the developing the solar cells that they were expected. Max Planck's Planck law defined the spectral dispersion of the solar spectrum in 1901 [9]. In his remarkable year of 1905, Einstein proposed the quantum theory of light and explained the effect of photoelectric [10], for which he was awarded the Nobel Prize in Physics in 1921. Photons drive electrons from the valence band (VB) in extensive semiconductor materials toward higher energy conduction band (CB), where they are caught and carried to the outer circuit, which is the theoretical basis for all solar cells. In 1904, Wilhelm Hallwachs developed a prototype of thin−film Schottky barrier devices by utilizing copper (Cu) and copper oxide (CuO) to construct a semiconductor junction solar cell device. In the same year,

Goldmann and Brodsky have approved this barrier layer at the metal−semiconductor interface. [11]. Later Walter Schottky, Neville Mott and others worked on more details in the 1930s [12]. The first applicable silicon (Si) solar cell devices were demonstrated by a team of scientists with a power conversion efficiency of 6% at Bell Lab in 1954 [13]. In 1958 the silicon based solar cell devices were utilized in the US satellite Vanguard I [14]. These achievements have benefited solar cell research and development.

1.3 Classification of Solar Cells
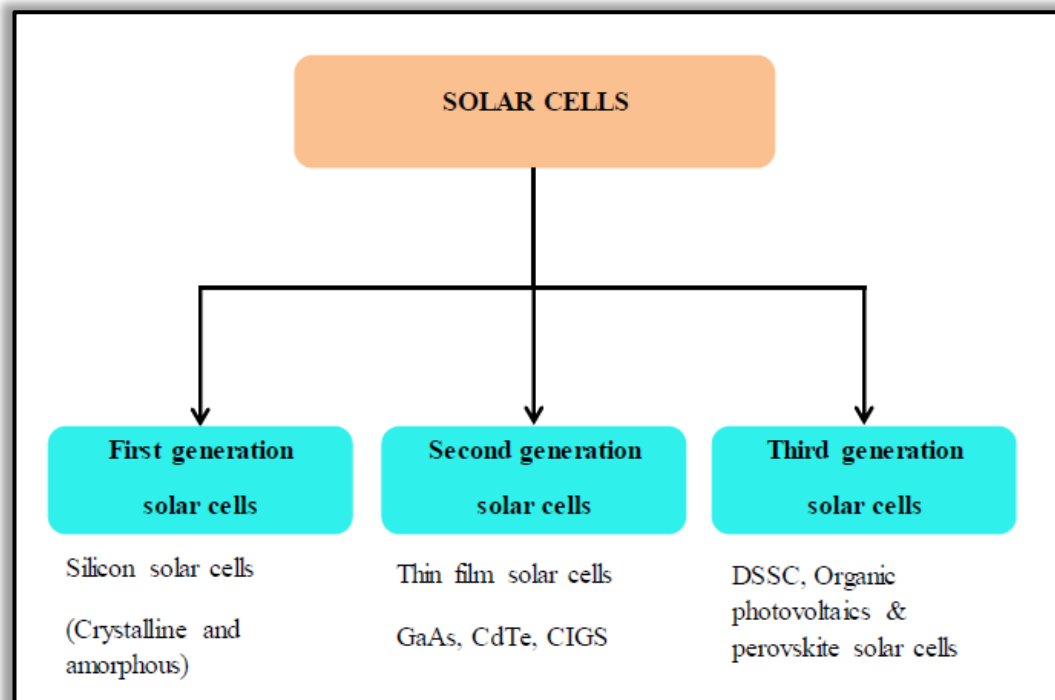
Figure 1.1: Classification of solar cells

Solar Cell technology science and industrial research and development will concentrate on "Golden Triangle Problems" which are high light to power conversion efficiency, high stability and low cost. The fourth eco−harmony issue could be emphasized by improved public cognizance of sustainable development as well [15].

Until today, three different generations of solar cell devices were built up to meet these challenges.

1. First Generation (silicon solar cells)
2. Second Generation (thin film solar cells)
3. Third Generation (DSSC, organic photovoltaics & provskite solar cells).

Wafer−based and traditional cells, also identified as the first generation solar cells were constructed of monocrystalline silicon (Si), polycrystalline Si and gallium arsenic (GaAs). The constructed cell efficiency of silicon, which is a raw material without reserve shortage, has increased since the first production, due to its characteristics such as durable crystal structure and non−toxicity; it has become a popular material. Silicon based solar cell devices have control over the photovoltaic industry and produce efficiencies ranging from 12% to 16%, depending on growing processes and quality of wafers. Despite this, the usage of polycrystalline Si rather than monocrystalline Si was spurred by the need for environmentally sustainable and inexpensive options due to the complex manufacturing stages and significant environmental costs.

Consisting of gallium and arsenic elements, gallium arsenic (GaAs) has a polycrystalline structure and the band gap is about 1.4 eV at 25 ^{o}C. Compared with silicon material, the distance required for photon absorption is shorter, and this feature allows GaAs to form solar cells by utilizing thinner and less material. Considering that the gallium element on Earth is not as common as silicon, it is less favored in solar cell construction than silicon. GaAs based solar cells are mostly used in systems with optical condensers produced for space applications. The main reason for using GaAs in solar cells in space applications is that it is more resistant to temperature and

radiation than silicon. The commercial efficiency of GaAs solar cells is above 22% and laboratory efficiency is above 25%. Around 30% power conversion efficiency was achieved in multi joint GaAs batteries created with other semiconductors [16−18].

Thin film technologies and other devices also called as second generation solar cells are bearing CdTe (cadmium telluride) and CIGS (copper indium gallium selenide). Through low temperature processes, material saving and high automation in sequence manufacture, particularly in variable cells, the thin film solar cell devices sandwich effective supplies among two conductive electrodes and give the potential for low cost in the production procedure. On the other hand, insufficient stability and difficult module technology were concluded in a low market share ($< 12\%$) of thin film cells.

The power conversion efficiency obtained from amorphous silicon solar cells is around 10 %, which does not display crystalline building and in trading modules, it is in the sequence of 5−7 %. Nowadays, these batteries are used as the power supply of small electronic devices such as clocks, calculators and toys. In another important application area of amorphous silicon batteries, it is estimated that it can be used as building exterior translucent and energy generator as translucent glass surfaces integrated into buildings. Solar cell development of cadmium sulfide−cadmium telluride (CdS / CdTe); cadmium telluride combines with cadmium sulfide to form a heterojoint structure. The CdS semiconductor is applied as a very thin layer, with a band gap of about 2.4 eV. CdS, that passes most of the solar radiation, acts as a window in a heterojoint structure. CdTe is one of the most suitable semiconductors for its electronic structure, sunlight spectrum. It is often used in combination with CdS. Moreover, the CdS / CdTe joint provide the electrical potential necessary for current

formation. While the efficiency data in this kind of solar cell devices reach 11 %, the cost of the panel is decreased to the lowest level among all technologies in the world.

After roughly thirty years, the 3rd generation of solar cells appeared. The 3rd generation of solar cells is also identified as arising photovoltaic devices, most of which are in the phase of investigation or production. Solar perovskite cells, dye sensitized solar cells and solar organic−polymer cells are the latest generations of PV technologies [19−23].

1.4 Objective of the Work

This thesis aims to manufacture the photo sensitizer which is one of the most important components of DSSCs. Firstly, two symmetrically substituted perylene diimides and three bay substituted perylene diimides were synthesized and characterized in detail as a photo sensitizer. Synthesis of bay substituted perylene diimides have been started with the bromination, followed by core modification and finalized with imidization.

Actually, ruthenium (Ru) based complexes have shown better power conversion efficiencies (around 14 % PCE) than metal free dyes [24]. But high−cost Ru based materials have some restrictions on their practice area like poor sources of the Ru metal in the earth's shell, low absorption of these dyes in the near−infrared range of the electromagnetic spectrum, low stability and problems of the synthesis and purification of these dyes. Nowadays, there are some trials to produce a DSSC based on other metal complexes by osmium, iron, platinum, copper metals [25]. Since metal free perylene dyes contain binding groups like hydroxyl groups, copper has been used to synthesize copper based complexes.

The DSSC devices are constructed using the synthesized metal free and copper based dyes. The binding ability of dyes were characterized by FTIR and solid state UV−vis absorption spectroscopic measurements.
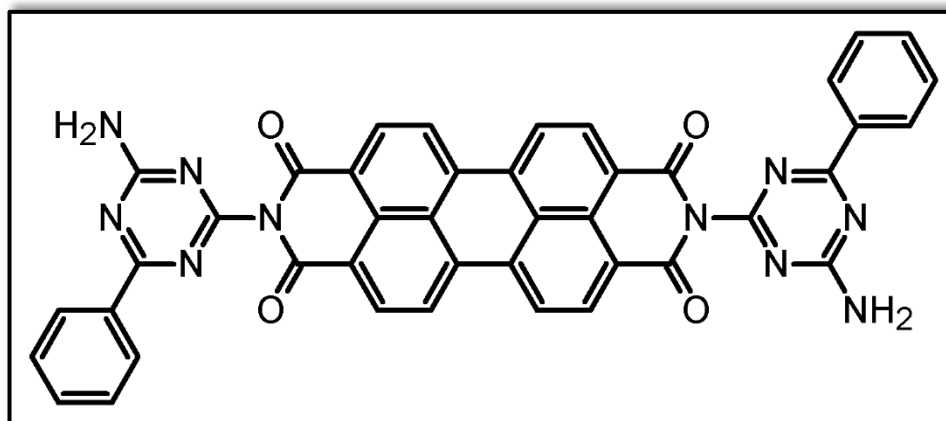
Figure 1.2: Chemical structure of
N,N'−Bis(3−amino−5−phenyl−2,4,6−triazinyl)perylene−3,4,9,10−tetracarboxylic diimide, TAPDI
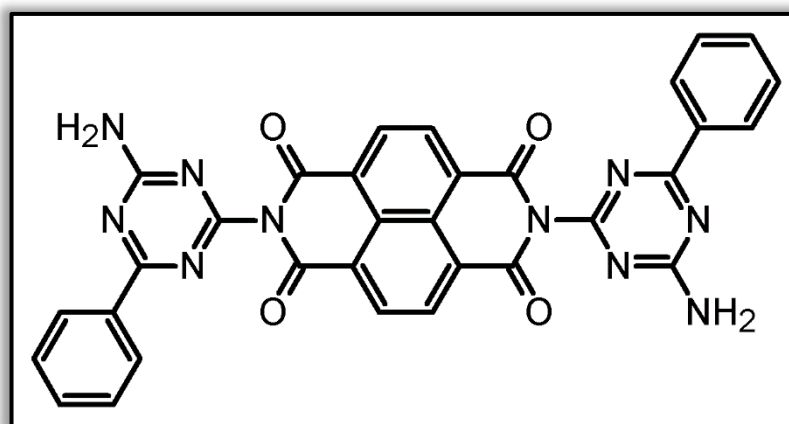
Figure 1.3: Chemical structure of
N,N'−Bis(3−amino−5−phenyl−2,4,6−triazinyl)naphthalene−1,4,5,8−tetracarboxylic diimide, TANDI
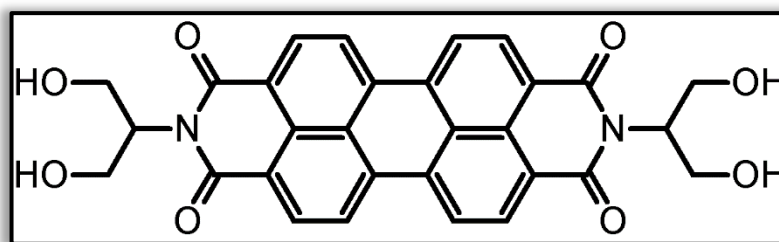
Figure 1.4: Chemical structure of
N,N'−Bis(2−hydroxy−1−(1−hydroxymethyl)ethyl)perylene−3,4,9,10−tetracarboxylic
diimide, HEPDI
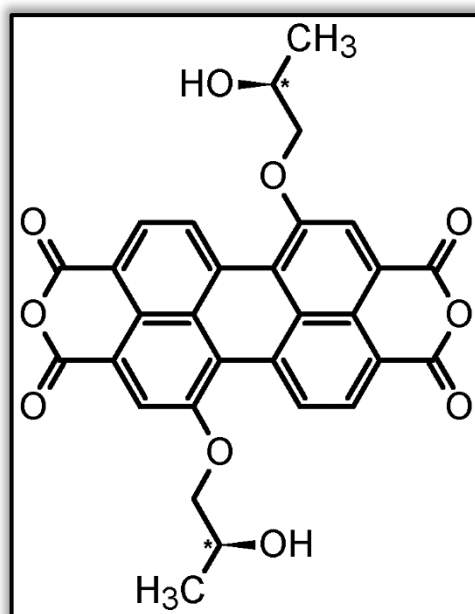
Figure 1.5: Chemical structure of 1,7−di((S)−2−hydroxypropoxy)
perylene−3,4,9,10−tetracarboxylic dianhydride, HP−PDA
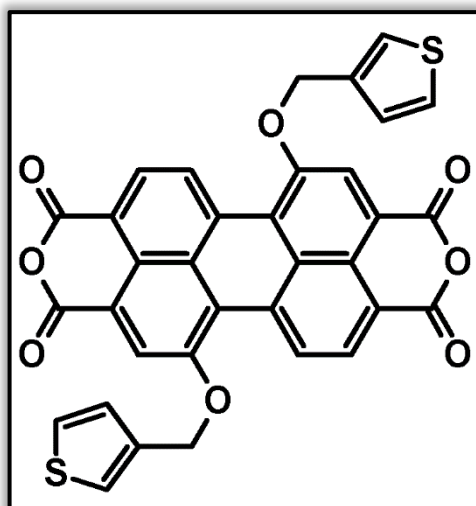
Figure 1.6: Chemical structure of 1,7–di(3–thiophenemethoxy) perylene–3,4,9,10–tetracarboxylic dianhydride, TM–PDA
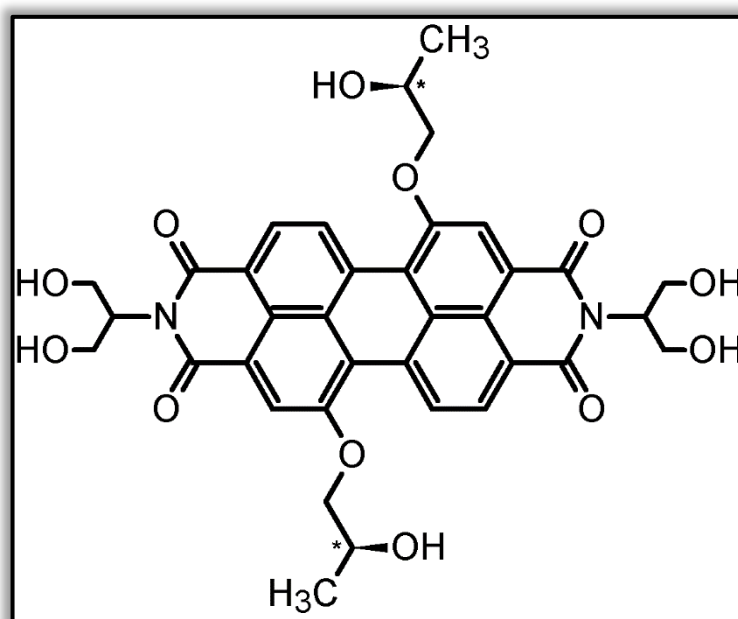
Figure 1.7: Chemical structure of *N,N'*–Bis(2–hydroxy–1–(1–hydroxymethyl) ethyl)–1,7–di((S)–2– hydroxypropoxy) perylene–3,4,9,10–tetracarboxylic diimide, HP–HEPDI
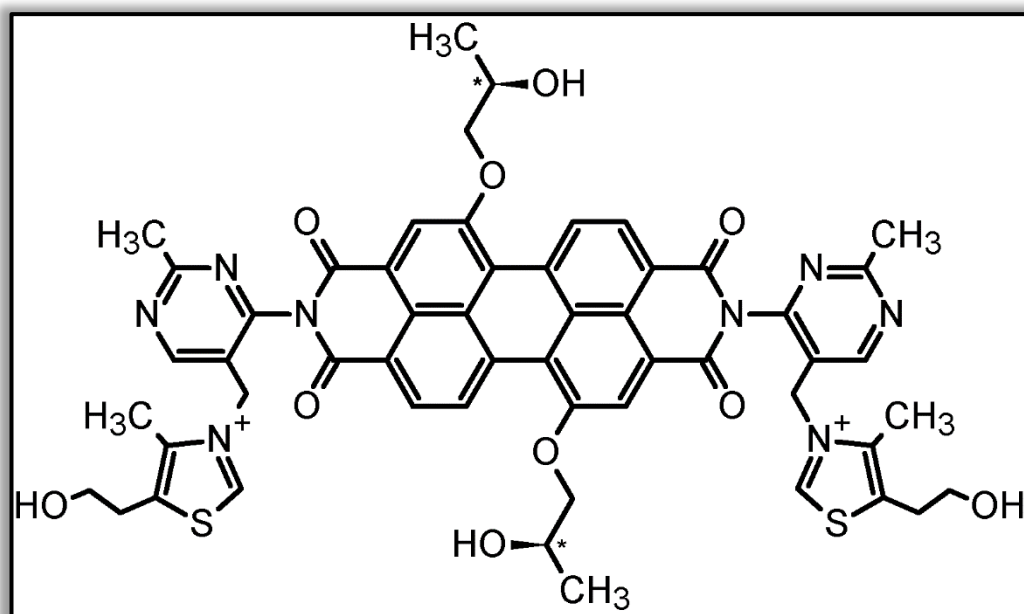
Figure 1.8: Chemical structure of *N,N'*−bis−[3−((2−methyl−5−pyrimidinyl) methyl) −5− (2−hydroxyethyl)−4−methylthiazolium]−1,7−di(2−hydroxy propoxy) perylene−3,4,9,10−tetracarboxylic diimide, HP−TCPDI
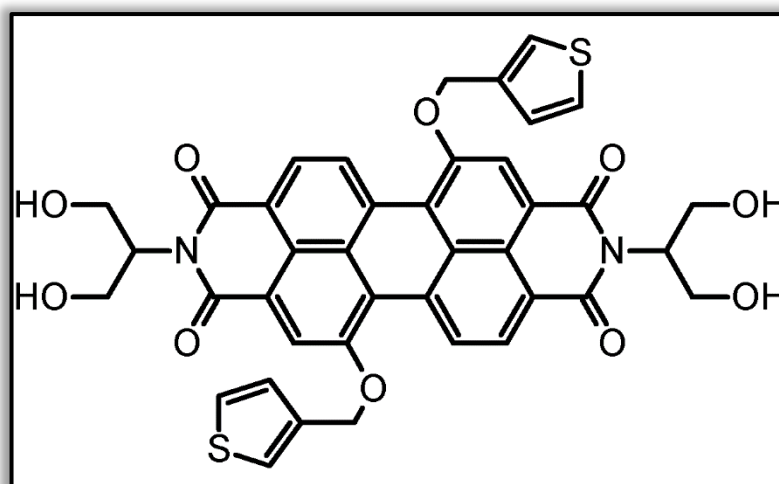
Figure 1.9: Chemical structure of *N,N'*−Bis(2−hydroxy−1−(1−hydroxymethyl) ethyl) − 1,7−di(3−thiophenemethoxy) perylene−3,4,9,10−tetracarboxylic diimide, TM−HEPDI

Chapter 2

THEORETICAL

2.1 Dye Sensitized Solar Cell (DSSC)

The development of dye sensitized solar cell (DSSC) devices was started by inspiration from nature. DSSCs are able to mimic the charge separation process which is occurring in the duration of photosynthesis in plants. Titanium dioxide semiconductor in the DSSC device has a stacked structure that looks like the piled thylakoid membrane in green leaves [26]. Electron generation and charge separation processes and the unique structure of DSSC differentiate it from all other solar cells. Dye sensitization of semiconductors with wide bandgaps, like TiO_2 and SnO_2, gives the fundamental idea of DSSCs. The optical bandgap of TiO_2 is almost 3.2 eV, which is much greater than the optical bandgap of the Si semiconductors (1.1 eV) in traditional solar cells. Moreover, semiconductors with a wide bandgap are not able to absorb most of the photon of light themselves and need to become sensitive to the visible light by means of dye sensitizers. In addition, wide bandgap semiconductors have some significant advantages over the silicon based semiconductor. Semiconductor materials with wide bandgap are very cheap, abundant and highly stable.

Before the discovery of DSSC, this idea (i.e. dye sensitization of wide bandgap semiconductors) had been utilized in xerography and colour photography industries [27]. The utilization of this vision in the photoelectrochemical (PEC) procedures has been published since the late 1960s. For instance, the sensitization of wide bandgap

semiconductor zinc oxide (ZnO) by organic dyes has been investigated [28]. In 1976, the efficiency of 1% was observed by Tsubomura et al. with the dye sensitized zinc oxide photocell. Dye sensitization of TiO_2 can be traced back to Chen et al. who announced such application, in a US patent issued at the end of 1978 [29].

In 1991, the important innovation in the field of research into DSSC resulted from the study of Grätzel and O'Regan published [30]. They developed ruthenium (Ru) based dye sensitizer and reached 7.1 % power conversion efficiency in a solar cell made of TiO_2 nanoparticles in their modern version of DSSC [30]. This power conversion efficiency was high enough to move the attention in DSSC's global work "as a significant competitor to other solar cell technologies". After three years the Grätzel group reached a power conversion efficiency of 10 % [31]. Until now, solar cells had the highest sunlight to electrical conversion efficiencies of more than 11 % which were constructed with Ru based N719, N3 and black dye photosensitizers, together with TiO_2 semiconductor material and redox pair (iodide/triiodide) [32−34]. In order to have this high power conversion performance, internal energy grades of all of the three major ingredients of dye sensitized solar cell devices which are photosensitizer, semiconductor material and redox couple have been adjusted decent. In 2011, the power conversion efficiency was reached 12 % by including cobalt (Co) based redox mediator switching the iodide/triiodide redox mediator in unification with a porphyrin−based dye molecule that was specially developed to delay interfacial back electron transfer mechanism [35]. Besides, to increase the power conversion efficiency, co−sensitization is done with this porphyrin−based dye and another alternative organic dye molecule.

The research focus in DSSC has risen significantly over the past two decades. But until 2013, the extensive investigation attempt to raise the performance of DSSC, which is up to this time, less than that of the traditional solar cell devices, has not been matched with a commensurate rise of the power conversion efficiency of this cell to commercialize. In 2014, a DSSC using zinc porphyrin colorant and $Co^{(II/III)}$ tris(bipyridine)−based electrolyte achieved an outstanding efficiency data of 13.00 %. Moreover, in 2015, a DSSC device using two different metal−free organic sensitizers and $Co^{(II/III)}$tris(phenanthroline)−based electrolyte obtained the supreme performance record of 14.3 %. With an unforeseen invention and magnificent results observed in solid−state DSSC (SS−DSSC) based on perovskite, absorbers have seen increasingly rapid advances in the DSSC region. DSSCs can be generally classified into solid state and liquid state cells, depending on the electrolyte used in their processing. The DSSC's new solid state formulation, in which a perovskite material is used as a light harvester and the electrolyte of the cell is substituted with organic hole transport material, increased the power conversion efficiency of DSSC to 25.2 % [36]. This new record performance would open up a new age for developing DSSC.

2.2 Device Structure

The main materials to construct a DSSC are the working electrode (WE), a photosensitizer (dye molecule), liquid electrolyte (redox intermediate) and counter electrode (CE). DSSC is a sum of WE adsorbed by a well−prepared dye solution and sealed to the CE drenched with an electrolyte which is applied as a thin layer

The working principle of DSSCs is concerned with the photosynthesis mechanism in plants where absorption of light and transportation of charge carriers are performed by distinct compounds.

2.2.1 Transparent and Conductive Substrate

DSSCs developed with two plates of conducting clear glasses working as a current collector, support also substrates for depositing the WE and Pt catalyst [37]. In DSSC devices, transparency and power conductivity are two important characteristics of glasses being used: First, the usage of transparent glass is needed by the electrode to let the transition of ideal solar light to the effective space of the cell more than 80 %. Also, for the effective charge transfer mechanism and minimized power sacrifice in DSSCs, the substrate should have superior energy conductivity. In general, the fluorine doped tin oxide (FTO, SnO_2: F) and indium doped tin oxide (ITO, In_2O_3: Sn) are performed as conductive glasses in DSSC. The FTO glass substrates with 8−20 Ω/square resistance are mostly used TCO glasses due to the higher conductivity, transparency and also higher stability upon sintering at higher temperatures (450 $^{\circ}$C) than ITO glasses.

2.2.2 Working Electrode (WE)

The thin sheet of oxide semiconducting parameters with wide band gap energy of 3− 3.2 eV like TiO_2, SnO_2, ZnO, Nb_2O_5 and NiO is used to prepare the working electrodes by placing them on a transparent conducting glass panel accomplished of ITO or FTO. TiO_2 nanoparticles are used mostly as a semiconducting layer as a photoanode owing to its being non−toxic, inexpensive and its easy availability. Because of its greater energy bandgap of 3.2 eV, the anatase allotropic type of TiO_2 is more suitable in DSSCs than the rutile one, which has a bandgap of roughly 3 eV [38]. Commercial Degussa (P25) TiO_2 contains of rutile and anatase form of TiO_2 with ratios from 20:80 to 30:70 is used for the preparation of working electrode in the construction of DSSCs. These working electrodes are then steeped in a photosensitizer dye solution. Anchoring groups on the structure of dye are covalently bound to the TiO_2 semiconducting layer

after immersing the created film in the dye solution. Because of the large surface region and the poriferous structure of the TiO_2, numerous dye structures adsorbed on the upper face of the working electrode, and thus, absorption of photon of light at the semiconductor surface improves.

2.2.3 Photosensitizer or Dye

The dye molecules as photosensitizers in the construction of DSSCs are the main constituent accountable for the strong absorption of vigorous light in the visible region to near infrared region of the electromagnetic spectrum. Any dye sensitizer used in construction of DSSCs should have electrochemical and photo physical features as follows:

1. The dye sensitizer should be photoluminescent, highly soluble, optically and thermally stable and nontoxic.

2. The dye molecule should have strong and wide absorption capacity from the UV−Vis to NIR region of the electromagnetic spectrum.

3. HOMO level (highest occupied molecular orbital) could be placed away from the surface of the TiO_2 conductive band and LUMO level (lowest unoccupied molecular orbital) should be located as close to the surface of the TiO_2, and afterwards should be higher with respect to the TiO_2 conductive band potential.

4. The HOMO value could be lower than the redox mediator value.

5. The surrounding of the sensitizer molecule could not be hydrophilic to improve the stability of cells, as it ensures minimized direct contact between anode and electrolyte; additionally, water induced distortion of the dye from the TiO_2 surface can emerge which can decrease the stability of cells.

6. In order of prevent the aggregation behaviors of the sensitizer molecules on the TiO_2 semiconductor, dye molecules are modified by using anchoring groups like

15

phosphoric acid, alkoxy−silyl, and the carboxylic acid groups which are attached between the dye molecule and TiO_2. The establishment of a robust association between TiO_2 and dye structure will limit the recombination processes between the electrolyte and electrons with in the TiO_2 semiconductor material [39].

2.2.4   Electrolyte

An electrolyte (I^-/I_3^-) has five fundamental ingredients as follows redox couple, additives, solvent, cations and ionic liquids. The features given below exist in a liquid electrolyte:

1. Redox couple (I^-/I_3^-) must have the capability to produce the dye molecule which is oxidized effectively.

2. Must have strong thermal, chemical, optical and electrochemical stabilities.

3. Should not be corrosive with parameters of DSSC.

4. Must be ability to give permission rapid diffusion of charge carriers, increase the conductivity, and compose efficient touch among the counter and working electrodes.

5. A dye molecule's absorption spectrum and an electrolyte absorption spectrum could not overlap.

I^-/I_3^- was indicated as an extremely effective electrolyte, but there are certain restrictions associated with DSSC applications. Electrolyte which is I^-/I_3^- corrodes glass/TiO_2/Pt; it has poor long time stable and is liable for dye desorption and photodegradation [40]. With high dielectric constant solvents like acetonitrile and N−methylpyrrolidine and solvent mixtures have been used in the preparation of liquid electrolyte. 4−Tert−butylpyridine was commonly utilized as an additional ingredient to raise the CB of the working electrode, resulting in an increase in the value of open-

circuit voltage (V_{OC}), decreased photocurrent of cell (J_{SC}), and reduced addition driving force. Recombination has been decreased by 4−Tert−butylpyridine on a TiO$_2$ semiconductor to back transfer to an electrolyte as it's known [41]. The leakage factor associated with ionic liquids is also a significant disadvantage. As a result, solid state electrolytes were devised to overcome the limitations of ionic liquid electrolytes. Long−term light−absorbing trials on sealed cells have also improved dramatically over the years to check for the collapse of the redox electrolyte or the sealing under long−term illumination.

2.2.5   Counter Electrode (CE)

Platinum (Pt) and carbon (C) are utilized frequently to prepare Counter Electrode in DSSCs. After the WE and CE are sealed jointly, a redox couple is completed by using an injector. The reduction process of redox couple (I^-/I_3^-) is catalyzed by the counter electrode which collects electrons from the hole transport materials. Pt is utilized essentially as a CE since it is an attractive catalyst for I_3^- reduction [42], but the replacement of Pt is much necessary owing to its less abundance and expense. Owing to the combination of satisfactory conductibility and heat strength as well as oxidation strength and electrocatalytic activity for the redox couple reduction carbon is an exciting inexpensive alternate for Pt.

2.3 Working Principles

The four basic and important steps in the working principle of a DSSC. These are photon absorption in the visible part of the electromagnetic spectrum, efficient electron injection, electron transportation, and current separation and collection. Conversion of photons of light to electrical power requires the following steps.

1. The photon of light is widely absorbed by a photosensitizer (dye) adsorbed on TiO$_2$, and thus, owing to absorption of a photon, electrons moved from the ground state (S) to the excited state (S*) of the photosensitizer, where the absorption for most of the dye is in the visible range which corresponds to the photon energy almost about 1.72 eV.

2. Electrons that are excited, are syringed into the CB of nanoporous a working electrode TiO$_2$ that lies under the excited state of the photosensitizer, where the working electrode absorbs a small fraction of the photons of light from the UV−vis region [43]. The dye molecule gets oxidized as a result.

$$S + h\upsilon \rightarrow S^* \tag{1}$$

$$S^* \rightarrow S^+ + e^- \tag{2}$$

3. Electrons were carried among TiO$_2$ semiconductor by diffusing to the FTO glass substrate and reach the counter electrode through the external circuit.

4. Reduction of I$_3{}^-$ to I$^-$ takes place at the counter electrode by electrons; thus, dye regeneration occurs owing to the electron accepting from I$^-$ ion redox mediator, and I$^-$ is oxidized to I$_3{}^-$.

$$S^+ + e^- \rightarrow S \tag{3}$$

5. The oxidizing agent (I$_3{}^-$) moves to the CE and reduces to I$^-$ ion again.

$$I_3^- + 2e^- \rightarrow 3I^- \tag{4}$$
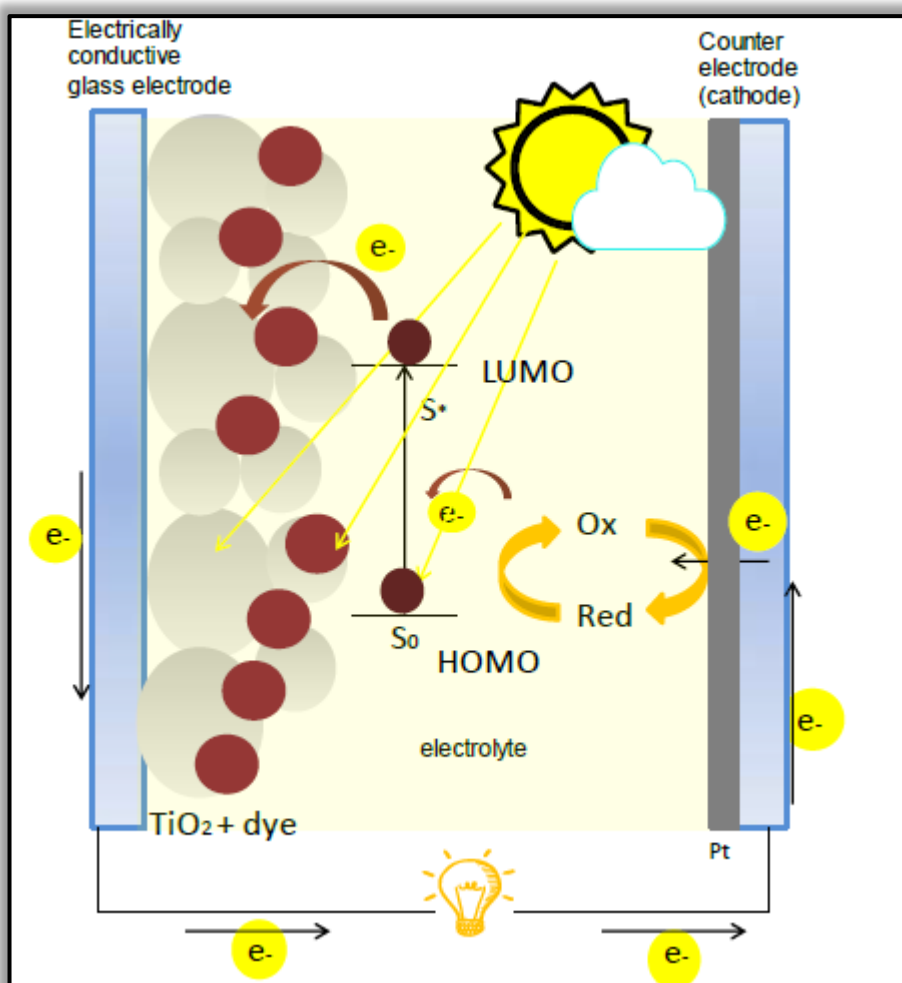
Figure 2.1: Working principle of DSSC

2.4 Perylene Dyes

Different types of modified perylene−3,4,9,10−tetracarboxylic acid diimides (abbreviated as PDIs) briefly called perylene diimide, present a model of an intrinsically potent and exceptionally adaptable class of organic materials that were used for a broad sequence of technological applications. The area of using perylene diimide derivatives was limited compared to pigments by virtue of their subdued dissolution in almost all of the organic solvents [44−46]. Also, until 1959, their other outstanding properties like unsurpassed fluorescence quantum yield and high absorption capacity were not explored. Recently, some of the perylene diimide

molecules are utilized in fiber applications, exclusively in first−rate industrial dye in the automobile sector and in carpet yarns [47].

2.5 Physical properties of Perylene Diimides

Perylene dyes and their derivatives show exciting absorption, emission and electrochemical properties, which has results in important research area on these dyes for many applications like OPVs and OFETs [44−46]. Most of perylene diimide dyes are red color powder with high melting points and excellent photochemical and thermal stabilities. However, perylene diimide pigments with different colors are also known due to, in some cases very clear aggregation properties, leading to the observed variation in solid state absorption spectra.

Perylene diimides are generally considered as a group of excellent organic dyes with large molar absorption coefficients at visible wavelengths of the electromagnetic spectrum, high fluorescence quantum yields near unity, and long singlet excited state lifetimes [44]. Perylene diimides are characterized by robust and wide absorbing light capacity in the visible range, and they show a strong emission like kind of mirror image to the absorption spectra in the solutions. The transitions for unsubstituted PDIs are principally transitions from HOMO level to LUMO level as reported. The absorbance of the $0 \rightarrow 0$ vibronic transition and the $0 \rightarrow 1$ vibronic band for perylene diimides in solution shows the relationship as $I_{0 \rightarrow 0} / I_{0 \rightarrow 1} > 1.6$, though molecular aggregation of perylene diimides causes a significant decrease in this value [48]. A difference of lower than 5 nm in the maximum absorption and fluorescence wavelengths could be determined by replacing the N−terminal groups with many substituents. Besides, the transition bands in absorption and emission spectra of the perylene diimides affected by substituents on the bay/core− or ortho− sites of perylene chromophore through the

intense electronic coupling among the π−orbital of the perylene diimides and the substituents on the bay position of the aromatic ring. For instance, almost 40 nm bathochromic shifts have occurred in the maximum emission and absorption wavelengths of the phenoxy groups inserted perylene dye from bay position compared to that of the unsubstituted perylene diimide dyes and the color of the emission turned to orange after this modification [48]. More certain spectral differences take place on substitution of the perylene cores with electron donating groups like pyrrolidino, which results perylene diimide derivatives with a dark shade of green color both in the solution state and solid state, owing to the redshift more than 150 nm. Because such a great spectral redshift is associated with the substituent to perylene internal charge transfer behavior, some solvatochromism is observed for these perylene diimide derivatives, and their fluorescence quantum yields are extremely reduced [48]. However, solvatochromism effect and limited spectral modifications are recognized if electron−withdrawing groups are incorporated into the bay position of the perylene diimides because of the inductive effect. In general, both the LUMO and HOMO levels will be lowered in a similar manner and there is no clear internal charge transfer present in these systems.

Also, the photochemical properties of perylene dyes are extremely depend on molarity and environmental conditions like polarity of solvent and temperature [48]. For instance, aggregation behavior between the perylene skeletons in solutions with high concentrations shows stronger absorption and a large red shift, with absorption which shifts through the NIR region of the electromagnetic spectra for perylene diimide derivatives. The strong aggregation behavior of perylene dyes caused the face to face

or edge to face π–π interactions led to an almost complete loss of fine transition bands in the absorption spectra [48].

Perylene diimides are good electron acceptors without substitution from their bay position of skeleton, and they are reduced easily and rather difficult oxidized in solution. One reversible oxidation peak and two reversible reduction peaks are determined for many unsubstituted perylene diimide compounds in the ideal solvents [48]. In general, PDI exhibit a first reduction potential comparable to that of fullerene and its derivatives, which makes them strong electron acceptor fast charge transfer material for replacing fullerene derivatives in photovoltaic applications with their relatively lower expense compared to fullerene derivatives as acceptors, as well as better light–harvesting, ease of synthesis and modification [49]. As was the case for their photochemical properties, comparatively less influence on the electrochemical features of perylene dyes in solution is recognized from a variety of the groups bonded from the imide positions. However, the distinct moieties at the core–/bay– position of the perylene chromophore have apparent impacts on the electrochemical data. As an example, bay substituted PDIs with cyano and fluoro groups are over 0.3 V more easily reduced and have a much higher oxidation potential than unsubstituted perylene diimide compounds [48]. The inductive effect from the electron–withdrawing groups shows these changes in the electrochemical properties, which could stabilize the PDIs by decreasing the energy levels of both the LUMO and HOMO to similar degrees. Bay substituted perylene diimide derivatives with conjugated substituents are somewhat more readily reduced in comparison with unsubstituted perylene diimides regardless of whether donor or acceptor groups are bonded. The reason could be the extension of conjugation as conjugated substituents are incorporated in their bay positions. The

substituents on imide position show limited effect on photochemical and electrochemical properties of perylene diimides, different functional groups was bonded to the imide positions in order to increase the solubility and molecular packing in the solid state, while their perylene diimides remain mostly unaffected. On the other hand, efforts on modification of perylene diimides with various optical and redox properties have been improved by attaching different moieties at the bay area of perylene dyes [48, 49].

2.6 Development of the Perylene Dyes

The preparation of the perylene dyes can be contemplated in three different synthetic routes. In the first generation, different perylene diimide dyes were obtained mainly by the diversity of the primary amine functional groups, which can particularly play a role in the solubility and the color of the perylene derivatives in the solid−state. [44−46]. Moreover, the versatility of these attempts is very restricted with respect to the development of either their electrochemical or photochemical features. In the second generation, the research area has been moved to substitution on the bay area modification (1−, 6−, 7−, and 12− positions of the perylene chromophore), which lead them not only to adjust their electronic and optical properties but also to improve the dissolution of dyes at the same time by inspiring a distortion in the aromatic perylene fluorophore [50]. The last generation includes the modification of the 2−, 5−, 8−, and 11− positions which are known as an ortho− area of the perylene chromophore, which mostly assisted in keeping the planarity of the perylene backbone on the functionalization [51]. This new way for functionalization arisen very recently and hereby it is still in the stage of improvement.
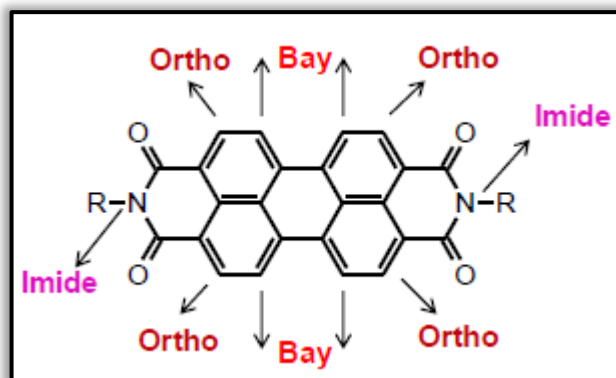
Figure 2.2: Modification of the perylene dyes

2.6.1 Imidization

Substitution at the imide position includes the condensation reaction mechanism between PDA and also aromatic or aliphatic amino functional groups, which concludes with the synthesis of the convenient perylene diimide derivatives after applicable purification methods in high yields [44−46, 50]. The solubility property of the synthesized perylene diimide derivatives modifies mainly with the effect of the imido−substituent groups. Short and aliphatic hydrocarbon alkyl units on the imide position because the perylene dyes to mostly indissoluble in commonly used solvents. Whereas the applications of perylene dyes in the electronics and organic photovoltaic field generally need these dyes with good solubility in organic solvents [51]. Accordingly, in 1995, 'swallow tails' are presented by Langhals and coworkers. Those bulky and steric hindering amino moieties have destroyed the planarity of the perylene fluorophore, thereby decreasing the intra and intermolecular face−to−face $\pi \rightarrow \pi$ interactions.

2.6.2 Bay modification

Optical and electronic features of the perylene dyes are strongly altered on substitution of the bay−positions on the perylene core with either electron−acceptor or electron−donor moieties [50]. For this reason, the exploration of Böhm and coworkers

that PDA was brominated to form highly pure 1,7−dibromo−PDA regioisomer in 1997 then, after the formation of imid, bromine (Br) atoms could be replaced with alkynyl, phenoxy, and alkoxy substituents, has founded a landmark in the area of perylene diimides. These chemical routes assisted to increase the dissolution of perylene dyes and opened up an influential path to tune their optical, electronic and redox features parallelly owing to modification of the perylene chromophore with either acceptor or donor moieties. Furthermore, the bay−/ core− functionalization was supplied as additional locations, intercalary through the imide positions, for the attachment of other fluorophores, which is requisite for the synthesis of the extra complicated molecules. In 2004, an exhaustive study was achieved by Würthner and coworkers, on the synthetic method utilized for the bromination of PDA and subsequent imido−substitution. Their work aimed to reveal that the bromination reaction forms 1,7− and 1,6−dibromoperylene dianhydrides (1,7− and 1,6− Br−PDA) mixture of isomers since it is not regioisomerically selective [48]. Hereby, the condensation reaction occurs after bromination for imide formation with cyclic amine and produces a mixture of 1,7− and 1,6−dibromoperylene diimides regioisomers as well, which could be characterized by using spectroscopic technics. Würthner and coworkers successfully isolated pure 1,7−dibromoperylene diimide regioisomer from the mixture by utilizing the crystallization technique and then characterized with nuclear magnetic resonance spectroscopy. Till now, it stays the only available synthetic way in order of yielding pure 1,7−dibromoperylene diimide regioisomer [48].
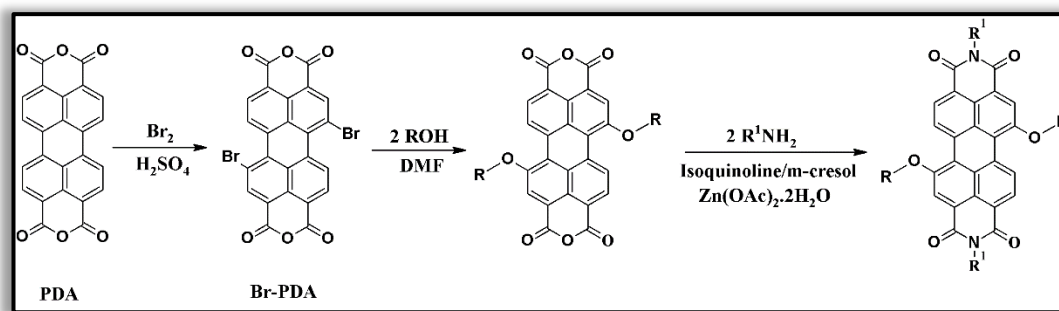
Figure 2.3: General synthesis scheme of bay substituted PDI

2.7 Self assembly

One of the major difficulties in supramolecular chemistry is to create excellent organized units whose function and chemical structure can be controlled in ways that are not possible with conventional modification techniques [52]. Solution−phase, bottom−up self−assembly of nanoscale systems constructed from stacked aromatic units offer a lot of promise for making functional units with massive structural and electrical characteristics. PDIs have arisen as an important sort of dyes for an ultimate realization of relations structural property in the different PDI systems, and a wide range of application areas in organic electronic, emission spectroscopy and solar cell devices [53]. Additionally, the facility of functionalization of the PDI system chemically by different substituents performs them a superb area for modifying those perylene diimides into ordered building blocks for oriented self−assembly. Owing to these properties, PDI dye assemblies have been widely employed as prototypical functional supramolecular systems for studying a variety of PDI fluorophore motifs [53]. Both H−type and J−type excitonically coupled states result from these perylene−perylene intermolecular interactions, and their differing characteristics and energies are greatly influenced by the stacking distance and also transverse and longitudinal offsets among neighbor perylene structures [54]. Both in self−assembled

26

arrays in the solid−state and solution−state, PDI structures without substitution from bay−/core− locations have a significant proclivity to develop face−to−face $\pi \rightarrow \pi$ interaction and slip−stacked H−aggregate geometry. In opposition to modified PDIs from four different bay positions show distinct packing motifs and in just infrequent situations with co−facial slip−stack, the rearrangement among adjacent perylene structures was reported [55].

2.8 Perylene Diimides in Dye Sensitized Solar Cells

The primary study corresponding to DSSCs introduced by Grätzel dates back to 1991 [56]. In DSSCs, sunlight to electic conversion efficiencies using Ru based complexes surpass 7% as the photo sensitizer stimulated the further development of this technology by both scientists and engineers. Perylene dyes were also performed in DSSCs as photosensitizers, in addition to their application in traditional solar cells, because they can be modified with anhydride or carboxylic acid groups that serve as anchoring groups for binding to working electrode which is semiconductor material. In addition, those extremely fluorescence perylene dyes simplify time−correlated emission studies, enabling charging injection rates to be calculated, beginning with the discovery of a 190 fs electron injection rate for 2,5−bis(tert−butyl)−9−methyl phosphonic acid perylene dye was adsorbed on semicontor surface [57]. This consequence outdoored a new era for the improvement of PDIs in DSSCs.

The solar cell application of perylene imide dyes as photosensitizers has been started with a sensitizing dye−semiconductor combination consisting of P1 and P2 (Figure 2.4) with a carboxylic acid group to anchor onto SnO_2 [58]. On a 2.5 m thick nanoporous SnO_2 layer, the dye was coated on FTO glass. The counter electrode, as well as a platinum−coated F−SnO_2 glass surface, were exhibited. Cells consisting of

photosensitizer P1 have shown the overall light to the power conversion performance of near 0.89% with such a device structure.
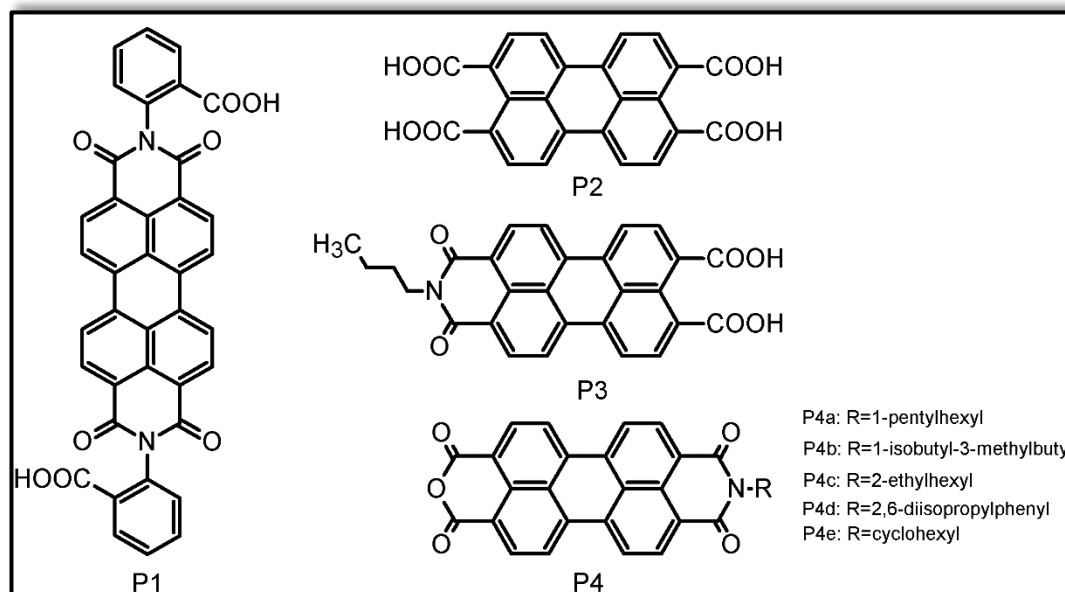
Figure 2.4: PDI derivatives for DSSCs

Although the efficiency of 0.89 % at the time was very moderate, the notion of using PDI derivatives for DSSCs could be confirmed. Later, many different PDI compounds were synthesized and explored. Examples of perylene diimide dyes adsorbed on TiO_2 semiconductor materials are the P2 and P3 sensitizers [59]. The working electrode which is TiO_2 nanocrystalline thin film bromine−doping would increase the maximum IPCE of P3 to 40% at 440−530 nm wavelength. In addition, anhydrides as anchoring groups were used to synthesize differen PDI derivatives as a photo−sensitizers P4 [60]. The aim of the investigation was to observe how the amino functional group diversity in perylene monoimide affected the cell power conversion efficiency of the device. The most important result was that perylene compounds with long alkyl and branched backbones were capable to reach higher photovoltaic performance, as an instance, photo−sensitizer P4a with a 1−pentylhexyl in the dye resulted in the highest light to

power conversion performance of 1.61%. Nevertheless, these efficiencies are so less than expectations for industrial applications. The weak part of the concept of P1−P4 is that these dyes have no intermolecular interaction because they are all lacking donor moieties. Only an ordinary fluorophore with a strong anchoring group is used in the photo−sensitizers. As a result, electron transport from the sensitizer molecule to the metal oxide's conduction band may be ineffective.

Later research focused on the substitution of donor groups on the perylene chromophore [61]. Derivatives of perylene monoimide monoanhydride substituted from bay position with the 1,6−pyrrolidine (compound P5−P8) are aimed to have the subsequent benefits. To begin with, pyrrolidine units have an effective donor aptitude that significantly moves to the first oxidation potential as well as the first reduction potential in a positive way. These could result in higher photovoltaic performance. Moreover, substituents from bay−/core− positions generally prohibit the aggregation of sensitizer molecules on the semiconductor layer and as a result, intermolecular charge recombination will be inhibited. The perylene monoimide monoanhydrides which are P5 and P6 worked better than the perylene diimides which are P7 and P8 with phenylcarboxy acid substituents as anchoring groups. Because phenyl carboxylic acid substituents kept the fluorophores at a larger space from the TiO_2 layer which is inconvenient for transportation of the electrons. Photo−sensitizer P5 has shown the highest efficiency of 2.6%.
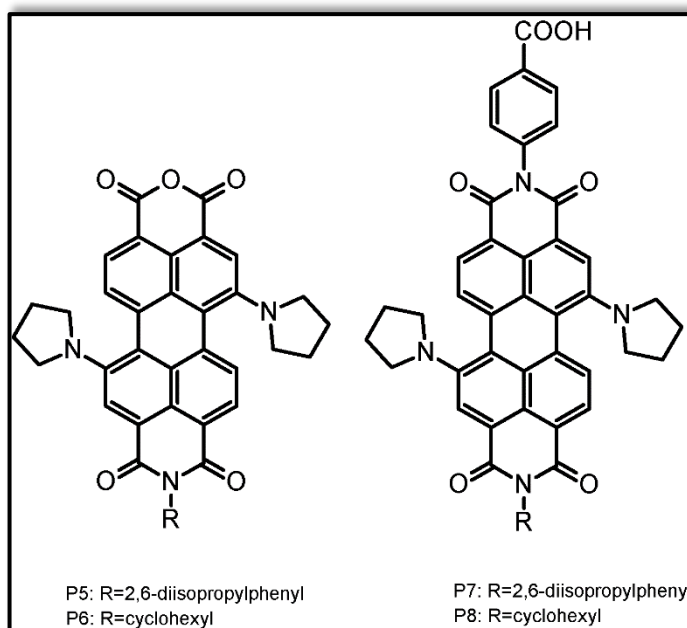
Figure 2.5: Bay−substituted PDI derivatives for DSSCs

Identical approaches were proposed to investigate the effects of, first, electron−donating substituents like piperidine or phenoxy on the perylene chromophore, second, the placement of the anchoring functional moiety, and third, the existence of a fused benzimidazole unit on power conversion efficiency [62]. Conversion efficiencies of the cells are improved from 0.2% to 2.3% with these dye molecules used in the construction of the device. Important inventions were, that first, structures with four different alkoxy moieties in the core area of PDI chromophore indicated a parallel attitude to systems with two piperidine systems. Systems with the alkoxy groups show less amount of aggregation and a slightly more efficiency. Second, the injection of electrons performance has been improved via the location of the anhydride, which is bonded to the perylene moiety directly, against benzoic acid, which stretches the space among the carboxylic acid anchoring group and a perylene core. Third, adding a benzimidazole group causes a redshift in the absorption spectra; however, because benzimidazole is an electron−rich compound, it could be deposited as far away from the anchoring and electron acceptor material as possible.

As a result, perylene diimide dyes indicate high efficiency in DSSCs owing to their excellent light absorbing capacity. Special attention is the perylene monoimide monoanhydride, as the utilization of anchoring groups like anhydride reduces the space between the semiconductor and chromophore. Perylene diimides and perylene monoimide monoanhydrides present no remarkable overall dipole. The inclusion of an electron−withdrawing group on both sites of the molecule precludes a directed photo−generated charge transfer from the dye to the CB of TiO_2. This could be the reason why perylene dyes in DSSCs only attain cell efficiencies of up to 3.08 percent and could not compete with Ru−based complexes [63].

2.9 Metal Complex Sensitizers in Dye Sensitized Solar Cell Devices

In general, metal coordinated photosensitizers have ancillary and anchoring groups used as ligands. Ligands with anchoring ability are chromophoric moieties and are also responsible for adsorption of the metal complex onto the TiO_2 thin film surface. Ancillary ligands have been utilized to improve the overall features of the metal coordinated dyes and are not bonded directly upon the semiconductor surface [64].

In the visible region of the electromagnetic spectrum, polypyridinic coordinated compounds containing d^6 metal atoms show efficient metal to ligand charge transfer (MLCT) bands with a potential affinity for increasing charge injection pathways to the conduction band of broad bandgap in TiO_2 semiconductor [64]. The power of the MLCT bands could be developed regularly by adjusting the anchoring ligands also via replacing its substituents or the ancillary ligands.

Because of the many various ways to regulate the MLCT energy, several distinct types of product for semiconductor sensitization have been developed. The highest power

conversion efficiency in between them was succeeded by applying Ru(II) polypyridyl dyes as sensitizers in the manufacturing of DSSCs. These complexes have been widely used as photosensitizers because of their good spectroscopic, excited−state and electrochemical properties. Especially carboxylic pyridine derivatives with ruthenium(II) complexes were reacted promptly with oxide superficies to produce the suitable ester molecules, allowing effective binding onto the TiO_2 surface and increased power conversion capacity, reaching good effects.

Most of the researches in manufacturing of DSSCs has concentrated on Ru(II) complexes essentially owing to their strong charge−transfer (CT) excitation ability across the near infrared region and wide and tunable oxitaditon and reduction characteristics [65]. But precious Ru based dyes have some clear disadvantages that restricted their industrial application such as the poor absorption capacity of these dyes in the near infrared region, limited sources of the Ru metal in the earth's crust, difficulties of the synthesis and purification of these complexes.

Transition, d−block metal coordinated sensitizers are used rarely in DSSCs, because of their lower power conversion performance and poor stability than Ru based complexes. Even though, the coordinated metal complexes have novel characteristics like attainability various organic compounds, processability, inexpensive starting materials and easy synthesis [66]. Recently, there are many efforts to construct a DSSCs based on other transition metal complexes, particularly osmium, iron, platinum, copper.
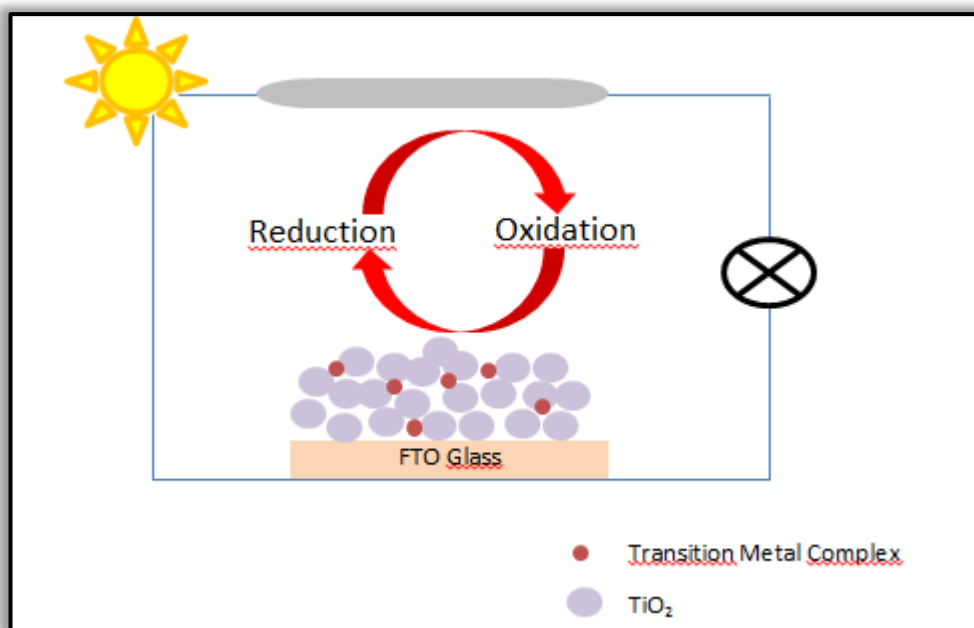
Figure 2.6: A schematic diagram of DSSC by using metal complexes

Copper metal complexes of 6,6'−disubstituted−2,2'−bipyridines have been described to be efficient photosensitizers for TiO_2. These complexes presented surprisingly high power conversion efficiencies for DSSCs. I−V components of these complexes were compared with that of N719 and were obtained to have solar light to electrical energy conversion efficiency of 1.9% and 2.3%, respectively [66].

2.10 Metal Complexation

Metal complexation can be considered as one of the elective procedures. A metal element can be attracted with a chelating agent which can be a neutral or an anion material with coordination features with two different methods. First, the metal ions compose coordination bonds with the particular ligands, ending in the generation of a metal coordinated complex compounds. In coordination bonds, the transition metals' unoccupied d−orbitals and d−shell electrons are incorporated in the interactions with the ligand lone pair electrons. Because the ligands are immediately bound to the center metal atom or ion, it is known as an inner−sphere complex. Also, metal ions can make

bonds with an anion or by other weak intermolecular interactions to form an outer−sphere complex, such as NaCl. Negatively charged ions, as well as solvent, are unable to compete with ligands for bonding to metal ions. Electrostatic and coordination attractions can happen at the same time. In many conditions, the electrostatic interactions between a negatively charged ion the metal ion and coordination ligand play also an important effect in transition element complexation.

2.10.1 Theory of Metal Complexation

In metal complex formation, a metal atom (M) is coordinated by ligands (L) by a coordination bond. Metal coordination has been resulted in an equation among the free shape of the complex components (metal and ligand) and the complex. Depend on the equilibrium constant (K) and the molarity of ligands and metal ions under the specific situations, the metal complex or the bob bonding components are mainly existing.

$$M + L \rightleftharpoons ML \tag{5}$$

$$K_1 = \frac{[ML]}{[M][L]} \tag{6}$$

The equilibrium constant presents a value describing the equilibrium among the molarity of metal complex and the free components. The inclusion of the metal complex is favored by a high value of the equilibrium constant, whereas the presence of non−bonded components is favored by a low value.

Chapter 3

EXPERIMENTAL

3.1 Materials

All the materials were purchased from commercial sources and used in synthesis and spectroscopic measurements without a further purification step. Otherwise, some of the solvents were purified by the distillation method when necessary before used. 2,4–diamino–6–phenyl–1,3,5–triazine, perylene–3,4,9,10–tetracarboxylicdianhydride, 1, 4,5,8–naphthalene tetracarboxylic dianhydride, 2–amino–1,3–propanediol 3–thiophenemethanol, (S)–(+)–1,2–propanediol, m–cresol, isoquinoline and zinc acetate were supplied from Aldrich.

3.2 Instrumentations

Fourier–transform infrared spectroscopic measurements of the synthesized compounds were recorded on 'JASCO FT–IR spectrophotometer' through potassium bromide (KBr) discs in wavenumber range from 4000 cm^{-1} to 400 cm^{-1}. Absorption spectroscopy of synthesized perylene diimides, naphthalene diimide and coordinated perylene dyes in different organic solvents and solid state were performed on 'Varian–Cary 100 spectrophotometer'. Moreover, 'Varian Cary Eclipse spectrophotometer' was used with a quartz cell to get all the emission and Φ_f measurements of compounds in the same solvents. 'Carlo Erba–1106 analyzer' was utilized to collect the percentage data of carbon, nitrogen, hydrogen and sulfur in the compound as an elemental analysis data. Mass spectrometry measurements were done

by using 'Finnigan MAT 311A instrument' and the results have shown in m/z (%) values. The ^{1}H NMR spectra of novel chromogenic dyes were performed on a 'Buker spectrometer' (400 MHz) by utilizing an internal reference which is TMS and chemical shifts have been represented in δ (ppm). TGA (thermogravimetric analysis) measurements were done on a 'Perkin Elmer–TGA Pyris1' equipment under N_2 atmosphere at a 10 ^{o}C.min^{-1} heating rate. DSC (differential scanning calorimetry) analysis for the synthesized compounds have been recorded on 'Perkin Elmer–DSC Model, Jade' equipment at heating and cooling rates of 10 ^{o}C min^{-1} under N_2 atmosphere. Electrochemical responses of synthesized products were characterized by using cyclic voltammetry (CV) technique in solution. Under argon atmosphere and at 25°C, the measurement was carried out with a CH 617E instruments workstation connected with PC monitoring. The cyclic voltammograms were obtained at 100 mVs^{-1} in dicholoromethane and in three electrode cell with the polished 2 mm glassy carbon as working electrode (WE), the Ag/AgCl as reference electrode (RE) and Pt wire as a counter electrode, respectively which were immersed in a supporting electrolyte which is 0.1 M of TBAPF$_6$ (tetrabutylammonium hexafluorophosphate). Ferrocene/ferrocenium (Fc/Fc$^+$) redox mediator was utilized as an internal reference.

3.3 Methods of Synthesis

Synthetic routes, applied purification methods and spectroscopic analyzes documents of two symmetrical perylene diimides and one naphthalene diimide, two different bay substituted perylene dianhydrides as an intermediate derivatives and their three bay substituted perylene diimide dyes have been discussed in this section. Crucially, all the synthesized products have novelty in their structural formula, high chemical and thermal stabilities and wide range of absorption spectra.

3.3.1 Schematic Illustration of Synthesis of Perylene and Naphthalene Diimides
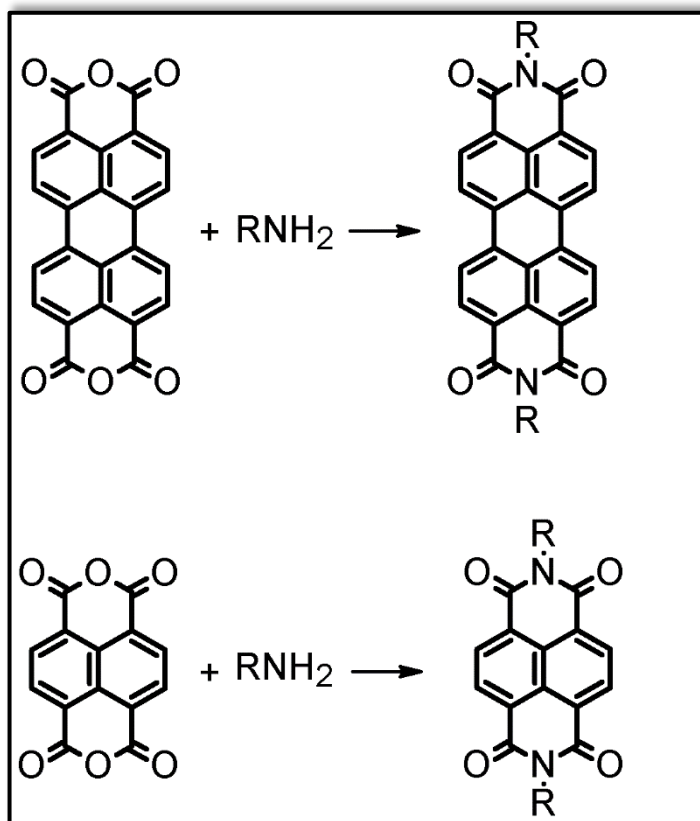
Figure 3.1: Synthesis scheme of perylene and naphthalene diimides R:
2,4–diamino–6–phenyl–1,3,5–triazine, 2–amino–1,3–propanediol

Symmetrical perylene and naphthalene diimides were produced by the synthetic routes reported earlier [44–46].

3.3.2 Schematic Illustration of Synthesis of Bay Substituted Perylene Diimides

The preparation of bay substituted perylene derivatives has been completed in three successive reaction steps of the first one is bromination, the second one is the substitution from the bay positions and the third one is imide functionalization that the common reaction diagram is represented below.

Step 1:
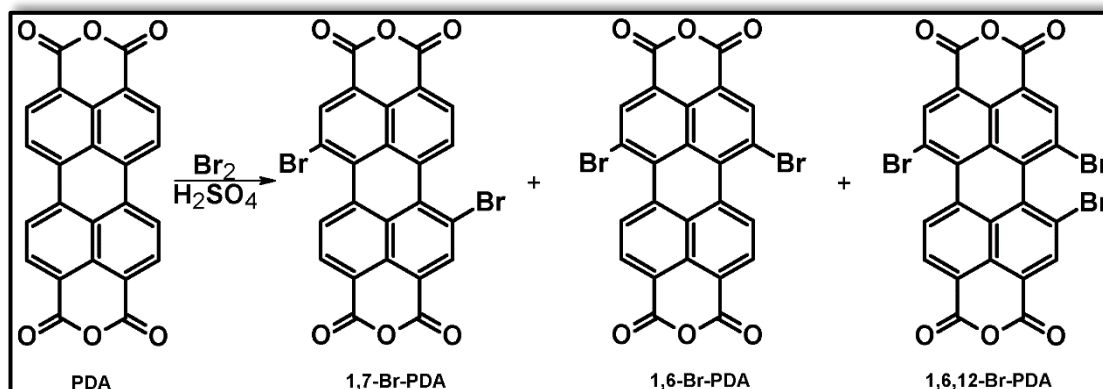
Figure 3.2: Synthesis scheme of brominated perylene dianhydride

Bromine substituted perylene tetracarboxylic dianhydride, shortly Br–PDA has synthesized with respect to the method given in the literature [50] and the crude compound was a mixture of 1,6– and 1,7–dibrominated perylene dianhydride regioisomers together with a small quantity of 1,6,12–trisubstituted one.

Step 2:
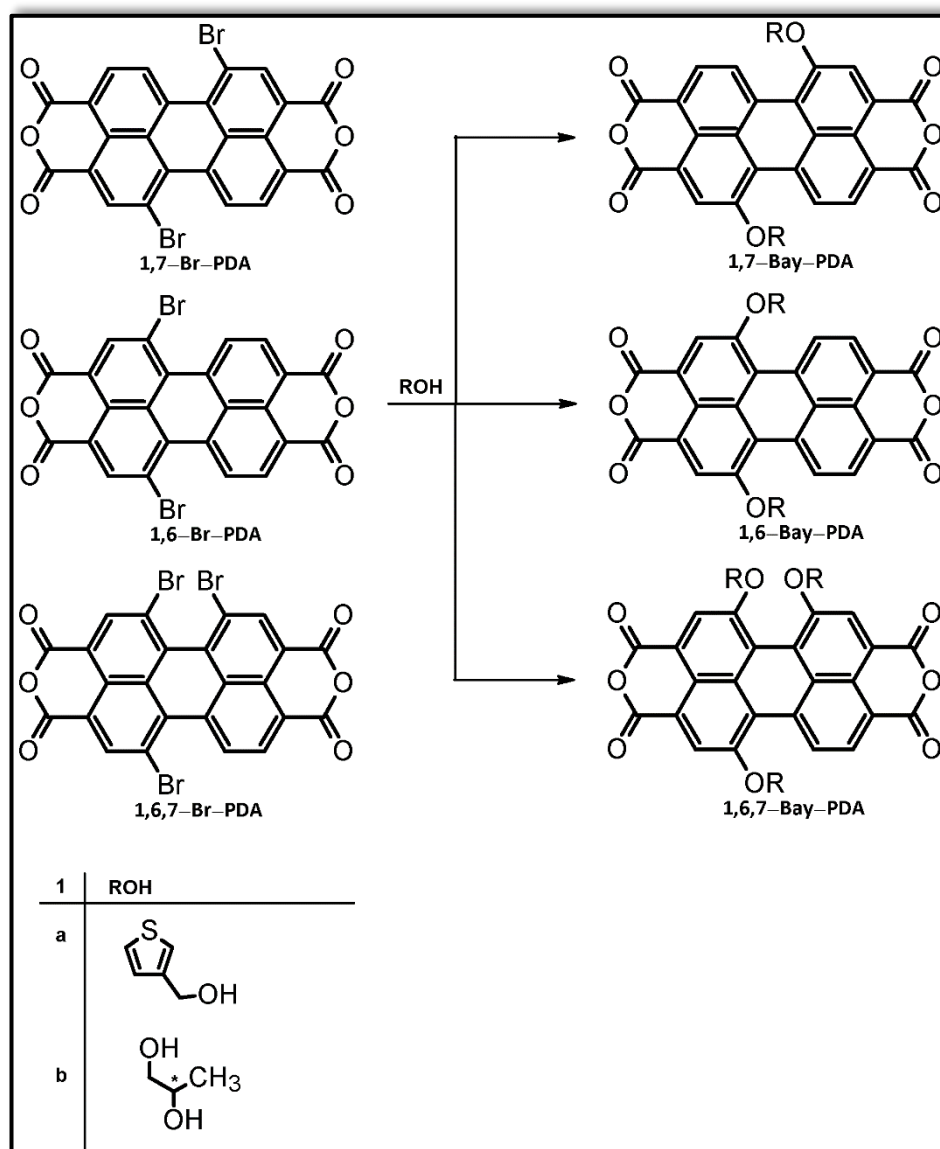
Figure 3.3: Synthesis scheme of bay substituted perylene dianhydride

The crude product of Br–PDA regioisomeric mixture and selected alcohols have been

entered the modification from bay substitution to reaction without isomeric isolation

of the mixture, according to the method of synthesis suggested in the literature [50].

Step 3:
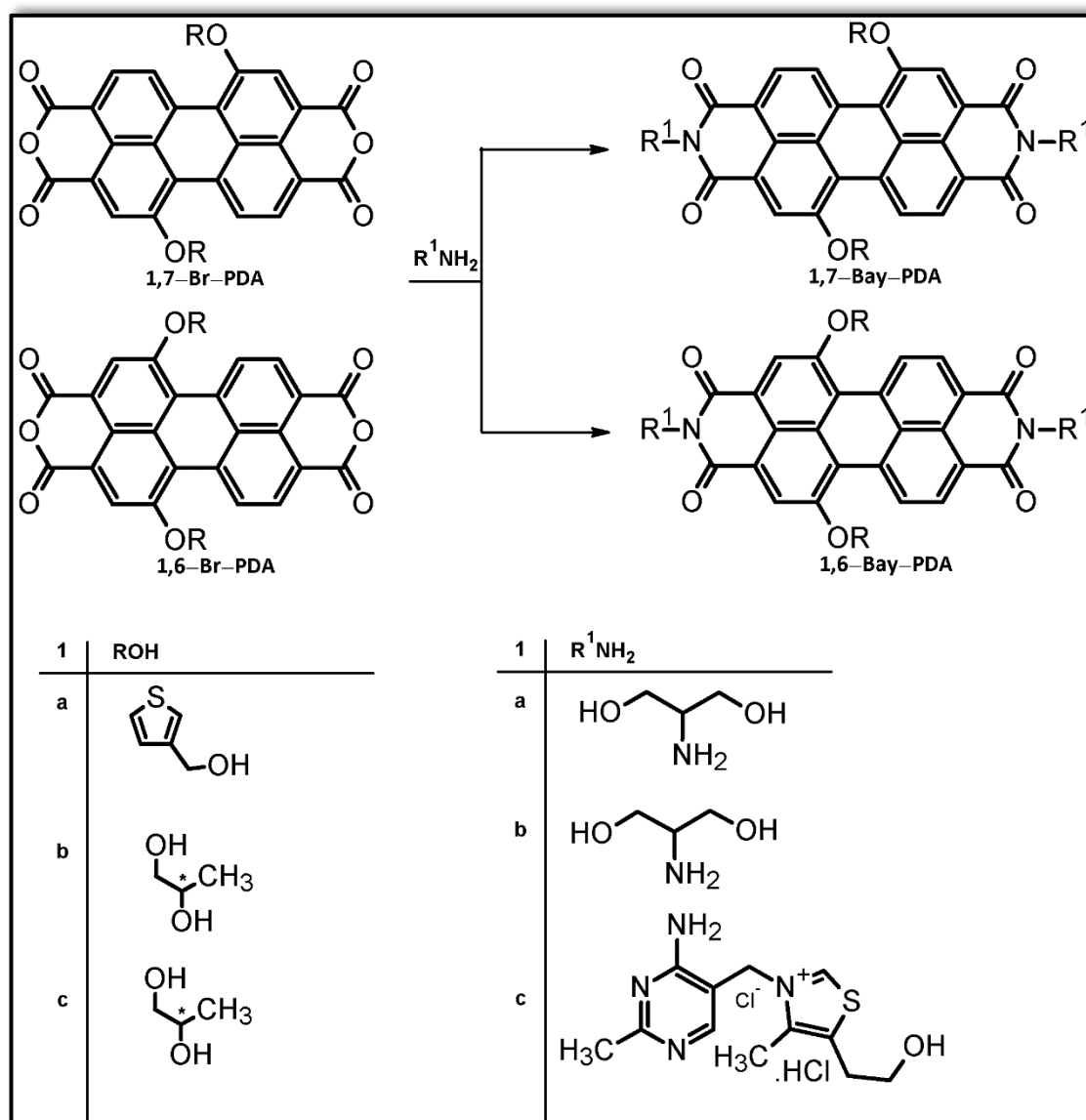
Figure 3.4: Synthesis scheme of bay substituted perylene diimide

The condensation reaction of bay substituted PDAs with distinct aromatic or bulky amine units was applied depending on the proposed procedure in the literature [44–46]. Since the solubility of the regioisomers mixture has been changed at this point, the purification of 1,6,7–trisubstituted regioisomer has been completed according to the literature [50]. As a result, 1,7–disubstituted derivative was observed in good amount comparing to the other regioisomer.

3.4 Synthetic Route of *N,N'*–bis(5–amino–3–phenyl–2,4,6–triazinyl) perylene–3,4,9,10–tetracarboxylic diimide (TAPDI)
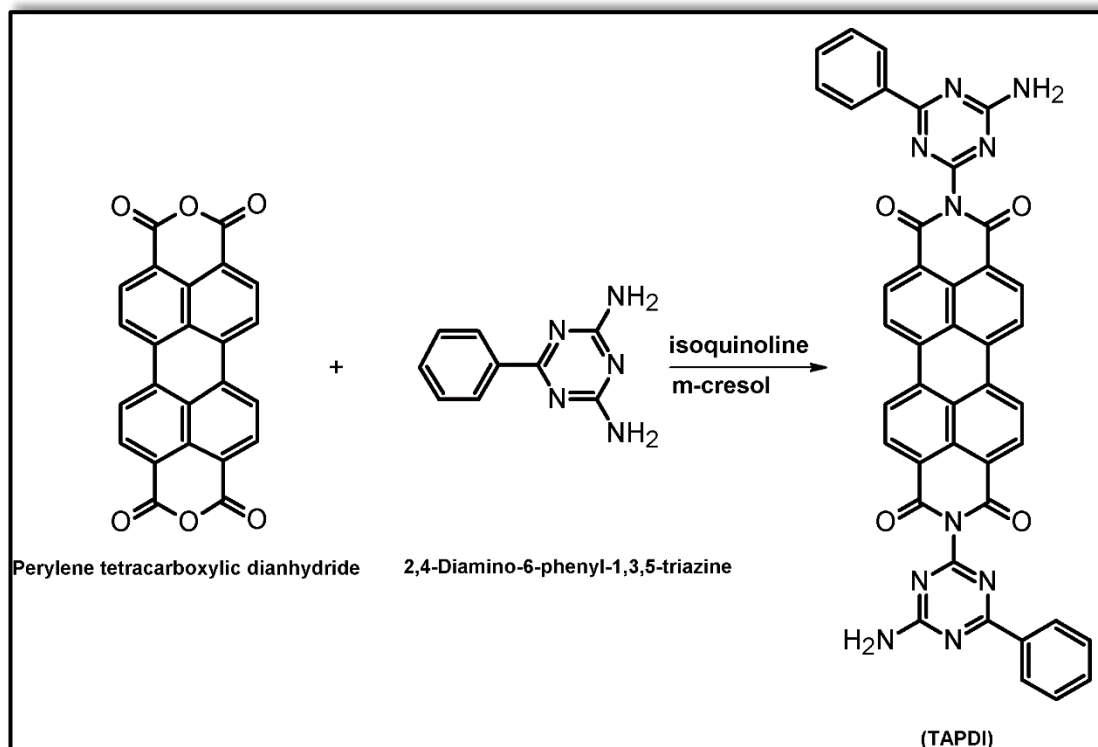
Figure 3.5: Synthesis scheme of
N,N'–bis(5–amino–3–phenyl–2,4,6–triazinyl)perylene–3,4,9,10–
tetracarboxylicdiimide (TAPDI)

The triazine substituted perylene diimide was synthesized by one–step condensation of aromatic amine 2,4–diamino–6–phenyl–1,3,5–triazine (5.84 g, 31.2 mmol) with PDA (1.0 g, 2.6 mmol) under an argon atmosphere in mixture of dried solvents (40 mL isoquinoline and 30 mL *m*–cresol). The mixture of reactants was stirred at 100℃ for 12h, at 140℃ for 5h, at 160℃ for 13h, at 180℃ for 16h and finally at 200℃ for 24h. The reaction mixture was let to decrease the temperature to 25°C and then allowed into 0.3 L of CH_3CH_2OH solvent. The crude product was filtrated and purified from high boiling point solvent and unreacted amine with acetone solvent by using the soxhlet apparatus. The pure compound was dried in a vacuum oven.
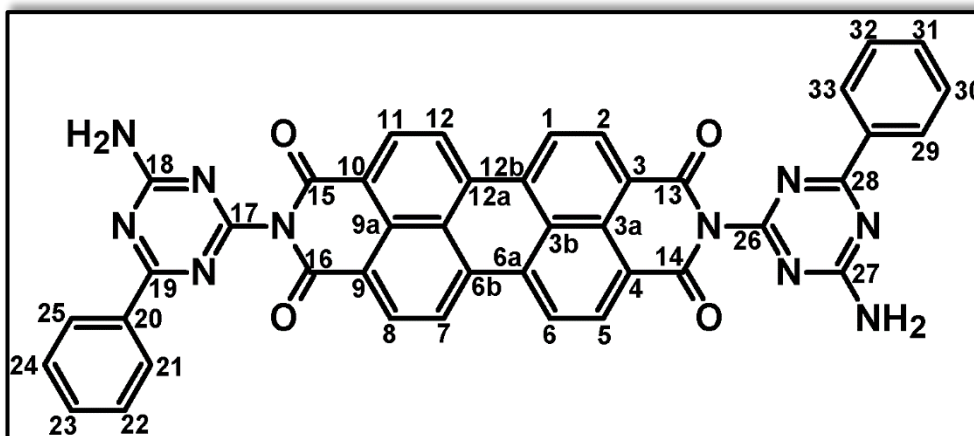
Figure 3.6: N,N'–bis(5–amino–3–phenyl–2,4,6–triazinyl)perylene–3,4,9,10–
tetracarboxylicdiimide (TAPDI)

Yield: % 65.43.

FT–IR (KBr, cm^{-1}): 3486, 3431, 3373 and 3326 (amine N–H stretch), 3228 and 3061 (aromatic C–H stretch), 1710 and 1667 (imide C=O stretch), 1619 (N–H bend), 1594 (aromatic stretch C=C), 1397, 1364 and 1344 (imide C–N stetch), 811,741 and 655 (aromatic C–H bend).

UV–vis (NMP) (λ_{max} / nm): 462, 492, 527, 679, 701, 712, 765, 794.

Fluorescence (NMP) (λ_{max} / nm): 541, 578, 631. **Φ_f = 0.60.**

Anal. Calcd. for (C$_{42}$H$_{22}$N$_{10}$O$_4$) (Mw, 730.68868)**:** C, 69.04; H, 3.03; N, 19.17; Found: C, 66.55; H, 3.71; N, 18.45.

^{1}H NMR, (δH ppm, 400 MHz, CDCl$_3$:CF$_3$COOD (3:1), Figure 4.85): 8.8 (dd, 8H, H–C(1), H–C(6), H–C(7), H–C(12), H–C(21), H–C(25), H–C(29), H–C(22)), 8.28

(d, 4H, H–C(2), H–C(5), H–C(8), H–C(11)), 8.02 (t, 4H H–C(23), H–C(31)), 7.83 (t, 4H, H–C(22), H–C(24), H–C(30), H–C(32)), 7.63 (s, 4H, H–C(18), H–C(27).

3.5 Synthetic Rotue of N,N'–Bis(2–hydroxy–1–(1–hydroxymethyl) ethyl)perylene–3,4,9,10–tetracarboxylic diimide (HEPDI)
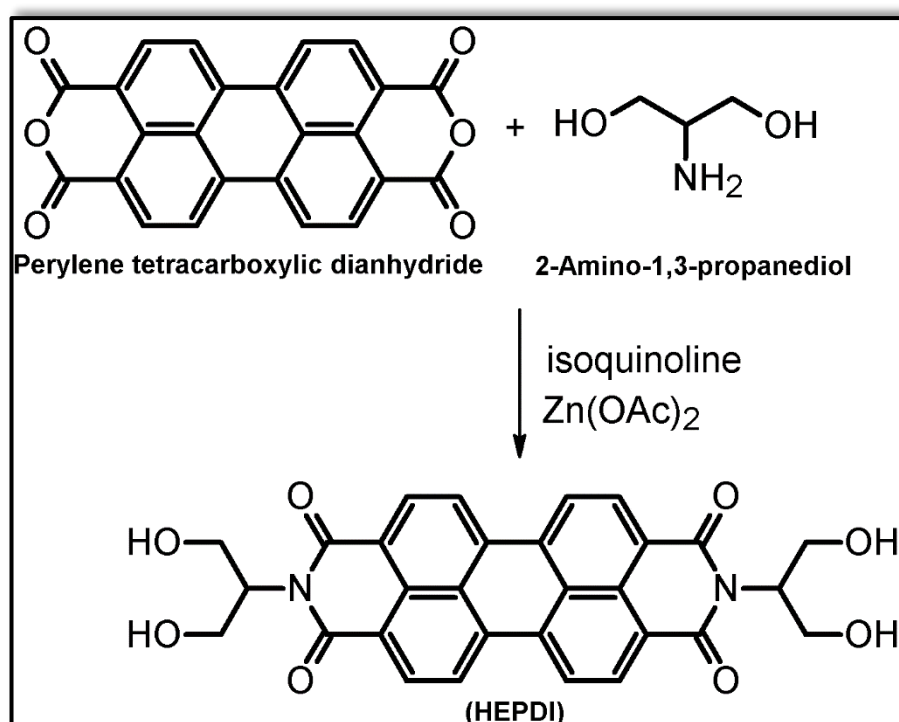
Figure 3.7: Synthesis scheme of N,N'–bis(2–hydroxy–1–(1–hydroxymethyl) ethyl)perylene–3,4,9,10–tetracarboxylicdiimide

The symmetric PDI was synthesized in a 100 mL under an argon atmosphere by condensation reaction of amine, 2,4–amino–1,3–propanediol (0.93 g, 10.2 mmol) with PDA (1.0 g, 2.55 mmol) in mixture of dried solvent mixture (40 mL of isoquinoline). The mixture of reactants was stirred at 80°C for 8h, at 100°C for 5h, at 120°C for 8h, 160°C for 4h, 180°C for 8h and lastly at 200°C for 3h. The reaction mixture was let to cool to 25°C and then added into 0.3 L of cold acetone. The crude product was filtrated

and later the compound was cleansed in a soxhlet apparatus with acetone solvent. The pure compound was dried in a vacuum oven.
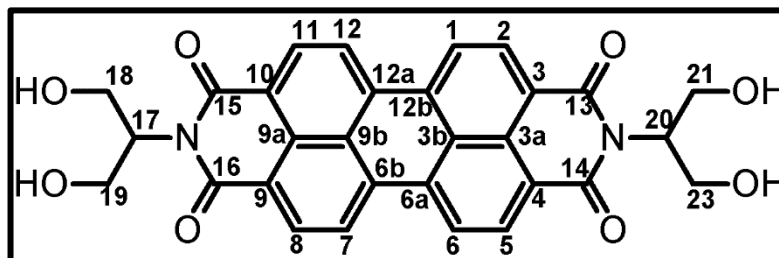
Figure 3.8: N,N'−Bis(2−hydroxy−1−(1−hydroxymethyl) ethyl)perylene−3,4,9,10−tetracarboxylicdiimide (HEPDI)

Color: black powder; **Yield:** % 86.50.

FT−IR (KBr, cm^{-1}): 3429 (O−H), 3054 (aromatic C−H stretch), 2924, 2851 (aliphatic C−H stretch) 1687 (imide C=O stretch), 1597 (aromatic C=C stretch), 1367 (imide C−N stretch), 809, 743 and 661 (aromatic C−H bend).

UV−vis (NMP) (λ_{max} / nm): 459, 489, 523.

Fluorescence (NMP) (λ_{max} / nm): 536, 576, 629. Φ_f = 0.03.

Anal. Calcd. for ($C_{30}H_{22}N_2O_8$) (Mw, 538.50): C, 66.91; H, 4.12; N, 5.20; Found: C, 69.20; H, 2.73; N, 7.69.

^{1}H NMR, (δH ppm, 400 MHz, CDCl$_3$:CF$_3$COOD (3:1), Figure 4.90): 8.34−8.11 (dd, 8H, H−C(1), H−C(2), H−C(5), H−C(6), H−C(7), H−C(8), H−C(11), H−C(12)), 4.25−4.04 (s, 4H, H−O), 3.30−3.17 (d, 8H, 2 H−C(21), 2 H−C(23), 2 H−C(18), 2 H−C(19)), 2.23−2.12 (m, 2H, H−C(17), H−C(20).

3.6 Synthetic Route of *N,N'*–bis(5–amino–3–phenyl–2,4,6–triazinyl) naphthalene–1,4,5,8–tetracarboxylic diimide (TANDI)
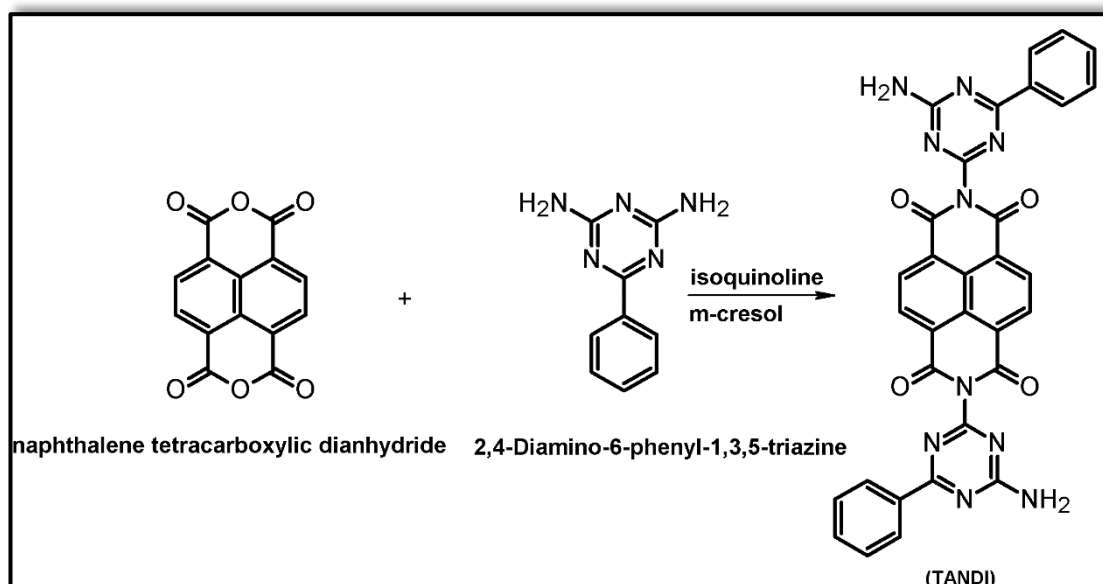
Figure 3.9: Synthesis scheme of
N,N'–bis(5–amino–3–phenyl–2,4,6–triazinyl)naphthalene–1,4,5,8–
tetracarboxylicdiimide (TANDI)

The naphthalene diimide was synthesized in a three–necked round–bottomed flask by one–step condensation of amine 2,4–diamino–6–phenyl–1,3,5–triazine (8.35 g, 44.4 mmol) with NDA (1.01 g, 3.7 mmol) in mixture of dried solvents (40 mL isoquinoline and 30 mL *m*–cresol) under an argon atmosphere. The reaction mixture was stirred at 80℃ for 8h, at 100℃ for 8h, at 120℃ for 5h, at 140℃ for 8h, at 160℃ for 8h, at 180℃ for 4h and finally at 200℃ for 6h. The reaction mixture was let to decrease the temperature to 25℃ and later added through 0.3 L of ethanol. The crude product was filtrated and dried under vacuum at 100 ℃. The synthesized NDI was later purified by using solid–liquid extraction methode with acetone solvent to get rid of high boiling point solvent and unreacted amine.
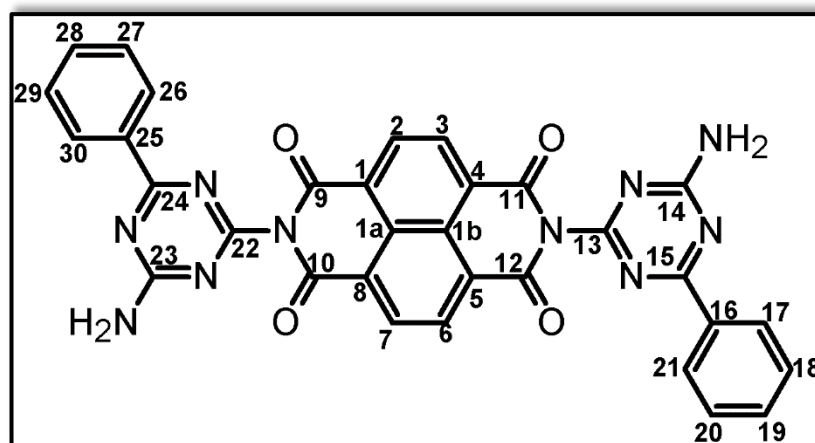
Figure 3.10: *N,N'*–bis(5–amino–3–phenyl–2,4,6–triazinyl) naphthalene–1,4,5,8–tetracarboxylicdiimide (TANDI)

Color: Yellow; **Yield:** 89 %

FT–IR (KBr, cm^{-1}): 3468 and 3341 (amide N–H stretch), 3197 and 3060 (aromatic C–H stretch), 1718 and 1682 (imide C=O stretch), 1621 (N–H bend), 1585 (aromatic stretch C=C), 1395, 1361 and 1344 (imide C–N stetch), 761, 703 and 651 (aromatic C–H bend).

UV–vis (NMP) (λ_{max} / nm): 340, 358, 378, 414.

Fluorescence (NMP) (λ_{max} / nm): 426, 459, 498. Φ_f = 0.01.

Anal. Calcd. for (C$_{32}$H$_{18}$N$_{10}$O$_4$) (Mw, 606.54992)**:** C, 63.37; H, 2.99; N, 23.09; Found: C, 63.39; H.3.17, ; N, 20.95.

^{1}H NMR, (δH ppm, 400 MHz, DMF), Figure 4.86–Figure 4.87: 8.45 (H–C(6)), 8.42 (H–C(7)), 8.32 (H–C(3)), 8.31 (H–C(2)), 7.63 (H–C(30)), 7.60 (H–C(25)), 7.58

(H–C(21)), 7.54 (H–C(17)), 7.53 (H–C(29)), 7.52 (H–C(27)), 7.51 (H–C(20)), 7.49

(H–C(18)), 7.47 (H–C(28)), 7.46 (H–C(19)), 6.67 (H–N), 6.69 (H–N)

3.7 Synthetic Route of *N,N'*–Bis(2–hydroxy–1–(1–hydroxymet hyl) e thyl)–1,7–di(3–thiophenemethoxy)perylene–3,4,9,10–tetracarboxylic diimide)
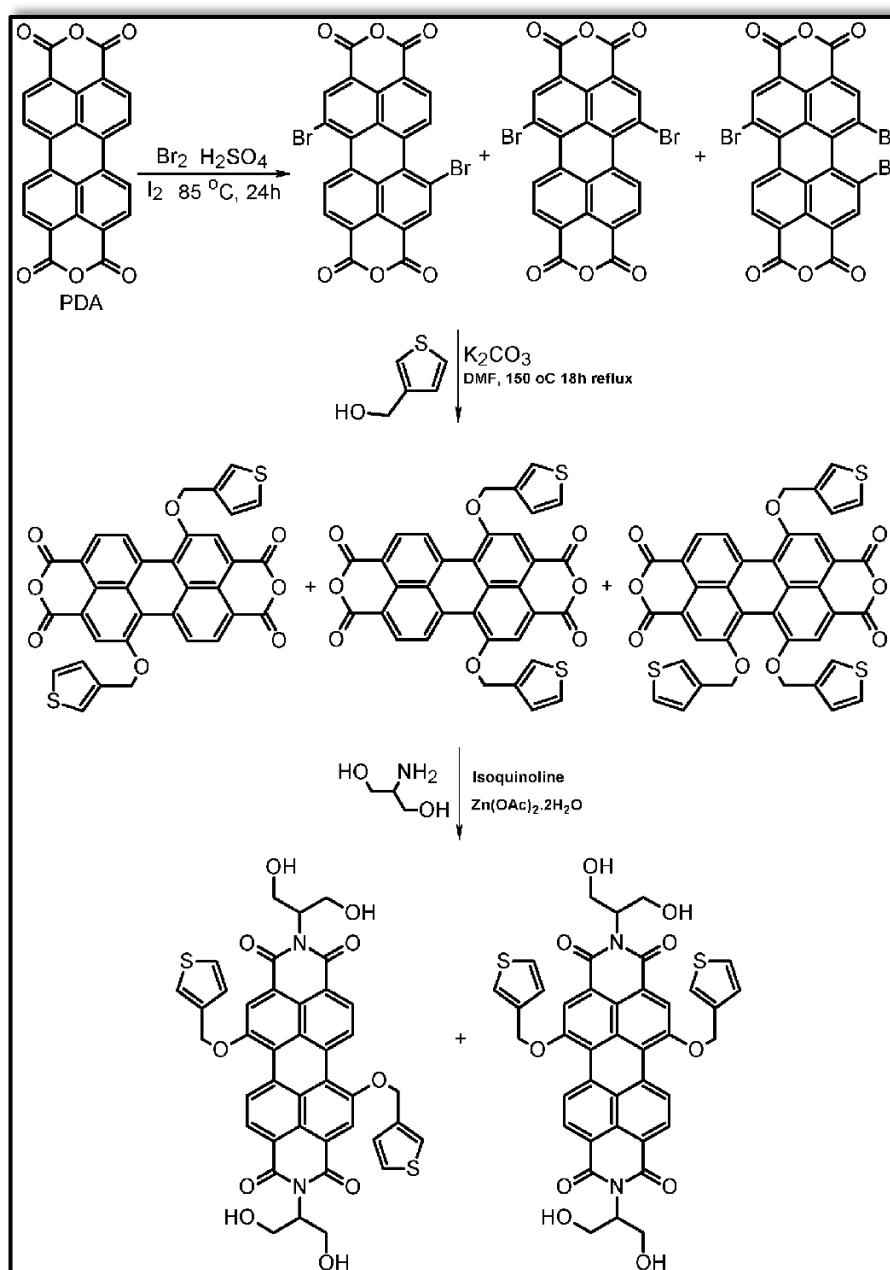
Figure 3.11: Synthesis scheme of *N,N'*–Bis(2–hydroxy–1–(1–hydroxymethyl)e thyl)–1,7–di(3–thiophenemethoxy)perylene–3,4,9,10–tetracarboxylicdiimide)

The imidization has been completed in three steps:

1) Synthesis of brominated perylene tetracarboxylic dianhydride (Br−PDA).

2) Synthesis of bay modified perylene tetracarboxylic dianhydride.

3) Synthesis of bay modified perylene tetracarboxylic diimide.

3.7.1 Synthesis of 1,7−Dibromoperylene−3,4,9,10−tetracarboxylic dianhydride

Bromination of perylene tetracarboxylic dianhydride was done according to the reference [50], 2 g (5.1×10^{-3} mol) of PDA was stirred in 30 mL of sulfuric acid (reaction grade, H_2SO_4) for 6h at 25°C and 24 h at 60°C. Later, 0.06 g (0.236 mmol) of catalyst which is iodine (I_2) was added at 25°C and stirred for 2h, and additional 5h at 55°C. The 0.8 mL of bromine (15.6×10^{-3} mol) was slowly put into solution in 1h with mixing continuously for 2h at 25°C, 24h at 85°C and 2h at 100°C when the reaction mixture was cooled to 25°C. Extra amount of Br_2 was displaced from reaction mixture with argon flash. After adding 20 mL of cold water gently, precipitate was settled down and later was collected by vacuum filtering. The compound is neutralized by using solid−liquid extraction technique in soxhlet apparatuses with pure water. The pure product was made ready to use in another reaction as a starting material after drying well in vacuum oven.
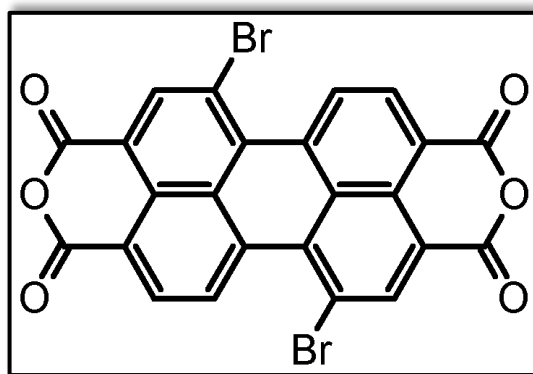
Figure 3.12: 1,7−Dibromoperylene−3,4,9,10−tetracarboxylicdianhydride (Br−PDA)

Color: Reddish–brown powder; **Yield:** %86 (2.4 g).

FT–IR (KBr, cm⁻1): υ: 3054 (aromatic C–H stretch), 1777, 1727 (anhydride C=O stretch), 1590 (conjugated C=C stretch), 1036 (anhydride C–O–C stretch), 751, 800 (C–H bend), 694 (C–Br stretch).

3.7.2 Synthesis of 1,7–di(3–thiophenemethoxy) perylene–3,4,9,10– tetracarboxylic dianhydride (TM–PDA)

Under argon atmosphere, a solution of 1 g of Br–PDA (1.82 mmol), 0.622 g K_2CO_3 (4.50 mmol) used as a catalyst, 0.507g of 3–thiophenemethanol (4.44 mmol) and dry DMF (30 mL) solvent is mixed carefully at 150°C for 18h. The reaction mixture is allowed through distilled water:acetic acid solvent mixture with 1:1 ratio and let to decrease the temperature to 0 °C for 24h when the reaction was completed. The precipitated compound is vacuum filtered the next day and cleansed in soxhlet equipment using water for three days. The dark maroon powder was dried in an oven for few days under vacuum at 100°C.

Figure 3.13: 1,7–di(3–thiophenemethoxy) perylene–3,4,9,10– tetracarboxylic dianhydride (TM–PDA)
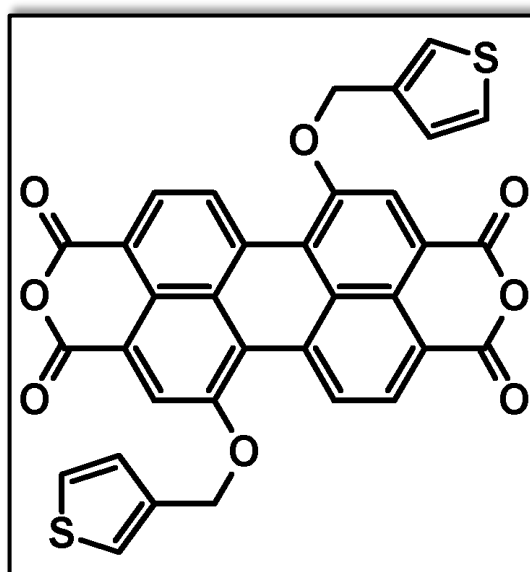
Color: Dark maroon powder; **Yield:** 49.3% (1.12 g).

FT−IR (KBr, thin film, cm^{-1}): 3063 (aromatic C−H stretch), 2923 and 2851 (aliphatic C−H stretch), 1769 and 1719 cm (anhydride C=O stretch), 1589 (conjugated C=C stretch), 1232 (ether C−O−C stretch), 1036 cm (anhydride C−O−C stretch).

UV−vis absorption (DMF) (λ$_{max}$ / nm): 486, 517.

Fluorescence (DMF) (λ$_{max}$ / nm): 549, 578, Φ_f =0.29.

Anal. Cald for C$_{34}$H$_{16}$O$_8$S$_2$ (Mw, 616.62**):** C, 66.67%; H, 2.62%; Found: C, 56.20%; H, 0.79%.

3.7.3 Synthesis of N,N−Bis(2−hydroxy−1−(1−hydroxymethyl)ethyl)−1,7−di(3−thiophenemethoxy)perylene−3,4,9,10−tetracarboxylic diimide (TM−HEPDI)

The perylene diimide was synthesized by one−step condensation of amine 2−Amino −1,3−propanediol (0.296 g, 3.24 mmol) with TM−PDA (0.5 g, 0.81 mmol) under a nitrogen atmosphere in mixture of dried solvents (40 mL isoquinoline). The mixture of reactants was heated stepwise at 60℃ for 5h, at 80℃ for 10h, at 100℃ for 8h, at 120℃ for 10h, at 180℃ for 13h and finally at 200℃ for 24h. The reaction mixture is let to decrease the temperature to 25℃ and then added through 0.3 L of acetone solvent. The crude product was filtered off and dried at 100 ℃ under vacuum (mp> 300 ℃). The compound is purified by a soxhlet apparatus in chloroform solvent to get rid of excess amount of amine, high boiling solvents, and the catalyst zinc acetate.
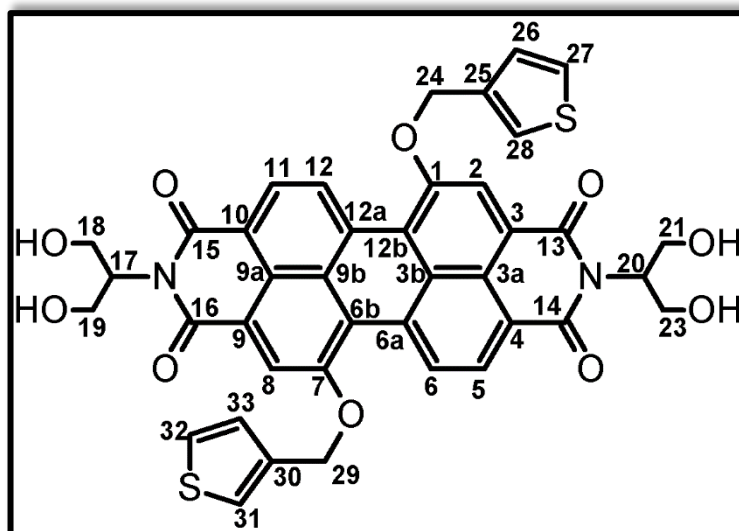
Figure 3.14: N,N–Bis(2–hydroxy–1–(1–hydroxymethyl)ethyl)–
1,7–di(3–thiophenemethoxy)perylene–3,4,9,10–tetracarboxylicdiimide
(TM–HEPDI)

Yield: 91%, black powder.

FT–IR (KBr, thin film, cm^{-1}): 3355 (O–H stretch), 3159, 3039 (aromatic C–H stretch), 2842 (aliphatic C–H stretch), 1679 (imide C=O stretch), 1582 (aromatic C=C stretch) 1264 (ether C–O–C stretch) and, 743 (aromatic C–H bend).

UV–vis absorption (NMP) (λ_{max} / nm): 484, 523, 675, 763.

Fluorescence (NMP) (λ_{max} / nm): 534, 574, Φ_f = 0.083.

^{1}H NMR, (δH ppm, 400 MHz, CDCl$_3$:CF$_3$COOD (3:1), Figure 4.89): 8.12 (dd, 6H, H–C(2), H–C(5), H–C(6), H–C(8), H–C(11), H–C(12)), 4.04 (s, 4H, H–O), 2.36–2.11 (d, 8H, 2 H–C(21), 2 H–C(23), 2 H–C(18), 2 H–C(19)), 1.43–1.31 (m, 2H, H–C(17), H–C(20).

3.8 Synthetic Route of N,N'–Bis(2–hydroxy–1–(1–hydroxymethyl) ethyl)–1,7–di(2–hydroxypropoxy)perylene–3,4,9,10–tetracarboxylic diimide (HP–HEPDI)
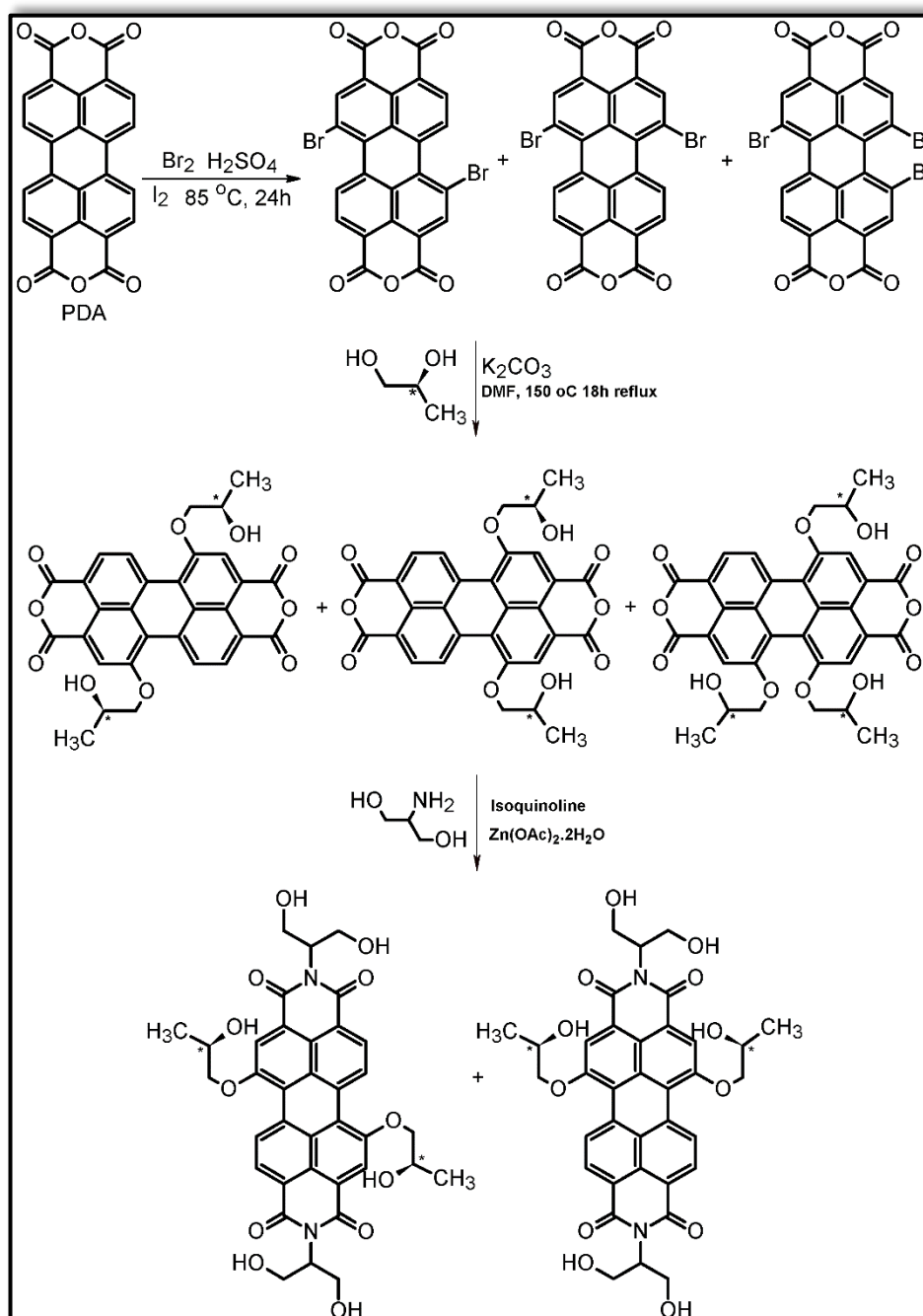
Figure 3.15: Synthesis scheme of N,N'–Bis(2–hydroxy–1–(1–hydroxymethyl) ethyl)–1,7–di(2–hydroxypropoxy)perylene–3,4,9,10–tetracarboxylic diimide (HP–HEPDI)

3.8.1 Synthesis of 1,7–di(2–hydroxypropoxy)perylene–3,4,9,10– tetracarboxylic dianhydride (HP–PDA)

A mixture of 0.338 g of S–(+)–1,2–propanediol (4.44 mmol), 1 g of Br–PDA (1.82 mmol), 0.622 g of K_2CO_3 (4.50 mmol) as catalyst and dried DMF (30 mL) were heated under argon atmosphere to 150°C for 18h. The mixture of reaction is allowed into cold water: acetic acid (1:1 ratio) mixture after completing the synthesis and was cooled at 0°C overnight. The next day, vacuum filtration was used to filter the crude product and purified by using soxhlet apparatus in pure water for 3 days. The black shiny crystals were dried in a vacuum oven.
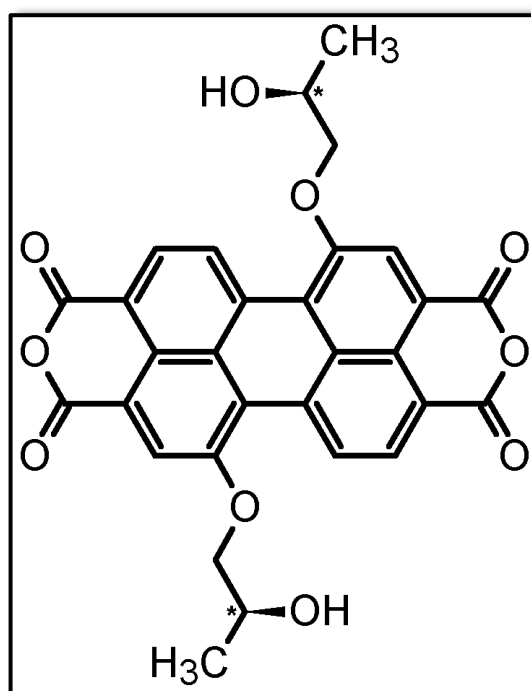
Figure 3.16:
1,7–Di(2–hydroxypropoxy)perylene–3,4,9,10–tetracarboxylicdianhydride
(HP–PDA)

Yield: 64 % (0.63 g); **Color:** black shiny crystals.

FT–IR (KBr, thin film, cm^{-1}): 2924 (aliphatic C–H stretch), 1760 and 1719 (anhydride C=O stretch), 1232 (ether C–O–C stretch), 1590 (aromatic C=C stretch) and 1012 (ether C–O–C stretch).

UV–vis absorption (DMF) (λ_{max} / nm): 418, 492, 518, 687, 755.

Fluorescence (DMF) (λ_{max} / nm): 533, 570. Φ_f = 0.03.

Anal. Calcd for $C_{30}H_{20}O_{10}$ (Mw, 540.47) Calculated: C, 66.67 %; H, 3.73 %; O, 29.60 %. Found: C, 61.43 %; H, 2.87 %; O, 35.7 %.

3.8.2 Synthesis of N,N'–Bis(2–hydroxy–1–(1–hydroxymethyl)ethyl)–1,7–di(2–hydroxypropoxy)perylene–3,4,9,10–tetracarboxylicdiimide(HP–HEPDI)

The perylene diimide was synthesized) in a three–necked round–bottomed flask by one–step condensation of amine, 2–Amino–1,3–propanediol (0.405 g, 4.44 mmol) with HP–PDA (0.8 g, 1.48 mmol) under a nitrogen atmosphere in mixture of dried solvents (40 mL isoquinoline). The mixture of reactants was stirred at 50°C for 2h, at 70°C for 8h, at 90°C for 13h, at 180°C for 16h and lastly at 200°C for 24h. The reaction mixture was let to decrease the temperature to 25°C and then allowed through 0.3 L of methanol solvent. The precipitated solution is filtrated and later purified by using solid–liquid extraction method with chloroform solvent in a soxhlet apparatus to get rid of excess amount of amine, high boiling solvents and the catalyst, zinc acetate. At the end, the pure compound was dried under vacuum.
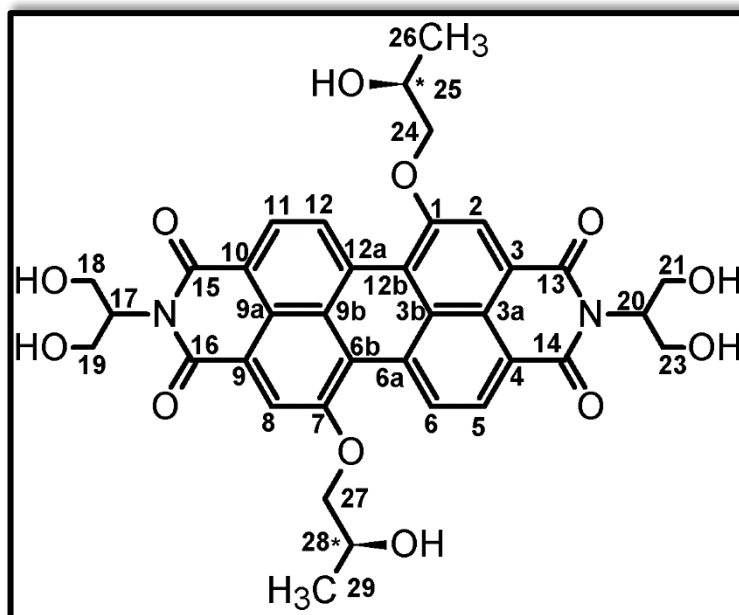
Figure 3.17: N,N'−Bis(2−hydroxy−1−(1−hydroxymethyl)ethyl)−
1,7−di(2−hydroxypropoxy)perylene−3,4,9,10−tetracarboxylicdiimide (HP−HEPDI)

Color: black powder; **Yield:** 77% (0.77 g).

FT−IR (KBr, thin film, cm^{-1}): 3053 (aromatic C−H stretch), 2924 and 2852 (aliphatic C−H stretch), 1704, 1656 and 1626 (imide C=O stretch), 1588 (aromatic C=C stretch) and, 1252 (ether C−O−C stretch) 833, 809 and 752 (aromatic C−H bend).

UV−vis absorption (NMP) (λ_{max} / nm): 489, 522, 547.

Fluorescence (NMP) (λ_{max} / nm): 535, 575, 626. **Φ_f = 0.07.**

Anal. Calcd for $C_{36}H_{34}N_2O_{12}$ (Mw, 686.66) Calculated: C, 62.97 %; H, 4.99 %; N, 4.08 %. Found: C, 61.70 %; H, 3.01 %; N, 6.80 %.

1H NMR, (δH ppm, 400 MHz, CDCl₃:CF₃COOD (3:1), Figure 4.88): 8.51–8.15 (dd, 6H, H–C(2), H–C(5), H–C(6), H–C(8), H–C(11), H–C(12)), 4.27–4.04 (s, 6H, H–O), 2.38–0.99 (dd, 22H, 2 H–C(21), 2 H–C(23), 2 H–C(18), 2 H–C(19), H–C(17), H–C(20), 2 H–C(24), 2 H–C(27), H–C(25), H–C(28), 3 H–C(26), 3 H–C(29)).

3.9 Synthetic Route of *N,N′*–bis–[3–((2–methyl–5–pyrimidinyl) methyl)–5–(2–hydroxyethyl)–4–methylthiazolium]–1,7–di(2–hydrox ypropoxy) perylene–3,4,9,10–tetracarboxylic diimide (HP–TCPDI)
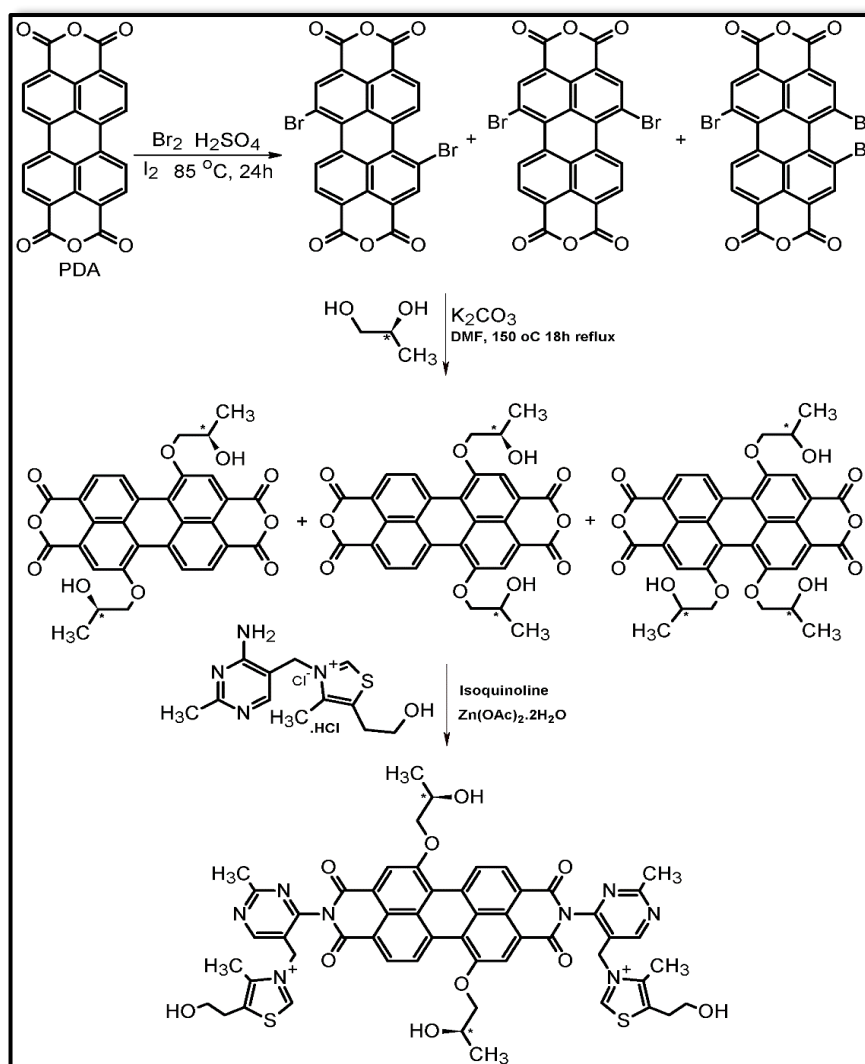
Figure 3.18: Synthesis scheme of *N,N′*–bis–[3–((2–methyl–5–pyrimidinyl) methyl)–5–(2–hydroxyethyl)–4–methylthiazolium]–1,7–di(2–hydroxy propoxy)perylene–3,4,9,10–tetracarboxylicdiimide (HP–TCPDI)

56

3.9.1 Synthesis of *N,N′*−bis[3−((2−methyl−5−pyrimidinyl) methyl)−5−(2−hydroxy ethyl)−4−methylthiazolium]−1,7−di(2−hydroxypropoxy)perylene−3,4,9,10−tetra carboxylic diimide (HP−TCPDI)

The perylene diimide was prepared under a nitrogen atmosphere by one−step imidization of amine, 2−[3−[(4−amino−2−methyl−5−pyrimidinyl)methyl]−5−(2− hydroxyethyl)−4−methyl−1,3−thiazol−3−ium−5−yl] ethanol; chloride;hydrochloride (1.25 g, 3.70 mmol) with HP−PDA (0.5 g, 9.25 mmol) in 40 mL of dried isoquinoline solvent in a round−bottomed flask. The mixture of starting materials was heated at 100°C for 12h, at 140°C for 5h, at 160°C for 13h, at 180°C for 16h and finally at 200°C for 48h. The temperature of the reaction mixture is decreased to 25°C and then allowed into 0.3 L cold acetone solvent. The raw compound is filtrated by under vacuum and then refluxed by using chloroform in a soxhlet apparatus to get rid of excess amount of amine, high boiling solvents and the catalyst, zinc acetate. The product was dried under vacuum.
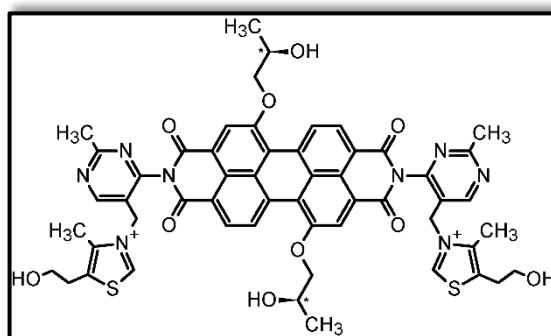
Figure 3.19: *N,N′*−bis− [3−((2−methyl−5−pyrimidinyl)methyl)−5−(2−hydroxyethyl) −4−methylthiazolium]−1,7−di(2−hydroxy propoxy)perylene−3,4,9,10−tetracarboxylicdiimide (HP−TCPDI)

Yield: 87%; **Color:** black powder.

FTIR (KBr, thin film, cm^{-1}): 3397 (O–H stretch), 3054 (aromatic C–H stretch), 2924 and 2852 (aliphatic C–H stretch), 1620 (imide C=O stretch), 1589 (aromatic C=C stretch) 1385 (C–N stretch) and 1272 (ether C–O–C stretch) 759 and 687 aromatic C–H bend).

UV–vis absorption (*m*–Cresol) (λ_{max} / nm): 508, 548.

Fluorescence (*m*–Cresol) (λ_{max} / nm): 534, 599.

3.10 Synthetic Route of Complex 1

The coordinated perylene diimide triad (complex 1) was synthesized under a nitrogen atmosphere by one step complexation of copper(II) perchlorate hexahydrate solution (0.051 g, 10 ml) with N,N–bis(5–amino–3–phenyl–2,4,6–triazinyl)perylene –3,4,9,10–tetracarbox ylicdiimide (0.05 g, 0.068 mmol) in 30 mL dried DMF solvent. The mixture of reactants was stirred at 50°C for 8h and in the end at 150°C for 24h. The reaction mixture is let to decrease the temperature to 25°C and later put in 0.3 L cold acetone solvent. The precipitated solution is filtrated and later purified with water in a Soxhlet apparatus to get rid of excess amount of copper salt and high boiling solvent. At the end pure compound is completely dried in vacuum oven.
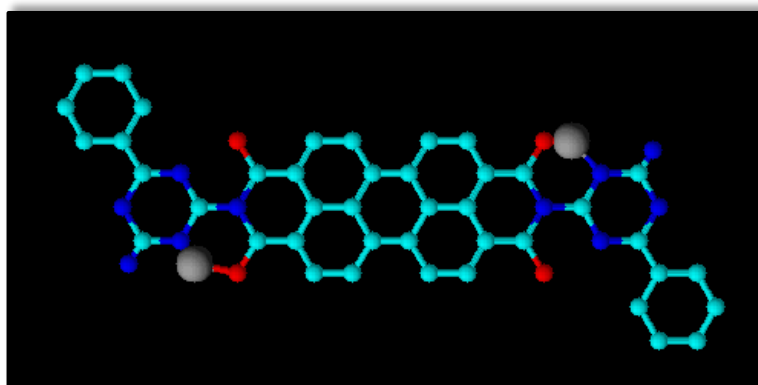
Figure 3.20: Chemical structure of complex 1

FT−IR (KBr, cm⁻¹): 3429 and 3325 (amine N−H stretch), 3054 (aromatic C−H stretch), 1704 and 1671 (imide C=O stretch), 1590 (aromatic C=C stretch), 1361 (imide C−N stretch), 809, 735 and 654 (aromatic C−H stretch).

UV−vis absorption (NMP) (λₘₐₓ / nm): 462, 493, 530.

Fluorescence (NMP) (λₘₐₓ / nm): 546, 583, 635.

3.11 Synthetic Route of Complex 2

The coordinated perylene diimide triad was synthesized in 30 mL dried DMF solvent by one step complexation of copper(II) perchlorate hexahydrate solution (0.216 g, 10 ml) with HP−HEPDI (0.2 g, 0.29 mmol) under a nitrogen atmosphere. The mixture of reactants is kept at 50°C for 8h and at 150°C for 24h. The reaction solution is let to decrease the temperature to 25°C and then allowed into 0.3 L cold acetone solvent. The precipitated product is filtered under vacuum and later purified with water in a Soxhlet equipment to get rid of excess amount of copper salt and high boiling solvent. Finally, pure product was dried in vacuum oven.
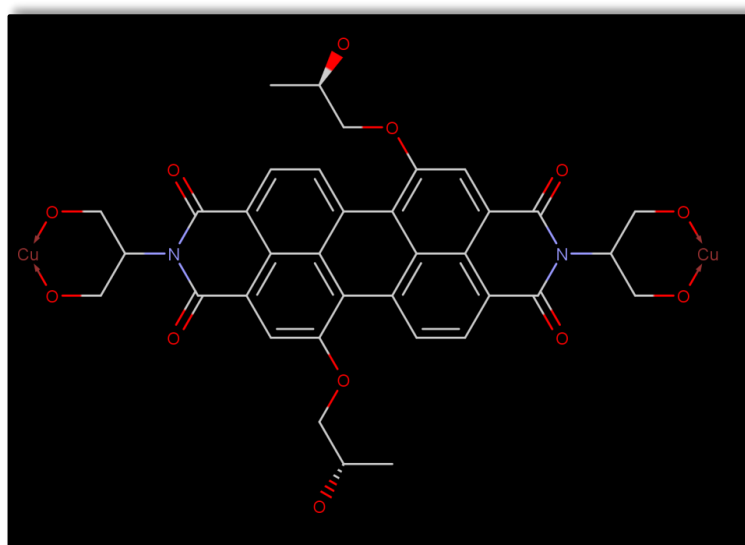
Figure 3.21: Chemical structure of complex 2

FT–IR (KBr, thin film, cm⁻¹): 3412 (O–H stretch), 3072 (aromatic C–H stretch), 2932 (aliphatic C–H str), 1686, 1623 (imide C=O stretch), 1598 (aromatic C=C stretch), 1265 (ether C–O–C stretch) and 751 (aromatic C–H bend).

3.12 Synthetic Route of Complex 3

The bay substituted perylene diimide and copper (II) complex was synthesized under a nitrogen atmosphere by one−step complexation of copper(II) perchlorate hexahydrate solution (0.216 g, 10 ml) with TM−HEPDI (0.2 g, 0.29 mmol) in 30 mL of dried dimethylformamide in a round−bottomed flask. The mixture of starting material is heated at 50ºC for 8h and finally at 150ºC for 24h. This solution is allowed to cool to 25ºC and then added into 0.3 L of cold acetone solvent. The product is filtrated and later purified with water in a soxhlet material to get rid of excess amount of copper salt and DMF solvent. As a last step, third metal complex dried carefully under vacuum in two days.
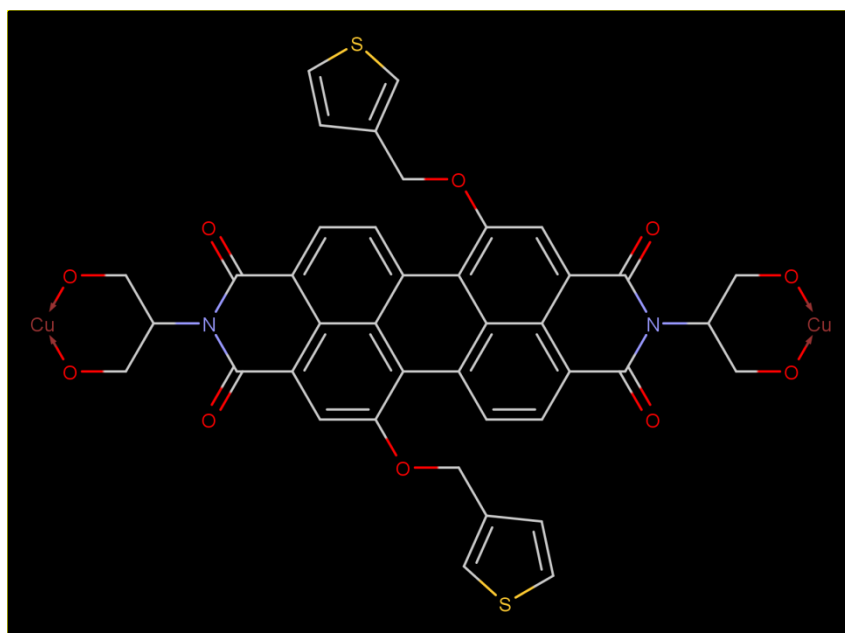
Figure 3.22: Chemical structure of complex 3

FT−IR (KBr, thin film, cm⁻¹): 3153 and 3042 (aromatic C−H stretch), 2838 (aliphatic C−H str), 1687 (imide C=O stretch), 1586 (aromatic C=C stretch), 1270 (ether C−O−C stretch) and 750 (aromatic C−H bend).

3.13 DSSC Devices Construction

3.13.1 Transparent Conducting Oxide Substrates (TCO)

The choice of transparent conducting oxide substrates is crucial for the construction of DSSC devices. TCO glass electrodes should expose poor absorption capacity of visible light in the electromagnetic spectrum and large electrical conductivity. But, the reducing of the resistance is related to a reduced transmission for a dedicated substance. Depend on the both standards need to be optimized for interested application. In the device construction, TCO glass electrodes that run like current collectors should pass the device's crucial processing criteria without affecting its physical characteristics. The transparent conducting oxide glass substrates are thermally stable more than the optimized deposition temperature. At high temperatures, some kind of glass substrates exhibit an improvement in resistance for a long term.

When ITO glass substrates are heated to 450°C and 500°C for 1 h, the resistance is raised by around 70% to 160%. The loss of oxygen vacancies, which operate as an electron source, can be attributed to the fact that oxygen atoms joined to a piece of the oxygen−vacant structure within the ITO glass substrate, resulting in a decrease in conductivity. In contrast, FTO (fluorine doped SnO_2) glass electrodes are strongly stable so that the softening of the electrodes is more limiting than any decomposition of the conducting layer thermally. In this research study, ITO glass substrates have been used as a TCO electrode.

The washing method is accomplished by keeping the electrodes sequentially in an ultrasonic bath for 10 minutes in detergent−water, ethanol, acetone solvents and pure water and then drying them in an oven at 100 °C before use. Air spray can be utilized to make the electrodes dried before TiO_2 application.

3.13.2 Preparation of Compact TiO_2 Layer

A TiO_2 compact layer inhibits contact directly among the FTO glass substrate with the redox electrolyte, concluded with a decrease in recombination. According to Yu et al., incorporating a TiO_2 compact layer on the photo anode increased the growth of adhesion of TiO_2 photo anode on FTO glass substrate, resulting in more electron paths for photo−generated electrons, allowing for higher light to electric conversion efficiency.

9 mL of ethanol and 3 mL of titanium (IV) isopropoxide were mixed in one beaker, ethanol (6 mL) solvent and acetyl acetone (2 mL) were put together in another beaker in the preparation of the TiO_2 compact layer. These two solutions are stirred ice bath for 24 hours and lowered the concentration with ethanol in 1:1 ratio. The prepared compact layer was casted FTO glass substrate using spin casting method (4000 rpm for 40 s, 3000 rpm for 10 s, 2000 rpm for 10 s and 1000 for 10 s).

3.13.3 Preparation Nanocrystalline TiO_2 Electrode

Nanocrystalline TiO_2 is made ready in accordance with the method published [62] and by utilizing commercially available TiO_2 (P25, Degussa) nanoparticles. In a porcelain mortar, 6 g of TiO_2 nanoparticles are mixed very well together with 2 mL of distilled water included 0.2 mL of acetylacetone to prevent reaggregation of the molecules. And in the blending step, 8 mL of distilled water was added slowly. Lastly, Triton X−100 (0.1 mL) is used to simplify the diffusion of the colloids up to the formation of dense

TiO$_2$ paste without coagulum. The nanocrystalline TiO$_2$ layer is casted as a second layer on the FTO glass substrate by spin casting technique after compact layer (4000 rpm for 40 s, 3000 rpm for 10 s, 2000 rpm for 10 s and 1000 for 10 s).

3.13.4 Sensitization

Before dye sensitization, the TiO$_2$ casted electrode is sintered at 450°C for 30min and decreased the temperature to 80°C before dipping in the perylene dye solutions. When preparing the solution to construct the devices, DMF solvent was utilized depend on the solubility of the perylene dyes used. The solution concentrations were kept constant and selected as 0.3–0.5 mM. The TiO$_2$ casted electrode was dipped into perylene dye solutions and kept for 1 day. After sensitization, the dye adsorbed electrode was washed with the acetonitrile solvent to get the extra amount of dye solution.

3.13.5 Deposition of Counter Electrode

Before depositing the platinum (Pt) electrode, the clean FTO glass substrate was treated with a 5 percent sodium hydroxide (NaOH) solution and washed with distilled water. The counter electrode (CE) is deposited by spin−casting on the FTO glass substrate with a 0.5 percent hydrogen hexacholoroplatinate (IV) solution in isopropanol solvent and annealing it for 30 minutes at 450°C.

As a result, the platinized counter electrode could be made in a couple of hours after heating at 450°C, because exposing Pt to the environment at 25°C lowers its catalytic activity.

3.13.6 Preparation of the Redox Mediator

0.6 M of 1−methyl−3−propyl−imidazolium iodide (PMII), 0.07 M of Lithium iodide (LiI) and 0.05 M of iodine (I$_2$) were dissolved in dried acetonitrile to prepare redox

mediator. Also, 0.05 M of t−butyl pyridine (TBP) was utilized as an additive.

3.13.7 Sealing of the Device

The DSSC devices are constructed by placing the TiO_2 casted FTO glass substrate on the top of the Pt casted FTO glass substrate, these electrodes came together by utilizing binders in sandwich geometry. Then some drops of the liquid electrolyte prepared freshly were injected directly into the gap among the counter electrode and working electrode to hinder the dehydration of the electrodes. The constructed DSSC device was used until the evaporation of the whole electrolyte.

Chapter 4

DATA AND CALCULATION

4.1 Optical and Photochemical Parameters

4.1.1 Molar Absorbance Coefficient

The molar absorbance coefficient (ε_{max}) has been estimated from the plot of the concentration of solutions and the intensity of $0\rightarrow0$ transition band in the absorption spectrum in accordance with Beer−Lambert's law. A five different concentrations (1.0×10^{-5}−6.25×10^{-7}) of the compound's solutions were prepared by dilution method. The maximum absorbance data for each concentration was then recorded in relation to the maximum absorption wavelength (λ_{max}). At the end, the slope was determined from the graph of concentration vs. molar absorbance has given the data of maximum molar absorbance coefficient.

Table 4.1: Concentration and their corresponding absorbance data of TAPDI in NMP

Concentration (mol/L)	Absorbance
1.0×10^{-5}	1.4
5×10^{-6}	0.87
2.5×10^{-6}	0.55
1.25×10^{-6}	0.34
6.25×10^{-7}	0.21
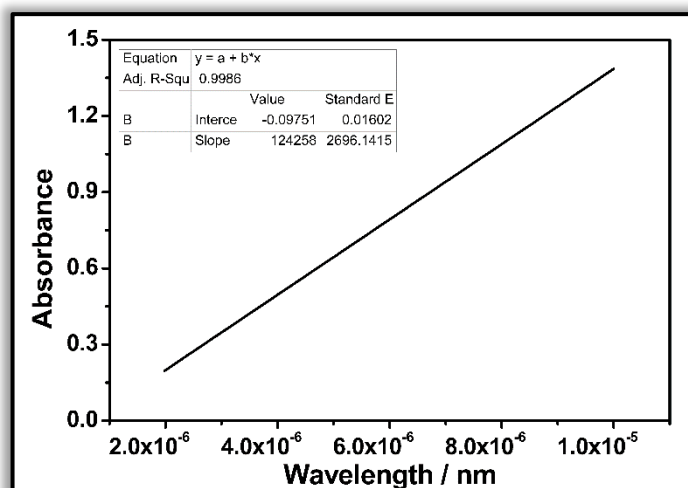
Figure 4.1: Plot of absorption vs. concentration of TAPDI in NMP

The slope of the plot, ε_{max}, is 124258 $Lmol^{-1}cm^{-1}$.

Table 4.2: Maximum wavelength (λ_{max}) and molar absorptivity (ε_{max}) data of TAPDI and TANDI in various solvents

	TAPDI		TANDI	
Solvent	λ_{max} (nm)	ε_{max} (L.mol^{-1}.cm^{-1})	λ_{max} (nm)	ε_{max} (L.mol^{-1}.cm^{-1})
NMP	527	124258	379	9037
DMAc	526	127893	379	17444
DMF	528	136172	378	6734
DMSO	531	125893	379	5530

Table 4.3: Molar absorptivity data of HP−PDA in various solvents

	HP−PDA	
Solvent	λ_{max} (nm)	ε_{max} (L.mol^{-1}.cm^{-1})
NMP	523	15620
DMF	518	14375
DMSO	519	14487

Table 4.4: Molar absorptivity data of TM−PDA in various solvents

	TM−PDA	
Solvent	λ_{max} (nm)	ε_{max} (L.mol^{-1}.cm^{-1})
NMP	517	129562
DMAc	516	89955
DMF	517	144633
DMSO	519	144952

Table 4.5: Molar absorptivity data of HEPDI in various solvents

	HEPDI	
Solvent	λ_{max} (nm)	ε_{max} (L.mol^{-1}.cm^{-1})
NMP	523	12735
DMAc	522	10799
DMF	522	12838
DMSO	526	13501

4.1.2 Fluorescence Quantum Yields

The quantum yield of fluorescence symbolized as Φ_f is expressed as the ratio of the number of photons emitted from sample as fluorescence to the number of photons absorbed. Φ_f is a substantial property to study in almost every compound. Williams's technique is one of the most credible equation to estimate Φ_f. There should be several well−analyzed references with identified Φ_f values. Standard and unknown compound solutions that have the same absorbance at the same excitation wavelength are considered to absorb the same number of photons. As a result, the Φ_f data could be calculated using a straightforward comparison of the integrated intensity of emission

spectra of the two dye solutions. Since Φ_f for the standard sample is known, Φ_f for the

unknown sample was calculated according to the following formula.

$$\Phi f\,(U) \;=\; \frac{A_{std}}{A_u} \;\times\; \frac{S_u}{S_{std}} \;\times\; \left[\frac{n_u}{n_{std}}\right]^2 \;\times\; \Phi f_{std} \tag{7}$$

Where,

$\Phi_f\,(U)$: Φ_f of unknown sample

A_{std}: Absorbance of the reference

A_u: Absorbance of the sample

S_{std}: The integrated emission area across the band of reference

S_u: The integrated emission area across the band of sample

n_{std}: Refractive index of solvent used to prepare reference dye solution

n_u: Refractive index of solvent used to prepare unknown sample dye solution

Φ_{std}: Fluorescence quantum yield of reference [67].

The N,N'−bis(dodecyl)−3,4,9,10−perylene bis(discarboximide) [67] in ChL solvent is

utilized as a reference sample in calculations of Φ_f for perylene dyes. Φ_f ($\lambda_{exc} = 485$

nm) of reference compound is equal to 1.

Φ_f calculation of TAPDI in NMP:

The reference is the N, N'−bis(dodecyl)−3,4,9,10−perylenebis(discarboximide).

$\Phi_{std} = 1$ in ChL

$A_{std} = 0.1082$

$A_u = 0.1047$

$S_u = 895.1430$

$S_{std} = 1597.0607$

$n_{std} = 1.4441$

$n_u = 1.4700$

$$\Phi f\,(U) \;=\; \frac{0.1082}{0.1047} \times \frac{895.1430}{1597.0607} \times \left[\frac{1.4700}{1.446}\right]^{2} \times 1$$

$$\Phi f\,(U) \;=\; 0.60$$

The fluorescence quantum yields of the TAPDI, TANDI, HP–PDA, HP–HEPDI, TM–PDA, TM–HEPDI and HEPDI in the various organic solvents are predicted with parallel methods and depicted in Table 4.6–4.9.

Table 4.6: Fluorescence quantum yield (Φ_f) data of TAPDI and TANDI in different solvents

	TAPDI	TANDI
Solvent	Φf	
Pyridine	0.54	–
NMP	0.60	0.019
DMAc	0.36	0.019
DMF	0.92	0.014
DMSO	0.11	0.012
m-Cresol	0.0032	–
TFAc	0.03	0.006

Table 4.7: Fluorescence quantum yield data of HP−PDA and HP−HEPDI in different solvents

Solvent	HP−PDA	HP−HEPDI
	Φf	
NMP	0.02	0.07
DMAc	0.03	0.04
DMF	0.03	0.06
DMSO	0.01	0.03
TFAc	0.04	0.095

Table 4.8: Fluorescence quantum yield data of TM−PDA and TM−HEPDI in different solvents

Solvent	TM−PDA	TM−HEPDI
	Φf	
NMP	0.23	0.083
DMAc	0.16	0.036
DMF	0.29	0.060
DMSO	0.05	0.028
m−Cresol	–	0.003
TFAc	–	0.034

Table 4.9: Fluorescence quantum yield data of HEPDI in different solvents

	HEPDI
Solvent	Φf
NMP	0.16
DMAc	0.12
DMF	0.09
DMSO	0.05
m−Cresol	0.12
TFAc	0.17

4.1.3 Half−widths of the Selected Absorption Band

The full width at half maximum is the half−width ($\Delta\bar{v}_{1/2}$) of the assigned maximum absorption. The half−widths of the selected maximum absorption were calculated according to following equation.

$$\Delta\bar{v}_{1/2} = \bar{v}_1 - \bar{v}_2 \tag{8}$$

Where,

$\bar{v}_1$ and $\bar{v}_2$: The frequencies from the absorption spectrum in cm^{-1}

$\Delta\bar{v}_{1/2}$: The half−width of the selected maximum absorption in cm^{-1}
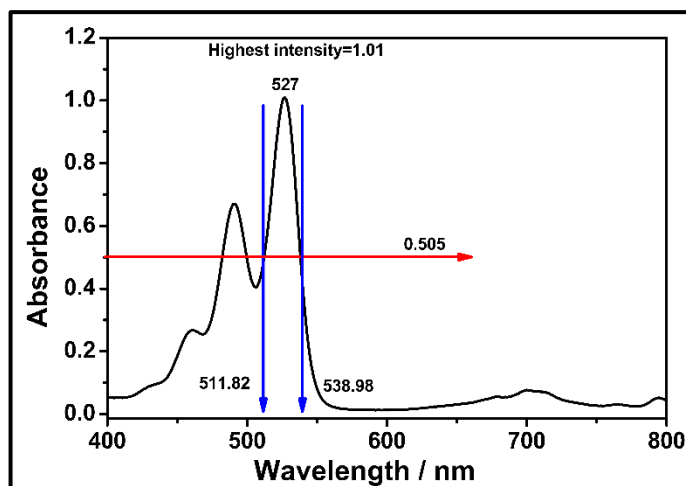
Figure 4.2: Absorption spectrum of TAPDI in NMP and half−width representation

According to Figure 4.2:

$\lambda_{max} = 527$ nm

Half−width absorption = 0.505

$\lambda_1 = 511.82$

$\lambda_2 = 538.98$

$$\lambda_1 = 511.82 \text{ nm} \times \frac{10^{-9}\text{m}}{1 \text{ nm}} \times \frac{1\text{cm}}{10^{-2}\text{m}} = 5.1182 \times 10^{-5} \text{ cm}$$

$$\bar{v}_1 = \frac{1}{5.1182 \times 10^{-5} \text{ cm}} = 19538.12 \text{ cm}^{-1}$$

$$\lambda_2 = 538.98 \text{ nm} \times \frac{10^{-9}\text{m}}{1 \text{ nm}} \times \frac{1\text{cm}}{10^{-2}\text{m}} = 5.3898 \times 10^{-5} \text{ cm}$$

$$\bar{v}_2 = \frac{1}{5.3898 \times 10^{-5} \text{ cm}} = 18553.56 \text{ cm}^{-1}$$

$$\Delta\bar{v}_{1/2} = \bar{v}_1 - \bar{v}_2 = 19538.12 \text{ cm}^{-1} - 18553.56 \text{ cm}^{-1}$$

$$= 950.76 \text{ cm}^{-1}$$

The half−widths of the produced compounds in various solvents should be analyzed carefully to determine the theoretical radiative lifetimes of the synthetic products.

$\Delta \bar{v}_{1/2}$ of the TAPDI, TANDI, HP–PDA, HP–HEPDI, TM–PDA, TM–HEPDI and HEPDI in the various organic solvents are predicted with parallel methods and depicted in Table 4.10–4.16.

Table 4.10: Half−widths of the selected absorptions of the TAPDI in various solvents

Solvent	$\lambda_{\mathbf{max}}$ (nm)	$\lambda_{\mathbf{1}}$ (nm)	$\lambda_{\mathbf{2}}$ (nm)	$\Delta \bar{\mathbf{v}}_{\mathbf{1/2}}$ ($\mathbf{cm^{-1}}$)
NMP	527	511.82	538.98	950.76
DMF	528	513.55	537.89	881.14
DMSO	531	514.27	541.43	975.43
MeOH	519	501.4	534.17	1223.53
TFAc	535	519.38	547.48	972.19

Table 4.11: Half−widths of the selected absorptions of the TANDI in various solvents

Solvent	λ_{max} (nm)	λ_1 (nm)	λ_2 (nm)	$\Delta \bar{v}_{1/2}$ ($\mathrm{cm^{-1}}$)
NMP	378	369	388	1327
DMAc	379	368	387	1334
DMF	379	368	385	1200
DMSO	378	370	387	1187

Table 4.12: Half−widths of the selected absorptions of the HP−PDA in various solvents

Solvent	λ_{max} (nm)	λ_1 (nm)	λ_2 (nm)	$\Delta\bar{v}_{1/2}$ (cm^{-1})
NMP	523	510	587	2572
DMAc	514	510	589	2630
DMF	518	509	584	2523
DMSO	519	443	597	5823
m-Cresol	532	426	627	7525
TFAc	521	432	591	6228

Table 4.13: Half−widths of the selected absorptions of the HP−HEPDI in various solvents

Solvent	λ_{max} (nm)	λ_1 (nm)	λ_2 (nm)	$\Delta\bar{v}_{1/2}$ (cm^{-1})
NMP	522	502	539	1367
DMAc	519	503	538	1293
DMF	519	501	539	1407
DMSO	521	502	541	1436
TFAc	530	469	620	5193

Table 4.14: Half−widths of the selected absorptions of the TM−PDA in various solvents

Solvent	λ_{max} (nm)	λ_1 (nm)	λ_2 (nm)	$\Delta\bar{v}_{1/2}$ (cm^{-1})
NMP	517	499	538	1452.7
DMAc	516	489	533	1688.2
DMF	517	500	535	1308.4
DMSO	519	502	539	1367.4

Table 4.15: Half–widths of the selected absorptions of the TM–HEPDI in various solvents

Solvent	λ_{max} (nm)	λ_1(nm)	λ_2 (nm)	$\Delta\bar{v}_{1/2}$ (cm^{-1})
NMP	523	508	546	1370
DMAc	520	508	543	1269
DMF	520	506	539	1210
DMSO	522	510	541	1124
m–Cresol	544	533	688	4227
TFAc	530	512	561	1706

Table 4.16: Half–widths of the selected absorptions of the HEPDI in different solvents

Solvent	λ_{max} (nm)	λ_1(nm)	λ_2 (nm)	$\Delta\bar{v}_{1/2}$ (cm^{-1})
NMP	523	504	542	1391
DMAc	522	505	539	1249
DMF	522	505	543	1386
DMSO	526	507	545	1375
m-Cresol	550	529	580	1662
TFAc	534	514	565	1756

4.1.4 Theoretical Radiative Lifetimes

The theoretical radiative lifetimes (τ_0) were estimated in the accordance with the following formula.

$$\tau_0 = \frac{3.5 \times 10^8}{\upsilon_{max}^2 \cdot \varepsilon_{max} \cdot \Delta\bar{v}_{1/2}} \qquad (9)$$

Where,

τ_0: Radiative lifetime in ns

ε_{max}: The molar absorption coefficient at the selected λ_{max} in L.mol^{-1}.cm^{-1}

$\Delta\bar{v}_{1/2}$: The half–width of the selected absorption in cm^{-1}

v_{max}^2: mean frequency of the maximum absorption band in cm^{-1}.

The calculation of the Theoretical Radiative Lifetime of TAPDI in NMP:

From Figure 4.1 and 4.2,

λ_{max}= 527 nm

$$\lambda_{max} = 527 \text{ nm} \times \frac{10^{-9}\text{m}}{1 \text{ nm}} \times \frac{1 \text{ cm}}{10^{-2}\text{m}} = 5.27 \times 10^{-5}\text{cm}$$

$$\nu_{max} = \frac{1}{5.27 \times 10^{-5} \text{ cm}} = 18975.33 \text{ cm}^{-1}$$

$$v_{max}^2 = (18975.33 \text{ cm}^{-1})^2 = 3.60 \times 10^8\text{cm}^{-2}$$

The Theoretical Radiative Lifetime;

$$\tau_0 = \frac{3.5 \times 10^8}{v_{max}^2 \cdot \varepsilon_{max} \cdot \Delta v_{1/2}} = \frac{3.5 \times 10^8}{3.60 \times 10^8 \times 124258 \times 950.76}$$

$$\tau_0 = 8.23 \times 10^{-9} s$$

$$\tau_0 = 8.23 \text{ ns}$$

τ_0 of TAPDI, TANDI, HP–PDA, TM–PDA and HEPDI in the various organic solvents are predicted with parallel methods and depicted in Table 4.17–4.21.

Table 4.17: Theoretical radiative lifetimes (τ_0) of TAPDI in different solvents

Solvent	λ_{max} (nm)	ε_{max} (L.mol^{-1}.cm^{-1})	$v_{max}^2 \times 10^8$ (cm^{-2})	$\Delta\bar{v}_{1/2}$(cm^{-1})	τ_0 (ns)
NMP	527	124258	3.60	950.76	8.23
DMF	528	136172	3.59	881.14	8.13
DMSO	531	125893	3.54	975.43	8.05

Table 4.18: τ_0 of TANDI in different solvents

Solvent	λ_{max} (nm)	ε_{max} (L.mol^{-1}.cm^{-1})	$\nu^2_{max} \times 10^8$ (cm^{-2})	$\Delta\bar{\nu}_{1/2}$ (cm^{-1})	τ_0 (ns)
NMP	379	9037	6.96	1327	41.92
DMAc	379	17444	6.96	1334	21.60
DMF	378	6734	7.00	1200	61.89
DMSO	379	5530	6.96	1187	76.59

Table 4.19: τ_0 of TANDI in different solvents of HP−PDA in different solvents

Solvent	λ_{max} (nm)	ε_{max} (L.mol^{-1}.cm^{-1})	$\nu^2_{max} \times 10^8$ (cm^{-2})	$\Delta\bar{\nu}_{1/2}$ (cm^{-1})	τ_0 (ns)
NMP	523	15620	3.66	2572	23.47
DMF	518	14375	3.73	2523	24.84
DMSO	519	14487	3.71	5823	11.18

Table 4.20: τ_0 of TM−PDA in different solvents

Solvent	λ_{max} (nm)	ε_{max} (L.mol^{-1}.cm^{-1})	ν^2_{max} (cm^{-2})	$\Delta\bar{\nu}_{1/2}$ (cm^{-1})	τ_0 (ns)
NMP	517	89955	3.74×10^8	1452.7	7.16
DMF	517	144633	3.74×10^8	1308.4	4.95
DMSO	519	144952	3.71×10^8	1367.4	4.76

Table 4.21: τ_0 of HEPDI in different solvents

Solvent	λ_{max} (nm)	ε_{max} (L.mol^{-1}.cm^{-1})	ν^2_{max} (cm^{-2})	$\Delta\bar{\nu}_{1/2}$ (cm^{-1})	τ_0 (ns)
NMP	523	12735	3.66×10^8	1391	54.04
DMF	522	12838	3.67×10^8	1386	53.60
DMSO	526	13500	3.61×10^8	1375	52.17

4.1.5 Theoretical Fluorescence Lifetimes

The theoretical fluorescence lifetimes (τ_f) were estimated in accordance with the following formula.

$$\tau_f = \tau_0 \cdot \Phi_f \tag{10}$$

Where,

τ_f: Fluorescence lifetime

τ_0: Theoretical radiative lifetime

Φ_f: Fluorescence quantum yield.

Theoretical Fluorescence Lifetime calculation of TAPDI in NMP:

$\tau_f = \tau_0 \cdot \Phi_f$

$\tau_0 = 8.23$ ns

$\tau_f = \tau_0 \cdot \Phi_f = 8.23 \times 0.60 = 4.94$ ns.

The Theoretical Fluorescence Lifetimes of TAPDI, TANDI, HP−PDA, TM−PDA and HEPDI in various solvents were estimated in accordance with parallel way and all of the results were depicted in the Table 4.22−4.26.

Table 4.22: Theoretical fluorescence lifetimes (τ_f) of TAPDI in various solvents

Solvent	Φ_f	τ_0 (ns)	τ_f (ns)
NMP	0.60	8.23	4.94
DMF	0.95	8.13	7.72
DMSO	0.10	8.05	0.81

Table 4.23: τ_f of TANDI in various solvents

Solvent	Φ_f	τ_0 (ns)	τ_f (ns)
NMP	0.019	41.92	0.79
DMAc	0.019	21.60	0.41
DMF	0.014	61.89	0.87
DMSO	0.012	76.59	0.92

Table 4.24: τ_f of HP−PDA in various solvents

Solvent	Φ_f	τ_0 (ns)	τ_f (ns)
NMP	0.02	23.47	0.75
DMF	0.03	24.84	0.75
DMSO	0.01	11.18	0.11

Table 4.25: τ_f of TM−PDA in various solvents

Solvent	Φ_f	τ_0 (ns)	τ_f (ns)
NMP	0.23	7.16	1.65
DMF	0.29	4.95	1.43
DMSO	0.05	4.76	0.24

Table 4.26: τ_f of HEPDI in various solvents

Solvent	Φ_f	τ_0 (ns)	τ_f (ns)
NMP	0.16	54.04	8.64
DMAc	0.12	70.71	8.48
DMF	0.09	53.60	4.82
DMSO	0.05	52.17	2.61

4.1.6 Fluorescence Rate Constants

The calculation of the fluorescence rate constants (k_f) of the synthetic product was done in accordance with following Turro's equation [68].

$$k_f = \frac{1}{\tau_0} \qquad (11)$$

Where,

k_f: The fluorescence rate constant in s^{-1}

τ_0: The theoretical radiative lifetime in s

The calculation for k_f of TAPDI in NMP at $\lambda_{max} = 527$ nm:

$$k_f = \frac{1}{\tau_0}$$

$$\tau_0 = 8.23 \text{ ns} = 0.823 \times 10^{-8} \text{s}$$

$$k_f = \frac{1}{0.823 \times 10^{-8} \text{s}} = 12.20 \times 10^7 \text{ s}^{-1}.$$

The fluorescence rate constant of TAPDI, TANDI, HP–PDA, TM–PDA in various organic solvents were determined by utilizing identical equation and all the calculated data were depicted in the Table 4.27–4.31.

Table 4.27: Theoretical fluorescence rate constant of TAPDI in different solvents

Solvent	λ_{max} (nm)	τ_0 (ns)	k_f (s^{-1})
NMP	527	8.23	12.20×10^7
DMF	528	8.13	12.30×10^7
DMSO	531	8.05	12.42×10^7

Table 4.28: Theoretical fluorescence rate constant of TANDI in different solvents

Solvent	λ_{max} (nm)	τ_0 (s)	k_f (s^{-1})
NMP	379	41.92	2.38×10^7
DMAc	379	21.60	4.63×10^7
DMF	378	61.89	1.62×10^7
DMSO	379	76.59	1.31×10^7

Table 4.29: Theoretical fluorescence rate constant of HP−PDA in different solvents

Solvent	λ_{max} (nm)	τ_0 (s)	k_f (s^{-1})
NMP	523	23.47	4.17×10^7
DMF	518	24.84	4.00×10^7
DMSO	519	11.18	3.64×10^7

Table 4.30: Theoretical fluorescence rate constant of TM−PDA in different solvents

Solvent	λ_{max} (nm)	τ_0 (s)	k_f (s^{-1})
NMP	517	7.16	13.97×10^7
DMF	517	4.95	20.2×10^7
DMSO	519	4.76	2.10×10^7

Table 4.31: Theoretical fluorescence rate constant of HEPDI in different solvents

Solvent	λ_{max} (nm)	τ_0 (s)	k_f (s^{-1})
NMP	523	2.38	41.7×10^7
DMAc	522	2.19	45.5×10^7
DMF	522	1.34	74.6×10^7
DMSO	526	0.68	14.7×10^8

4.1.7 Rate Constants of Radiationless Deactivation

The equation given below was used to estimate the rate constants of radiationless deactivations (k_d) of the compounds.

$$k_d = \left(\frac{k_f}{\Phi_f}\right) - k_f \tag{12}$$

Where,

k_d: Rate constant of radiationless deactivation in s^{-1}

k_f: Fluorescence rate constant in s^{-1}

Φ_f: Fluorescence quantum yield.

The calculation for the Rate Constant of Radiationless Deactivation of TAPDI in NMP:

$$k_d = \left(\frac{k_f}{\Phi_f}\right) - k_f = \left(\frac{12.20 \times 10^7 \text{ s}^{-1}}{0.60}\right) - 12.20 \times 10^7 \text{ s}^{-1}$$

$$= 8.13 \times 10^7 \text{ s}^{-1}$$

The rate constants of radiationless deactivation of TAPDI, TANDI, HP−PDA, TM−PDA and HEPDI in various organic solvents were found by using similar method and the calculated values are presented in the Table 4.32−4.36.

Table 4.32: k_d data of TAPDI in various solvents

Solvent	Φ_f	k_f (s^{-1})	k_d (s^{-1})
NMP	0.60	12.20×10^7	8.13×10^7
DMF	0.95	12.30×10^7	0.65×10^7
DMSO	0.10	12.42×10^7	112.8×10^7

Table 4.33: k_d data of TANDI in various solvents

Solvent	Φ_f	k_f (s^{-1})	k_d (s^{-1})
NMP	0.019	2.38×10^7	12.28×10^8
DMAc	0.019	4.63×10^7	23.91×10^8
DMF	0.014	1.62×10^7	11.41×10^8
DMSO	0.012	1.31×10^7	10.79×10^8

Table 4.34: k_d data of HP−PDA in various solvents

Solvent	Φ_f	k_f (s^{-1})	k_d (s^{-1})
NMP	0.02	4.17×10^7	2.27×10^9
DMF	0.03	4.00×10^7	1.29×10^9
DMSO	0.01	3.64×10^7	3.60×10^9

Table 4.35: k_d data of TM−PDA in different solvents

Solvent	Φ_f	k_f (s^{-1})	k_d (s^{-1})
NMP	0.23	13.97×10^7	4.68×10^8
DMF	0.29	20.2×10^7	4.95×10^8
DMSO	0.05	2.10×10^7	3.99×10^8

Table 4.36: k_d data of HEPDI in different solvents

Solvent	Φ_f	$k_f\,(s^{-1})$	$k_d\,(s^{-1})$
NMP	0.16	41.7×10^7	2.19×10^9
DMAc	0.12	45.5×10^7	3.34×10^9
DMF	0.09	74.6×10^7	7.54×10^9
DMSO	0.05	14.7×10^8	2.79×10^{10}

4.1.8 Oscillator Strengths

The strength of an electronic transition is expressed as a dimensionless quantity called oscillator strength (*f*). The oscillator strength is estimated using the given formula below.

$$f = 4.32 \times 10^{-9}\, \Delta\bar{v}_{1/2}\varepsilon_{max} \tag{13}$$

Where,

f : Oscillator strength

$\Delta\bar{v}_{1/2}$: Half−width of the selected absorption in cm^{-1}

ε_{max} : Molar absorbance coefficient

The calculation for *f* of TAPDI in NMP at λmax:

$$f = 4.32 \times 10^{-9}\, \Delta\bar{v}_{1/2}\, \varepsilon_{max} = 4.32 \times 10^{-9} \times 950.76 \times 124258$$

$$f = 0.51.$$

The oscillator strengths of the TAPDI, TANDI, HP−PDA, TM−PDA and HEPDI in various organic solvents were found in accordance with similar technique and the calculated values are represented in the Table 4.37−4.41.

Table 4.37: f data of the TAPDI in various solvents

Solvent	λ_{max} (nm)	$\Delta\bar{v}_{1/2}$ (cm^{-1})	ε_{max} (L.mol^{-1}.cm^{-1})	f
NMP	527	950.76	124258	0.51
DMF	527	881.14	136172	0.52
DMSO	529	975.43	125983	0.53

Table 4.38: f data of the TANDI in different solvents

Solvent	λ_{max} (nm)	$\Delta\bar{v}_{1/2}$ (cm^{-1})	ε_{max} (L.mol^{-1}.cm^{-1})	f
NMP	378	1327	9037	0.052
DMAc	379	1334	17444	0.101
DMF	379	1200	6734	0.035
DMSO	378	1187	5530	0.028

Table 4.39: f data of the HP−PDA in different solvents

Solvent	λ_{max} (nm)	$\Delta\bar{v}_{1/2}$ (cm^{-1})	ε_{max} (L.mol^{-1}.cm^{-1})	f
NMP	523	2572	15620	0.17
DMF	518	2523	14375	0.16
DMSO	519	5823	14487	0.36

Table 4.40: *f* data of the TM−PDA in different solvents

Solvent	λ_{max} (nm)	$\Delta\bar{v}_{1/2}$ (cm^{-1})	ε_{max} (L.mol^{-1}.cm^{-1})	*f*
NMP	517	1452.7	89955	0.56
DMF	517	1308.4	144633	0.82
DMSO	519	1367.4	144952	0.86

Table 4.41: *f* data of the HEPDI in different solvents

Solvent	λ_{max} (nm)	$\Delta\bar{v}_{1/2}$ (cm^{-1})	ε_{max} (L.mol^{-1}.cm^{-1})	*f*
NMP	523	1391	12735	0.077
DMAc	522	1249	10799	0.058
DMF	522	1386	12838	0.077
DMSO	526	1375	13501	0.080

4.1.9 Singlet Energies

The amount of energy required for an electronic transition from the ground state to the excited state is known as singlet energy. The singlet energies, E_s (kcal.mol^{-1}) were calculated according to following formula.

$$E_s = \frac{2.86 \times 10^5}{\lambda_{max}} \qquad (14)$$

Where,

E_s: Singlet energy in kcal.mol^{-1}

λ_{max}: Maximum absorption wavelength in Å

The calculation singlet energy for TAPDI in NMP at $\lambda_{max} = 527$ nm:

$$E_s = \frac{2.86 \times 10^5}{\lambda_{max}} = \frac{2.86 \times 10^5}{5270} = 54.27 \text{ kcal mol}^{-1}.$$

The E_s of the TAPDI, TANDI, HP–PDA, TM–PDA and HEPDI in organic solvents were determined by using same equation and all the calculated E_s values were depicted in the Table 4.42–4.48.

Table 4.42: The singlet energies of the TAPDI in different solvents

Solvent	λ_{max} (Å)	E_s (kcal mol^{-1})
NMP	5270	54.27
DMF	5270	54.27
DMSO	5290	54.06
TFAc	5350	53.46

Table 4.43: The singlet energies of the TANDI in different solvents

Solvent	λ_{max} (Å)	E_s (kcal mol^{-1})
NMP	3780	75.66
DMAc	3790	75.46
DMF	3790	75.46
DMSO	3780	75.66

Table 4.44: The singlet energies of the HP−PDA in different solvents

Solvent	λ_{max} (Å)	E_s (kcal mol^{-1})
NMP	5230	54.69
DMAc	5200	55.00
DMF	5200	55.00
DMSO	5220	54.79
m-Cresol	5320	53.76
TFAc	521	54.89

Table 4.45: The singlet energies of the HP−HEPDI in different solvents

Solvent	λ_{max} (Å)	E_s (kcal mol^{-1})
NMP	5220	54.79
DMAc	5190	55.11
DMF	5190	55.11
DMSO	5210	54.89
TFAc	530	53.96

Table 4.46: The singlet energies of the TM−PDA in different solvents

Solvent	λ_{max} (Å)	E_s (kcal mol^{-1})
NMP	517	55.32
DMAc	516	55.43
DMF	517	55.32
DMSO	519	55.10

Table 4.47: The singlet energies of the TM–HEPDI in different solvents

Solvent	λ_{max} (Å)	E_s (kcal mol^{-1})
NMP	5230	54.69
DMAc	5200	55.00
DMF	5200	55.00
DMSO	5220	54.79
m–Cresol	5440	52.57
TFAc	5300	53.96

Table 4.48: The singlet energies of the HEPDI in different solvents

Solvent	λ_{max} (Å)	E_s (kcal mol^{-1})
NMP	5230	54.69
DMAc	5220	54.79
DMF	5220	54.79
DMSO	5260	54.37
m–Cresol	5500	52.00
TFAc	5340	53.56

Table 4.49: Maximum wavelength of the absorption λ_{max} (nm), molar extinction coefficient ε_{max} ((L.mol^{-1}.cm^{-1}), oscillator strength f, fluorescence quantum yield Φ_f (λ_{exc}= 485 nm), radiative life time τ_0 (ns), fluorescence life time τ_f (ns), fluorescence rate constant k_f (s^{-1}), rate–constant of radiationless deactivation k_d (s^{-1}), and singlet–energy E$_s$ (kcal mol^{-1}) data of TAPDI, TANDI, HP–PDA and TM–PDA

Solvents	λ_{max}	ε_{max}	f	Φ_f	τ_0	τ_f	$k_f \times 10^7$	k_d	E$_s$
					TAPDI				
NMP	527	124258	0.51	0.60	8.23	4.94	12.20	8.13×10^7	54.27
DMF	528	136172	0.52	0.95	8.13	7.72	12.30	0.65×10^7	54.27
DMSO	531	125893	0.53	0.10	8.05	0.81	12.42	11.3×10^8	54.06
					TANDI				
NMP	379	9037	0.052	0.019	41.9	0.79	2.38	12.28×10^8	75.66
DMAc	379	17444	0.101	0.019	21.6	0.41	4.63	23.91×10^8	75.46
DMF	378	6734	0.035	0.014	61.9	0.87	1.62	11.41×10^8	75.46
DMSO	379	5530	0.028	0.012	76.6	0.92	1.31	10.79×10^8	75.66
					HP–PDA				
NMP	523	15620	0.17	0.018	23.47	0.75	4.17	2.27×10^9	54.69
DMF	518	14375	0.16	0.03	24.84	0.75	4.00	1.29×10^9	55.00
DMSO	519	14487	0.36	0.01	11.18	0.11	3.64	3.60×10^9	54.79
					TM–PDA				
NMP	517	89955	0.56	0.23	7.16	1.65	13.97	4.68×10^8	55.32
DMF	517	144633	0.82	0.29	4.95	1.43	20.20	4.95×10^8	55.32
DMSO	519	144952	0.86	0.05	4.76	0.24	2.10	3.99×10^8	55.10
					HEPDI				
NMP	523	12735	0.077	0.16	54.0	8.64	41.7	2.19×10^9	54.69
DMAc	522	10799	0.058	0.12	70.7	8.48	45.5	3.34×10^9	54.79
DMF	522	12838	0.077	0.09	53.6	4.82	74.6	7.54×10^9	54.79
DMSO	526	13501	0.080	0.05	52.2	2.61	147	2.79×10^{10}	54.37

4.2 Electrochemical Data Calculations

Cyclic voltammetry (CV) is an efficient and popular electrochemical technique frequently employed to study the reduction/oxidation processes of molecular species. Electrochemical parameters of the synthetic products are studied by using the CV technique (acetonitrile containing 0.1 M TBAP$_6$ as a supporting electrolyte at 100 mVs^{-1} scan rate) in solution.

4.2.1 Redox Potentials / Half–Wave Potentials (E$_{1/2}$)

The average value of the anodic and cathodic peak potentials evaluated approximately at the half height of the anodic and cathodic peaks equation can be operated to determine the half–wave or mid–point potentials (E$_{1/2}$).

$$E_{1/2} = \frac{E_{pc} + E_{pa}}{2} \tag{15}$$

E$_{1/2}$: Half–wave or mid–point potentials (V)

E$_{pc}$: Potential of cathodic peak (V)

E$_{pa}$: Potential of anodic peak (V).

Redox Potential of TAPDI:

The cyclic voltammograms of TAPDI represented two reversible reduction peaks in DMF solvent (Figure 4.80). The redox potentials of TAPDI in DMF are calculated to the reference electrode as it is shown below.

$$E_{red1,1/2} vs. Ag/AgCl = \frac{E_{pc} + E_{pa}}{2} = \frac{-0.640 - 0.490}{2} = -0.565\ V$$

$$E_{red2,1/2} vs. Ag/AgCl = \frac{E_{pc} + E_{pa}}{2} = \frac{-0.830 - 0.680}{2} = -0.755\ V$$

where $E_{red1,1/2}$ and $E_{red2,1/2}$ represents the first and second reduction potentials.

The number of electrons transported by utilizing the same anodic and cathodic peak potentials can be calculated using the equation below, which shows the peak separations for both redox processes.

$$\Delta E = E_{pa} - E_{pc} = \frac{0.059}{n} \, V \tag{16}$$

Peak Potential Separations of TAPDI:

$$\Delta E = E_{pa} - E_{pc}$$

$$\Delta E_{P,1} = -0.490 + 0.640 = 0.15 \text{ V} = 150 \text{ mV}$$

$$\Delta E_{P,2} = -0.680 + 0.830 = 0.15 \text{ V} = 150 \text{ mV}.$$

The oxidation potential of internal reference which is ferrocene (Fc) was determined 0.410 V (E_{ox}= 0.410 V). The redox potentials can be calculated proportionately to Fc.

$$E_{red^1/_2} \, vs. \, Fc = E_{red^1/_2} \, vs. \frac{Ag}{AgCl} - E_{ox} vs. \frac{Ag}{AgCl} \tag{17}$$

$$E_{red \, 1,^1/_2} \, vs. \, Fc = -0.565 - 0.410 = -0.975 \text{ V}$$

$$E_{red \, 2,^1/_2} \, vs. \, Fc = -0.755 - 0.410 = -1.165 \text{ V}$$

4.2.2 LUMO and HOMO Energy Level

HOMO, the highest occupied molecular orbital was is the energy that is defined to provide an electron from a molecule that could be named as an oxidation procedure. LUMO, the lowest unoccupied molecular orbital is the energy required to design an electron to a molecule which is accepted as a reduction procedure. The LUMO and HOMO energy levels could be established by utilizing the redox potentials which are E_{red} and E_{ox}. To determine the HOMO–LUMO energy levels, Fc is used as a reference.

$$E_{LUMO} = -\left(4.8 + E_{1/_2}\right) \tag{18}$$

E_{LUMO}: Energy level of LUMO (eV)

$E_{1/_2}$: Mid−point potential ($E_{red\ 1/_2}$ vs Fc)

E$_{LUMO}$ of TAPDI

$$E_{LUMO} = -(4.8 + E_{1/_2})$$

$$E_{LUMO} = -(4.8 + (-0.960)) = -3.84\ eV.$$

The LUMO energy values of TAPDI in various solvents were determined as clarified in advance and the calculated values were tabulated in Table 4.50.

4.2.3 Optical Band−gap Energies (E$_g$)

E$_g$ is described as the distance among the conduction band (CB) and the valence band (VB) of electrons. The determination of the optical band gap is what amount of the electromagnetic spectrum a PV absorbs. A semiconductor cannot absorb a photon of light with an energy lower than the bandgap, and the energy of the electron−hole pair generated by a photon is equal to the bandgap energy. The optical band gap will be determined by changing the wavelength in the given equation below with the UV−vis absorption spectra of the product at the absorption edge value.

$$\text{Eg} = \frac{1240\ eV\ nm}{\lambda} \tag{19}$$

E$_g$: Band gap energy

λ: Cut−off wavelength of the absorption band in nm

Band gap energy of TAPDI in DMF solvent:

The UV−vis spectrum of the compound in DMF solvent and the extrapolation of maximal to 0 represented in the Figure 4.3. The λ is determined as 549 nm.

$$\text{Eg} = \frac{1240\ eV\ nm}{\lambda}$$

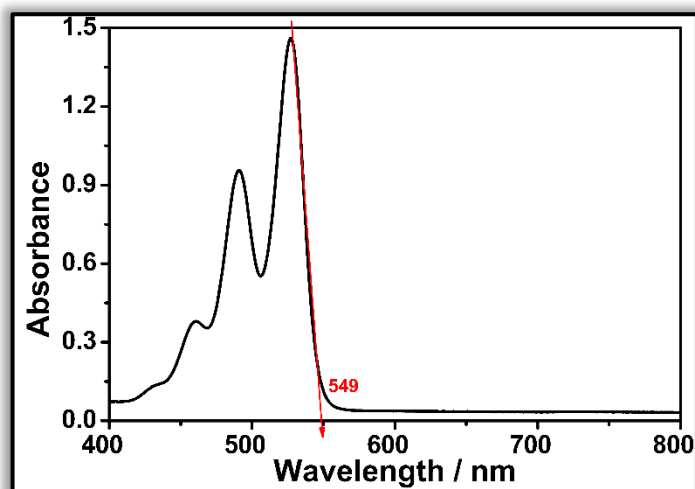$$\text{Eg} = \frac{1240\ eV\ nm}{540\ nm}$$

$= 2.31\ eV$

Figure 4.3: Absorption spectrum of TAPDI in DMF

4.2.4 HOMO Energy Level

The HOMO energy level could be obtained by utilizing the formula given below.

$$E_{HOMO} = E_{LUMO} - E_g \hspace{4cm} (20)$$

E_{HOMO} : Energy of HOMO level in eV

E_{LUMO} : Energy of LUMO level in eV

E_g : Band gap energy

HOMO energy level of TAPDI:

$E_{HOMO} = E_{LUMO} - E_g$

$E_{HOMO} = -3.84 - 2.31 = -6.15$ eV

Table 4.50: Cyclic voltammetry data of TAPDI and TAPPI

	E_{pc}[b] (V)	E_{pa}[c] (V)	ΔE_p[d] (mV)	$E_{red, on}$[e] (V)	$E_{1/2}$[f] vs. Ag/AgCl[g] (V)	E_{Fc}[h] vs. Ag/AgCl (V)	$E_{1/2}$ vs. Fc (V)	$E_{ox on}$ vs. Ag/AgCl (V)	Eg_{CV}[i] (eV)	Eg_{Opt}[j] (eV)	HOMO[k] (eV)	LUMO[l] (eV)
TAPDI	-0.640	-0.490	150	-0.460	-0.565	0.410	-0.960	1.62[m]	1.90	2.31	-5.83	-3.93
	-0.830	-0.680	150		-0.755	0.410	-1.165	(1.44)[n]		1.93[**]	-5.93[*]	-3.14[*]
TAPPI	-0.810	-0.670	140	-0.380	-0.740	0.410	-1.15	1.82[m]	2.09	2.28	-6.10	-4.01
								(1.71)[n]		1.46[**]	-6.03[*]	-3.45[*]

[a] in acetonitrile solution with supporting electrolyte, 0.1 M tetrabutylammonium hexafluorophosphate TBAPF$_6$ at 100 mVs^{-1}. [b] E_{pc}: cathodic potential. [c] E_{pa}: anodic potential. [d] ΔE_p: peak potential separations. [e] $E_{red, onset}$: reduction potential onset. [f] $E_{1/2,red}$: reduction half wave potential (reversible). [g] Ag/AgCl: silver/silver chloride reference electrode. [h] E_{Fc}: oxidation potential of ferrocene (internal reference). [i] Eg_{CV}: electrochemical band gap energy. [j] Eg_{opt}: optical band gap energy, $Eg_{opt} = 1240/\lambda_{onset}$ eV. [k] HOMO: highest occupied molecular orbital. [l] LUMO: lowest unoccupied molecular orbital. [m] E_{ox}: oxidation potential (irreversible). [n] $E_{ox, onset}$: oxidation potential onset. [*] From Density function theory (DFT) study. [**] Eg_{opt}: optical band gap energy in solid state.

4.3 Characterization of parameters in DSSCs

4.3.1 Short Circuit Current (I_{sc})

I_{sc} is obtained at the situation where the applied potential (V) is equivalent to 0 V. I_{sc} could be collected by using the I−V curve at Figure 4.4.
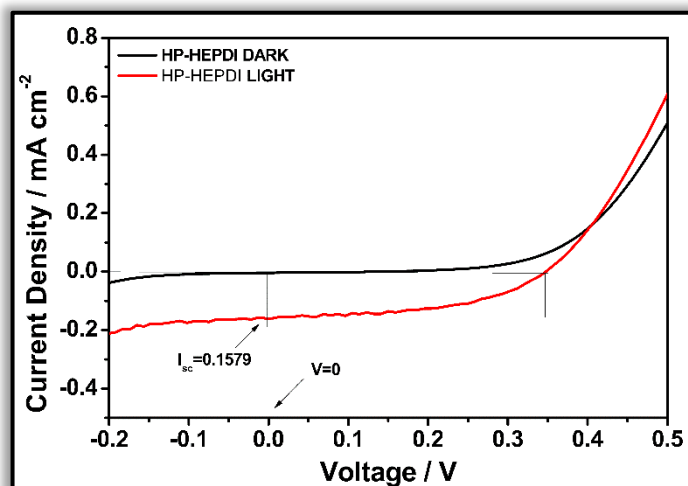

Figure 4.4: Graphic illustration of I_{sc} on IV curve of dye HP−HEPDI in dark and under light at 100 mW/cm^2

Dye synthesized solar cell devices were constructed with perylene derivatives, their Isc were obtained with the same technique represented in advance and the collected data were depicted in Table 4.51.

Table 4.51: I_{sc} of DSSC using different dyes

Compound	I_{sc} (mA cm^{-2})
TAPDI	0.4320
Complex 1	1.9200
TANDI	0.1240
TM−PDA	0.0997
HP−PDA	0.0948
HP−HEPDI	0.1579
TM−HEPDI	0.0713
HEPDI	0.0021
HP−TCPDI	0.1750

4.3.2 Open Circuit Voltage (V_{oc})

Voc determined when the current is equal to 0 in the cell. Open circuit voltage could

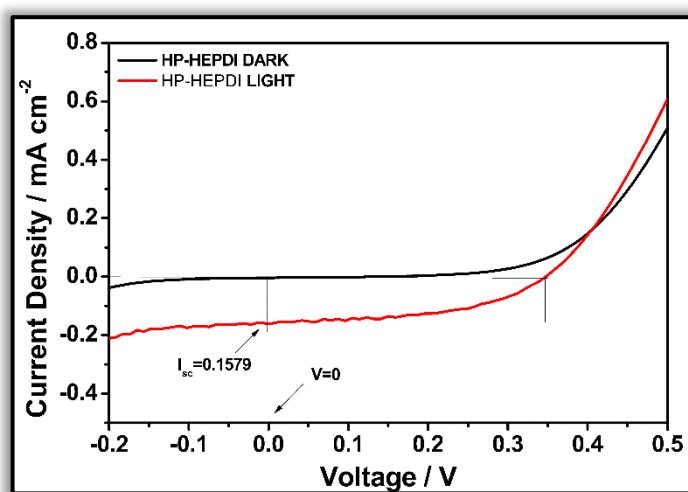be found by analyzing the I−V curve shown in the Figure 4.5.

Figure 4.5: Graphic illustration of V_{oc} on IV curve of dye HP−HEPDI in dark and under light at 100 mW/cm^2

97

Dye synthesized solar cell devices were constructed with perylene dyes, their V_{oc} were obtained by utilizing same technique as its represented and the collected data were depicted in the table given below.

Table 4.52: V_{oc} of DSSC by utilizing different dyes

Compound	V_{oc} (V)
TAPDI	0.3160
Complex 1	0.1896
TANDI	0.3480
TM–PDA	0.2768
HP–PDA	0.2290
HP–HEPDI	0.3482
TM–HEPDI	0.2484
HEPDI	0.1944
HP–TCPDI	0.3774

4.3.3 Maximal power output (P_{max})

In the DSSC, power could be determined with the equation given below.

$$P = V \times I \tag{21}$$

P_{max}, or maximum power output, could be constructed by drawing graphic of the collected P data from the equation given versus the voltage applied. The P_{max} could be also showed visually by plotting out the greatest area that complies with the I–V curve. I_{max} and V_{max} are the current and voltage collected from the I–V curve of HP–HEPDI as shown in Figure 4.6.
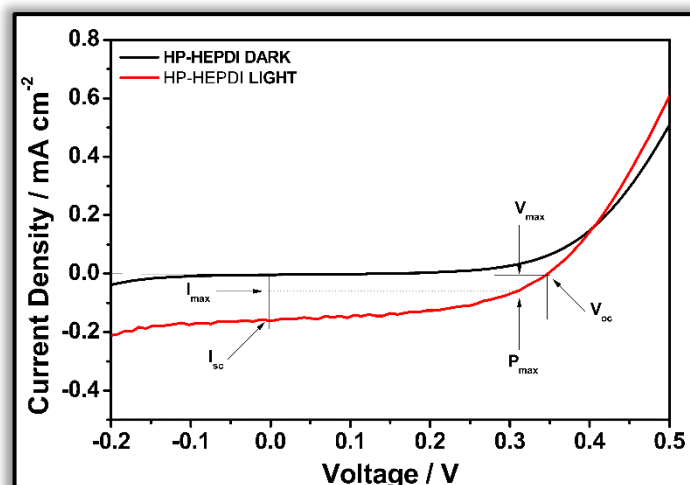
Figure 4.6: I–V curve with the photovoltaic parameters of HP–HEPDI in dark and under light at 100 mW/cm^2

DSSC devices constructed by using different PDIs, NDI and metal complex and their V_{max}, I_{max} and P_{max} were found and tabulated in the Table 4.53.

Table 4.53: V_{max}, I_{max}, P_{max} of DSSC utilizing different dyes

Compound	V_{max} (V)	I_{max} (mA cm^{-2})	P_{max} (mW)
Complex 1	0.7940	0.0884	0.0702
TANDI	0.2780	0.0740	0.0206
TM–PDA	0.1956	0.0756	0.0148
HP–PDA	0.1351	0.0615	0.0083
HP–HEPDI	0.2465	0.0615	0.0152
TM–HEPDI	0.1444	0.0451	0.0065
HEPDI	0.0901	0.0012	0.0001
HP–TCPDI	0.1725	0.0844	0.1456

4.3.4 Fill Factor

The fill factor abbreviated as FF in DSSC is an amount of how nearly a dye sensitized solar cell behaves like an optimal source. FF is the proportion of the P_{max} to the V_{oc} and I_{sc} data as it is shown equation.

$$FF = \frac{P_{max}}{P_{theoretical}} = \frac{V_{max} \times I_{max}}{V_{oc} \times I_{sc}} \tag{22}$$

When fill factor is equal to 1, the optimal efficiency in solar cell is reached. The fill factor of DSSC by using HP−HEPDI as a photosensitizer:

$$FF = \frac{0.2465 \times 0.1119}{0.3482 \times 0.1579} = 0.50$$

The FF data of the DSSC by using perylene dyes is tabulated in the table given below.

Table 4.54: V_{oc}, V_{max}, I_{sc}, I_{max}, FF of DSSC by utilizing different dyes

Compound	V_{oc} (V)	V_{max} (V)	I_{sc} (mA cm^{-2})	I_{max} (mA cm^{-2})	FF
Complex 1	0.1896	0.0884	1.9200	0.7940	0.19
TANDI	0.3480	0.2780	0.1240	0.0740	0.48
TM−PDA	0.2768	0.1956	0.0997	0.0756	0.54
HP−PDA	0.2290	0.1351	0.0948	0.0615	0.38
HP−HEPDI	0.3482	0.2465	0.1579	0.0615	0.50
TM−HEPDI	0.2484	0.1444	0.0713	0.0451	0.38
HEPDI	0.1944	0.0901	0.0021	0.0012	0.27
HP−TCPDI	0.3774	0.1725	0.1750	0.0844	0.22

4.3.5 Efficiency (η)

The efficiency is the measure of the performance of DSSC and is determined by using the equation given below.

$$\eta\% = \frac{V_{oc} \times I_{sc} \times FF}{P_{in}} \times 100 \qquad (23)$$

The power conversion performance of the DSSC by utilizing HP−HEPDI:

$$\eta\% = \frac{0.3482 \times 0.1579 \times 0.50}{100} \times 100$$

$$\eta\% = 0.028$$

The η % of the DSSC by utilizing PDIs, NDI and metal complex is tabulated in the

Table 4.55.

Table 4.55: V_{oc}, I_{sc}, FF and η of DSSC by utilizing different dyes

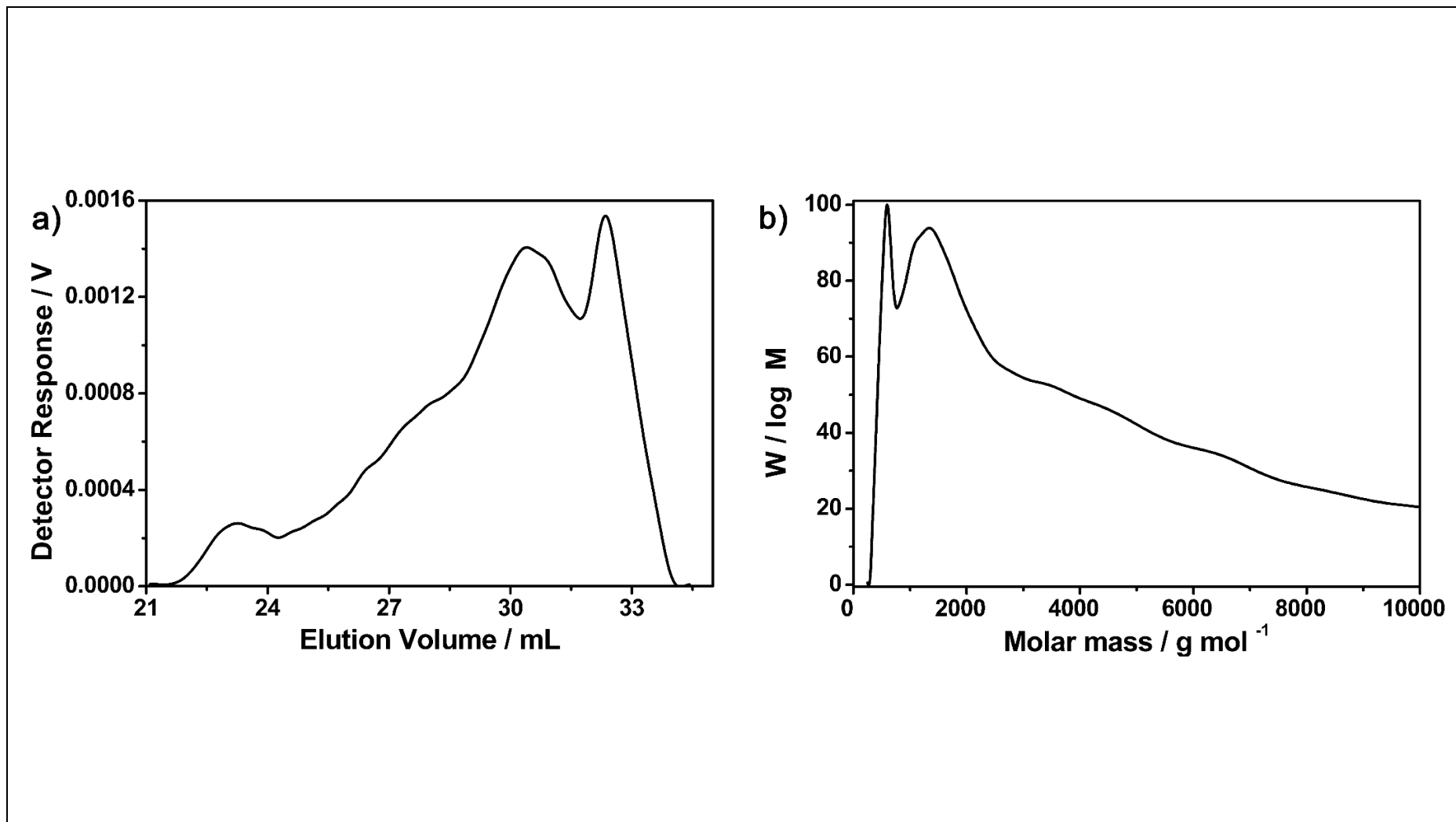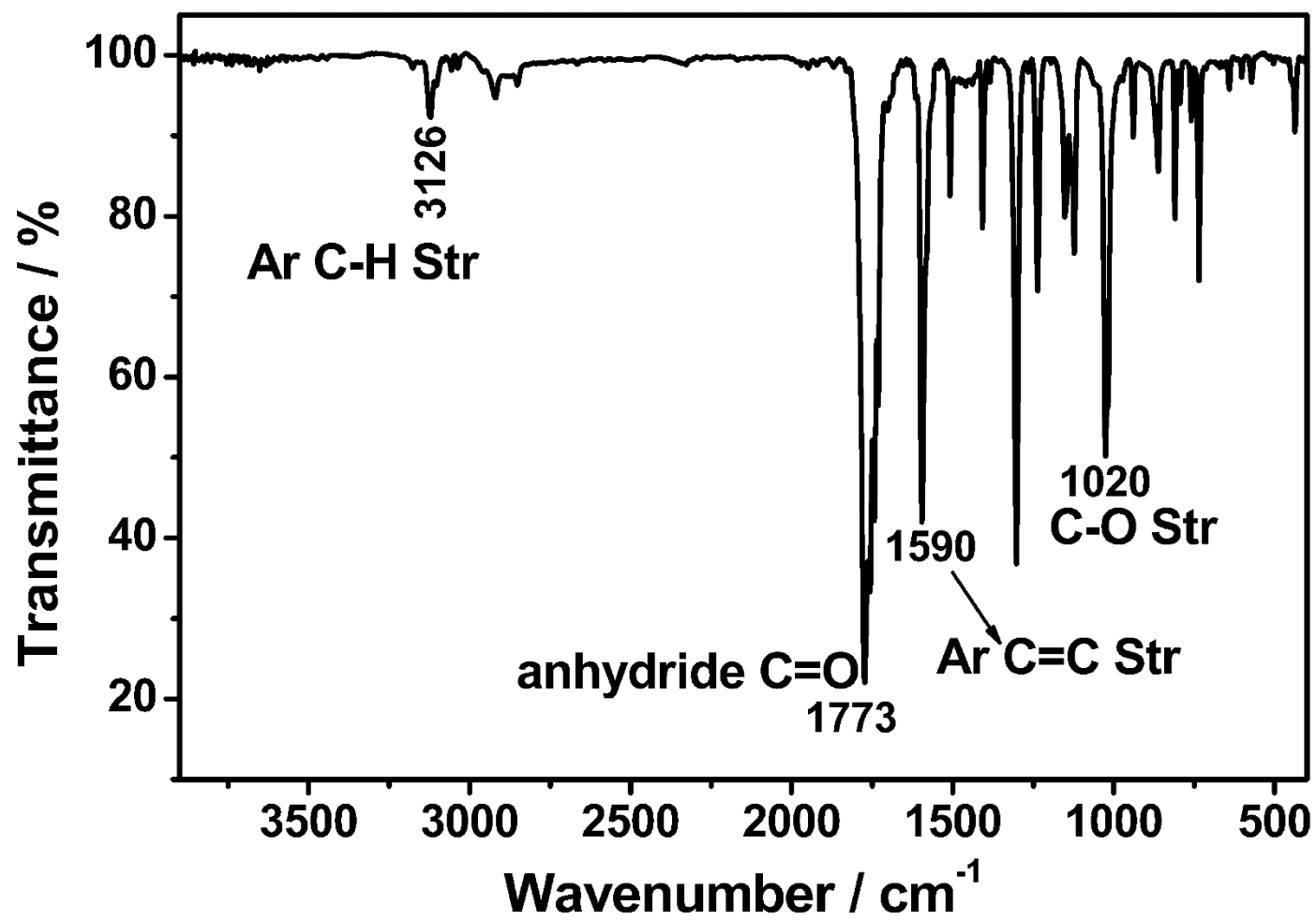| Compound	V_{oc} (V)	I_{sc} (mA cm^{-2})	FF	η
TAPDI	0.3160	0.4320	0.08	0.011
Complex 1	0.1896	1.9200	0.19	0.069
TANDI	0.3480	0.1240	0.48	0.023
TM−PDA	0.2768	0.0997	0.54	0.014
HP−PDA	0.2290	0.0948	0.38	0.008
HP−HEPDI	0.3482	0.1579	0.50	0.028
TM−HEPDI	0.2484	0.0713	0.38	0.007
HEPDI	0.1944	0.0021	0.27	0.0001
HP−TCPDI	0.3774	0.1750	0.22	0.015

Figure 4.7: GPC of TAPPI
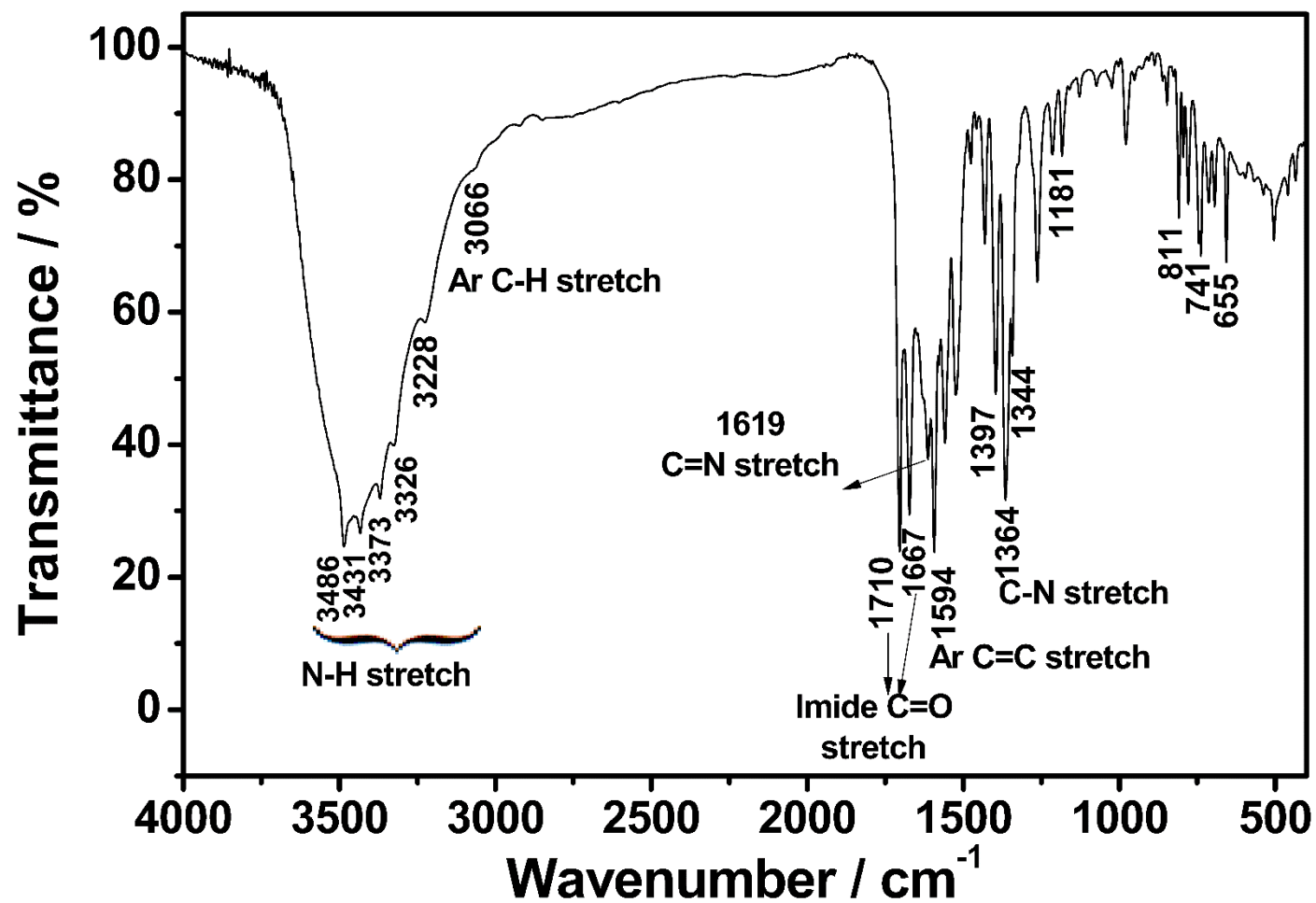
Figure 4.8: FT−IR spectrum of PDA
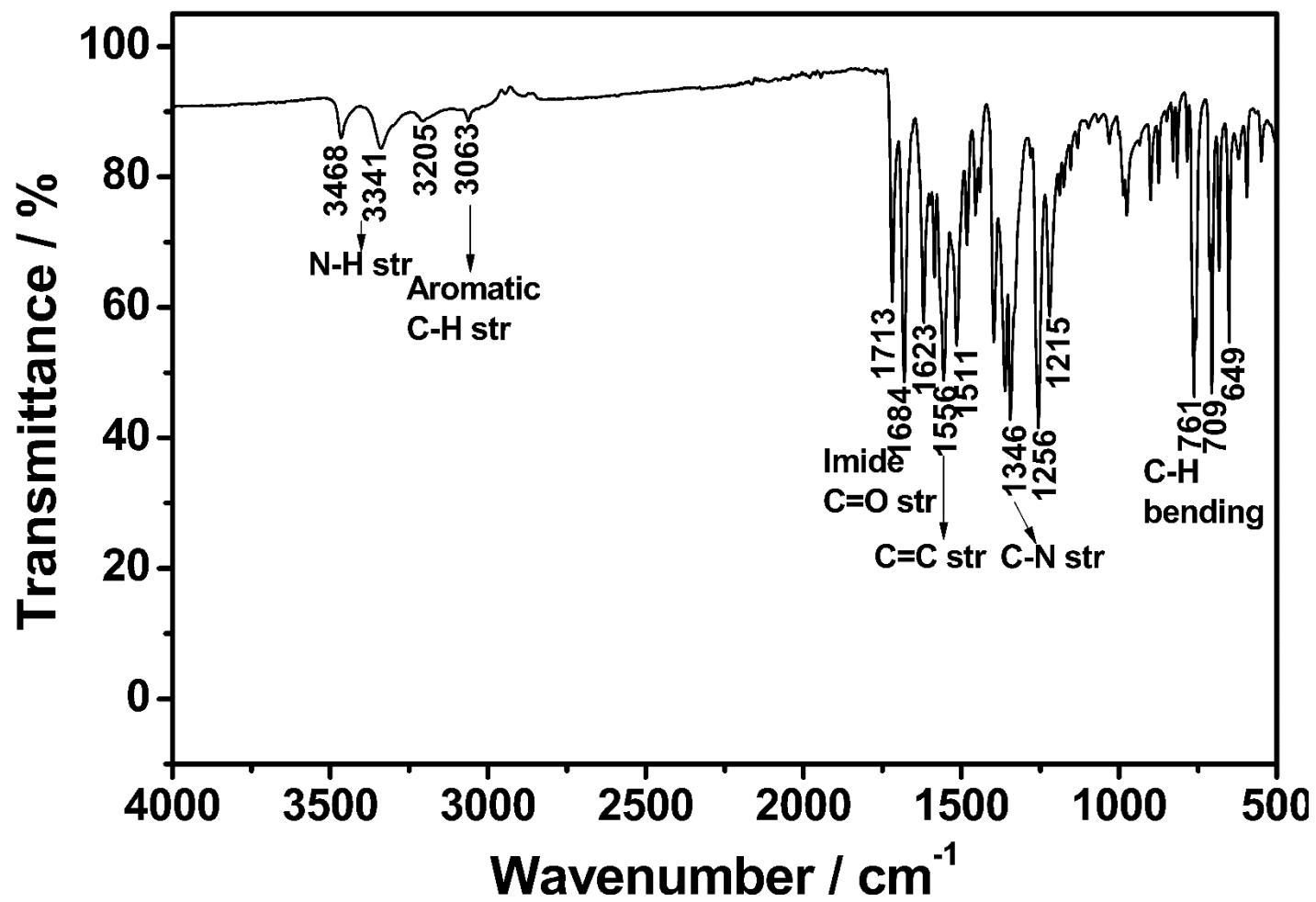
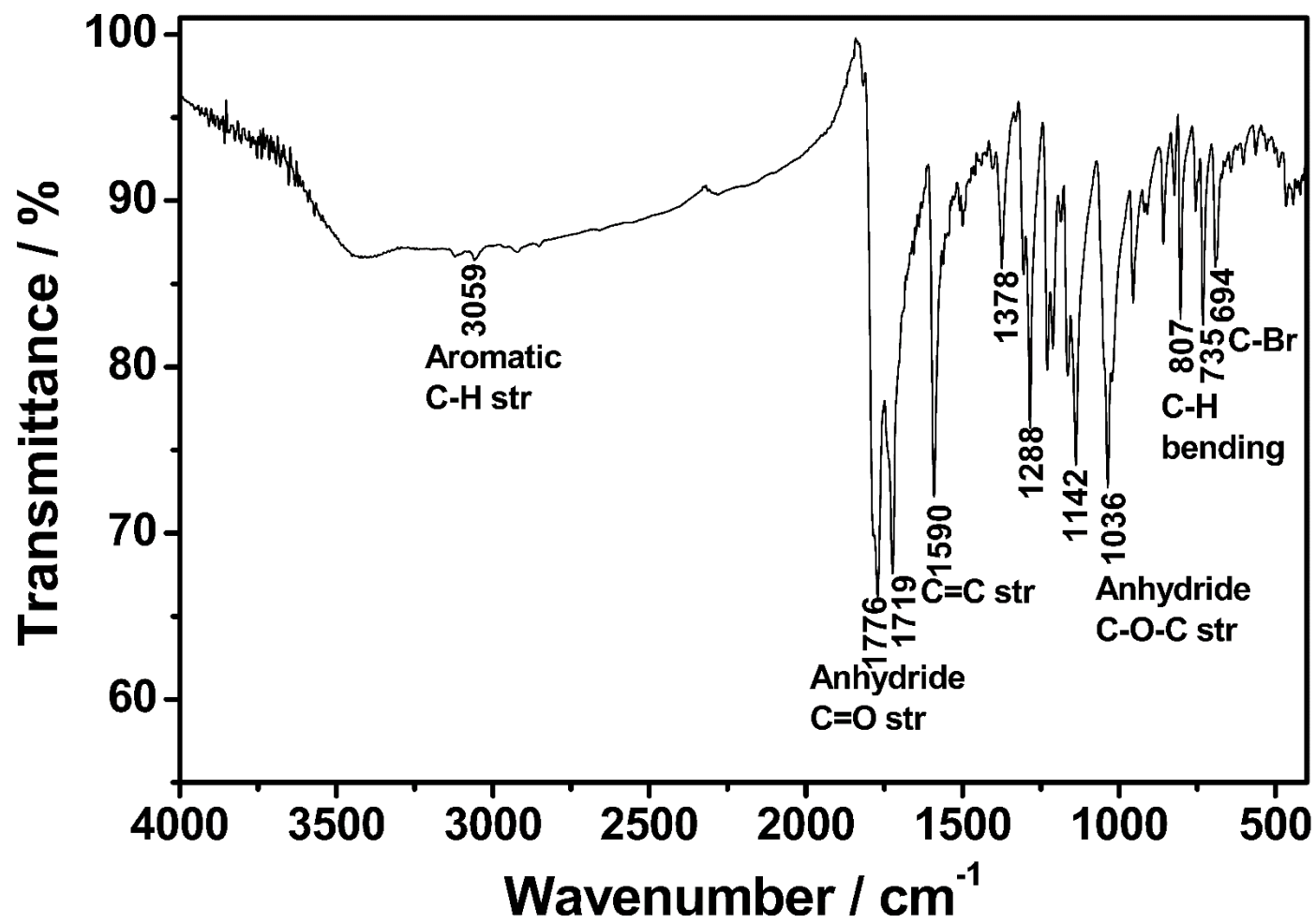Figure 4.9: FT−IR spectrum of TAPDI

Figure 4.10: FT−IR spectrum of TANDI

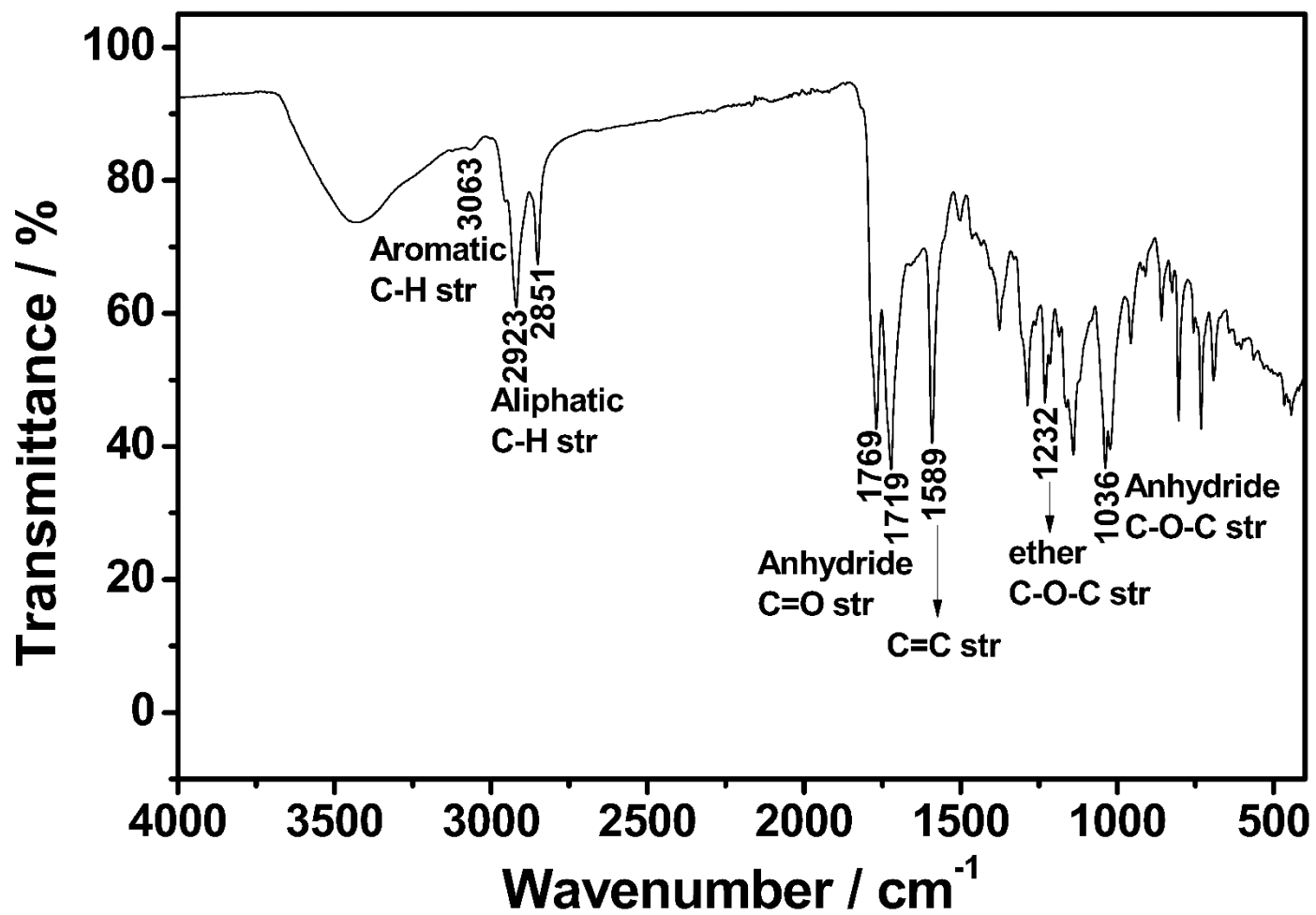Figure 4.11: FT−IR spectrum of Br−PDA

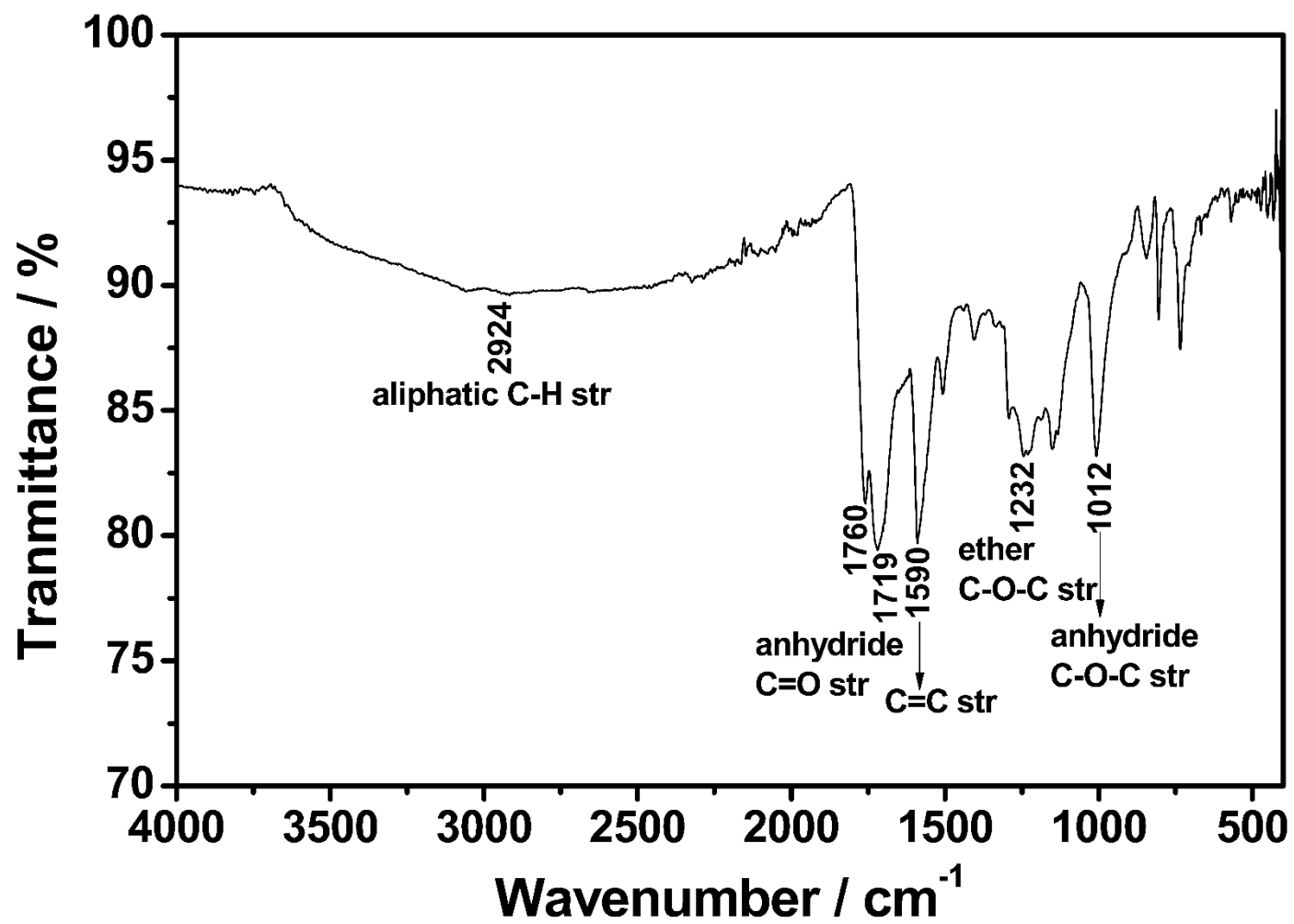Figure 4.12: FT−IR spectrum of TM−PDA

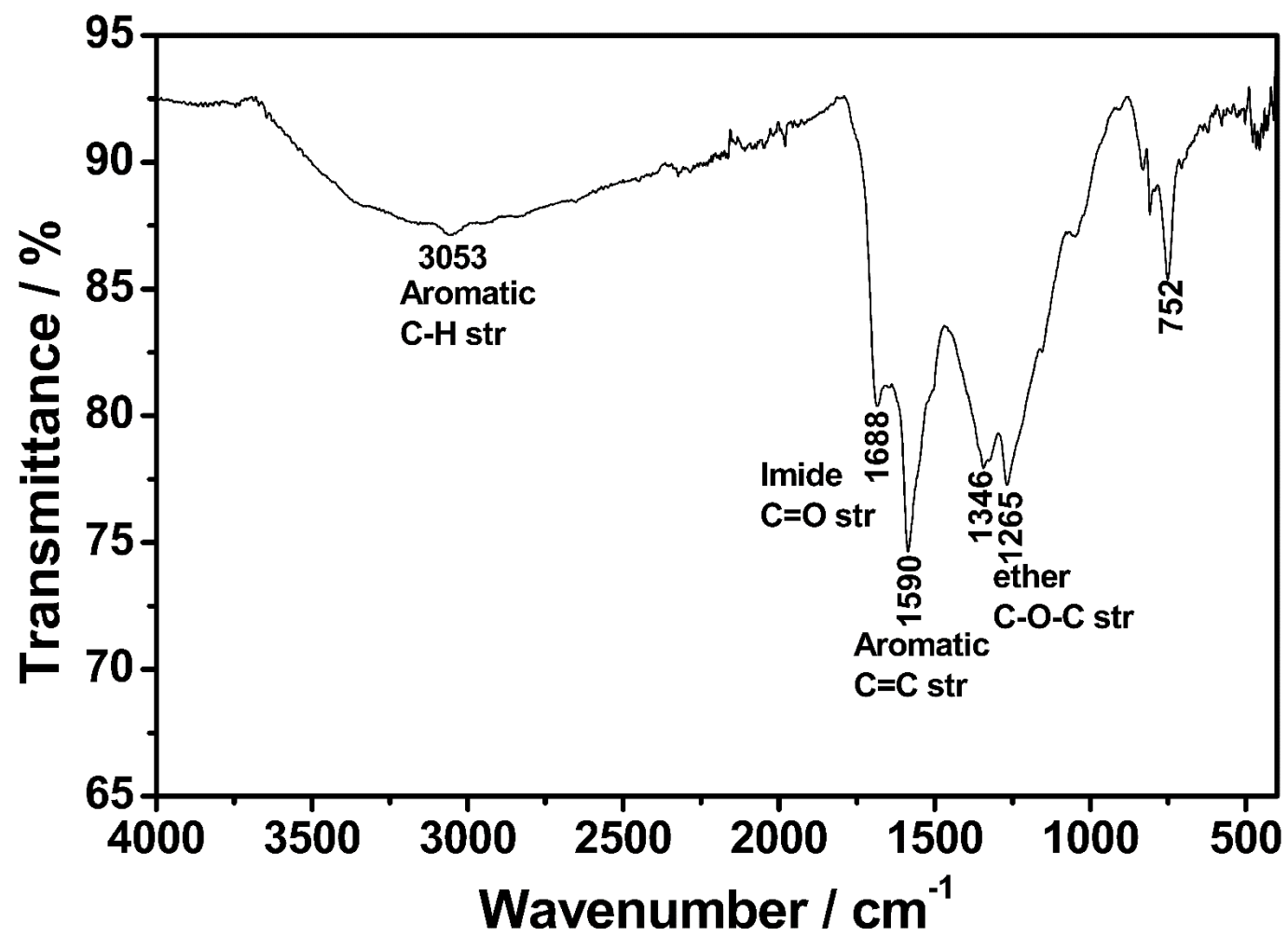Figure 4.13: FT−IR spectrum of HP−PDA

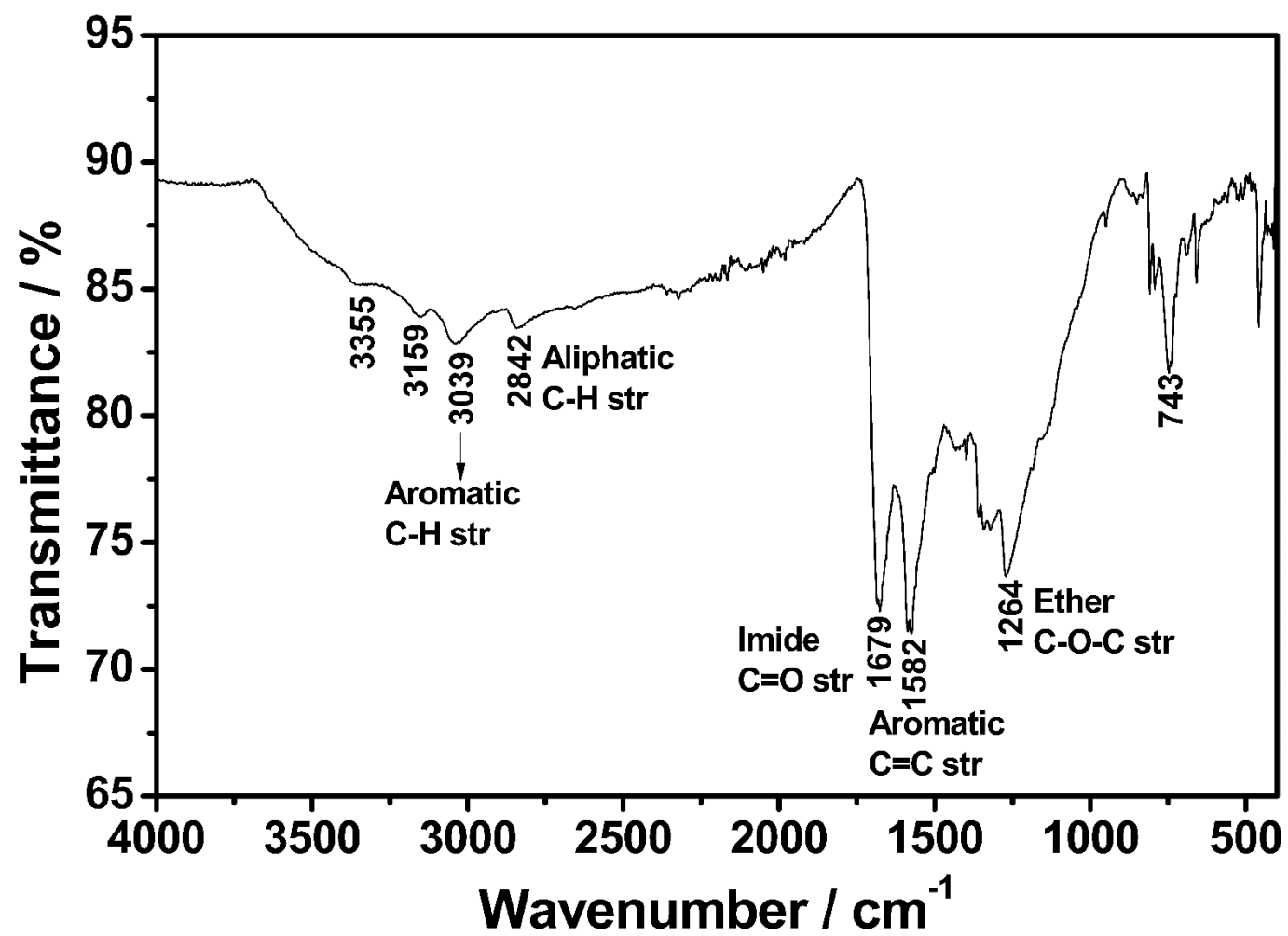Figure 4.14: FT−IR spectrum of HP−HEPDI

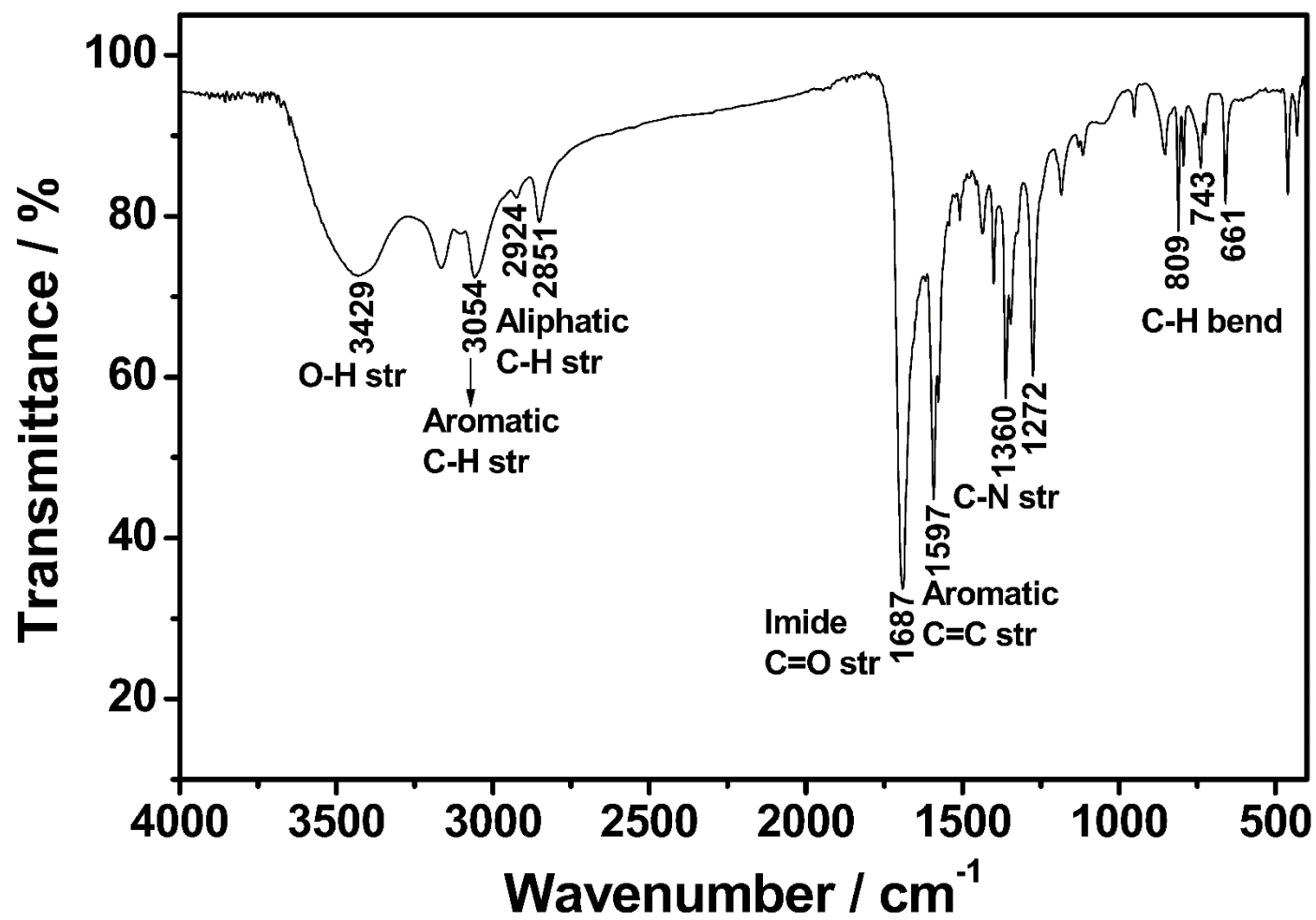Figure 4.15: FT−IR spectrum of TM−HEPDI

Figure 4.16: FT−IR spectrum of HEPDI
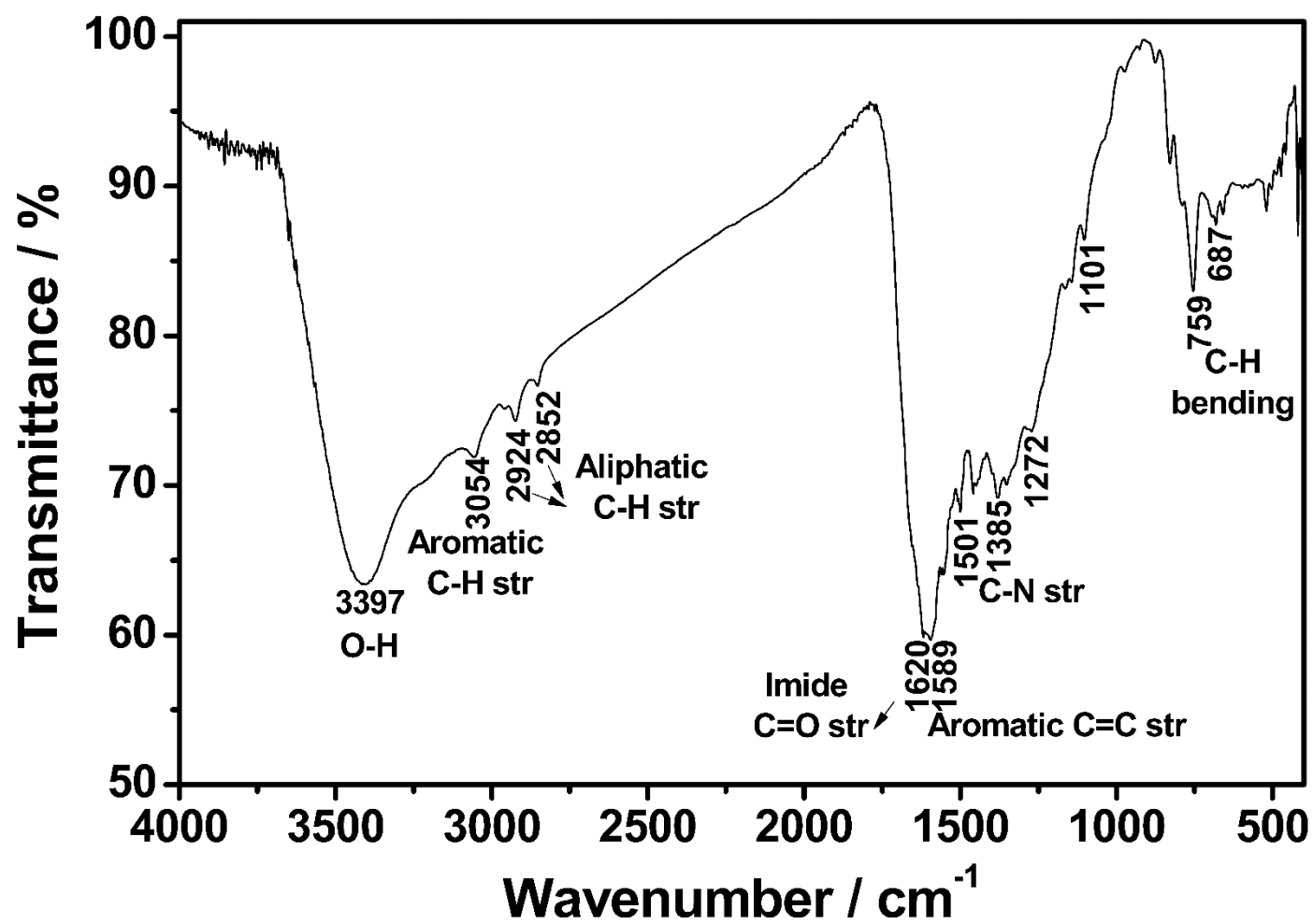
Figure 4.17: FT−IR spectrum of HP−TCPDI
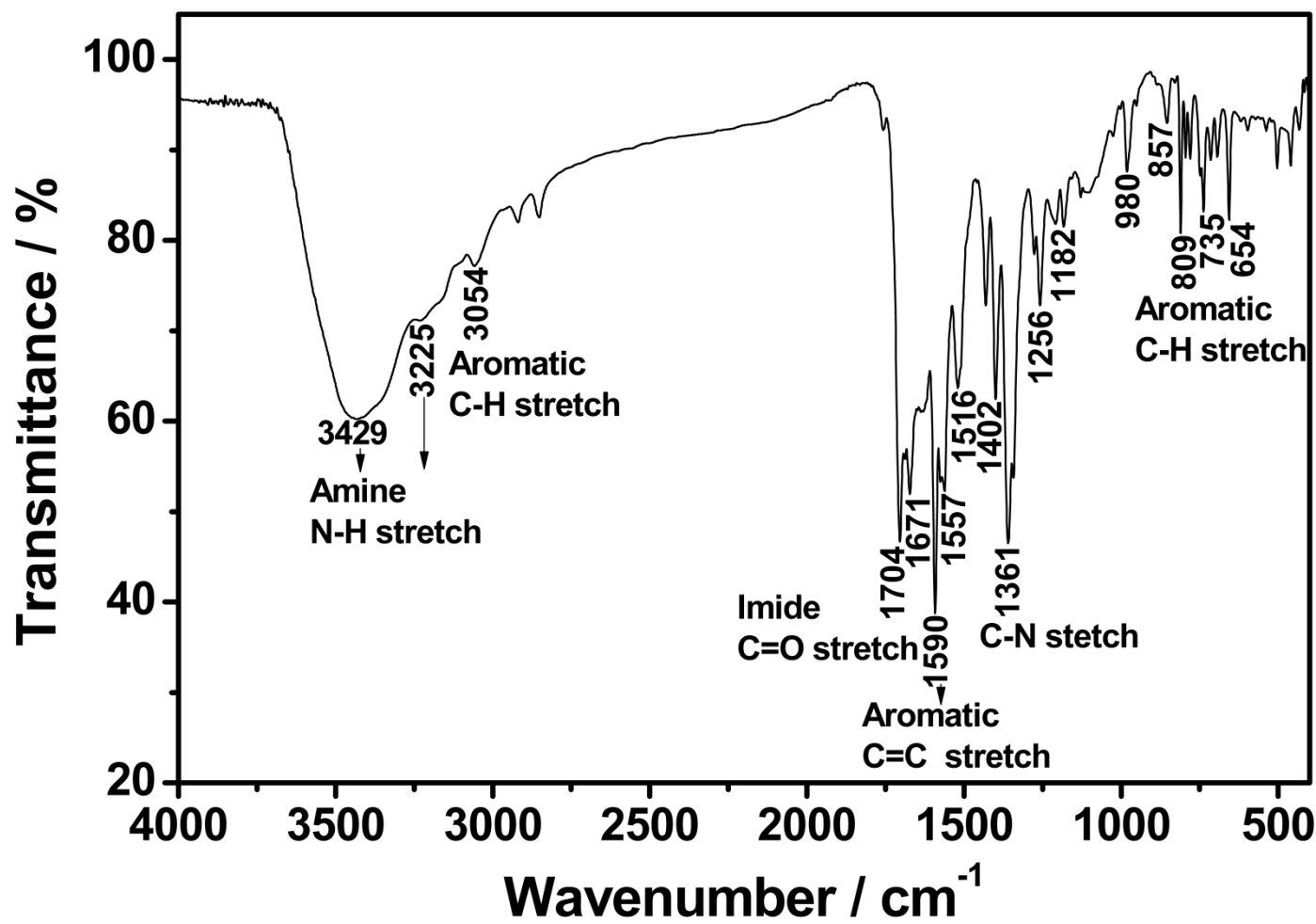
Figure 4.18: FT−IR spectrum of complex 1
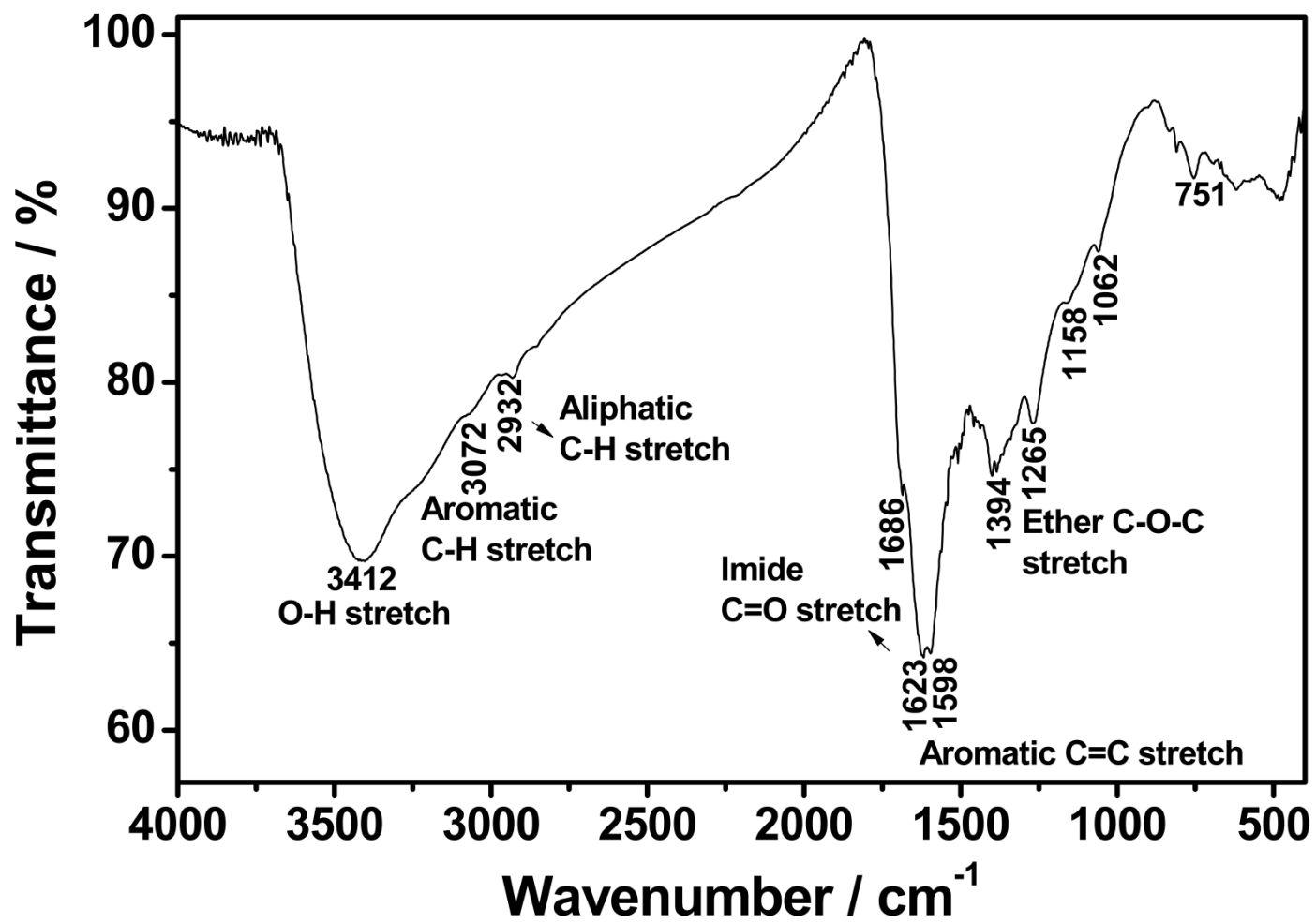
Figure 4.19: FT−IR spectrum of complex 2
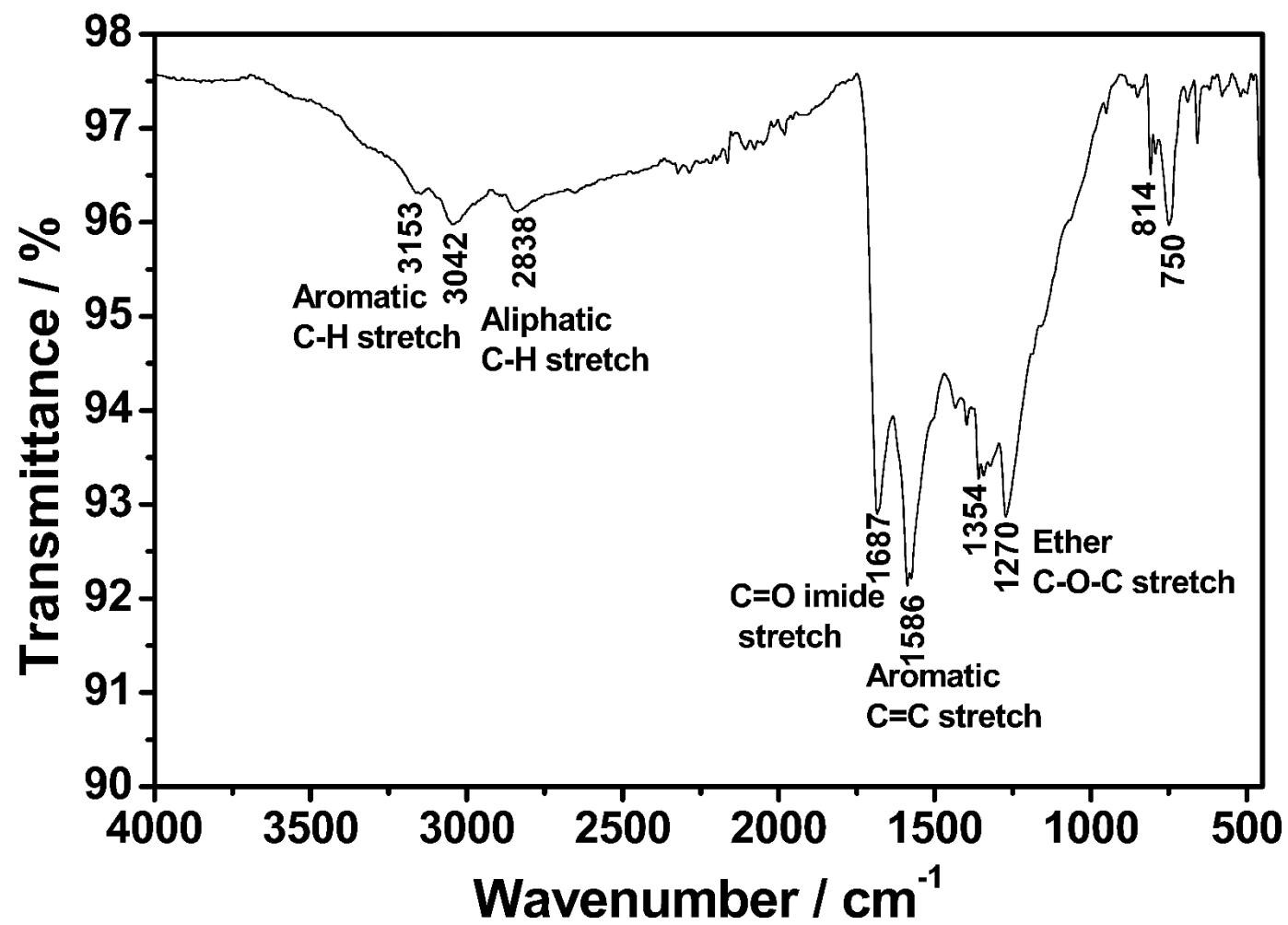
Figure 4.20: FT−IR spectrum of complex 3
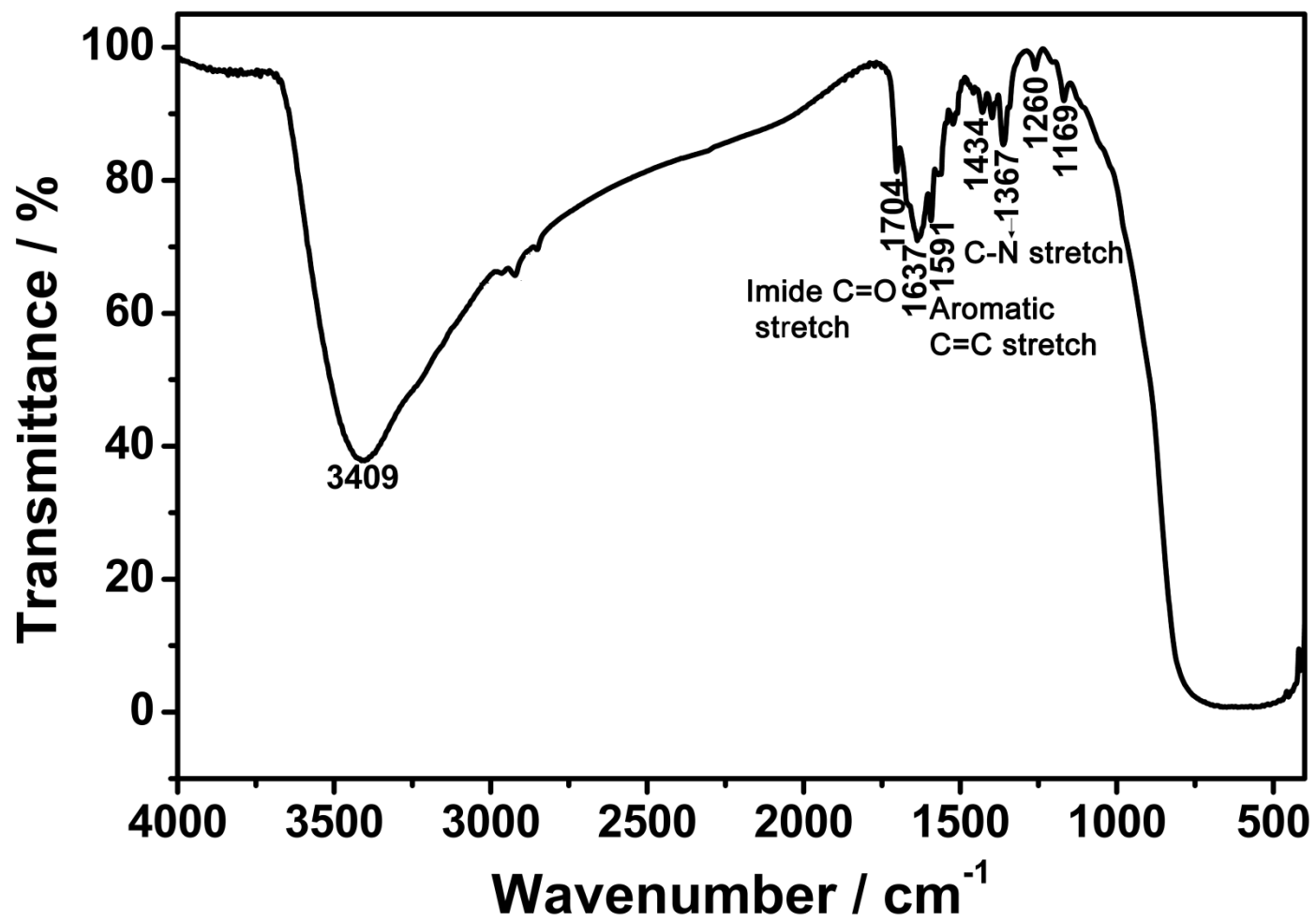
Figure 4.21: FT−IR spectrum of TAPDI binded to TiO_2
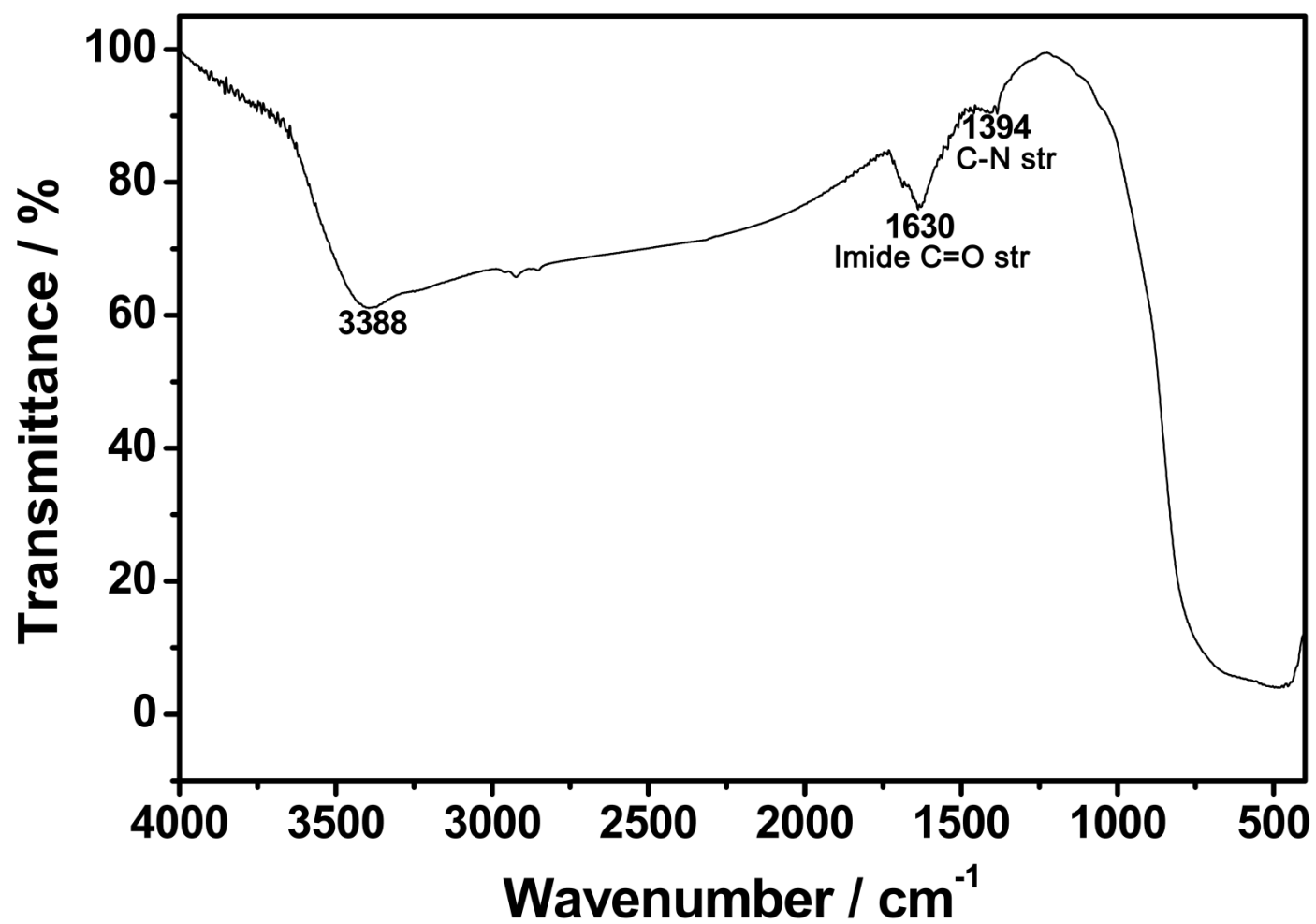
Figure 4.22: FT−IR spectrum of TANDI binded to TiO_2
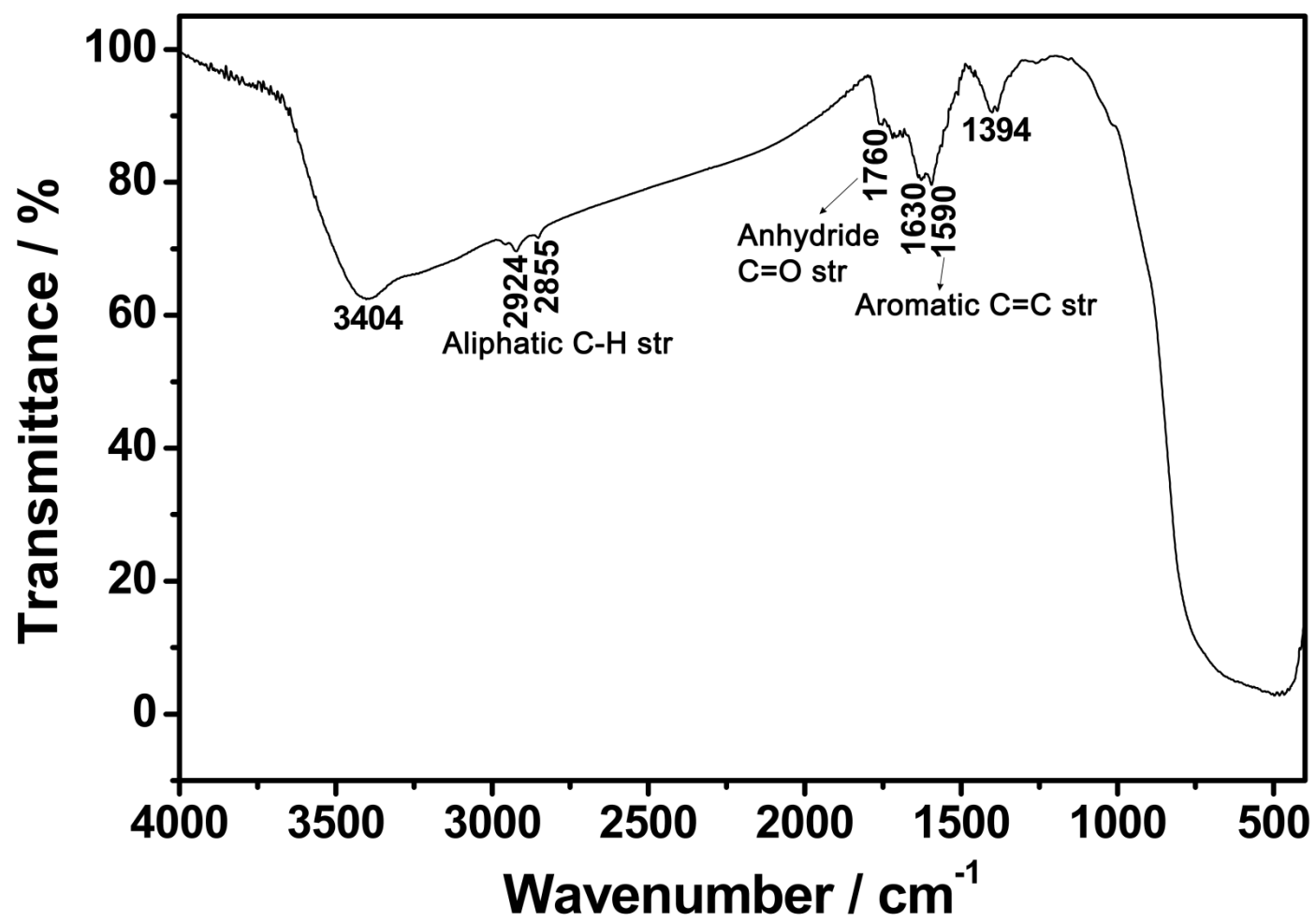
Figure 4.23: FT−IR spectrum of HP−PDA binded to TiO$_2$
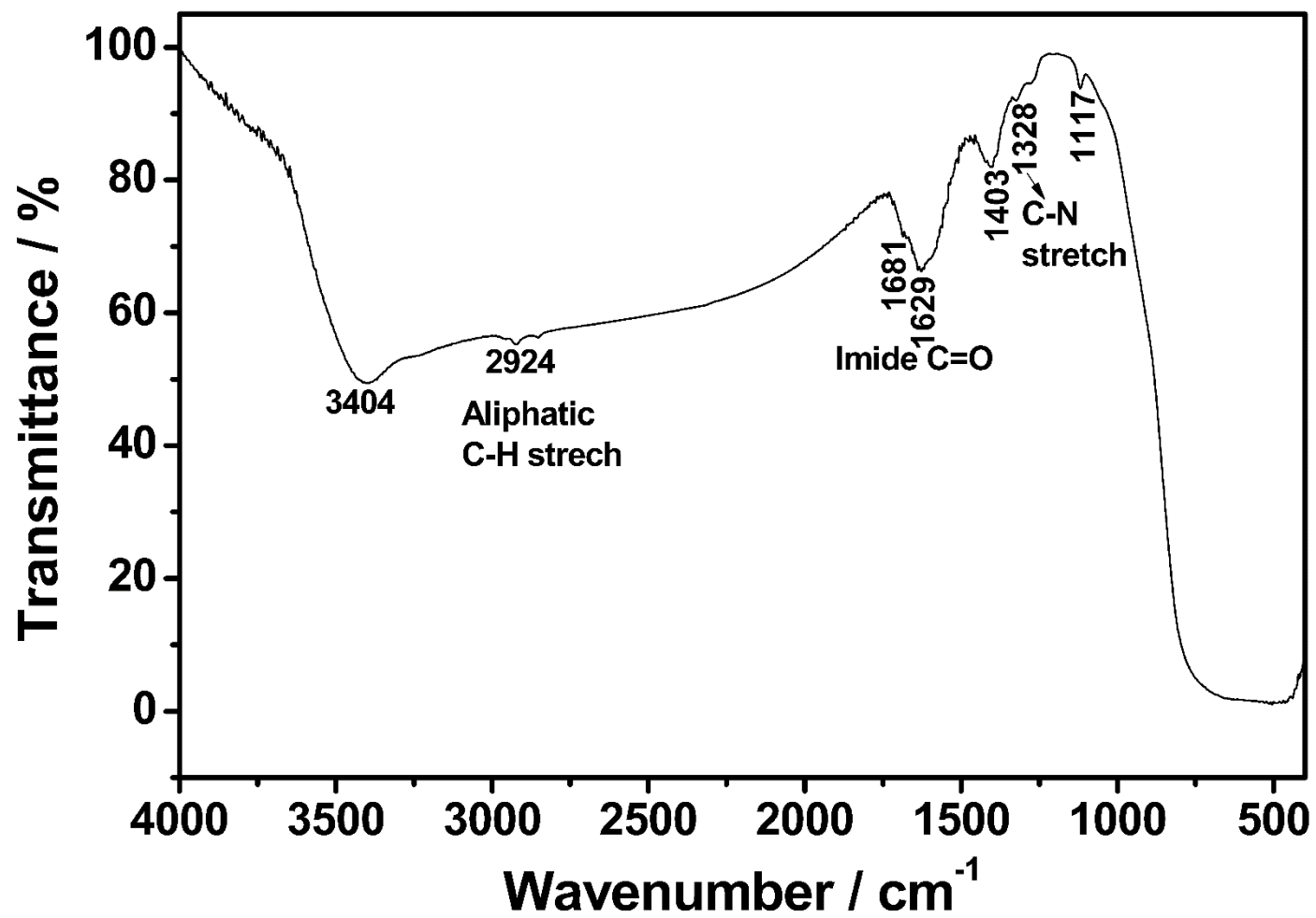
Figure 4.24: FT−IR spectrum of HP−HEPDI binded to TiO$_2$
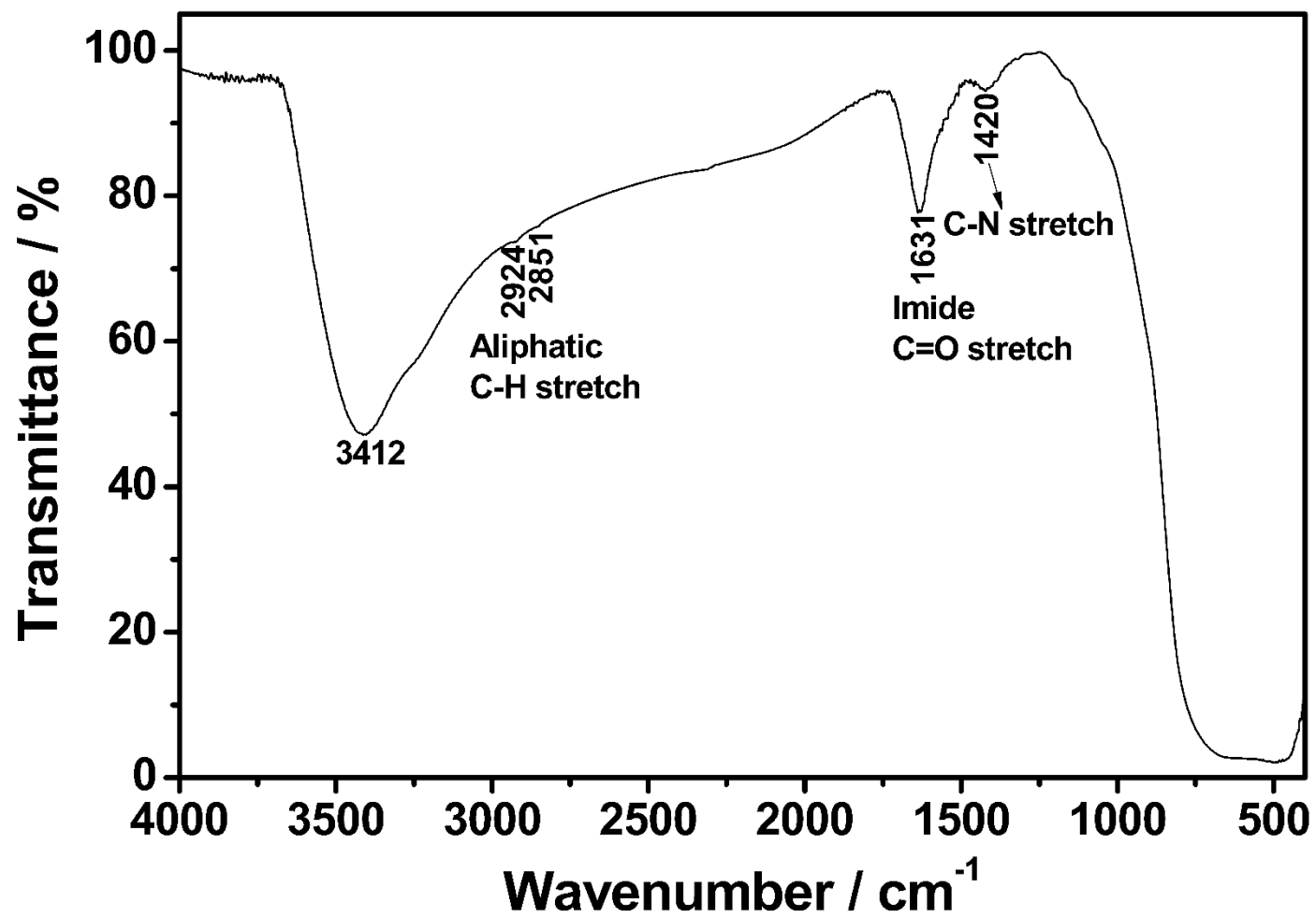
Figure 4.25: FT−IR spectrum of HP−TCPDI binded to TiO_2
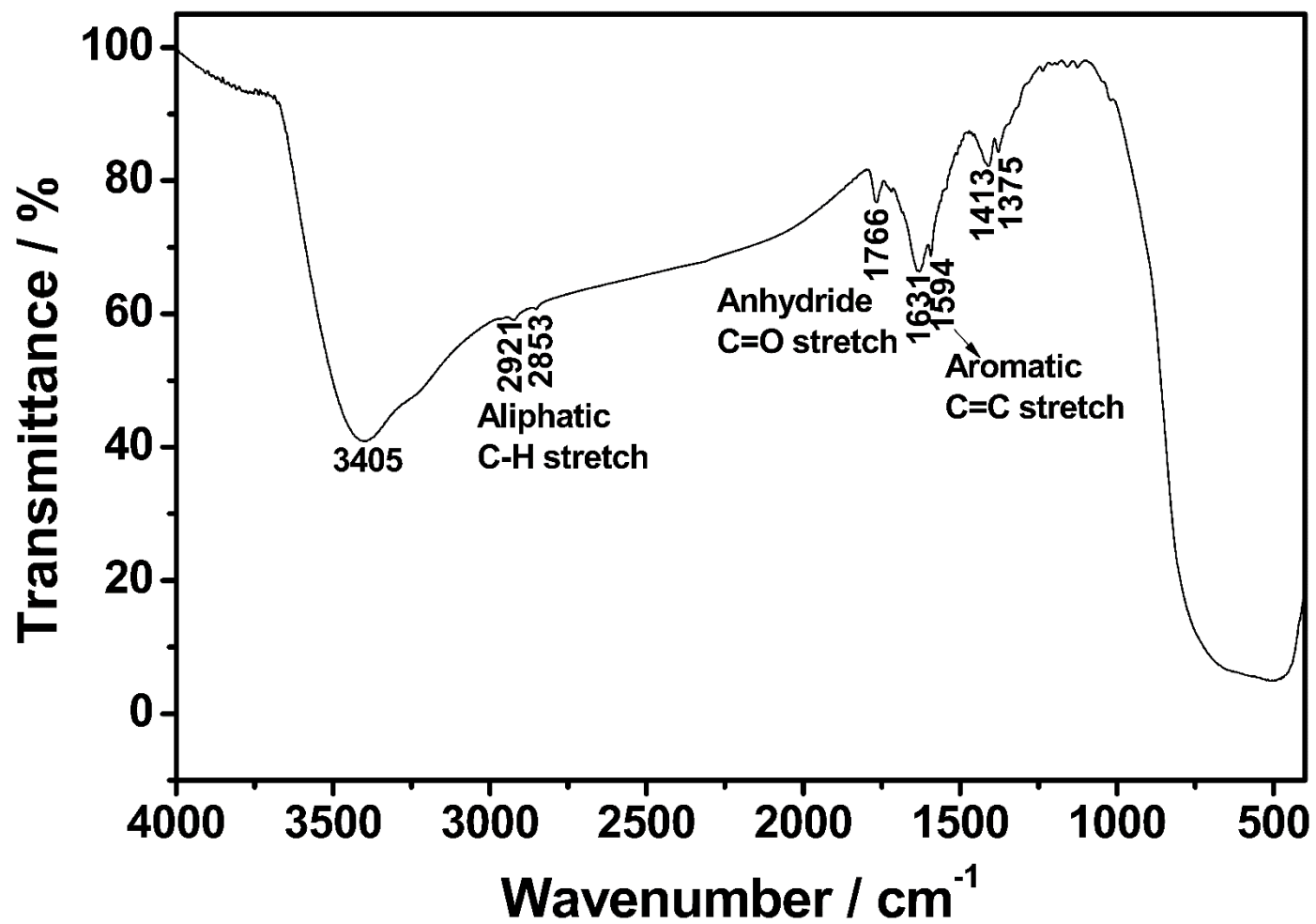
Figure 4.26: FT−IR spectrum of TM−PDA binded to TiO_2
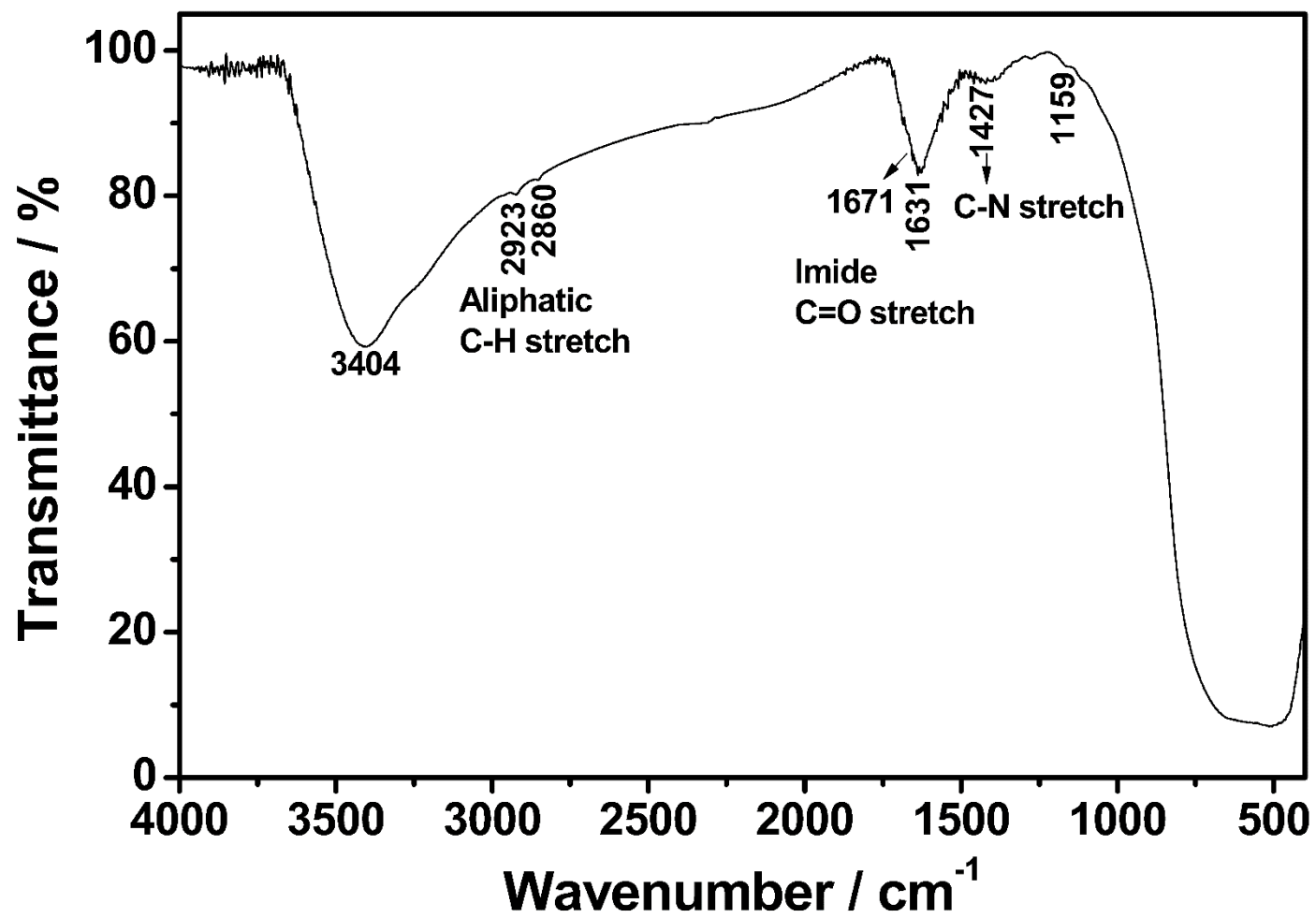
Figure 4.27: FT−IR spectrum of TM−HEPDI binded to TiO_2
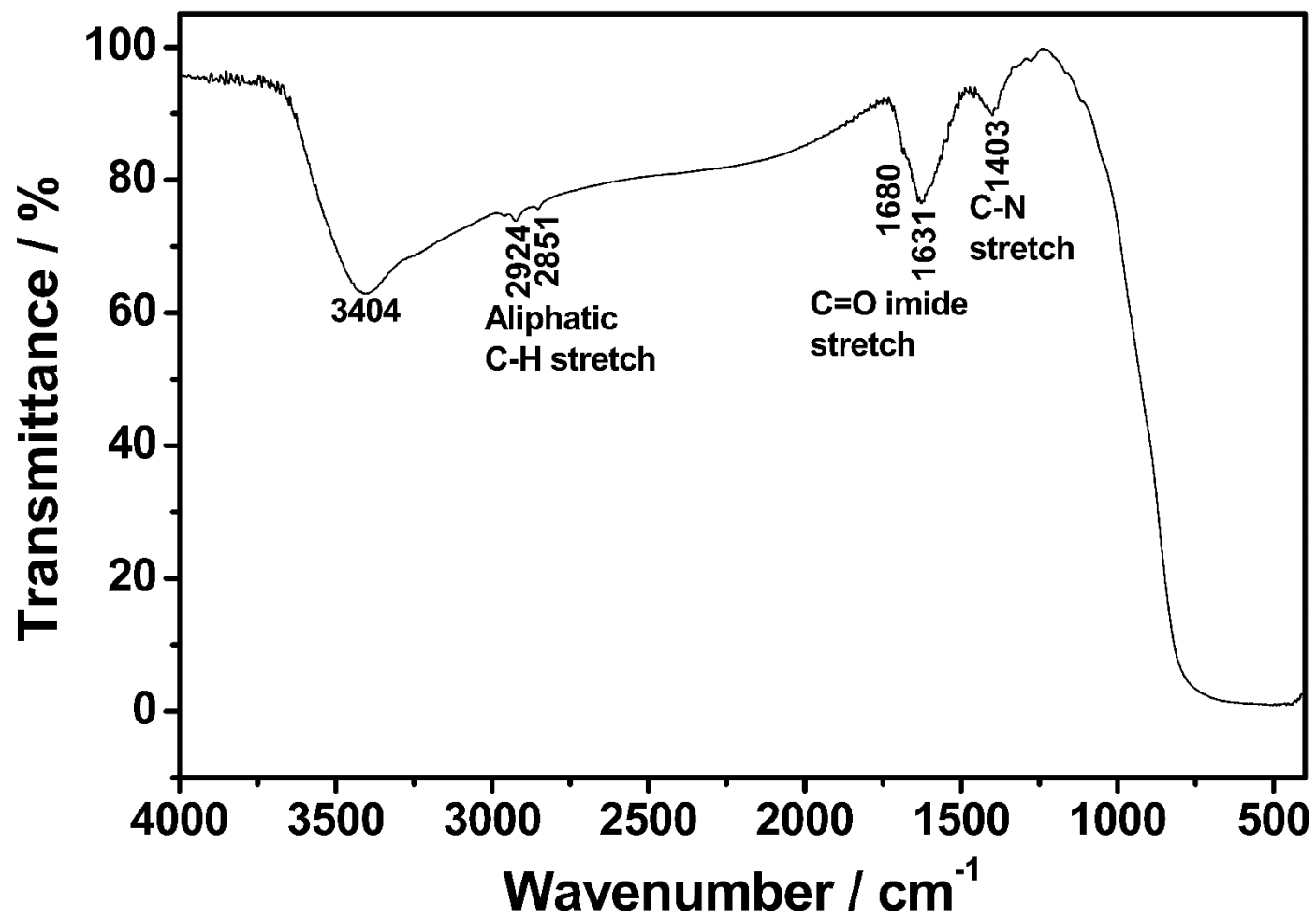
Figure 4.28: FT−IR spectrum of HEPDI binded to TiO_2

Figure 4.29: (a.) TAPDI absorption spectra in different solvents (b.) Emission spectra at excitation wavelength of 485 nm in different solvents

Figure 4.30: Concentration dependent absorption spectra of TAPDI in (a.) NMP, (b.) DMF and (c) DMSO

Figure 4.31: Concentration dependent emission spectra of TAPDI in (a.) NMP, (b.) DMF and (c) DMSO
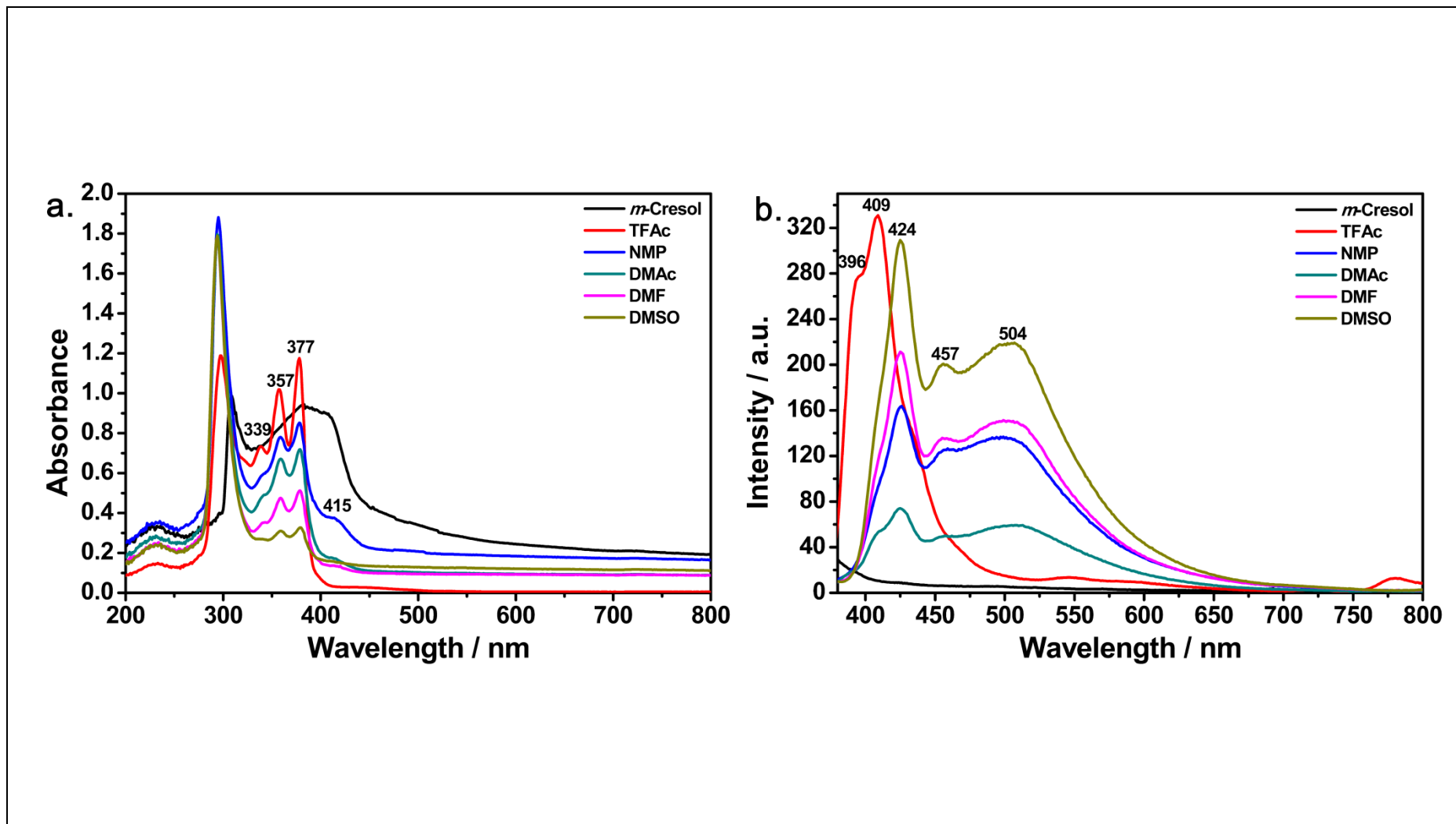
Figure 4.32: (a.) TANDI absorption spectra in different solvents (b.) Emission spectra at excitation wavelength of 485 nm in different solvents
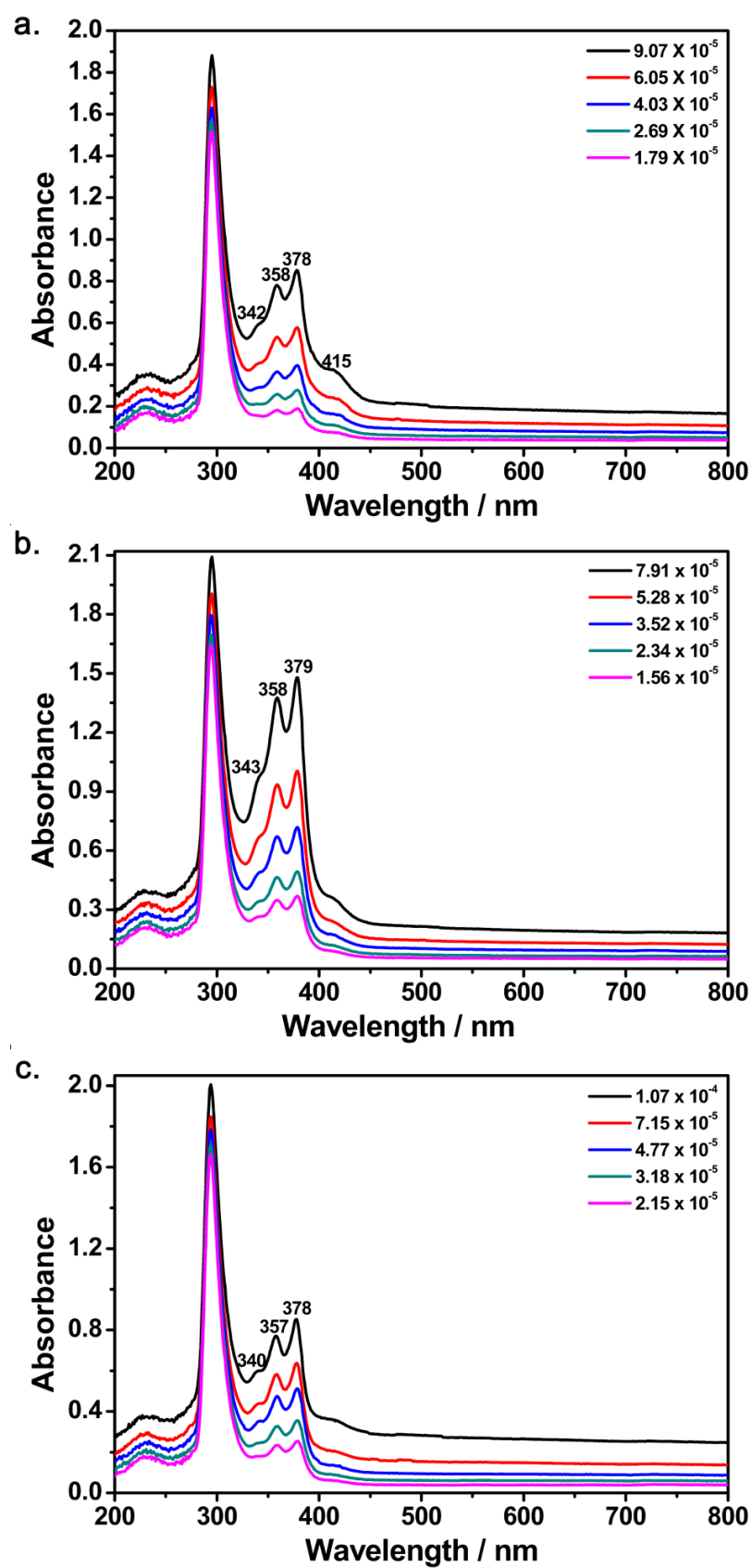
Figure 4.33: Concentration dependent absorption spectra of TANDI in (a.) NMP, (b.) DMAc and (c) DMF
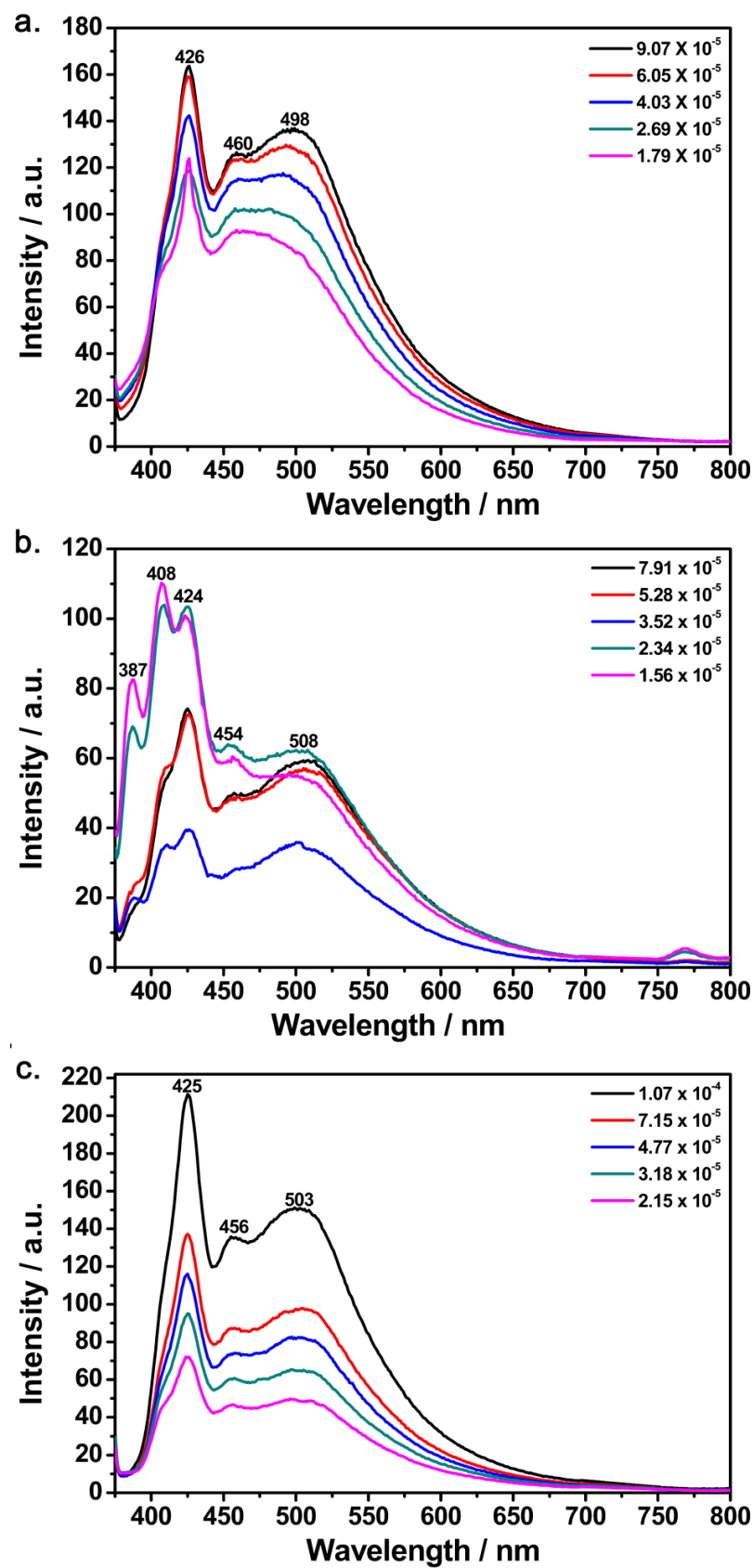
Figure 4.34: Concentration dependent emission spectra of TANDI in (a.) NMP, (b.) DMAc and (c) DMF
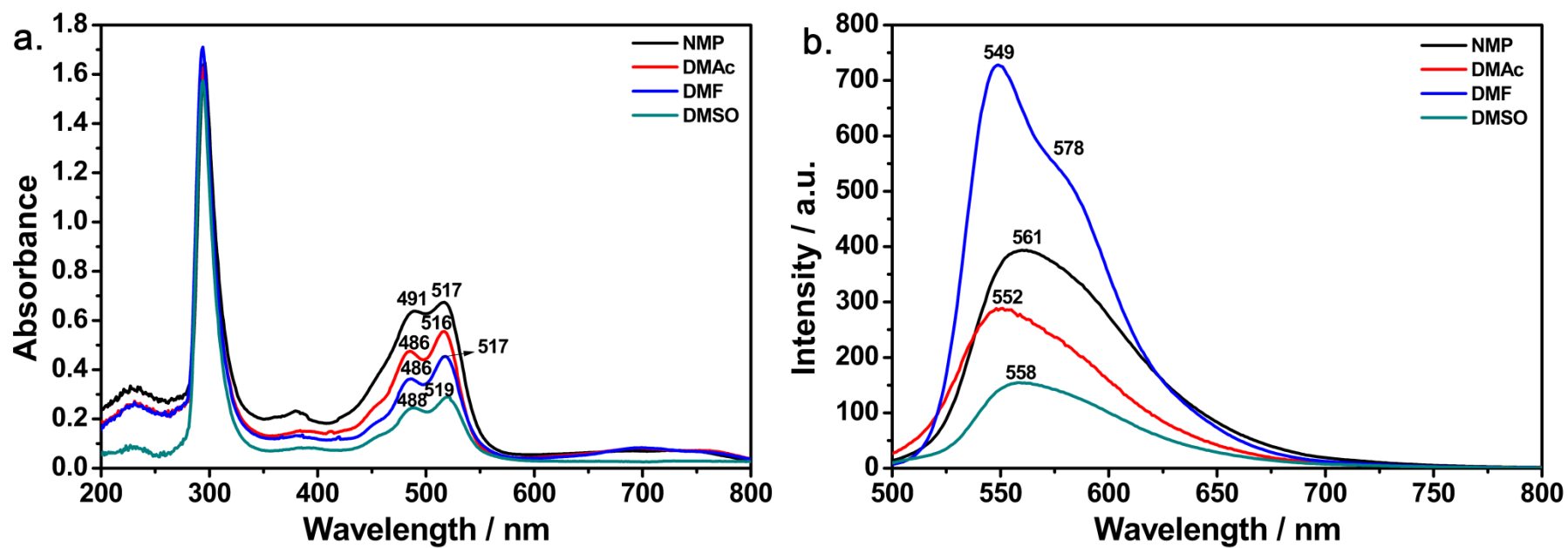
Figure 4.35: (a.) TM−PDA absorption spectra in different solvents. (b.) Emission spectra at excitation wavelength of 485 nm in different solvents
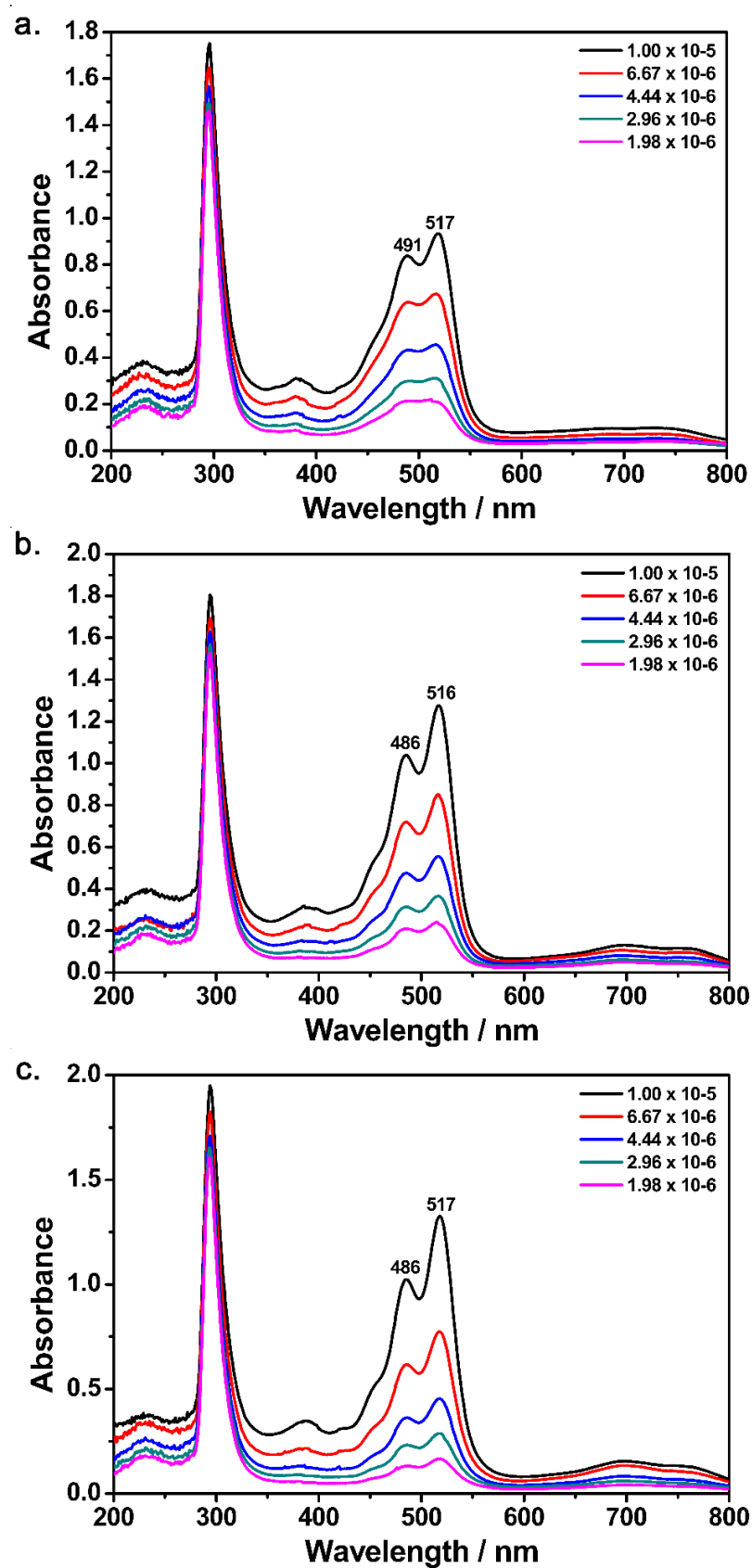
Figure 4.36: Concentration dependent absorption spectra of TM−PDA (a.) NMP, (b.) DMF and (c.) DMSO
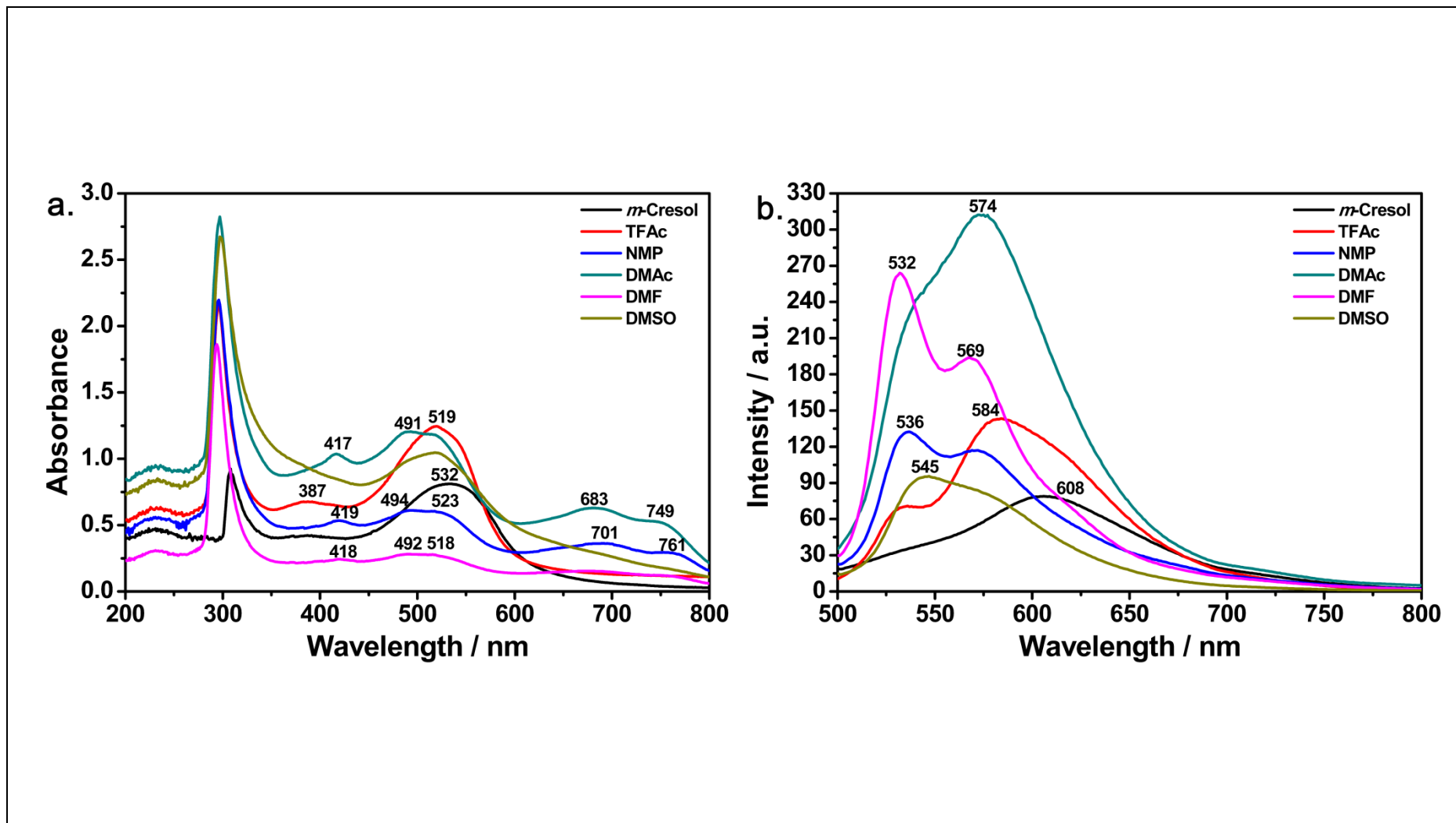
Figure 4.37: (a.) HP−PDA absorption spectra in different solvents (b.) Emission spectra at excitation wavelength of 485 nm in different solvents
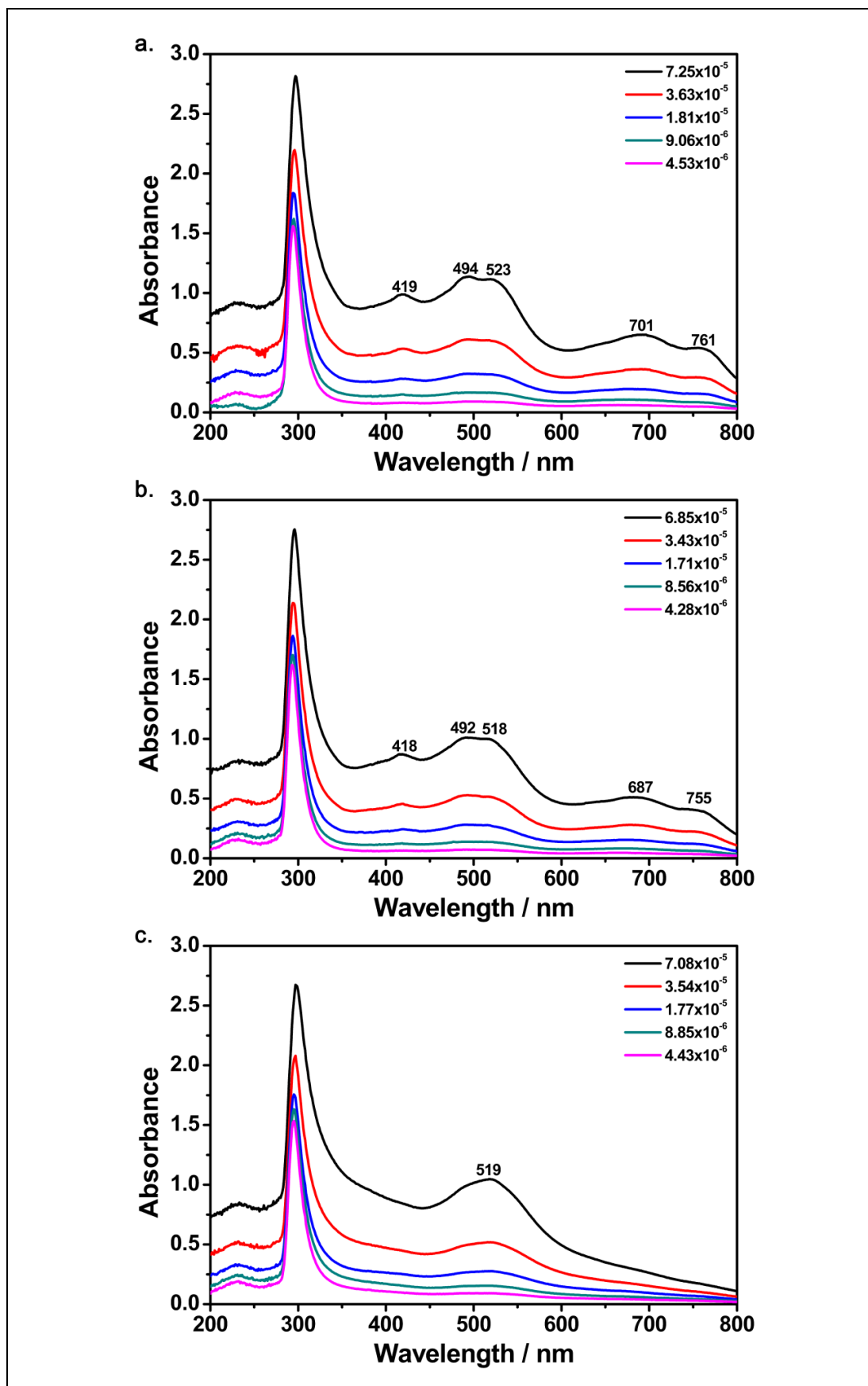
Figure 4.38: Concentration dependent absorption spectra of HP−PDA in (a.) NMP, (b.) DMF and (c.) DMSO
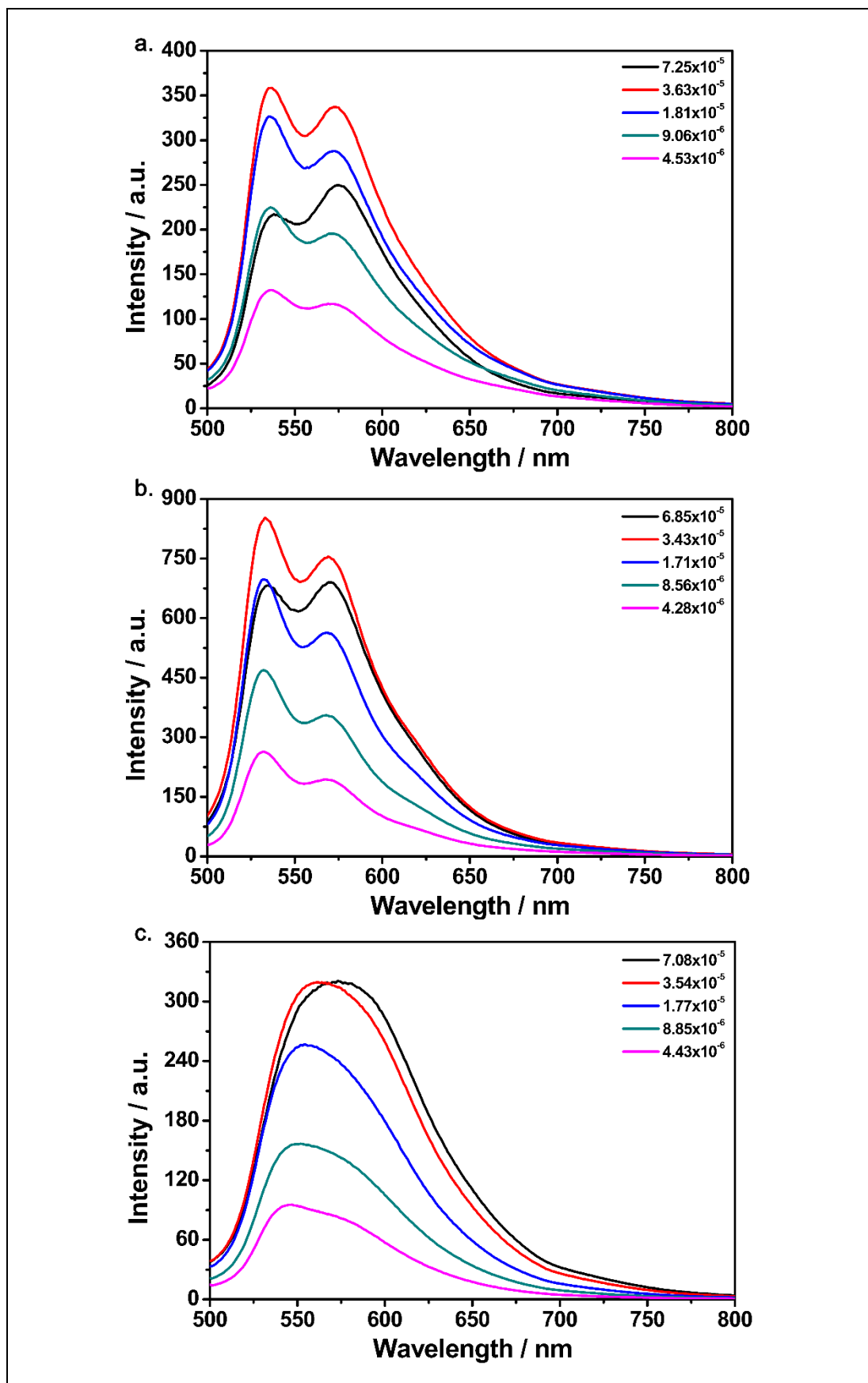
Figure 4.39: Concentration dependent emission spectra of HP−PDA (a.) NMP, (b.) DMF and (c.) DMSO at excitation wavelength of 485 nm
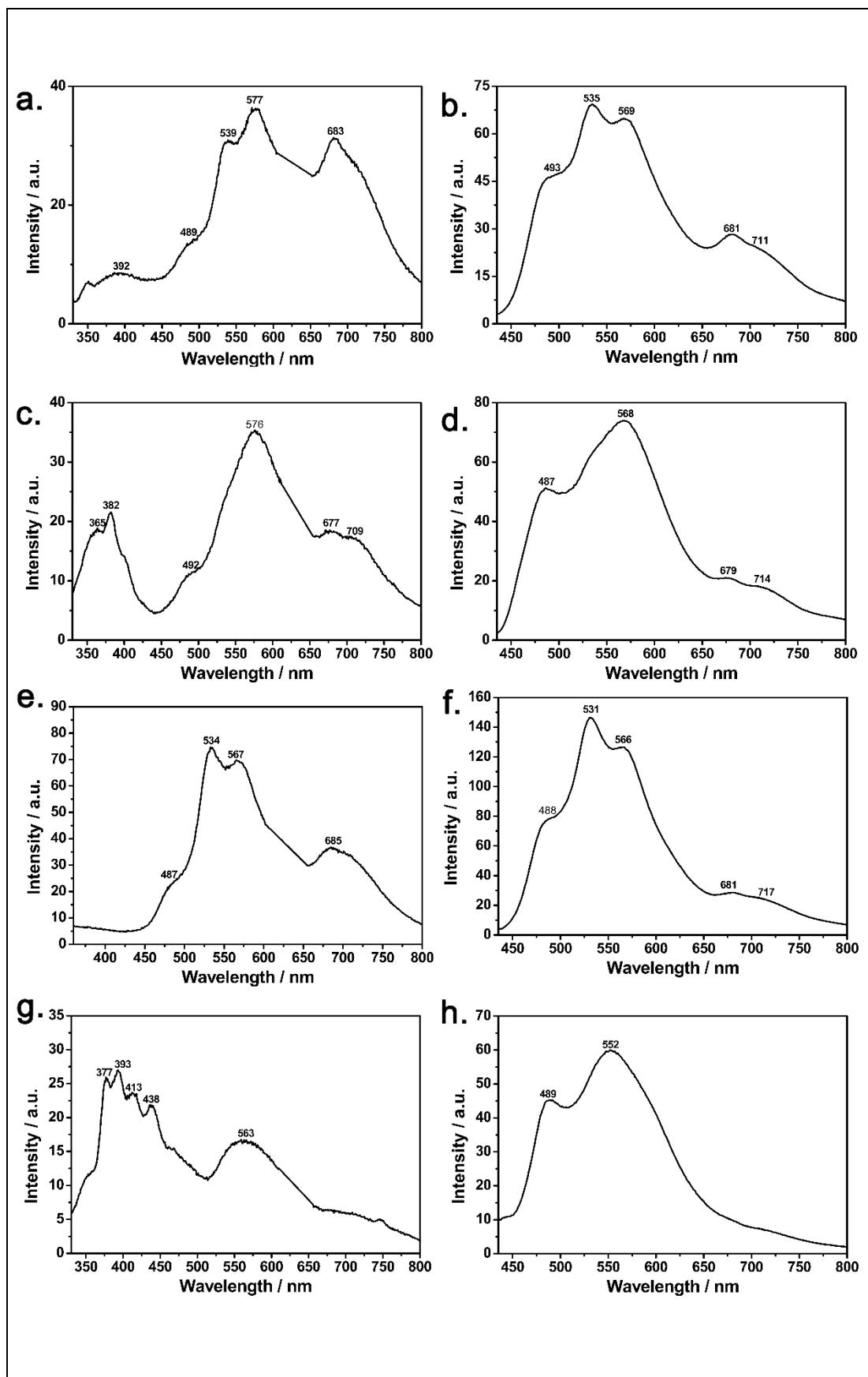
Figure 4.40: Emission spectra of HP−PDA at excitation wavelength of 315 nm (a,c,e,g) and 420 nm (b,d,f,h) in NMP (a,b), DMAc (c,d), DMF (e,f), DMSO (g,h)
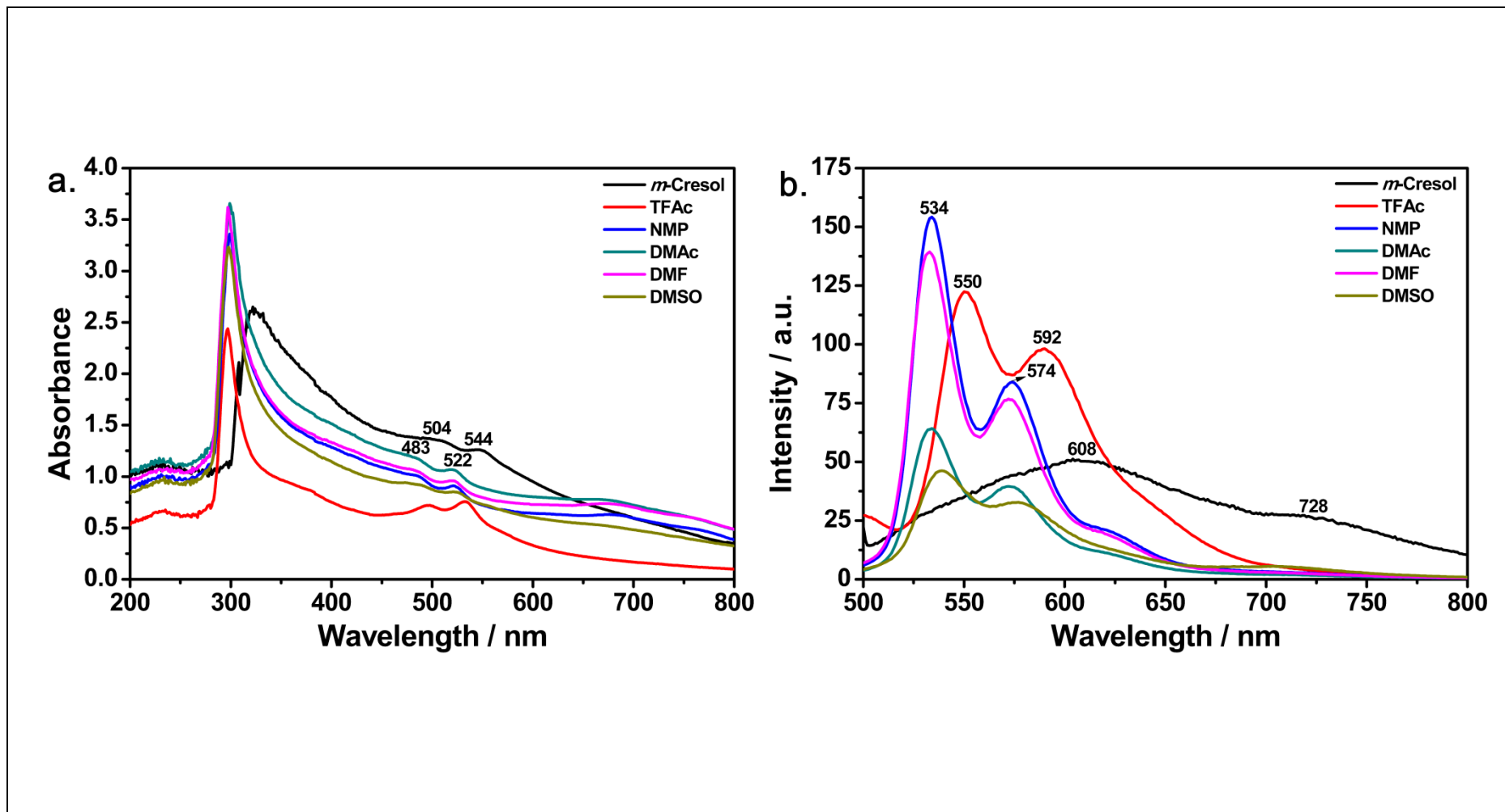
Figure 4.41: (a.)TM−HEPDI absorption spectra in different solvents (b.)Emission spectra at excitation wavelength of 485 nm in different solvents
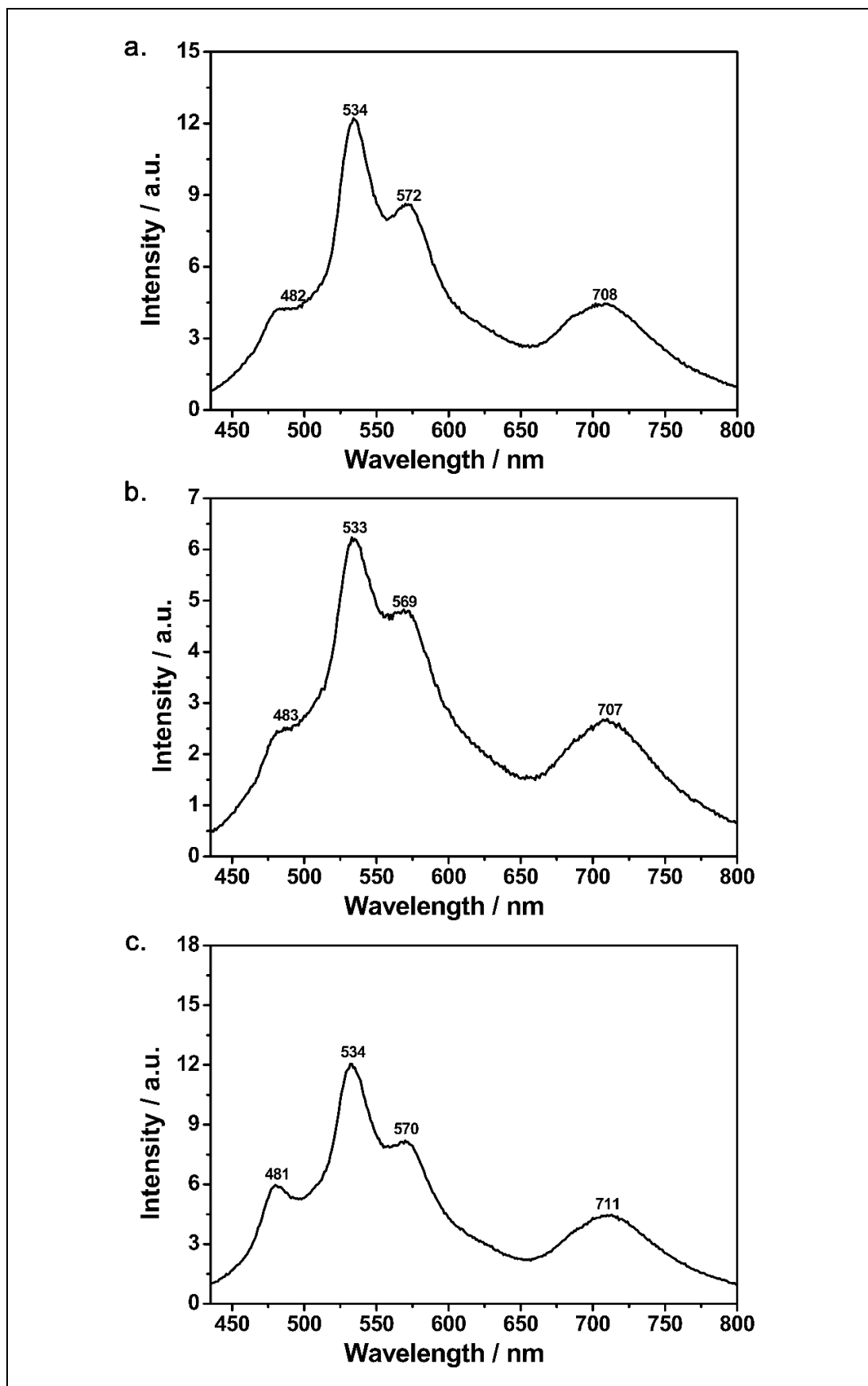
Figure 4.42: Emission spectra of TM−HEPDI at excitation wavelength of 420 nm in NMP (a), DMAc (b), DMF (c)
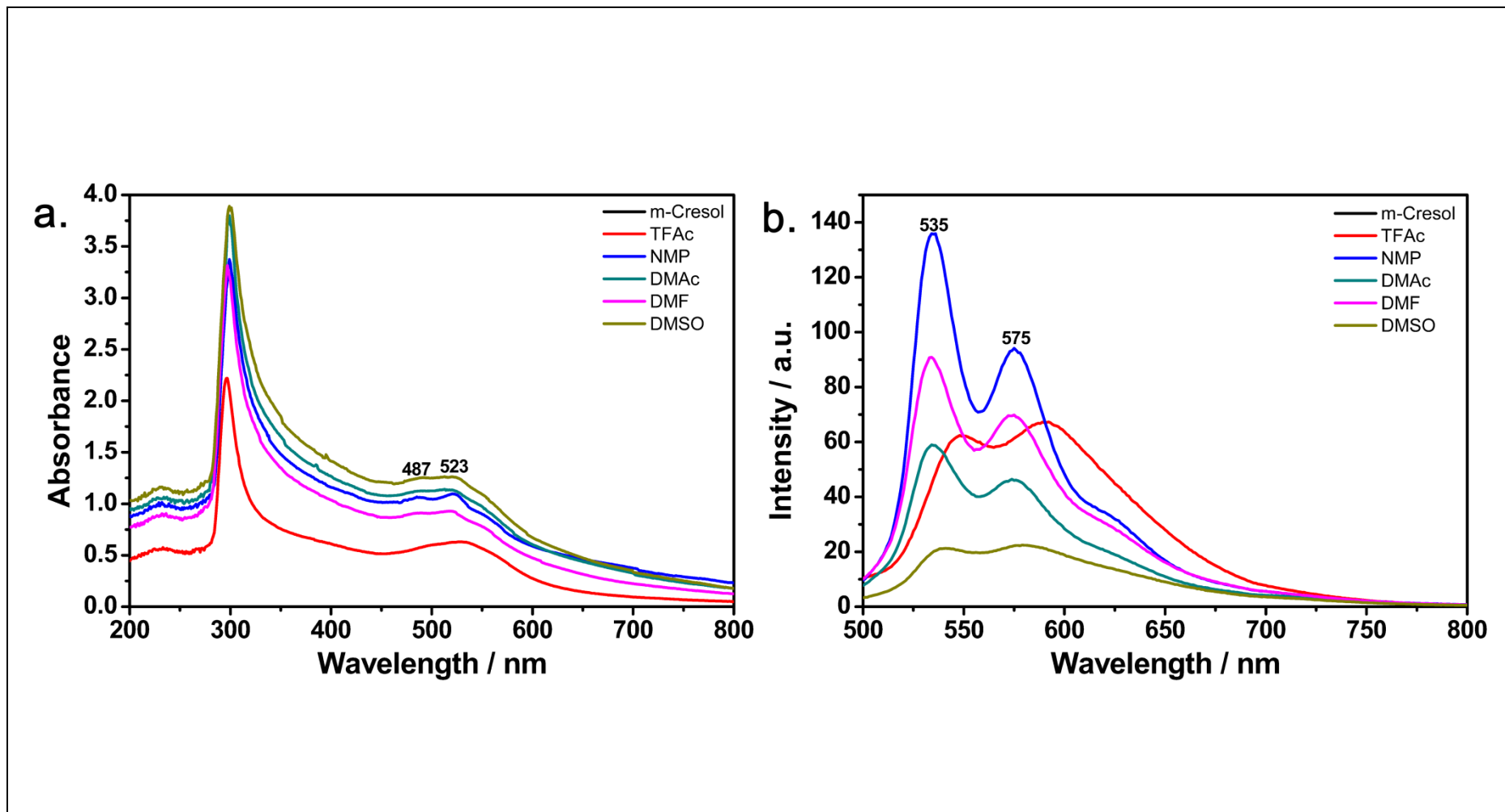
Figure 4.43: (a.) HP−HEPDI absorption spectra in different solvents (b.) Emission spectra at excitation wavelength of 485 nm in different solvents
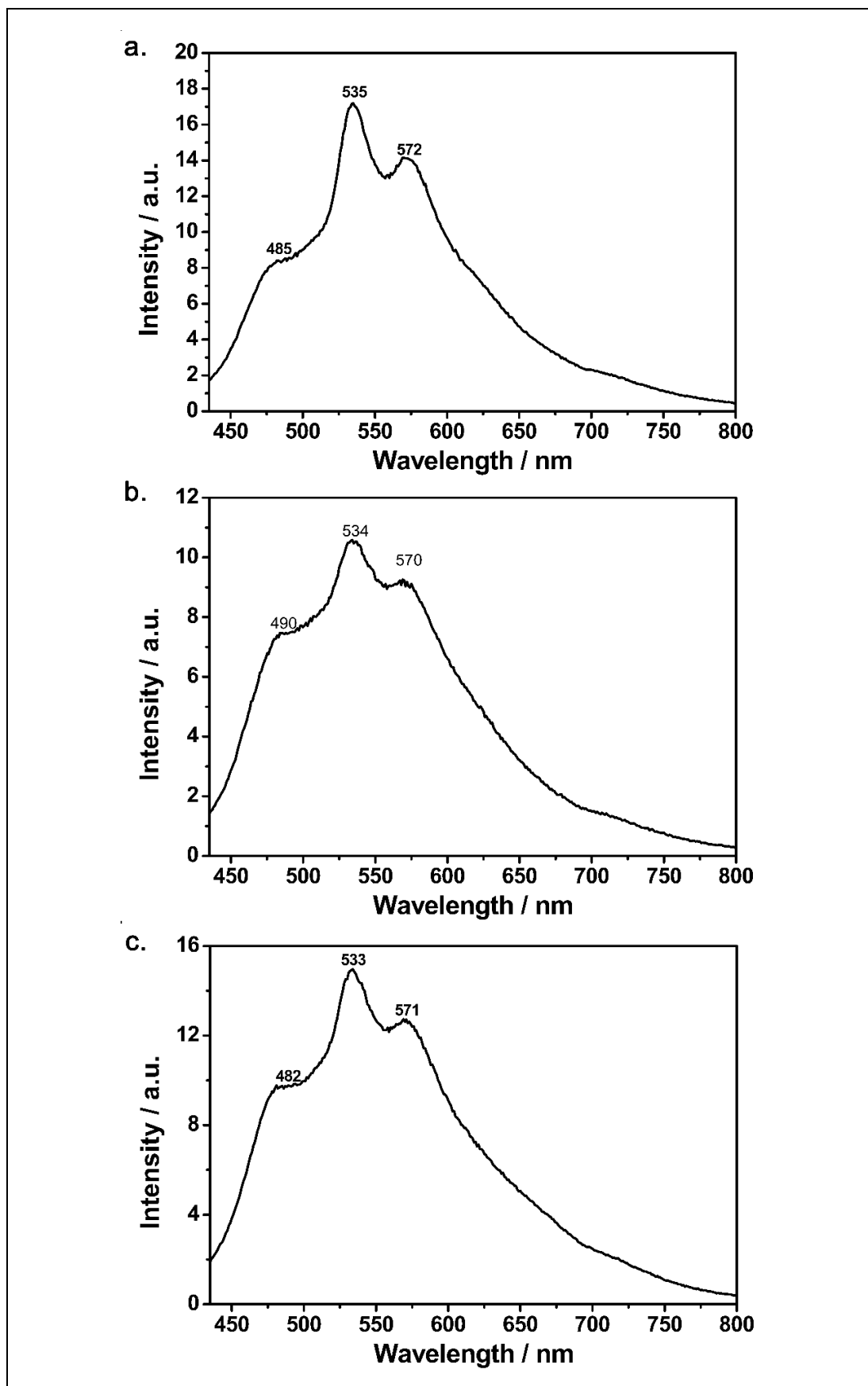
Figure 4.44: Emission spectra of HP−HEPDI at excitation wavelength of 420 nm in NMP (a), DMAc (b), DMF (c)
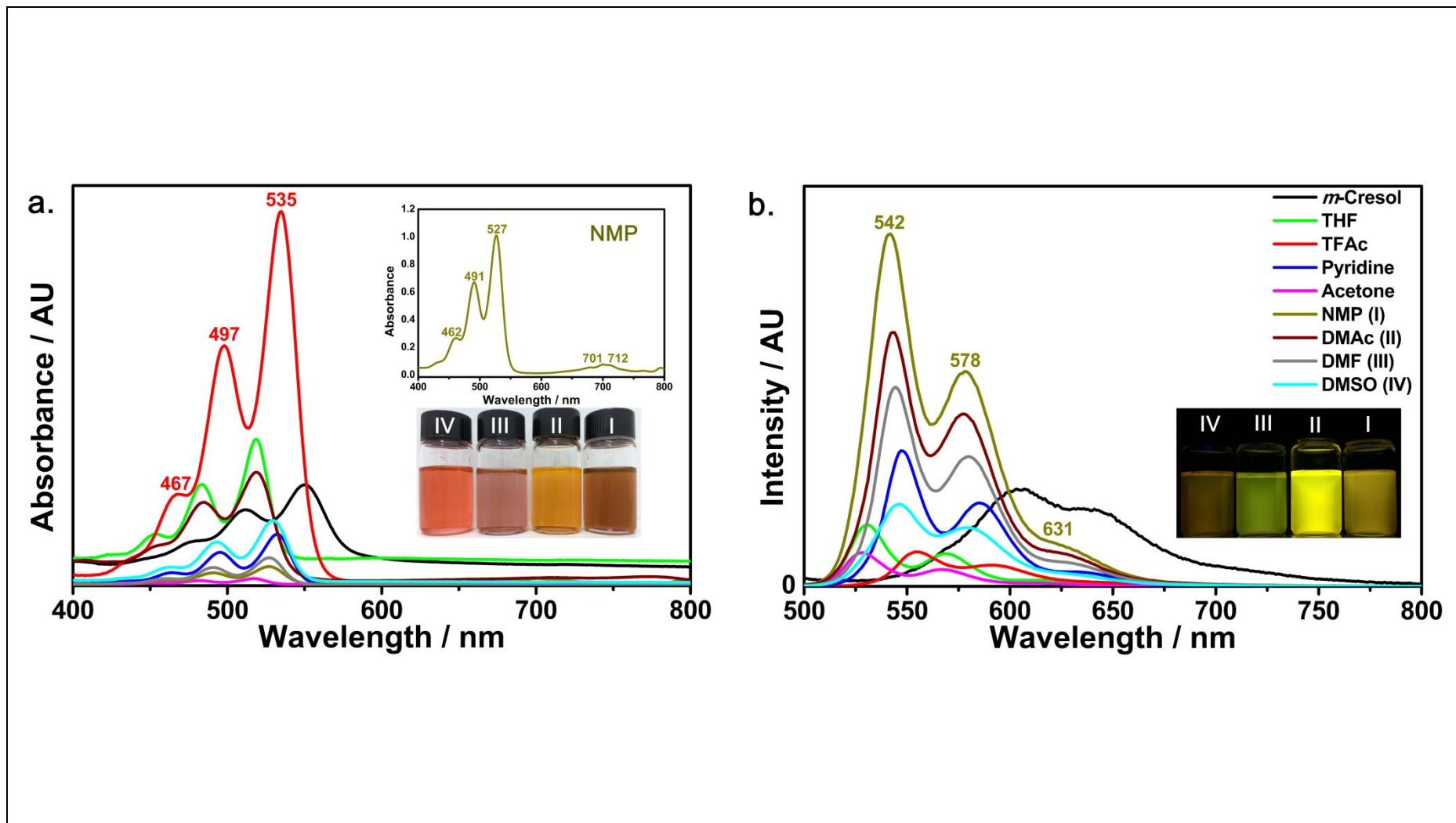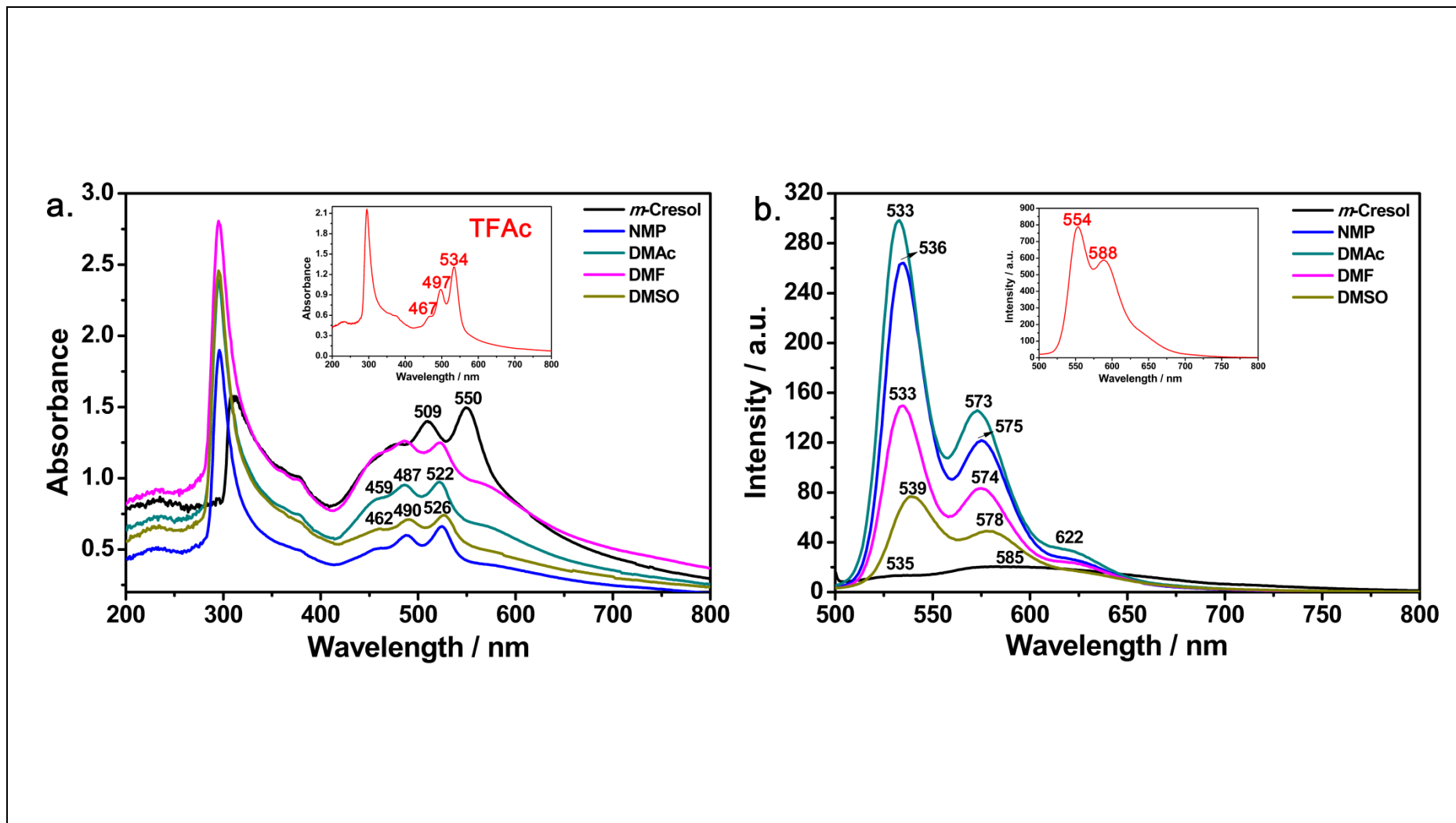
Figure 4.45: (a.) HEPDI absorption spectra in different solvents (b.) Emission spectra at excitation wavelength of 485 nm in different solvents
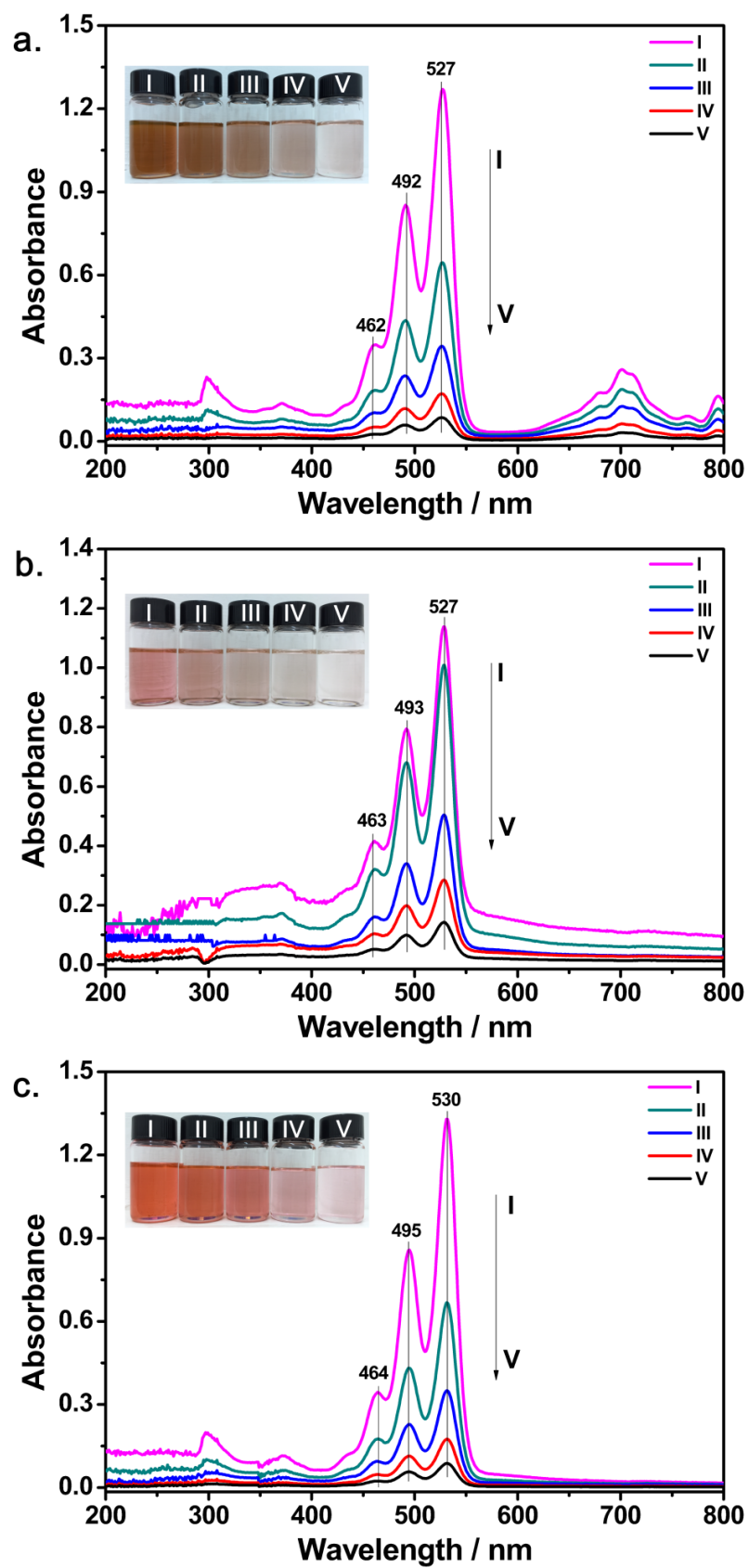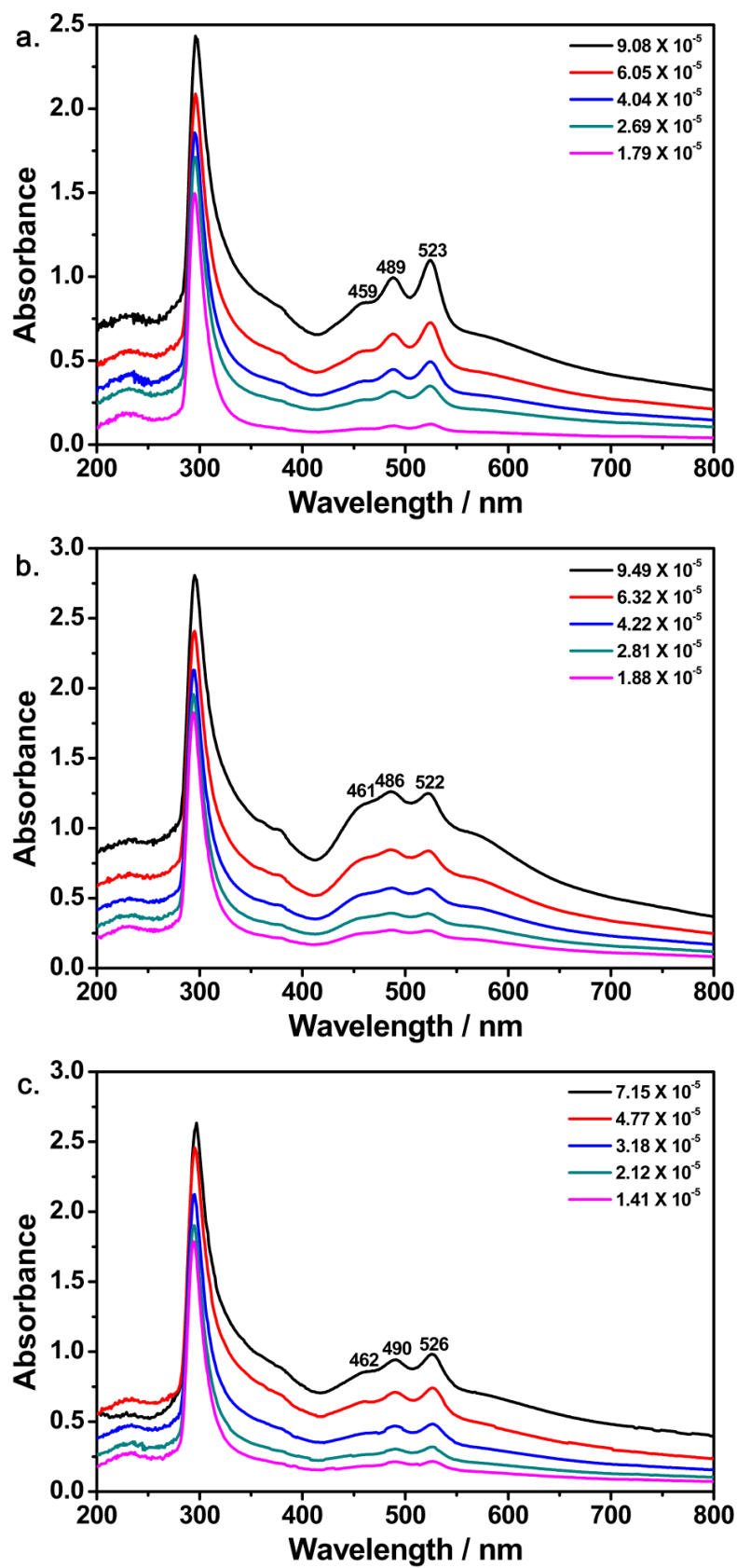
Figure 4.46: Concentration dependent absorption spectra of HEPDI in (a.) NMP, (b.) DMF and (c) DMSO
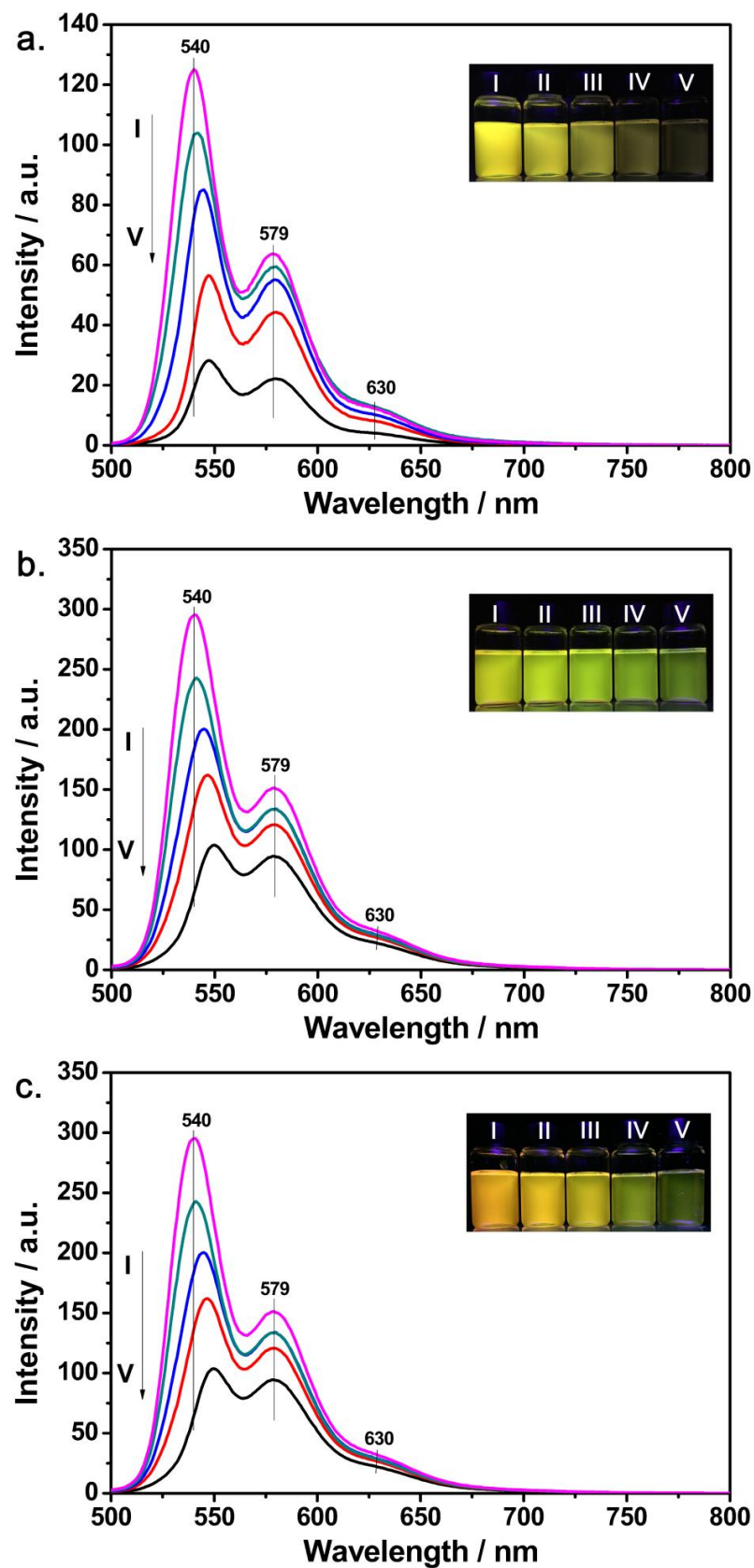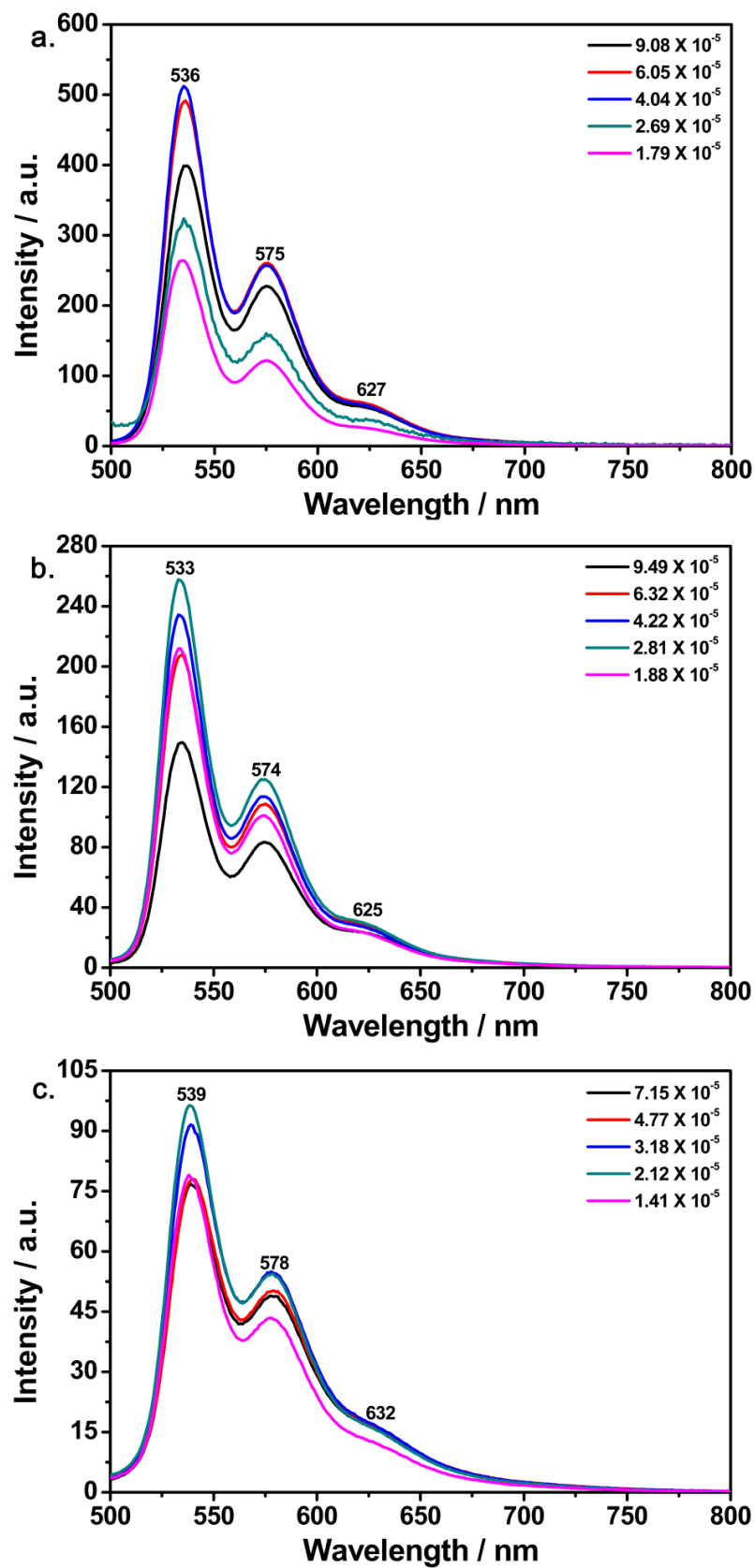
Figure 4.47: Concentration dependent emission spectra of HEPDI in (a.) NMP, (b.) DMF and (c) DMSO
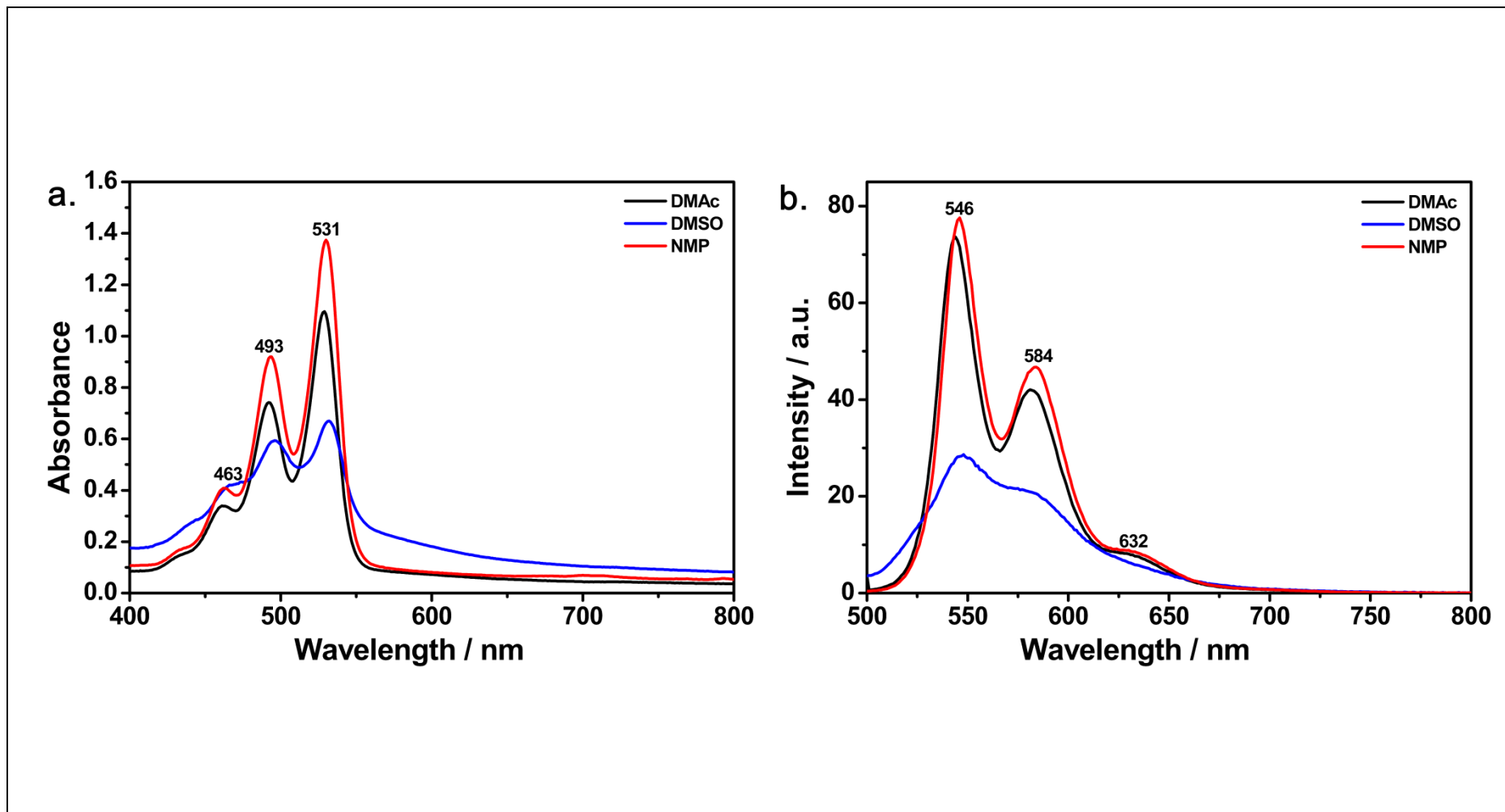
Figure 4.48: (a.) Complex 1 absorption spectra in different solvents. (b.) Emission spectra at excitation wavelength of 485 nm in different solvents
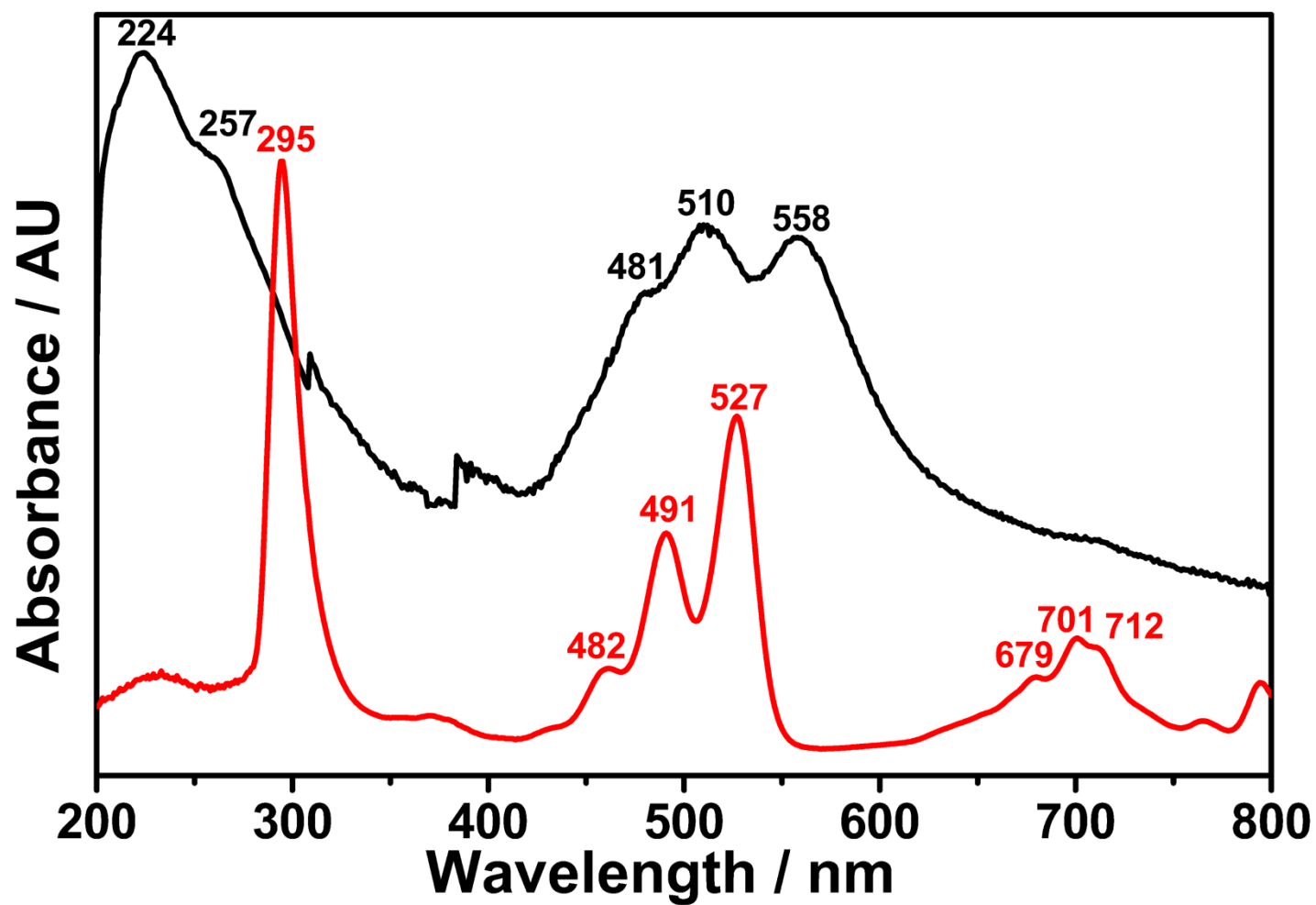
Figure 4.49: Solid−state absorption spectrum of TAPDI is shown by black color, absorption spectrum in NMP is shown by red color
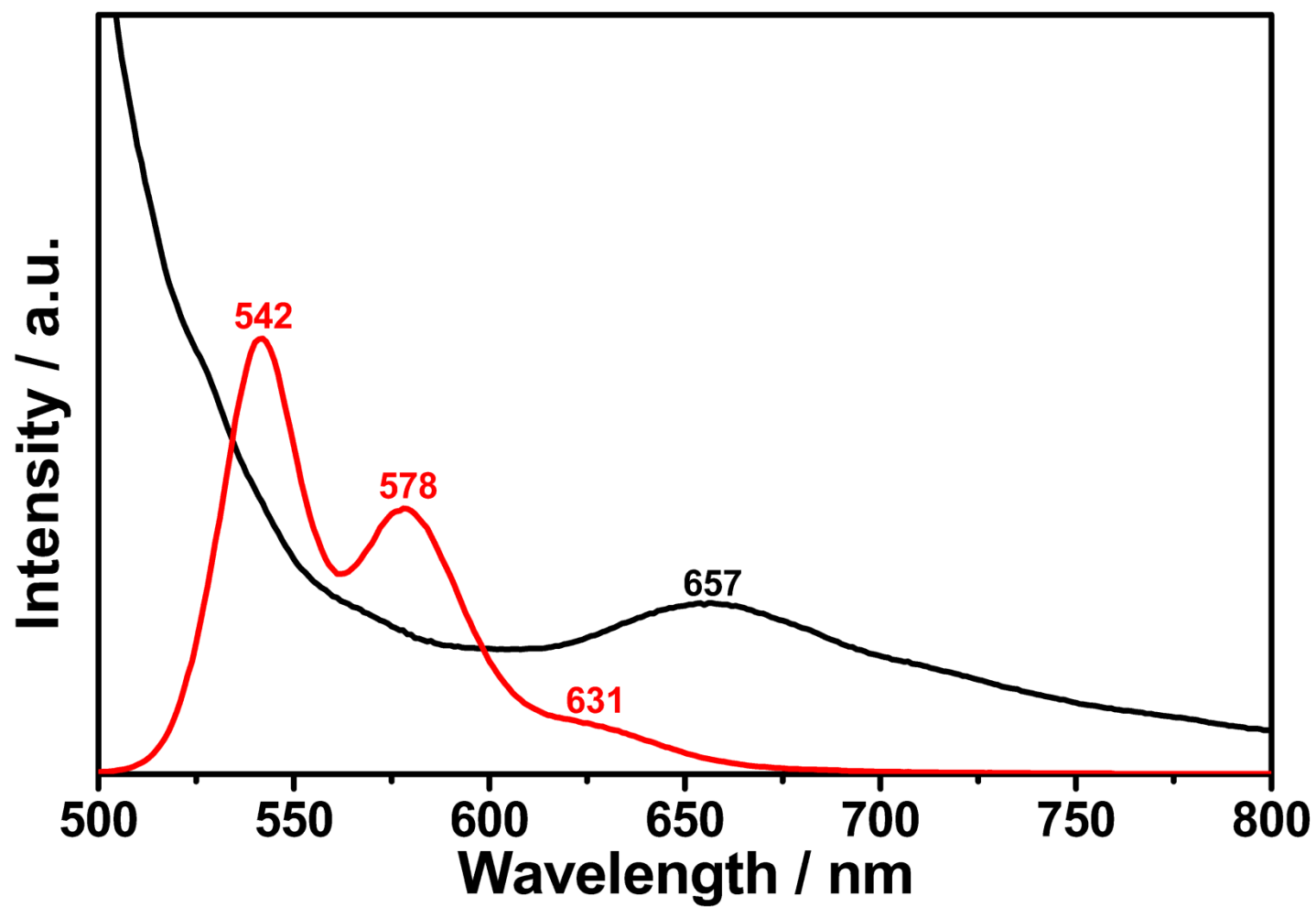
Figure 4.50: Solid−state emission spectrum of TAPDI is shown by black color, emission spectrum in NMP is shown by red color
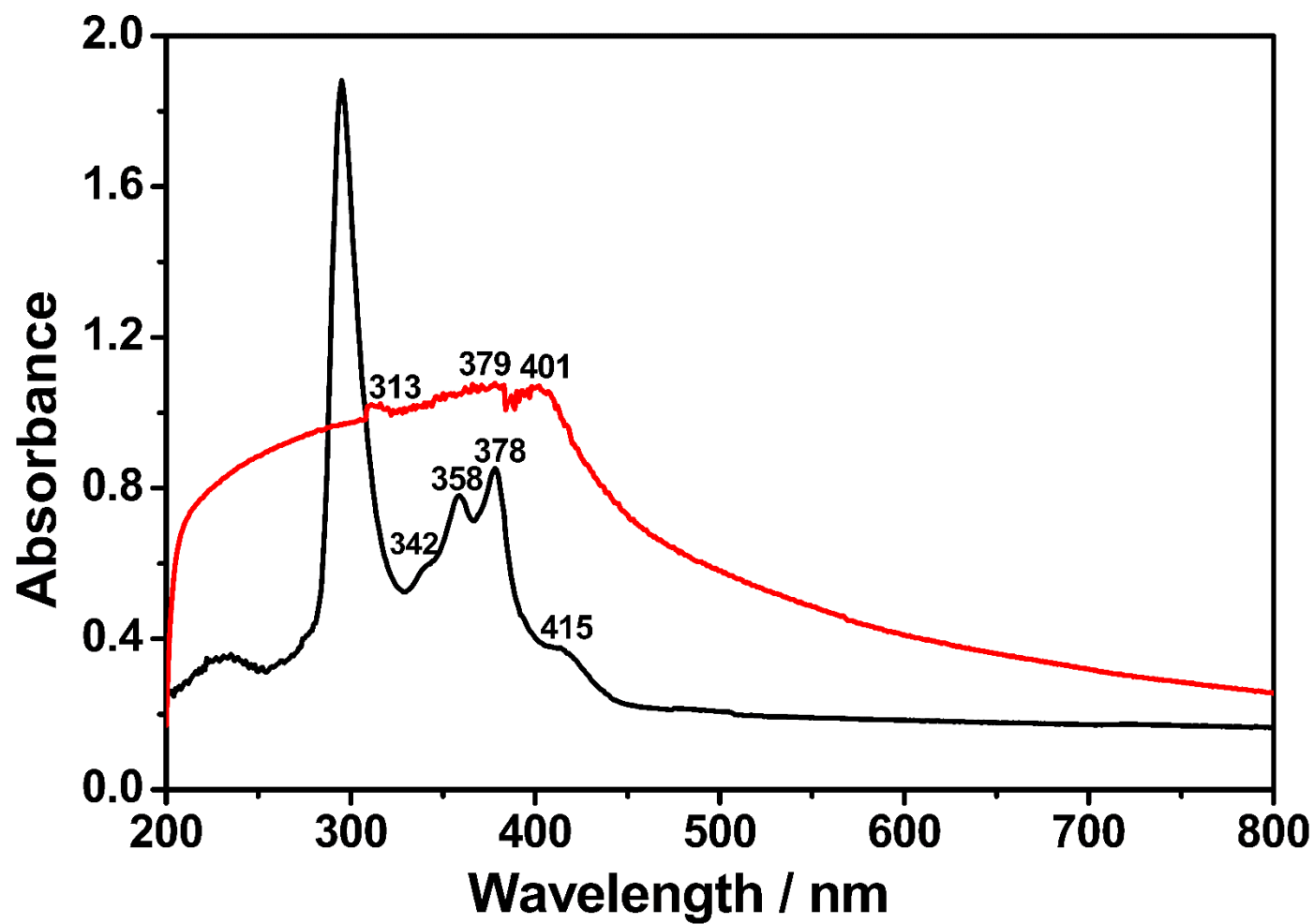
Figure 4.51: Solid−state absorption spectrum of TANDI is shown by black color, absorption spectrum in NMP is shown by red color
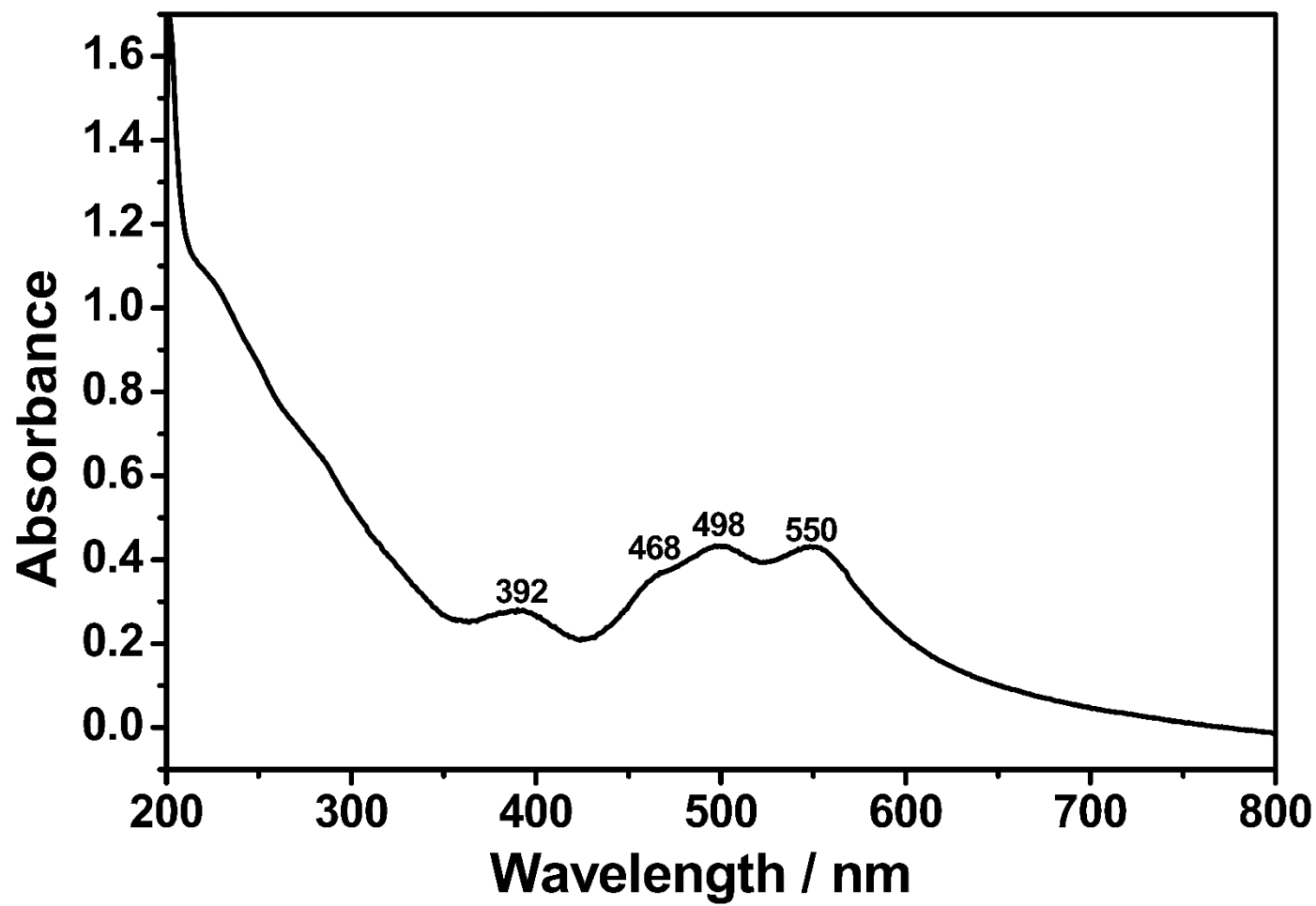
Figure 4.52: Solid−state absorption spectrum of TM−PDA
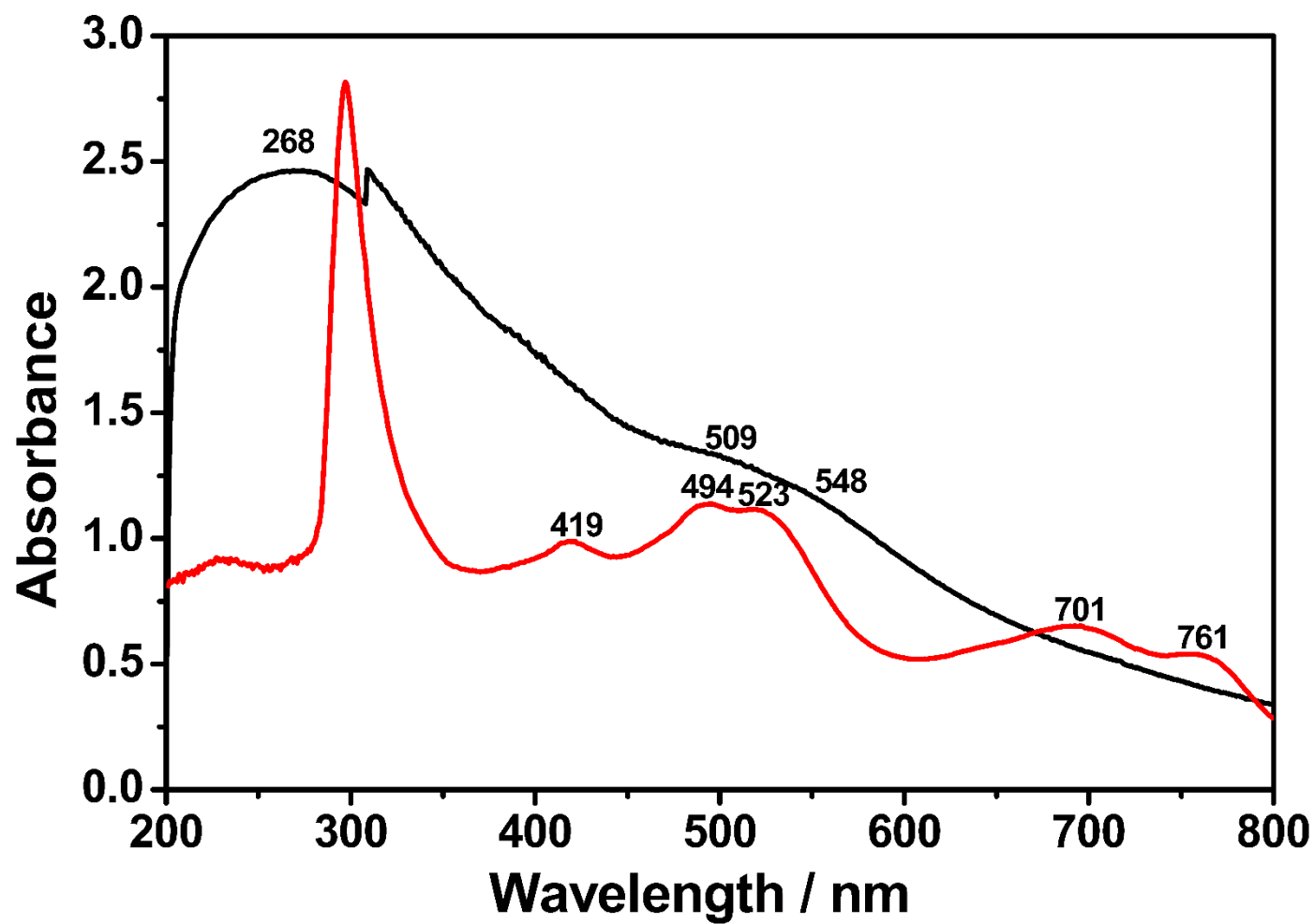
Figure 4.53: Solid−state absorption spectrum of HP−PDA is shown by black color, absorption spectrum in NMP is shown by red color
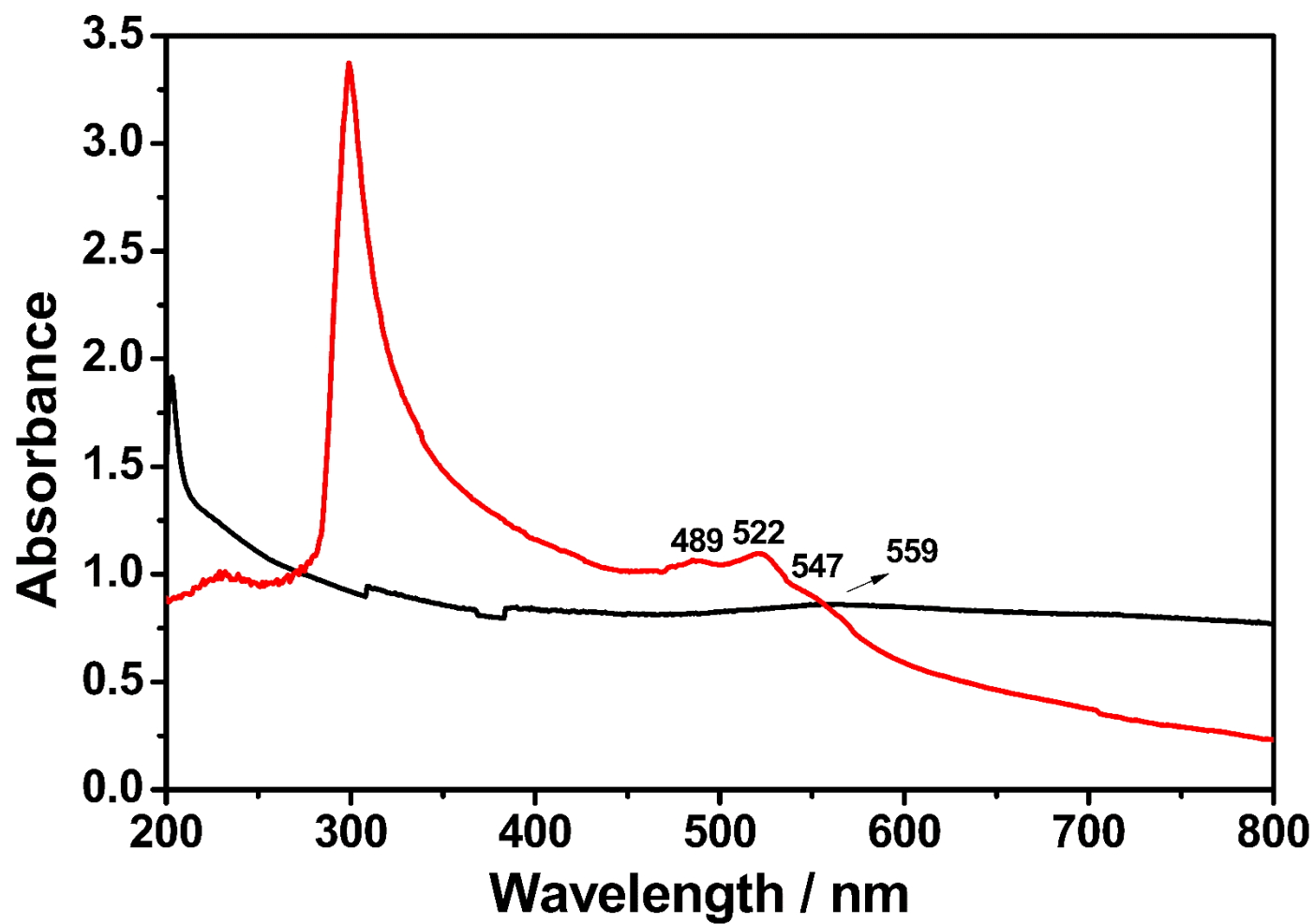
Figure 4.54: Solid−state absorption spectrum of HP−HEPDI is shown by black color, absorption spectrum in NMP is shown by red color
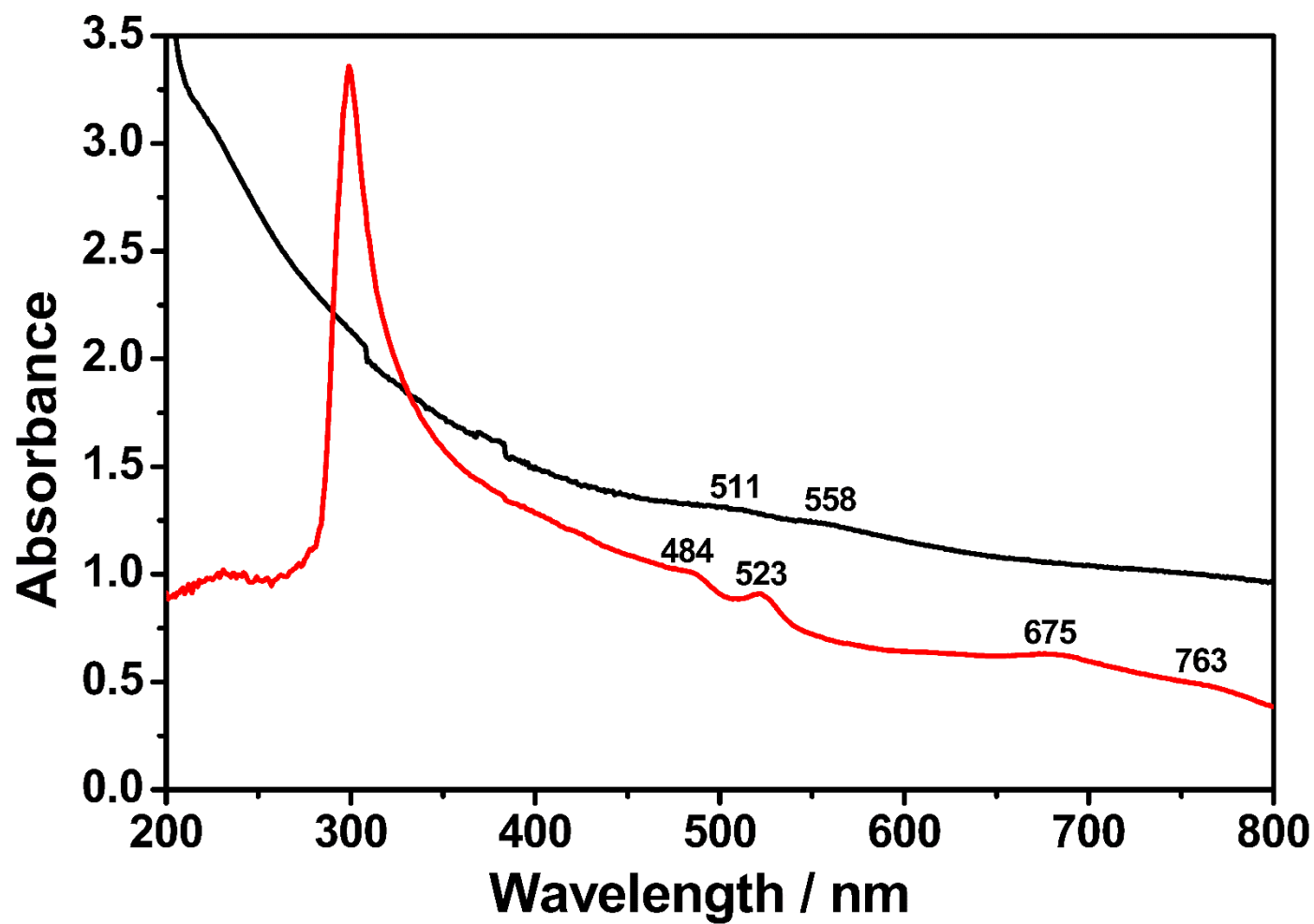
Figure 4.55: Solid−state absorption spectrum of TM−HEPDI is shown by black color, absorption spectrum in NMP is shown by red color
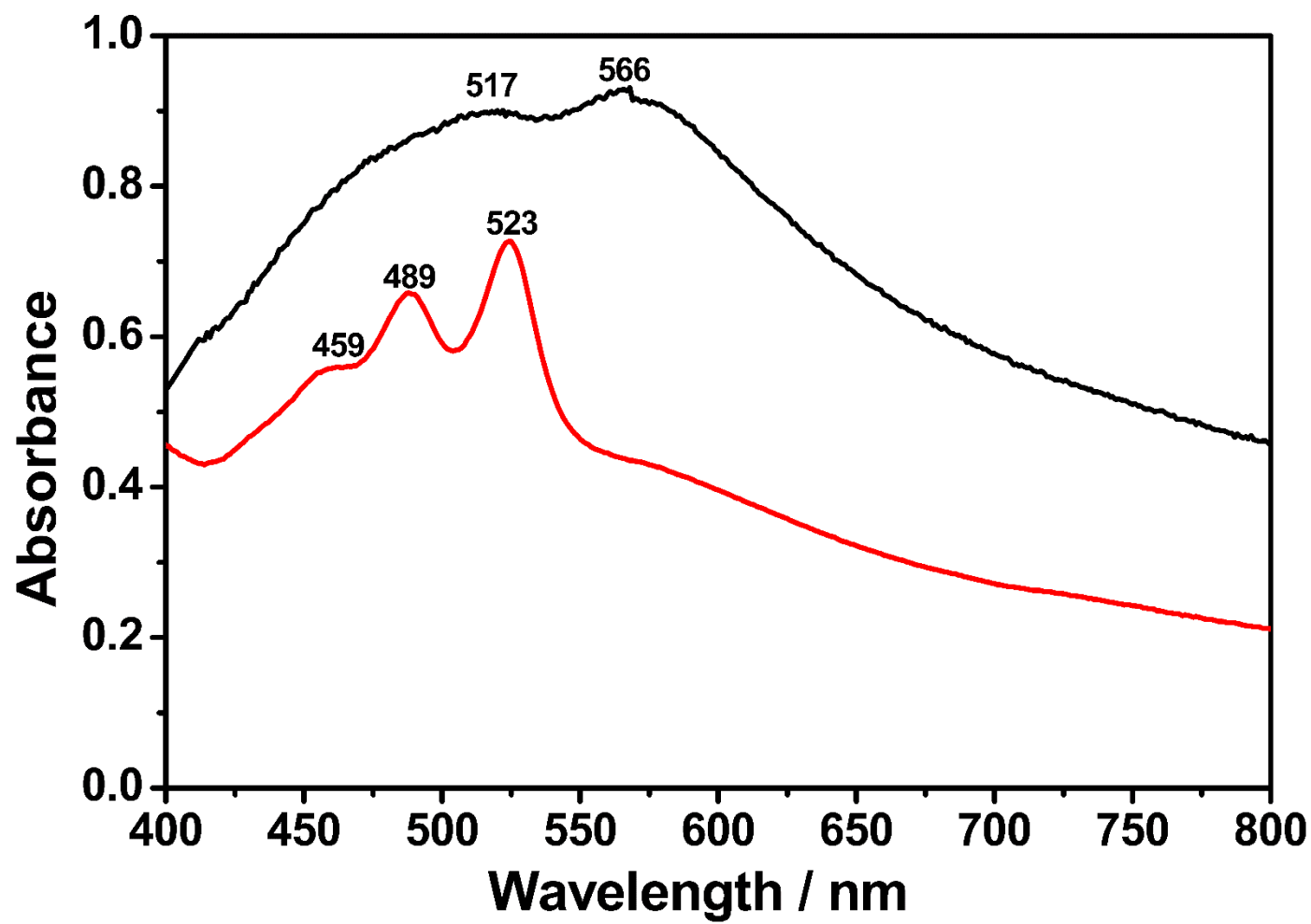
Figure 4.56: Solid−state absorption spectrum of HEPDI is shown by black color, absorption spectrum in NMP is shown by red color
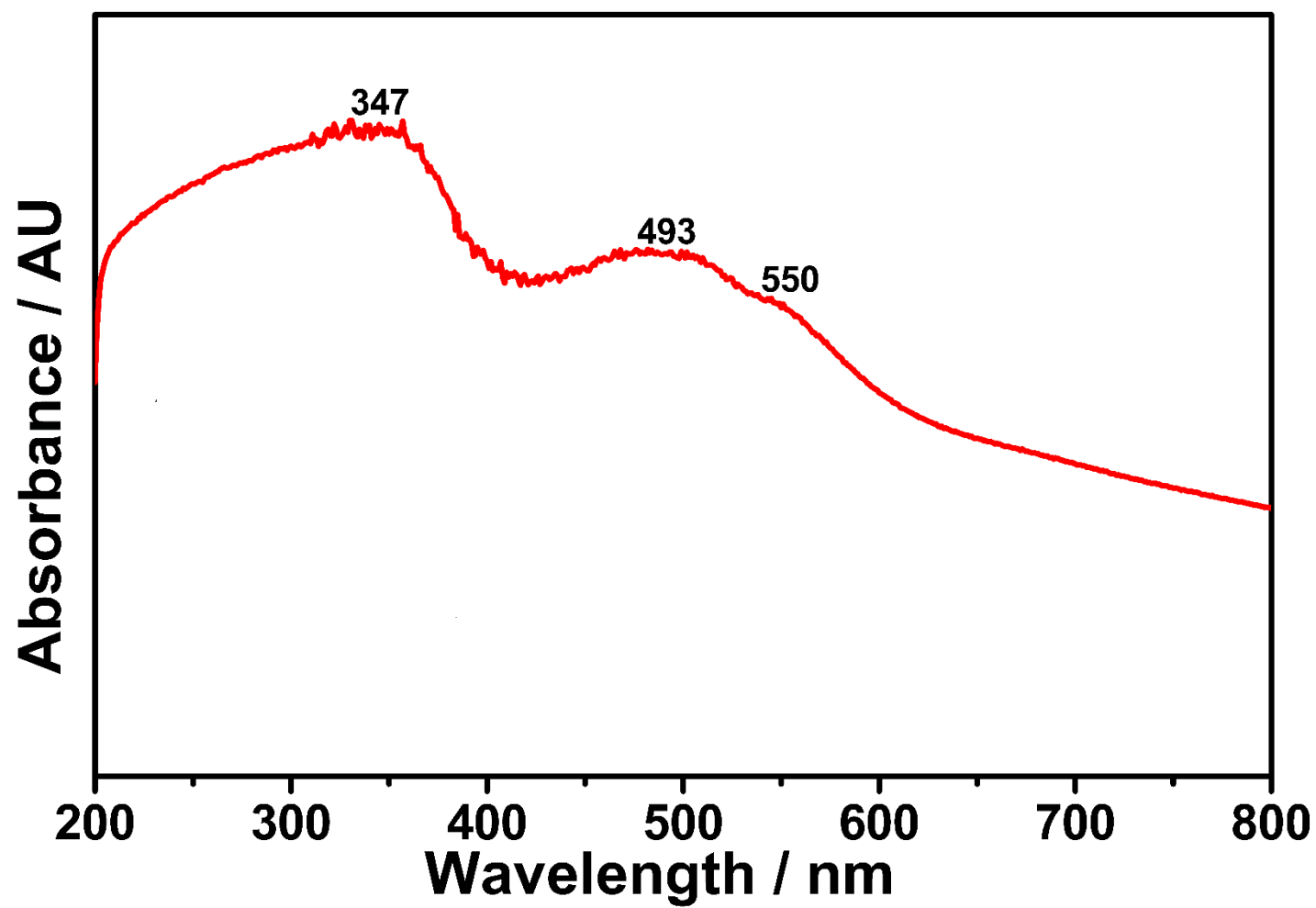
Figure 4.57: Solid−state absorption spectrum of TAPDI binded to TiO_2
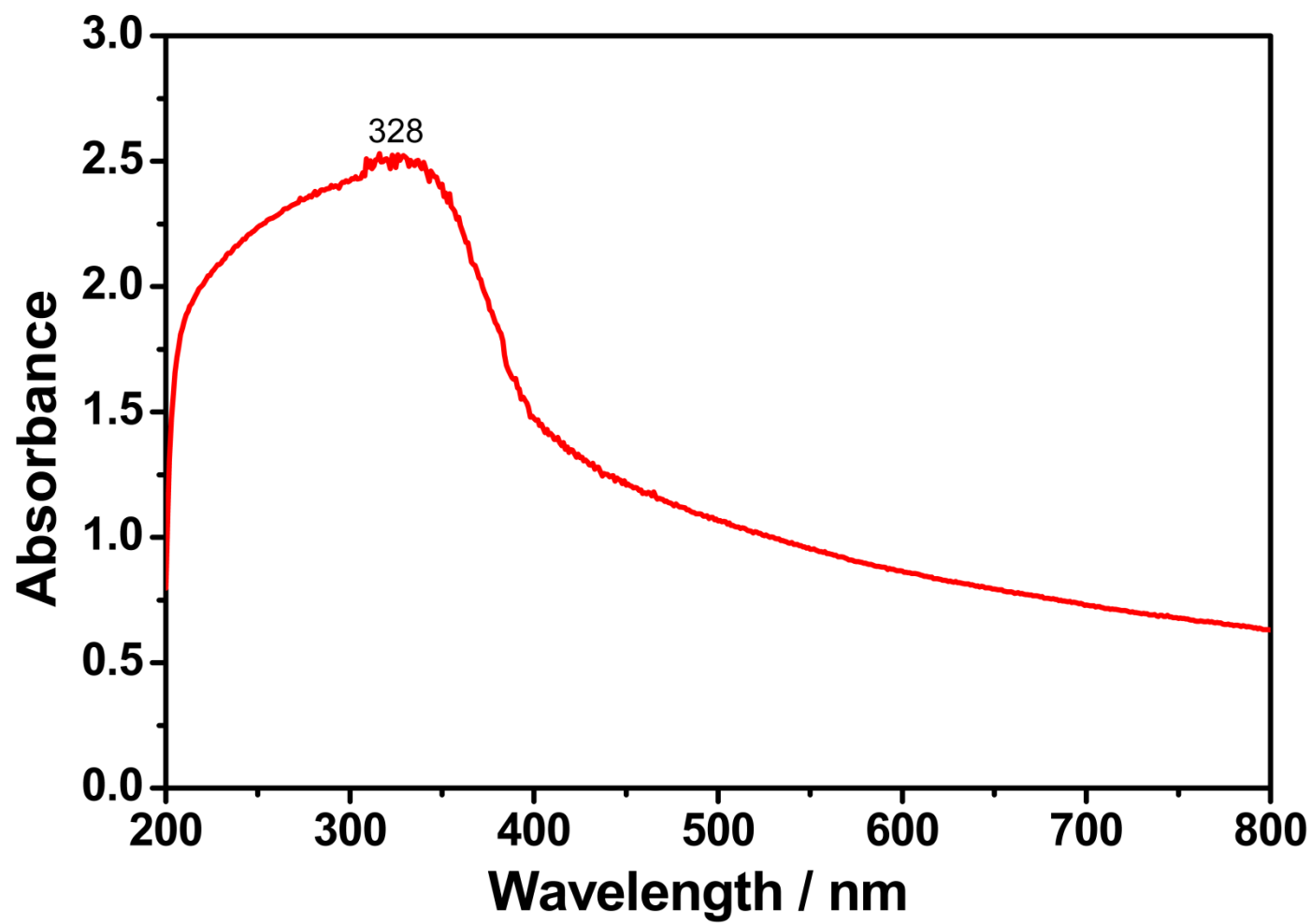
Figure 4.58: Solid−state absorption spectrum of TANDI binded to TiO$_2$
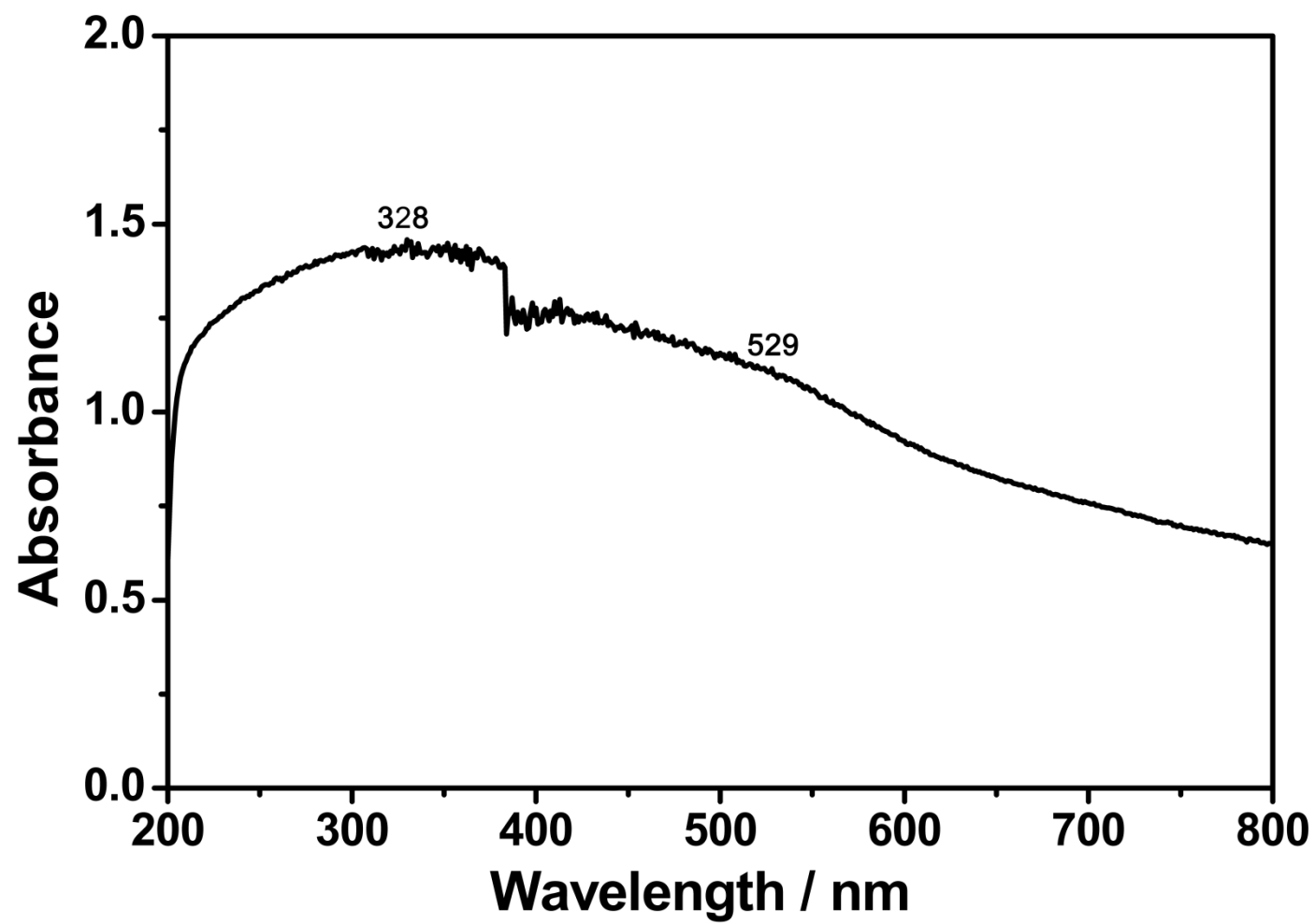
Figure 4.59: Solid−state absorption spectrum of HP−PDA binded to TiO_2
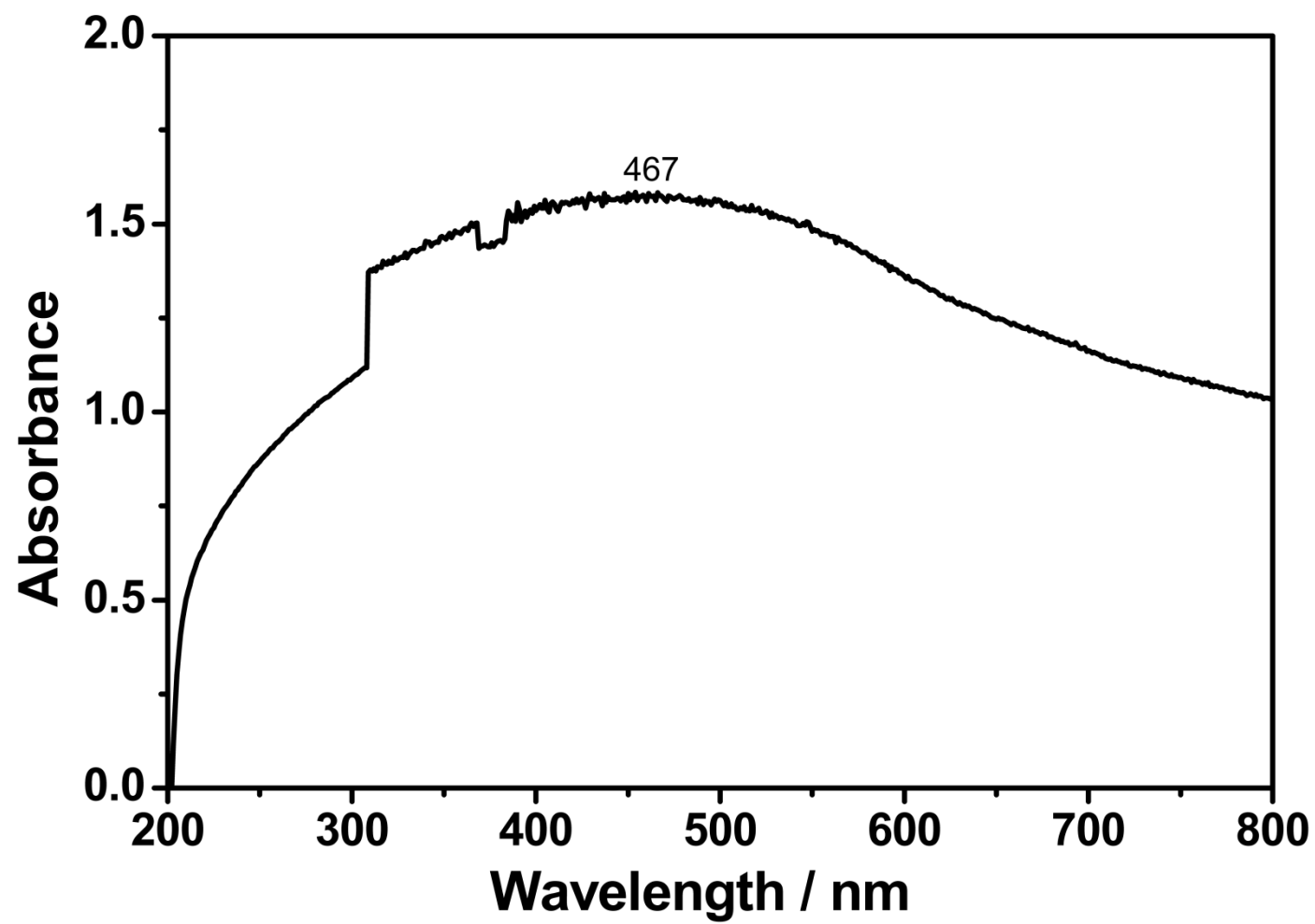
Figure 4.60: Solid−state absorption spectrum of HP−HEPDI binded to TiO$_2$
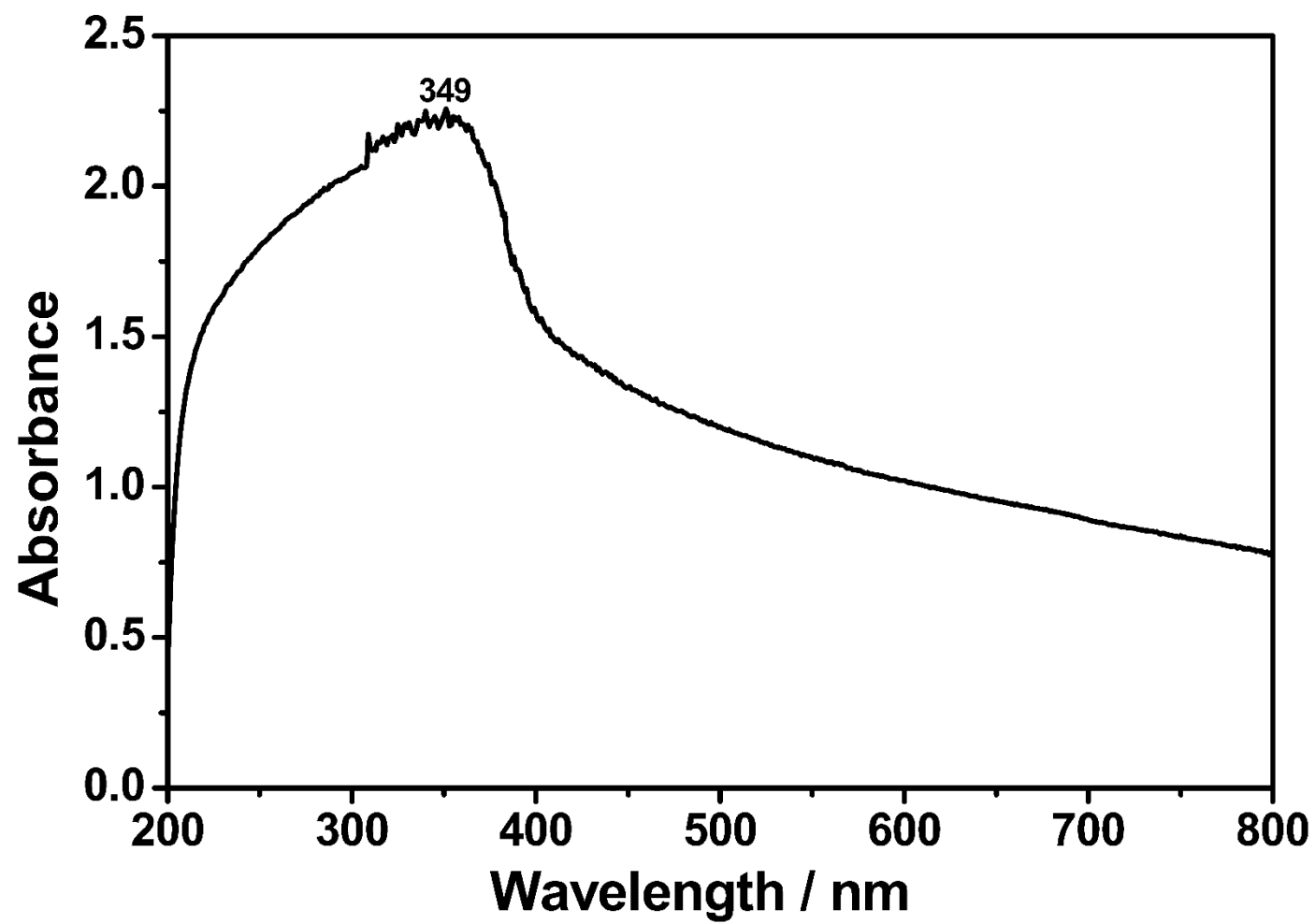
Figure 4.61: Solid−state absorption spectrum of HP−TCPDI binded to TiO_2
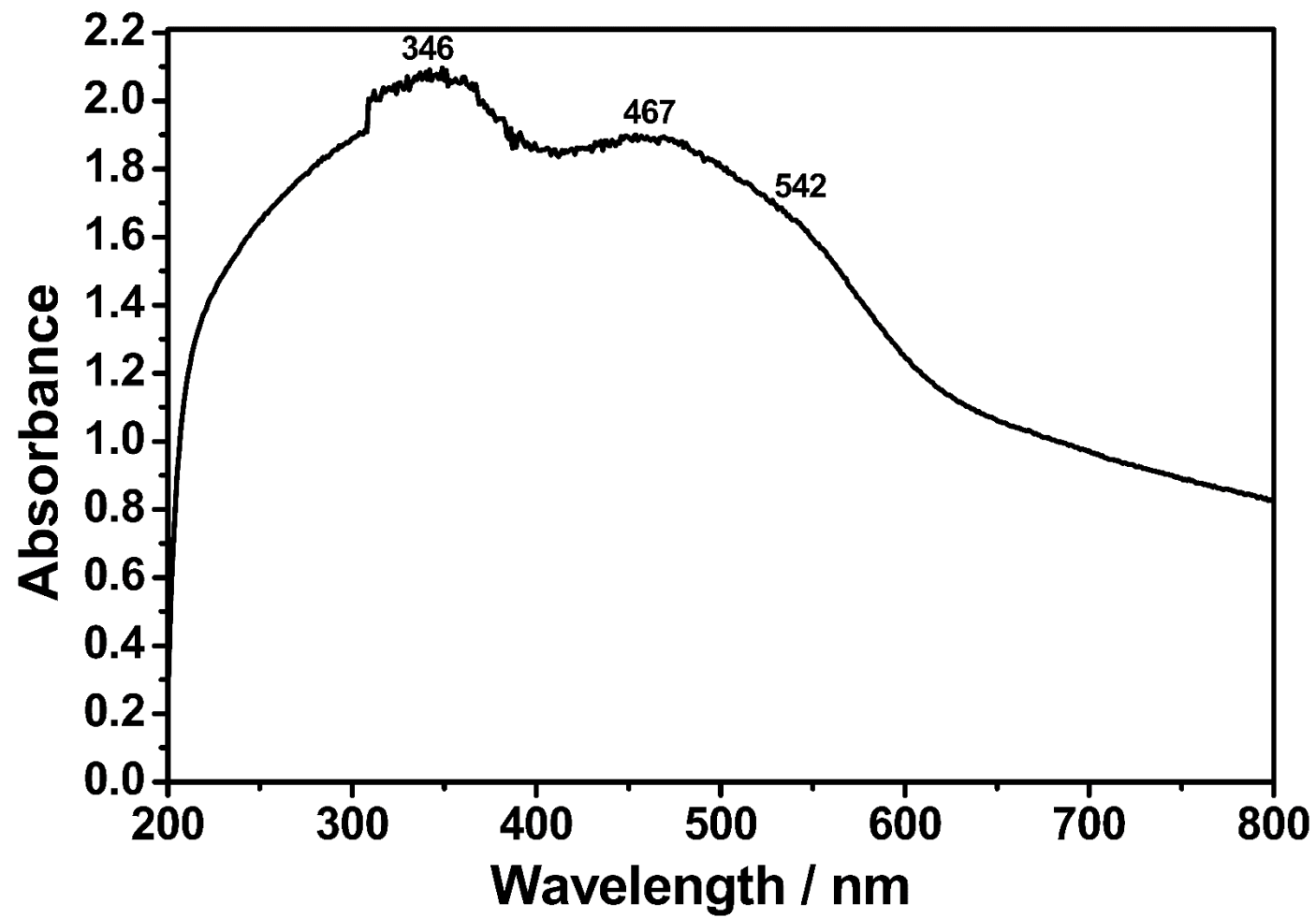
Figure 4.62: Solid−state absorption spectrum of TM−PDA binded to TiO$_2$
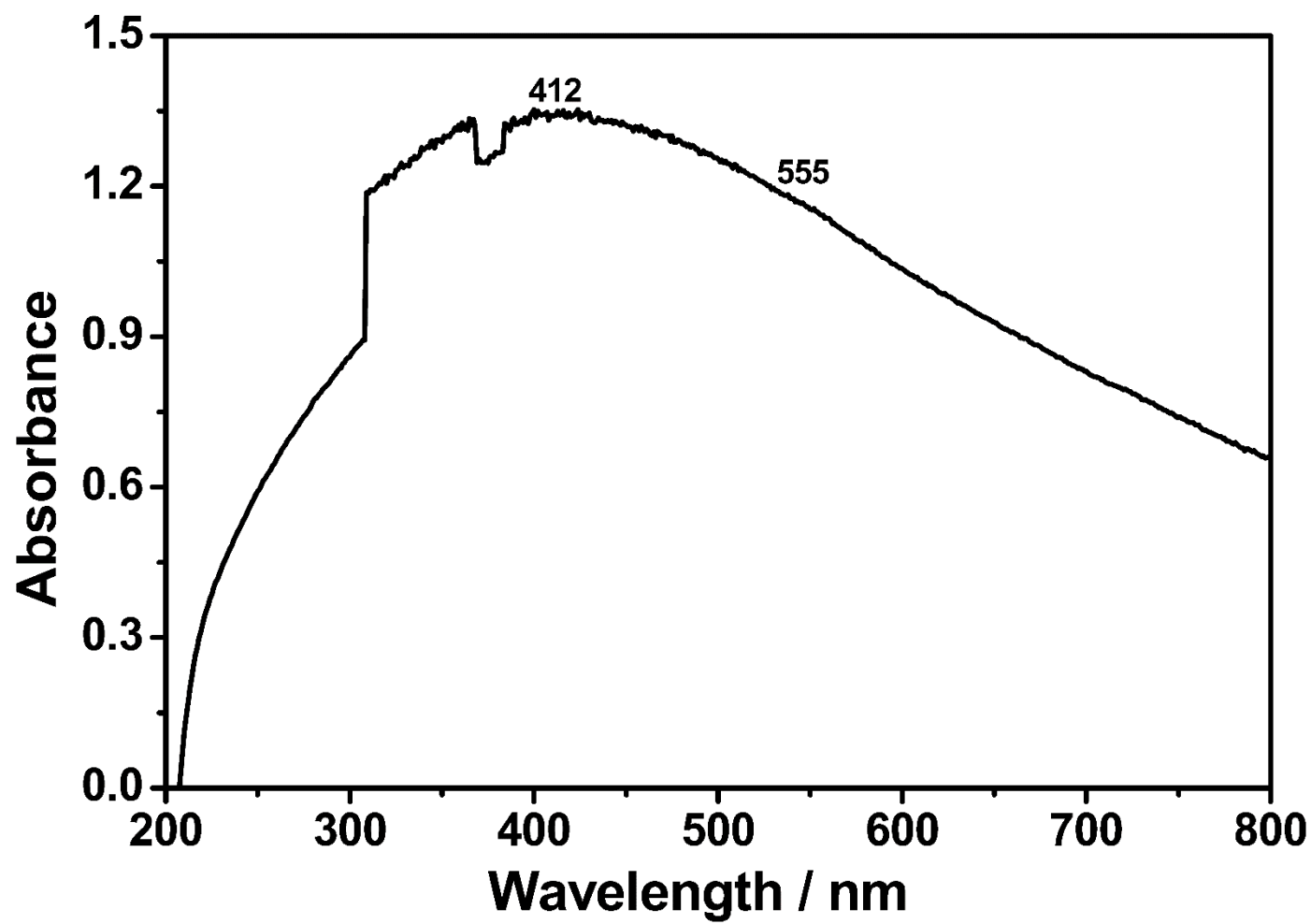
Figure 4.63: Solid−state absorption spectrum of TM−HEPDI binded to TiO_2
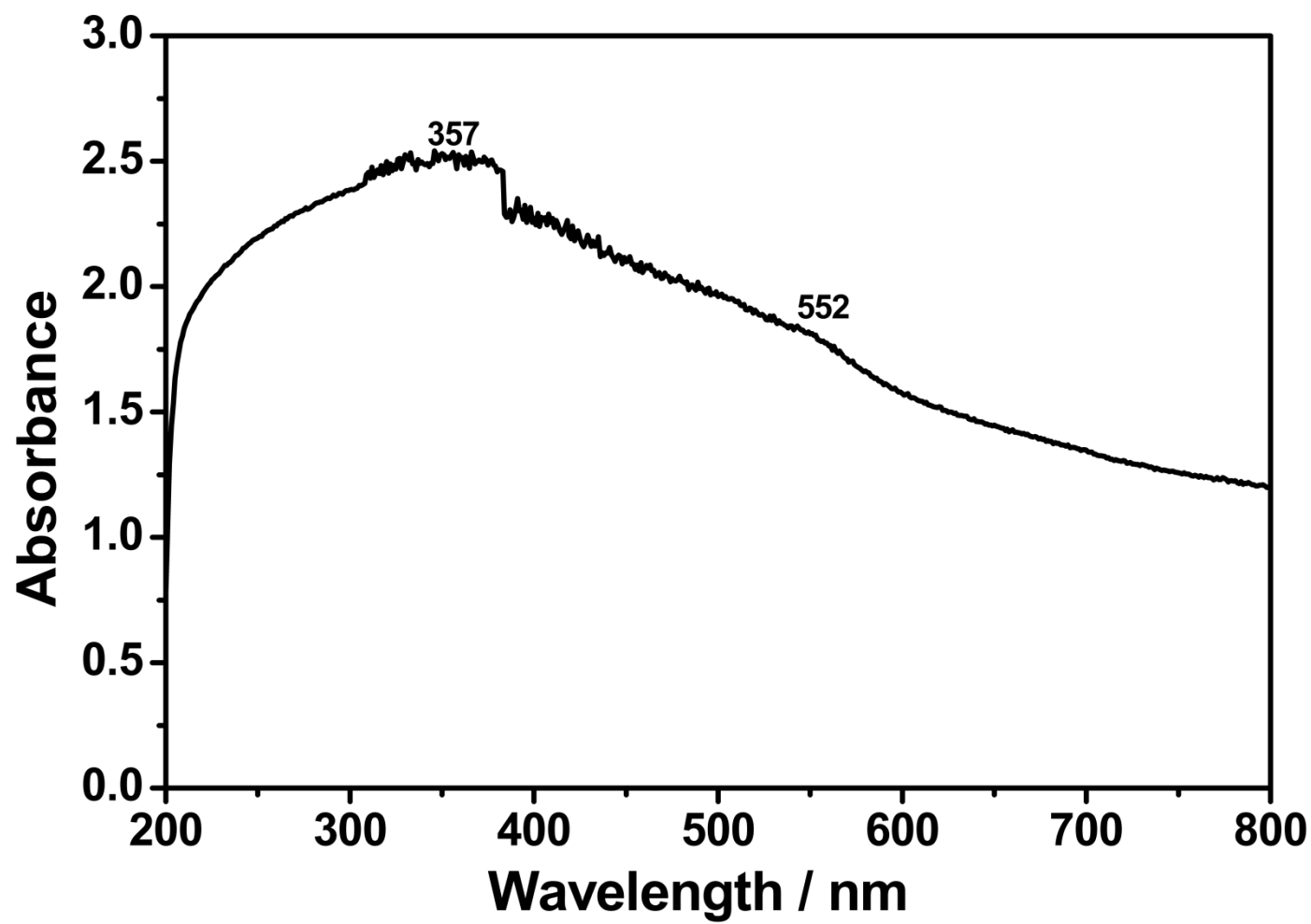
Figure 4.64: Solid−state absorption spectrum of HEPDI binded to TiO_2
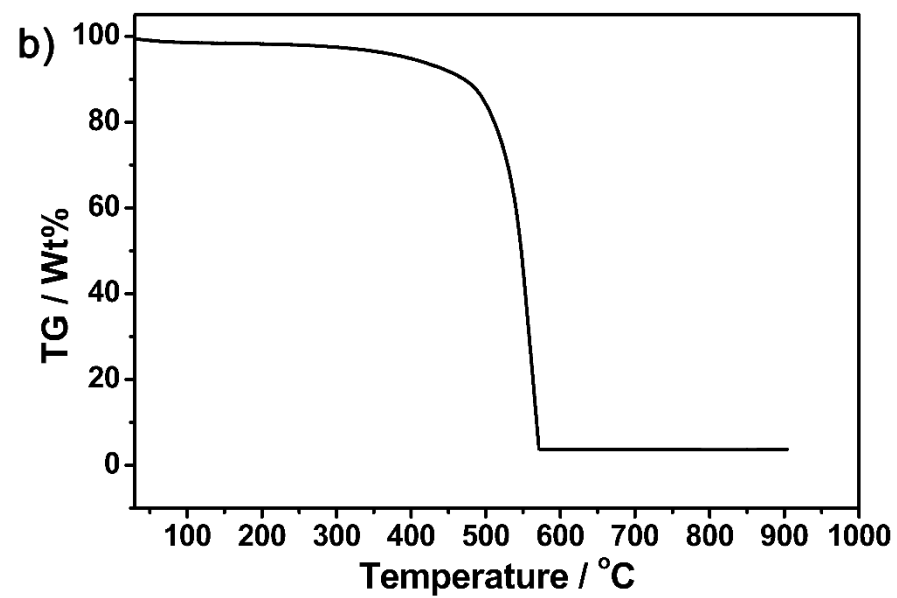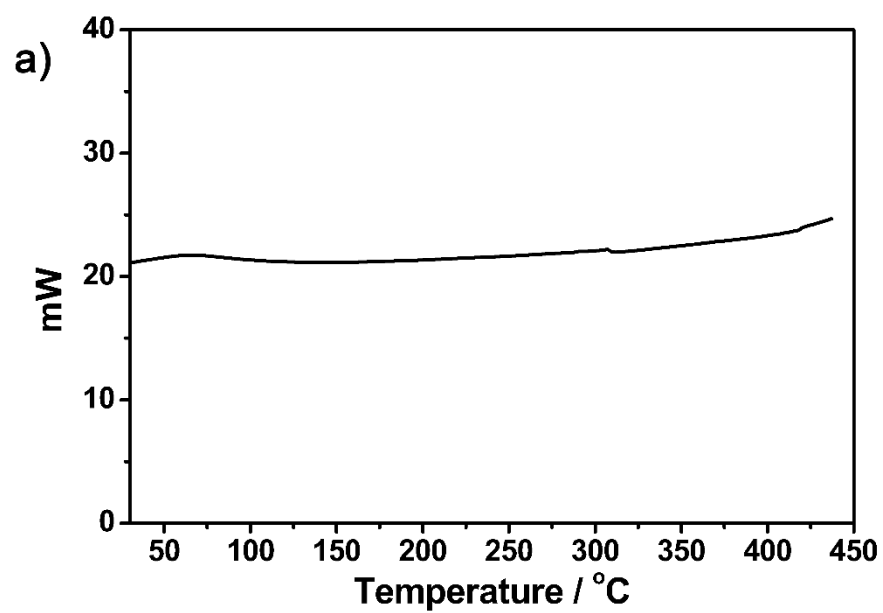
Figure 4.65: DSC thermogram (a.) and TGA curve (b.) of TAPPI at a heating rate of 10 °C min^{-1}
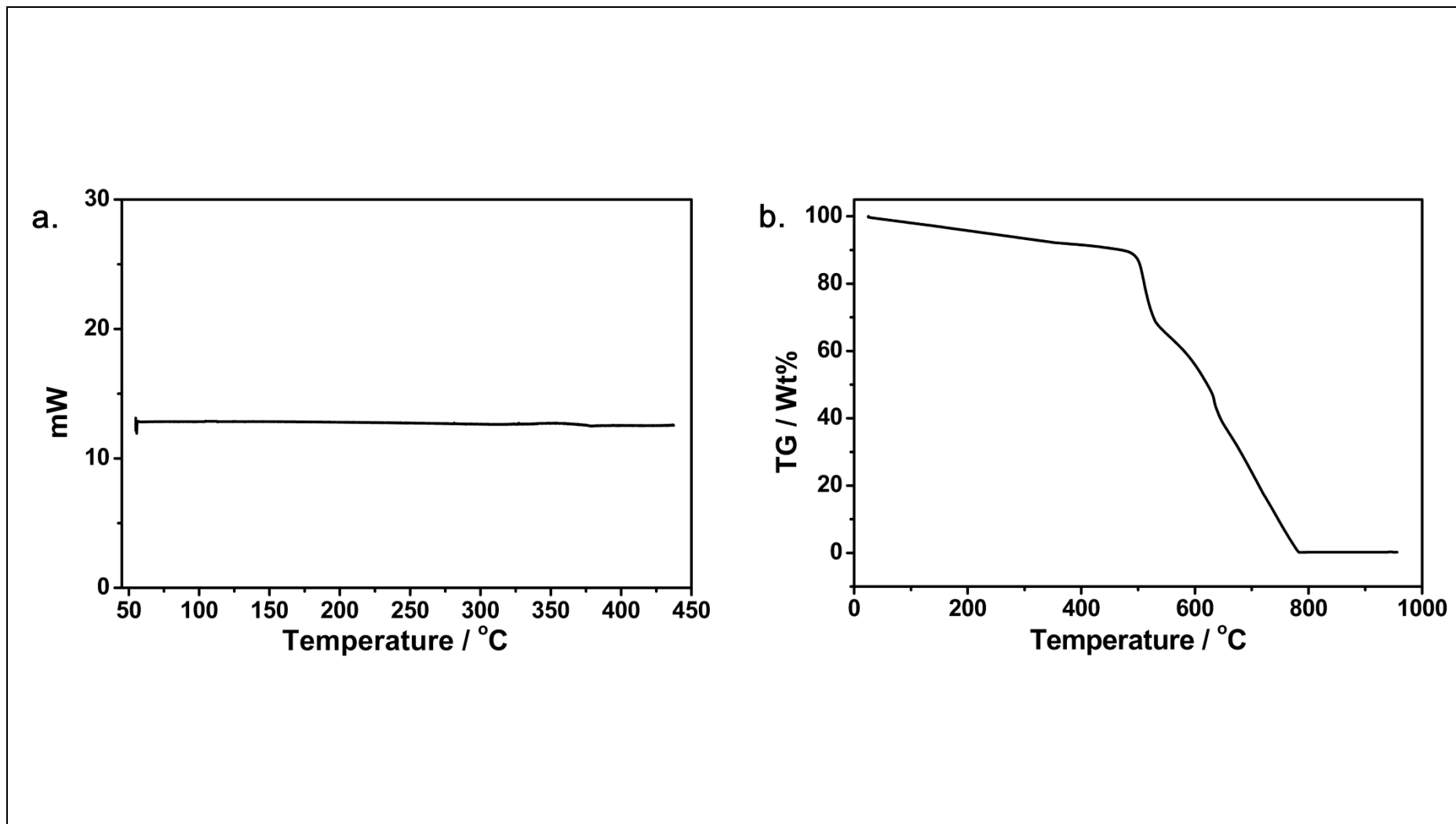
Figure 4.66: DSC thermogram (a.) and TGA curve (b.) of TAPDI at a heating rate of 10 °C min^{-1}
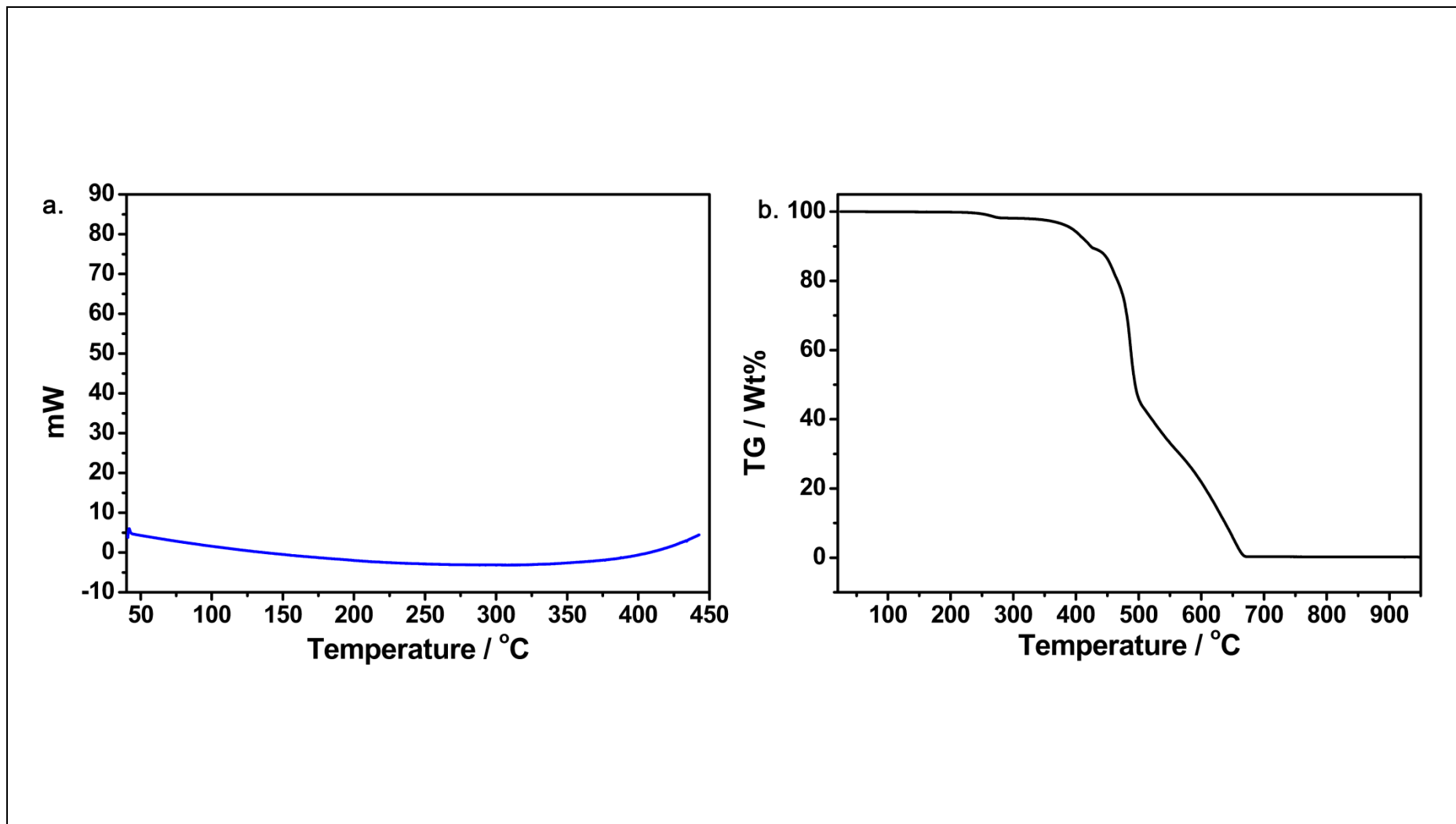
Figure 4.67: DSC thermogram (a.) and TGA curve (b.) of TANDI at a heating rate of 10 °C min^{-1}
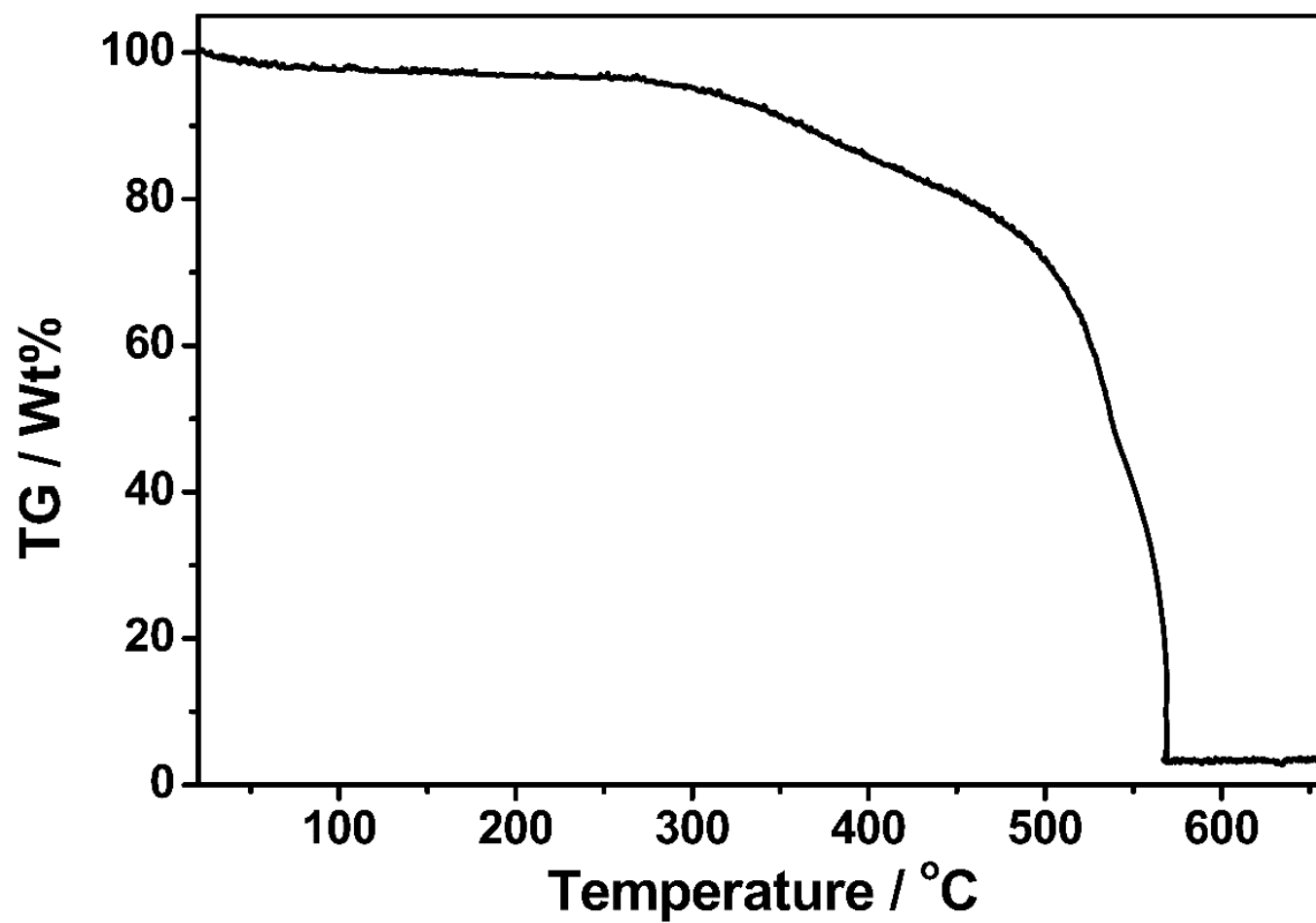
Figure 4.68: TGA curve of HEPDI at a heating rate of 10 °C min^{-1}
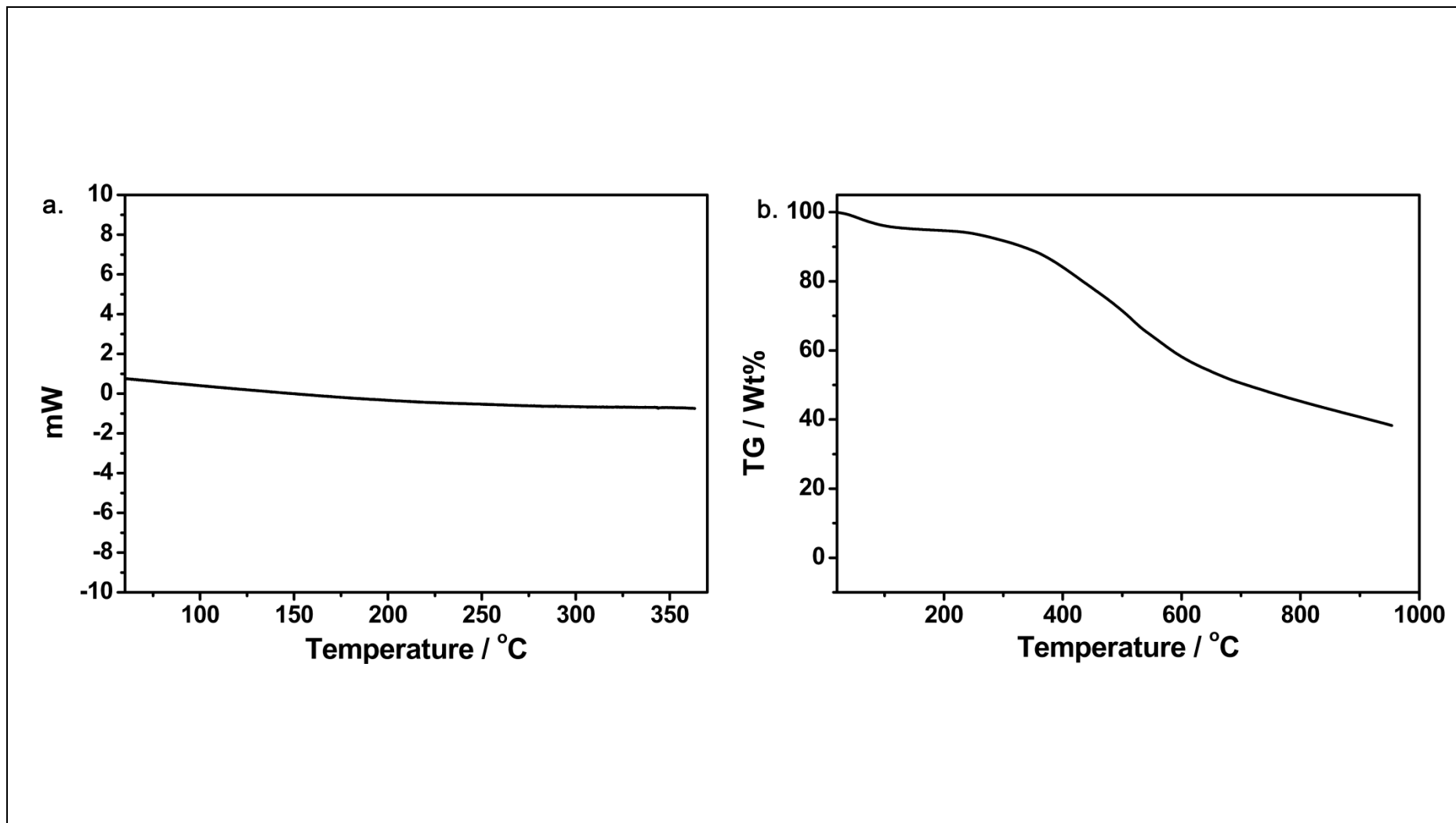
Figure 4.69: DSC thermogram (a.) and TGA curve (b.) of HP−PDA at a heating rate of 10 °C min^{-1}
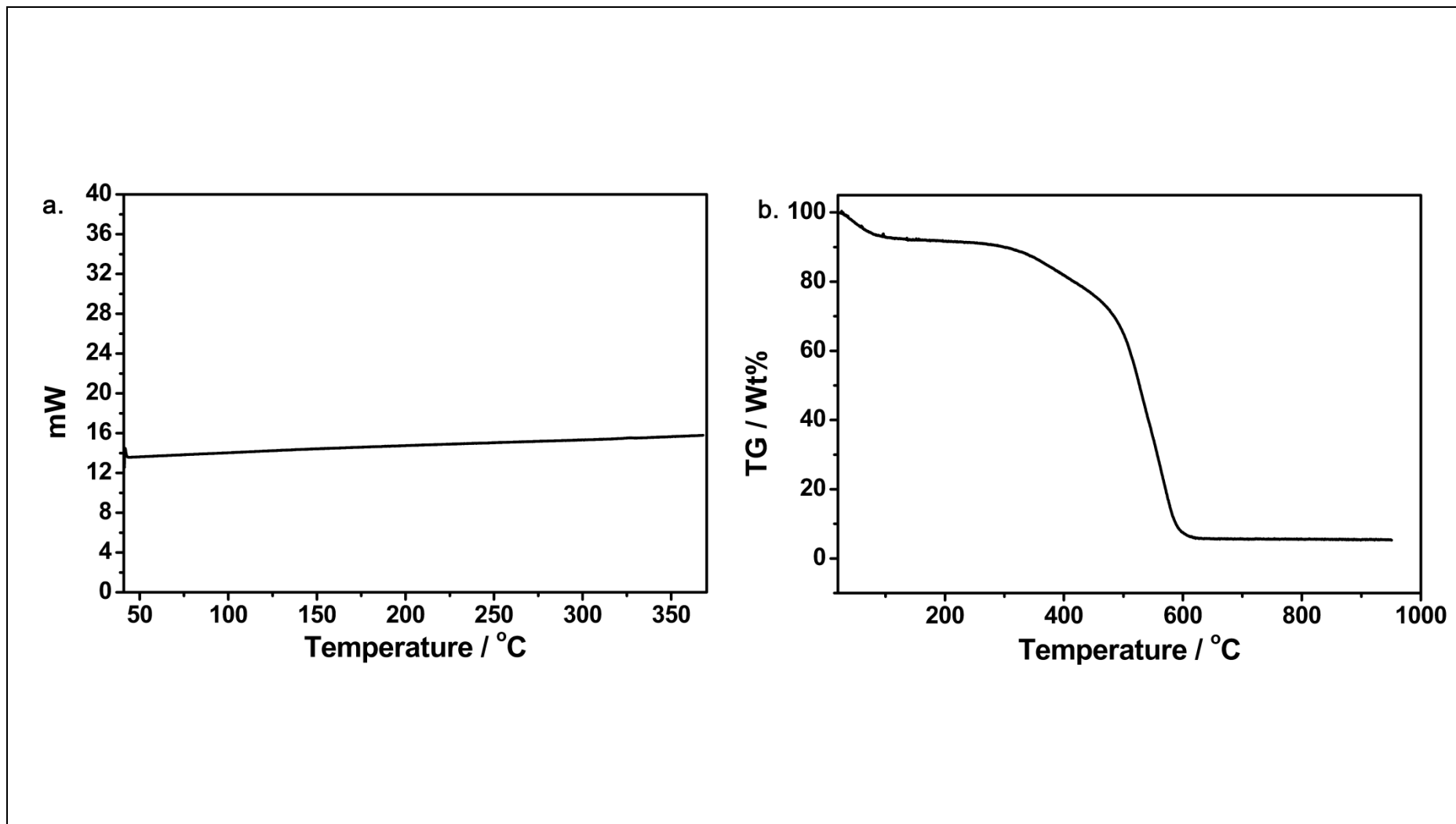
Figure 4.70: DSC thermogram (a.) and TGA curve (b.) of HP−HEPDI at a heating rate of 10 °C min^{-1}
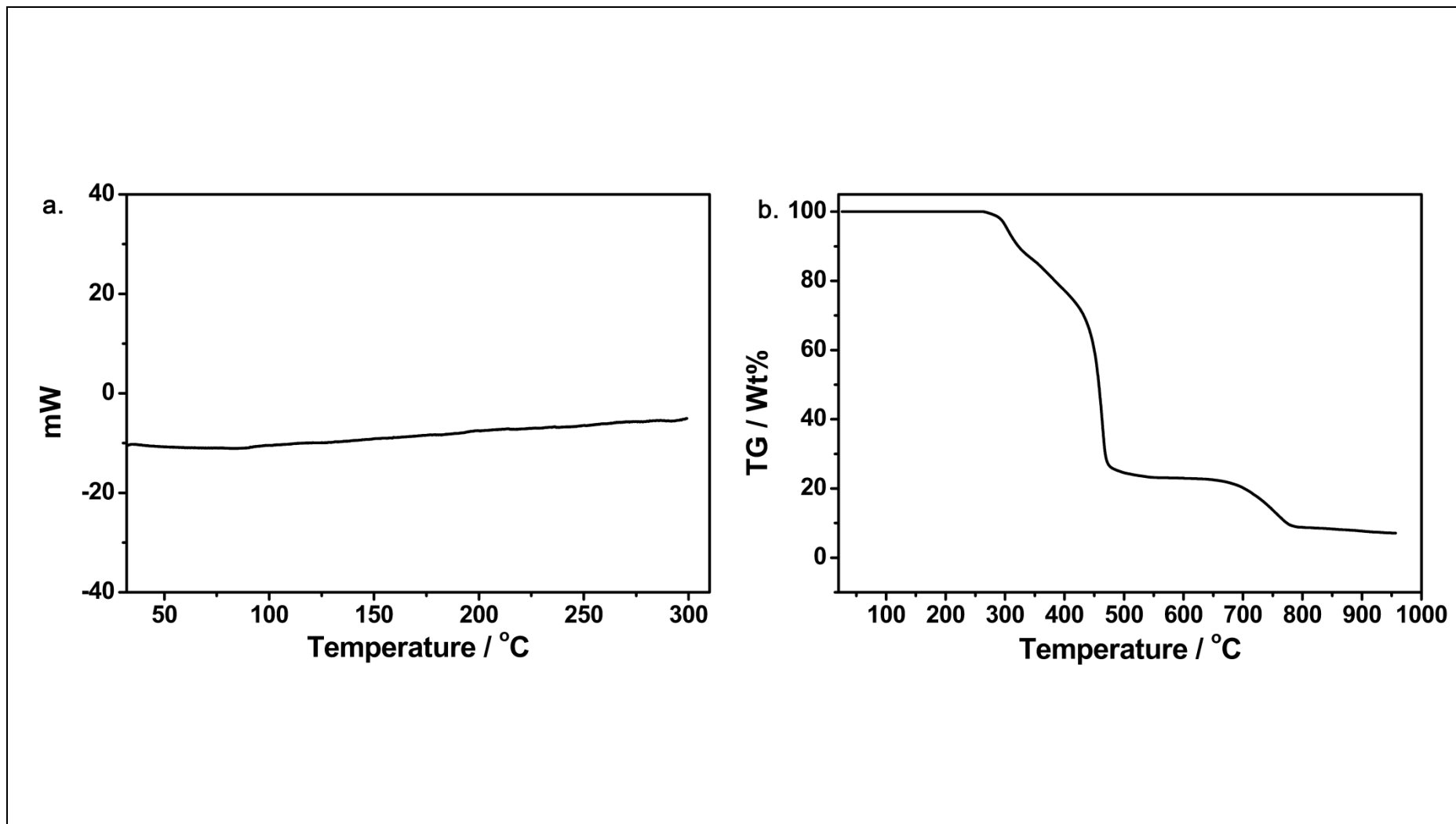
Figure 4.71: DSC thermogram (a.) and TGA curve (b.) of TM−PDA at a heating rate of 10 °C min^{-1}
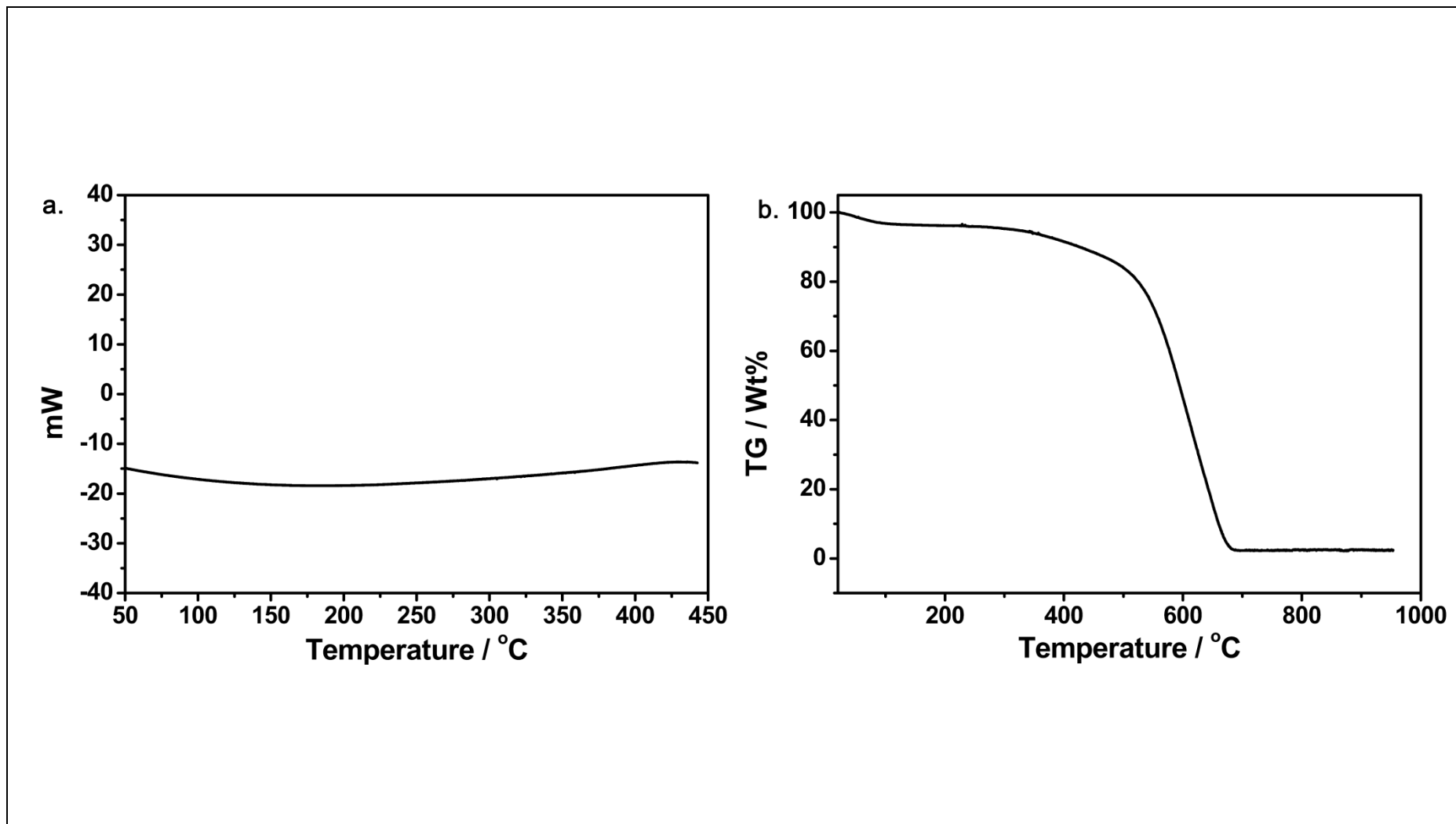
Figure 4.72: DSC thermogram (a.) and TGA curve (b.) of TM−HEPDI at a heating rate of 10 °C min^{-1}
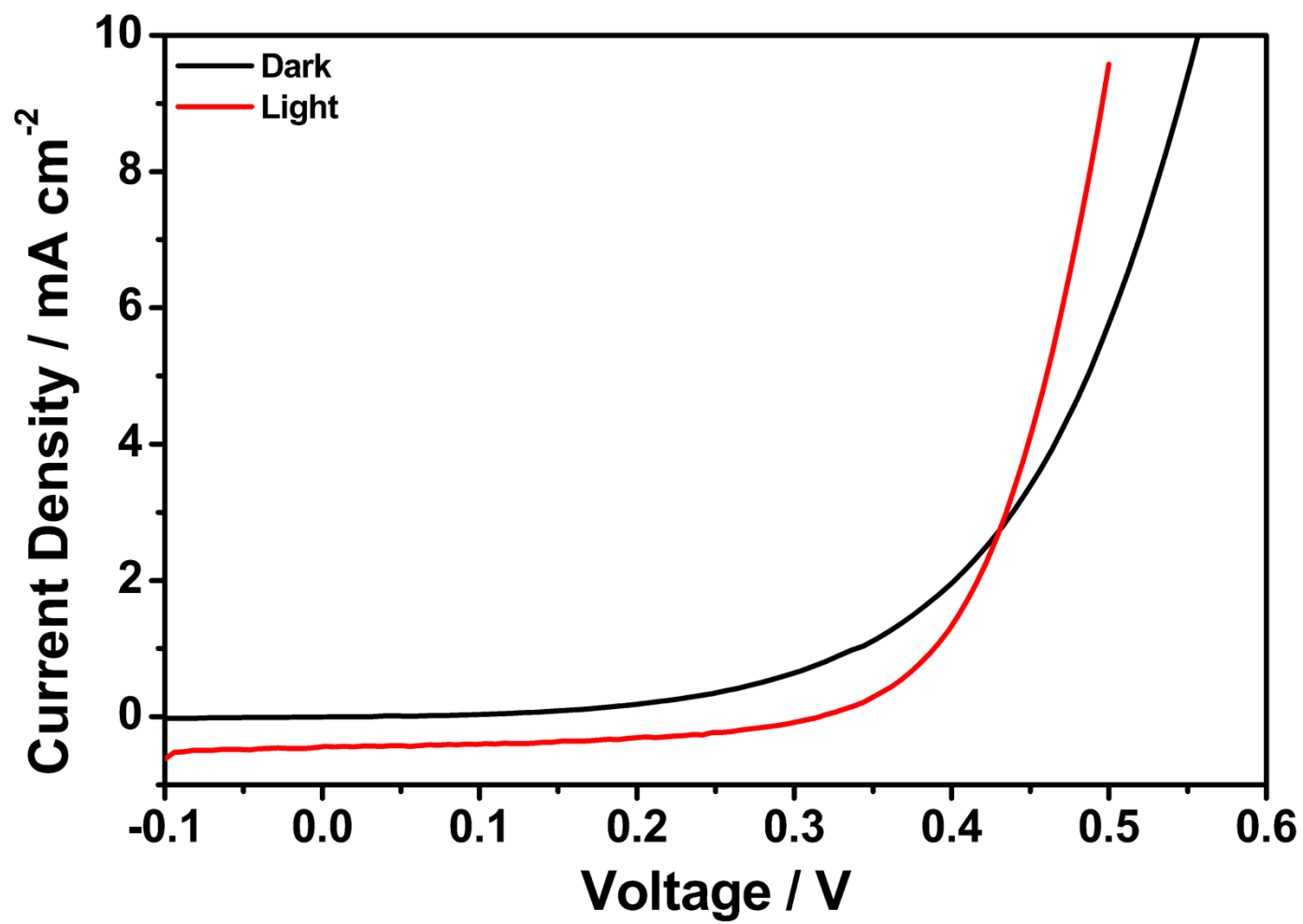
Figure 4.73: I−V curve of TAPDI
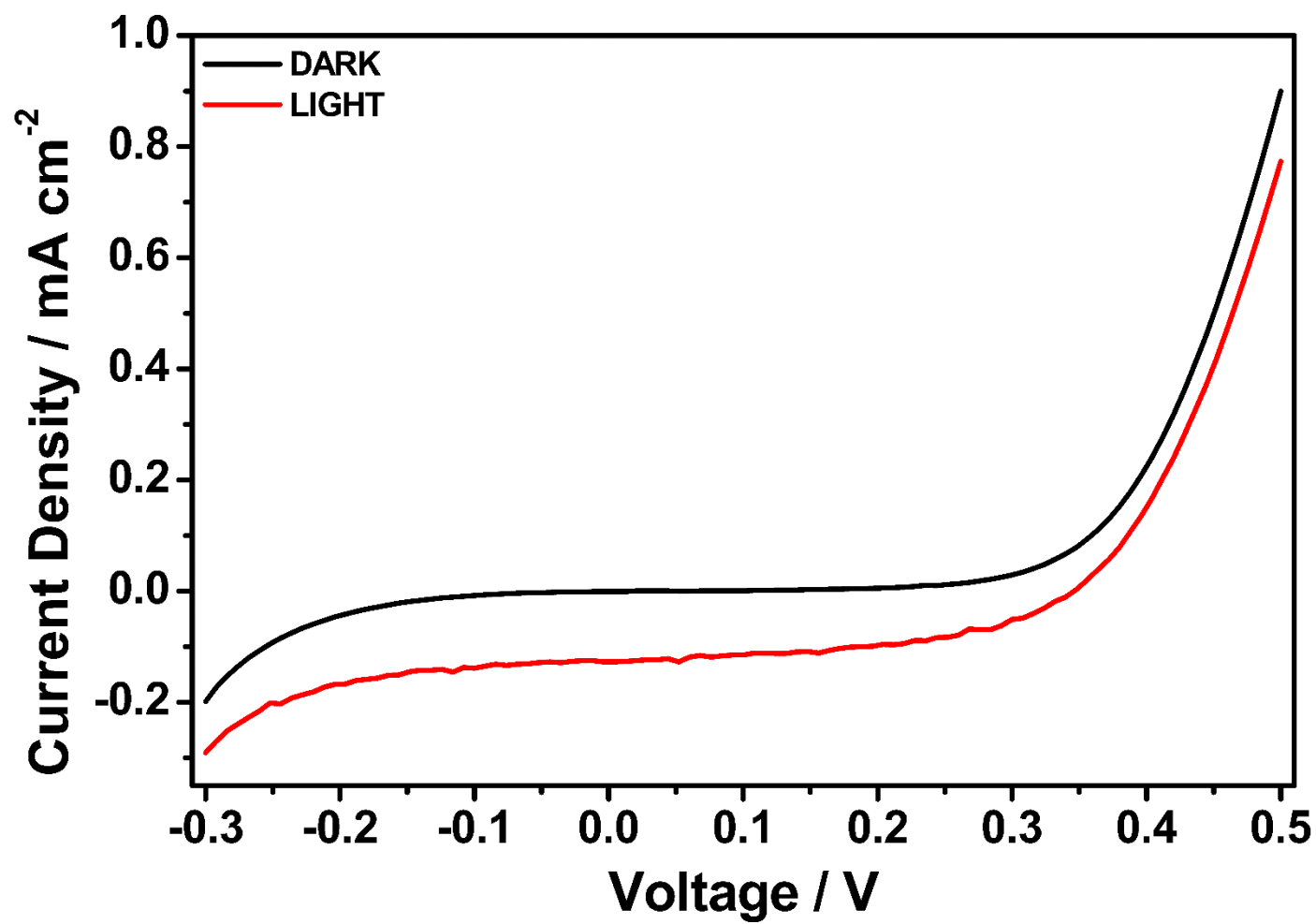
Figure 4.74: I−V curve of TANDI
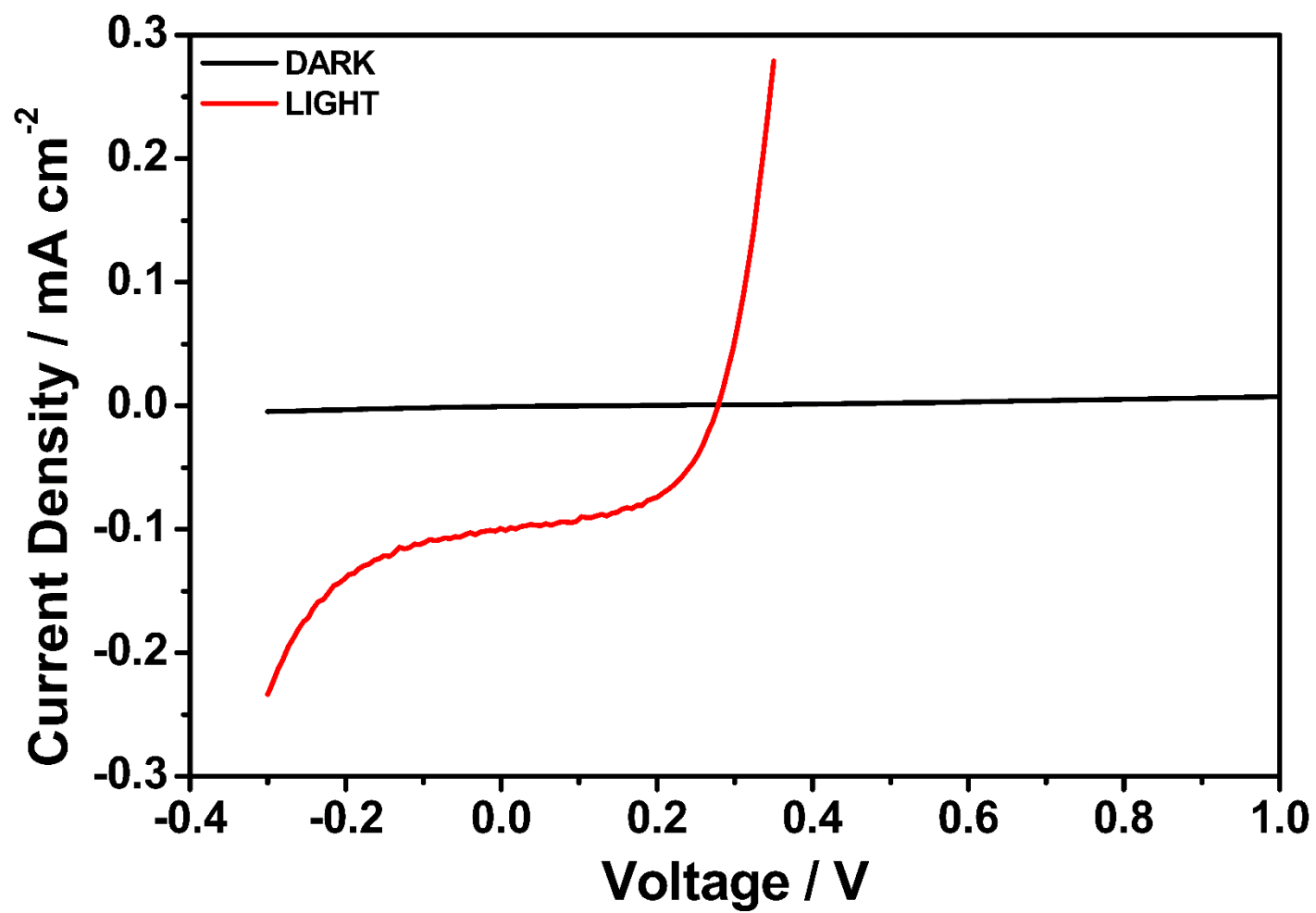
Figure 4.75: I–V curve of TM–PDA
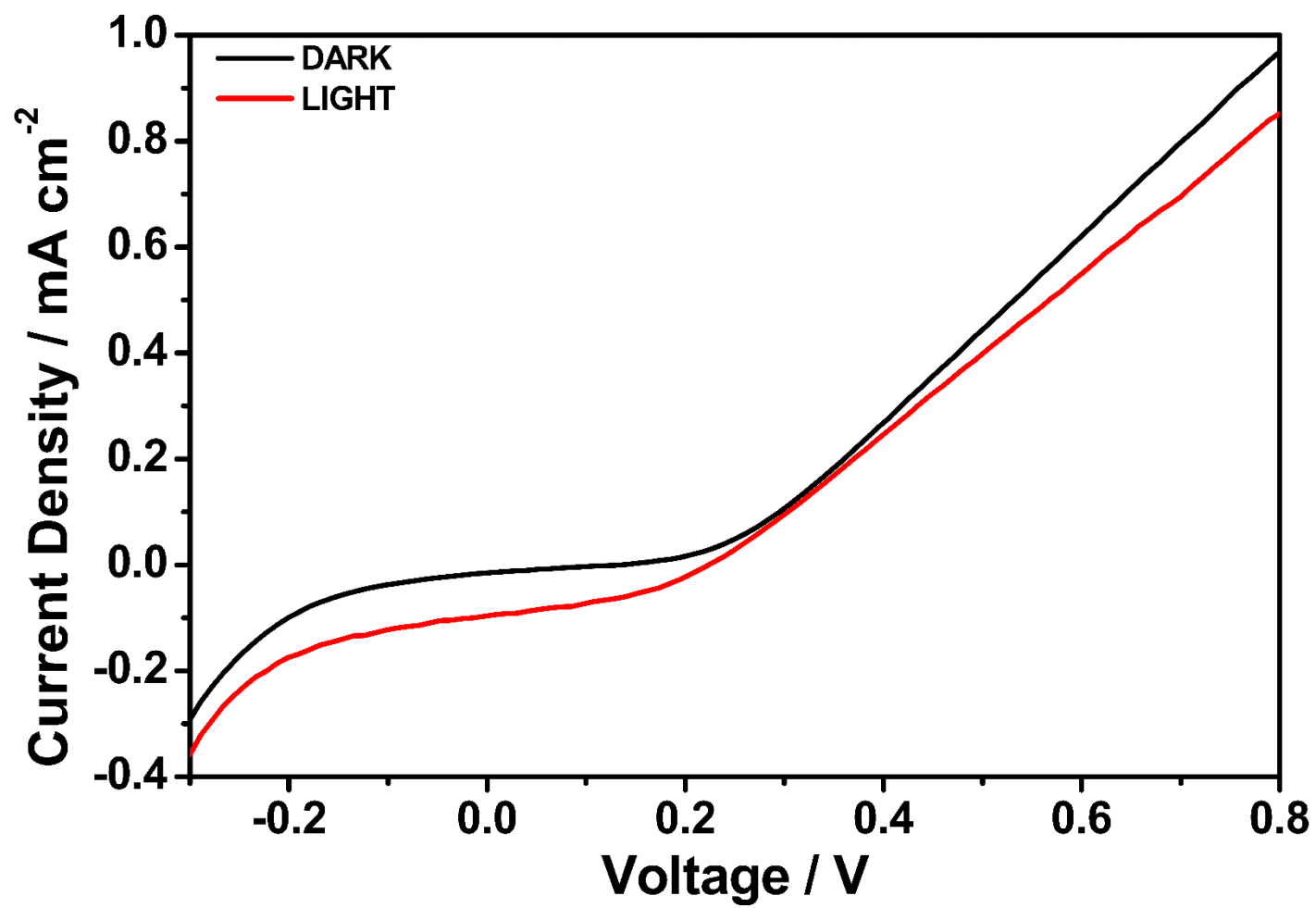
Figure 4.76: I–V curve of HP–PDA
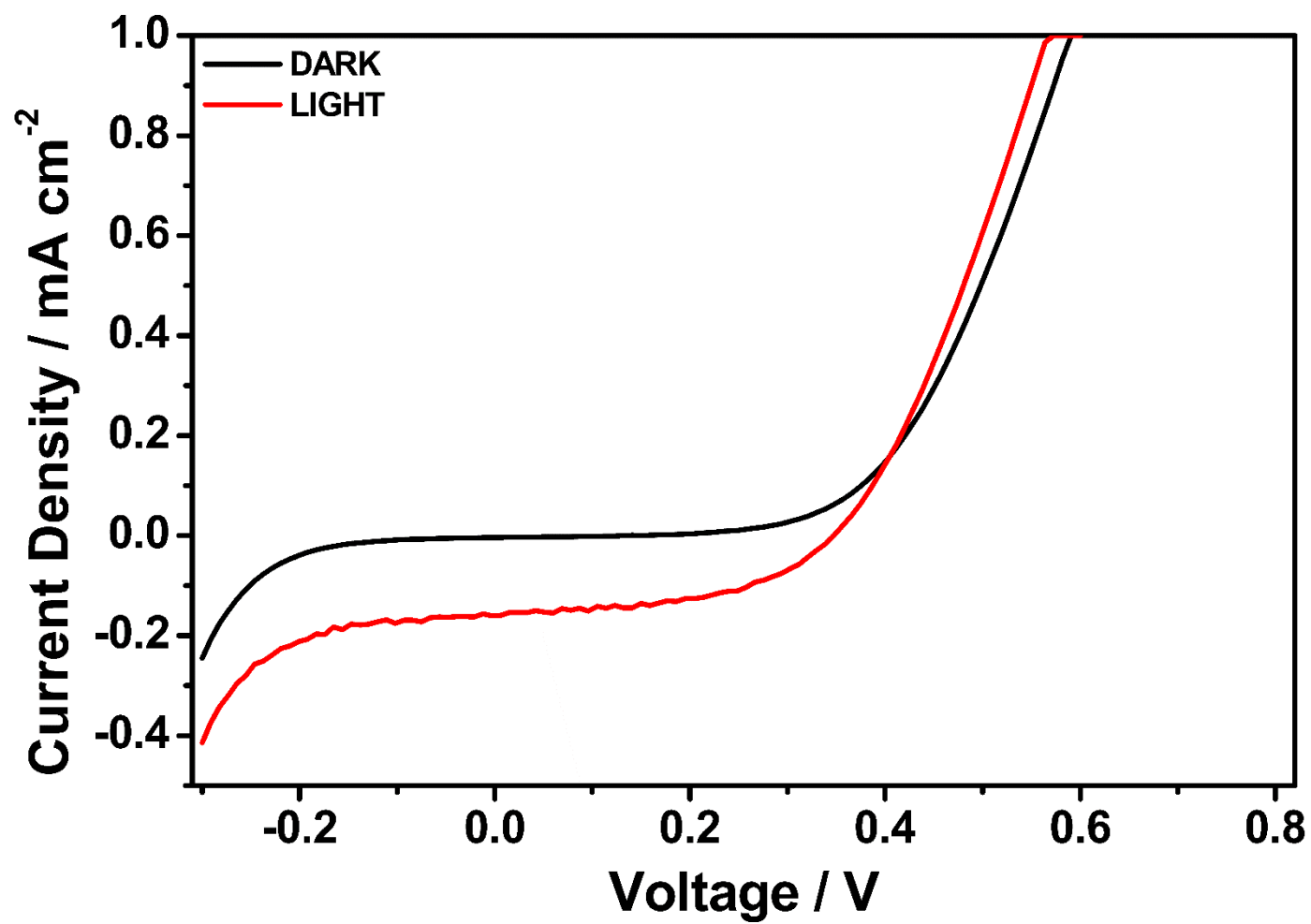
Figure 4.77: I–V curve of HP–HEPDI
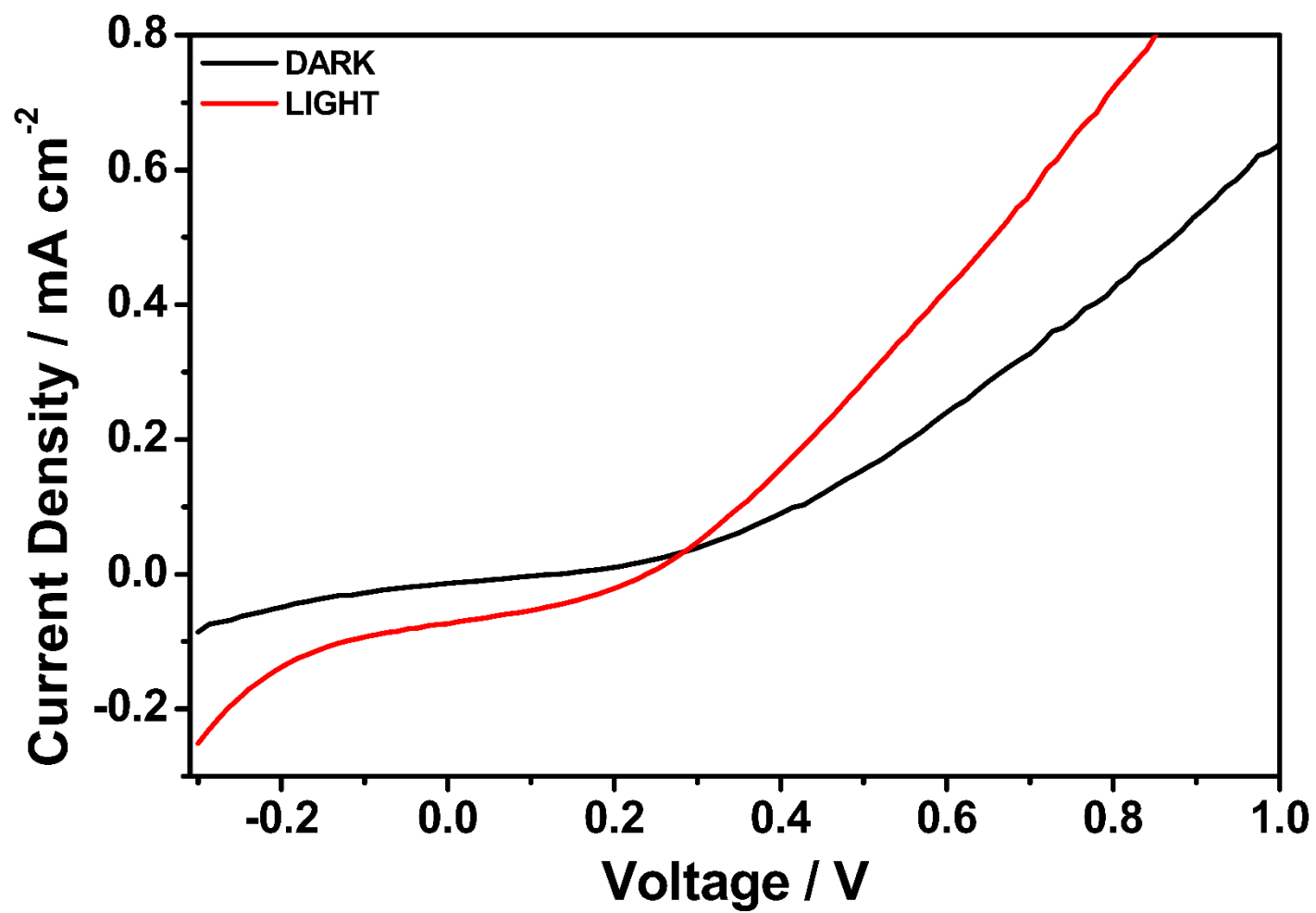
Figure 4.78: I–V curve of TM–HEPDI
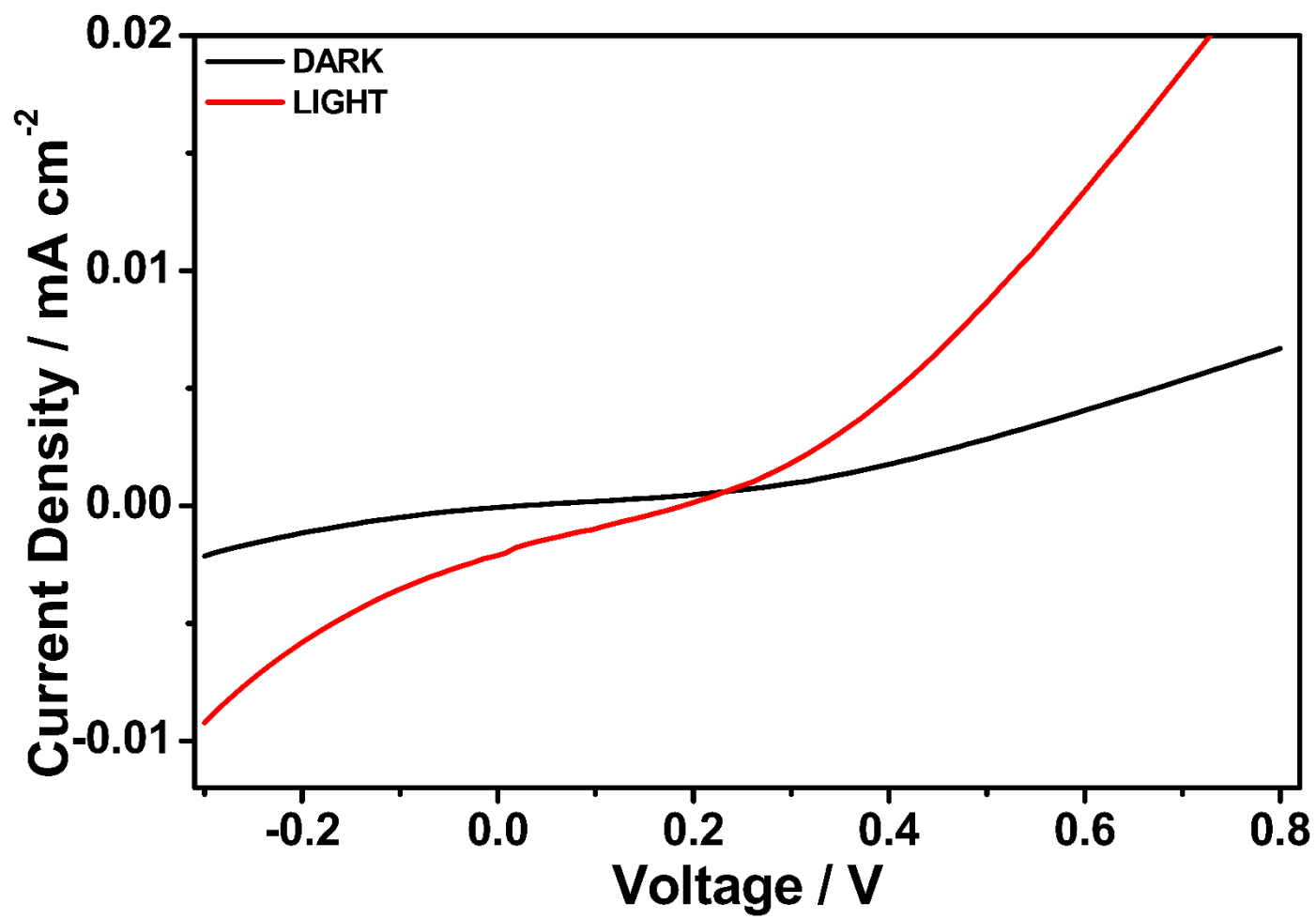
Figure 4.79: I–V curve of HEPDI
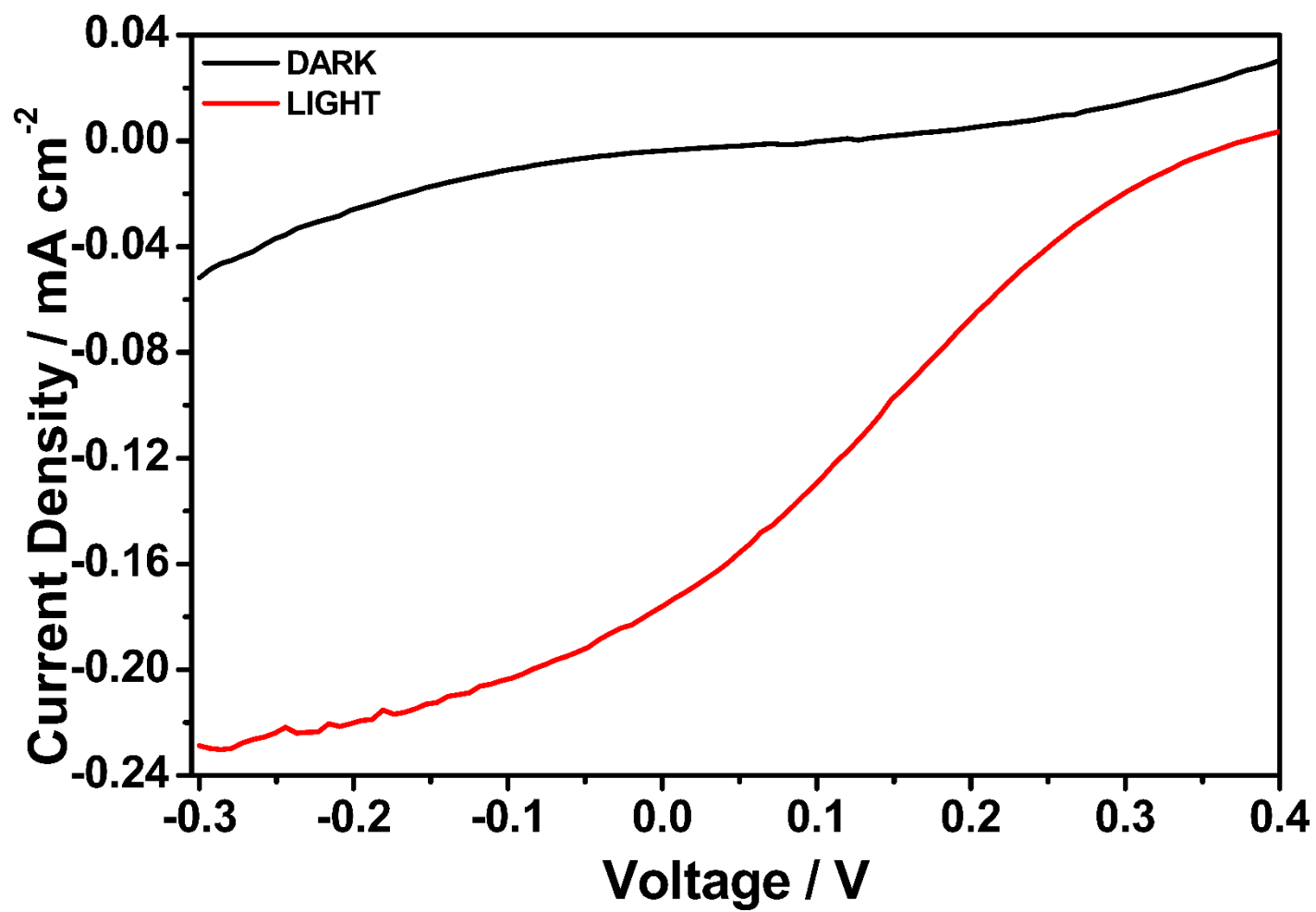
Figure 4.80: I–V curve of HP–TCPDI
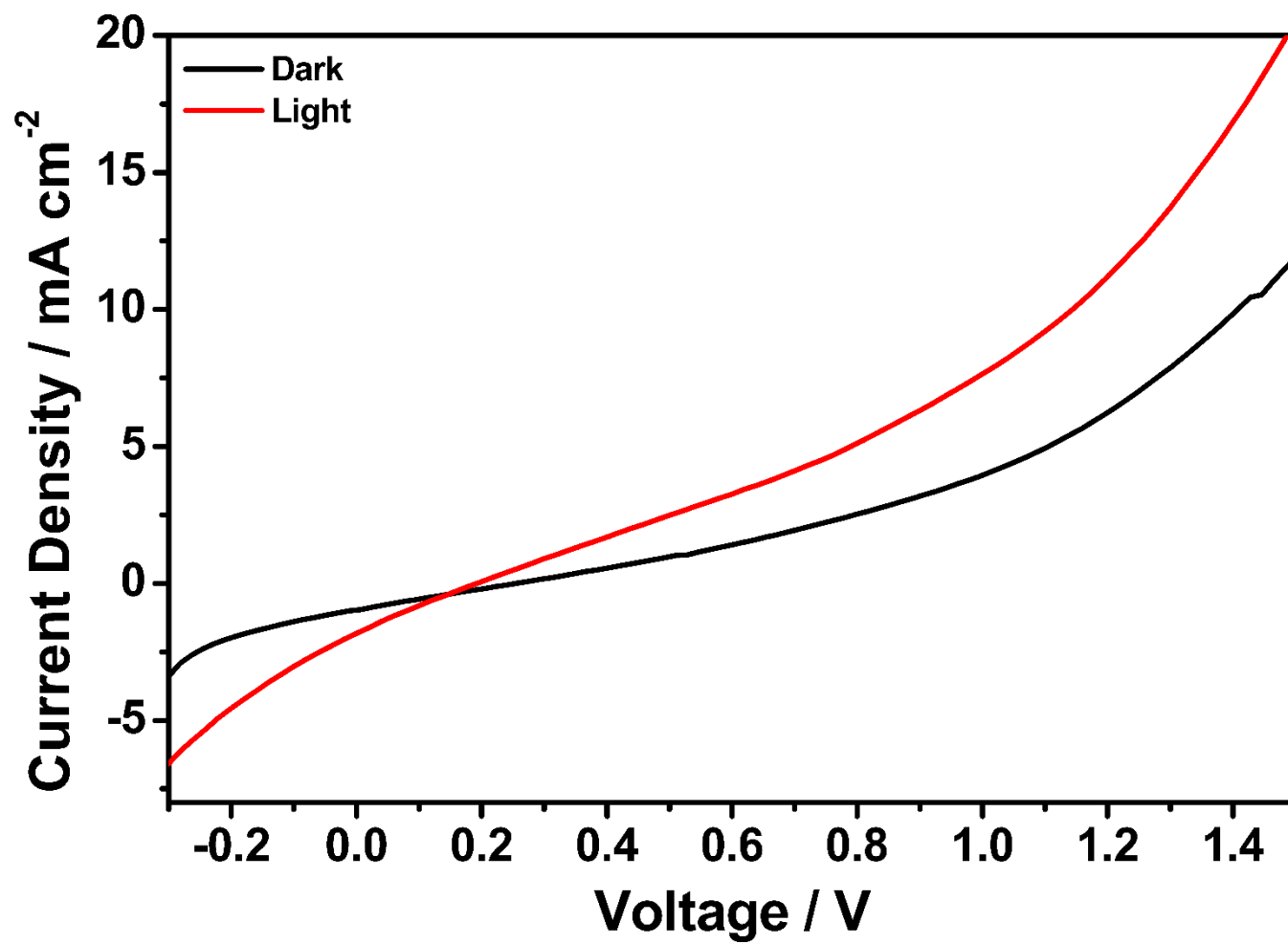
Figure 4.81: I–V curve of complex 1
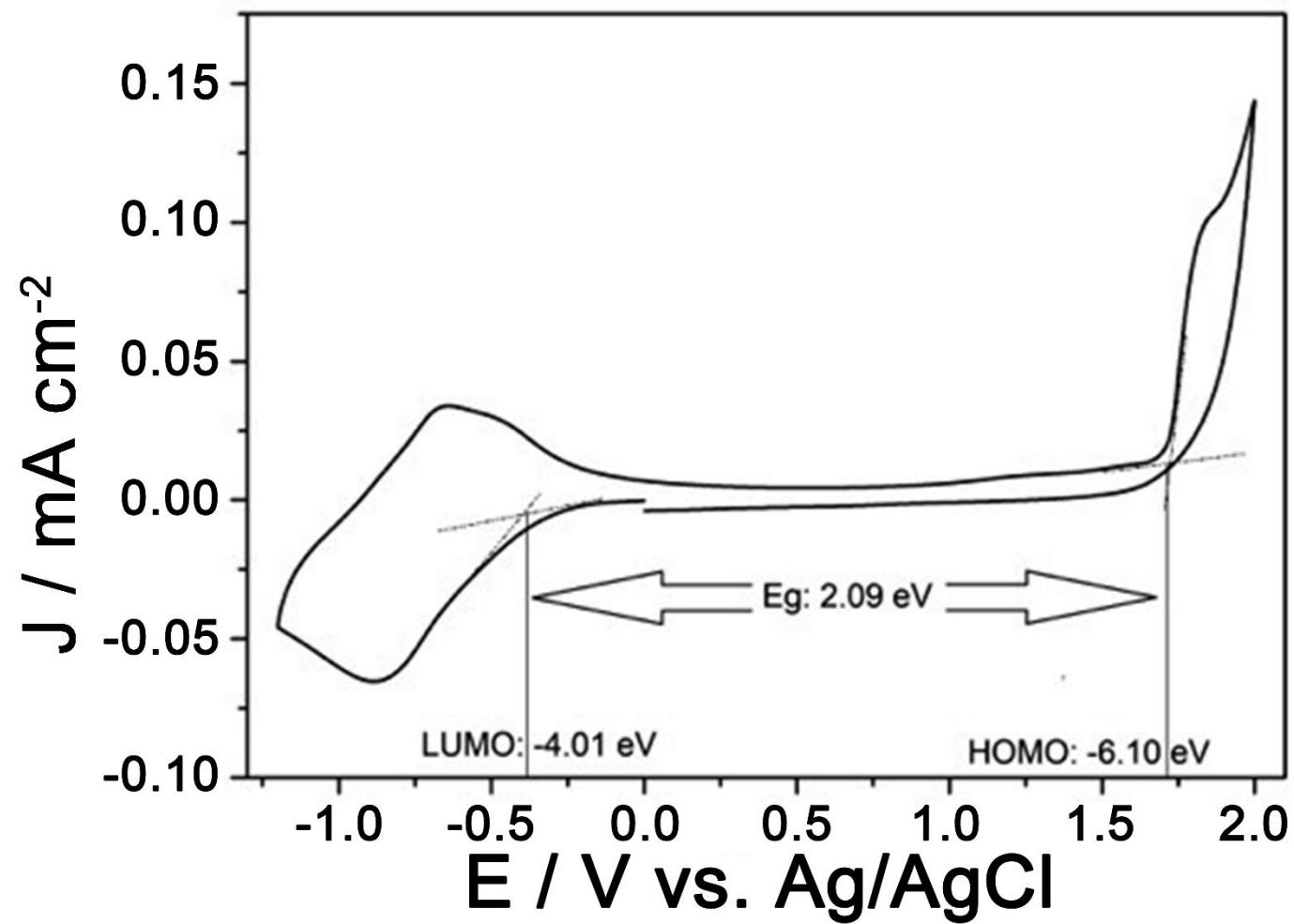
Figure 4.82: CV spectrum of TAPPI
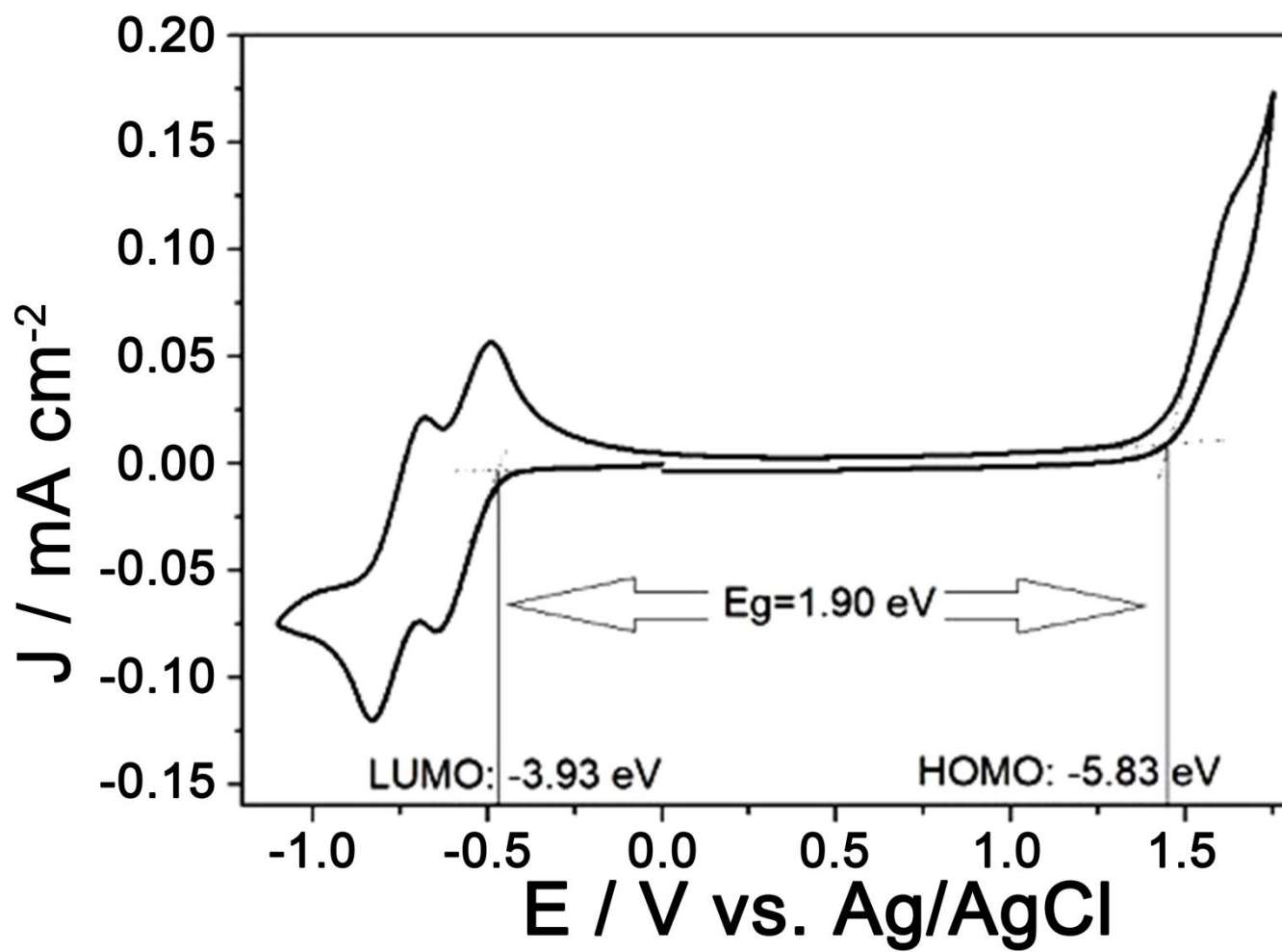
Figure 4.83: CV spectrum of TAPDI
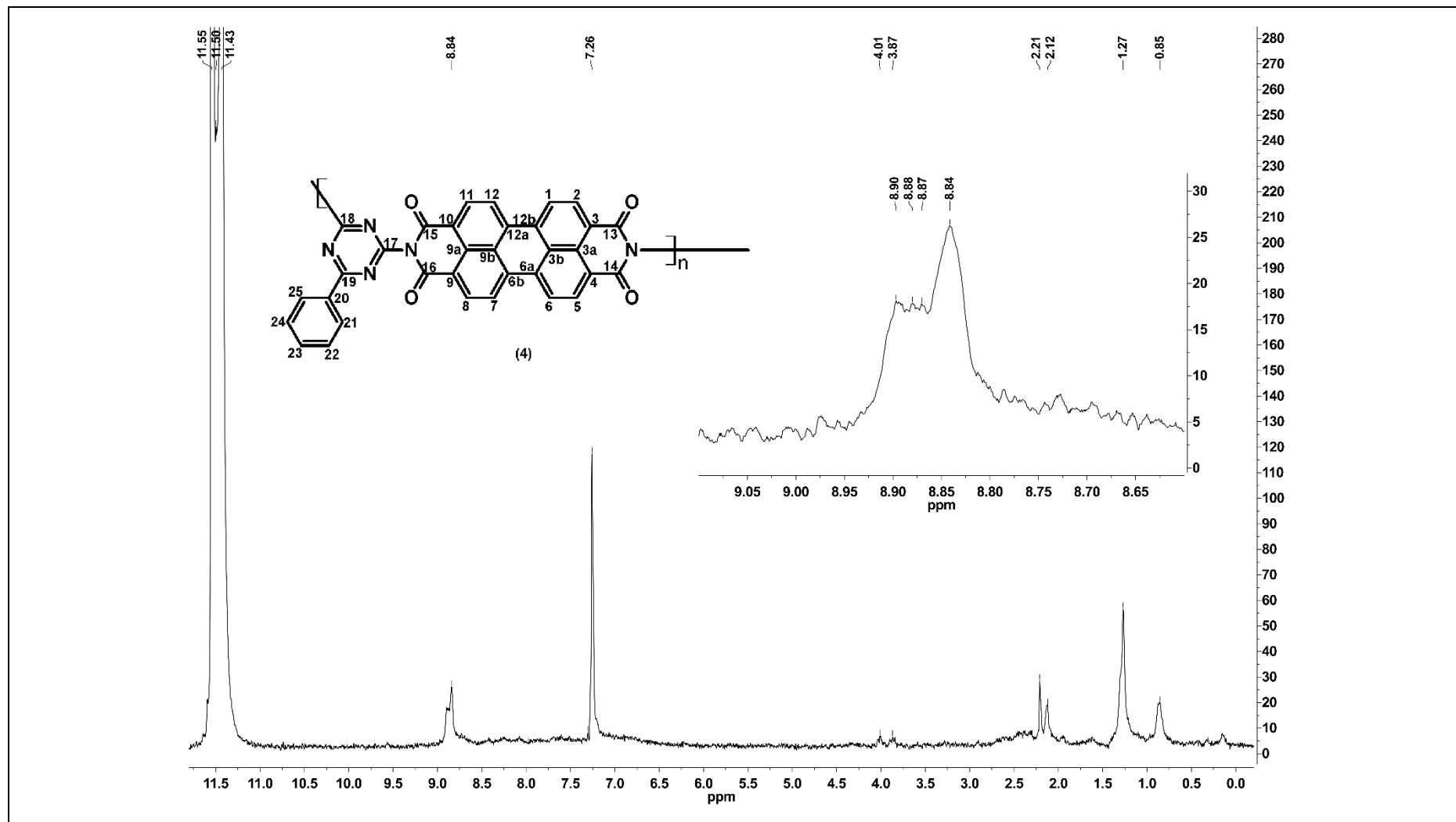
Figure 4.84: ^{1}H NMR of TAPPI
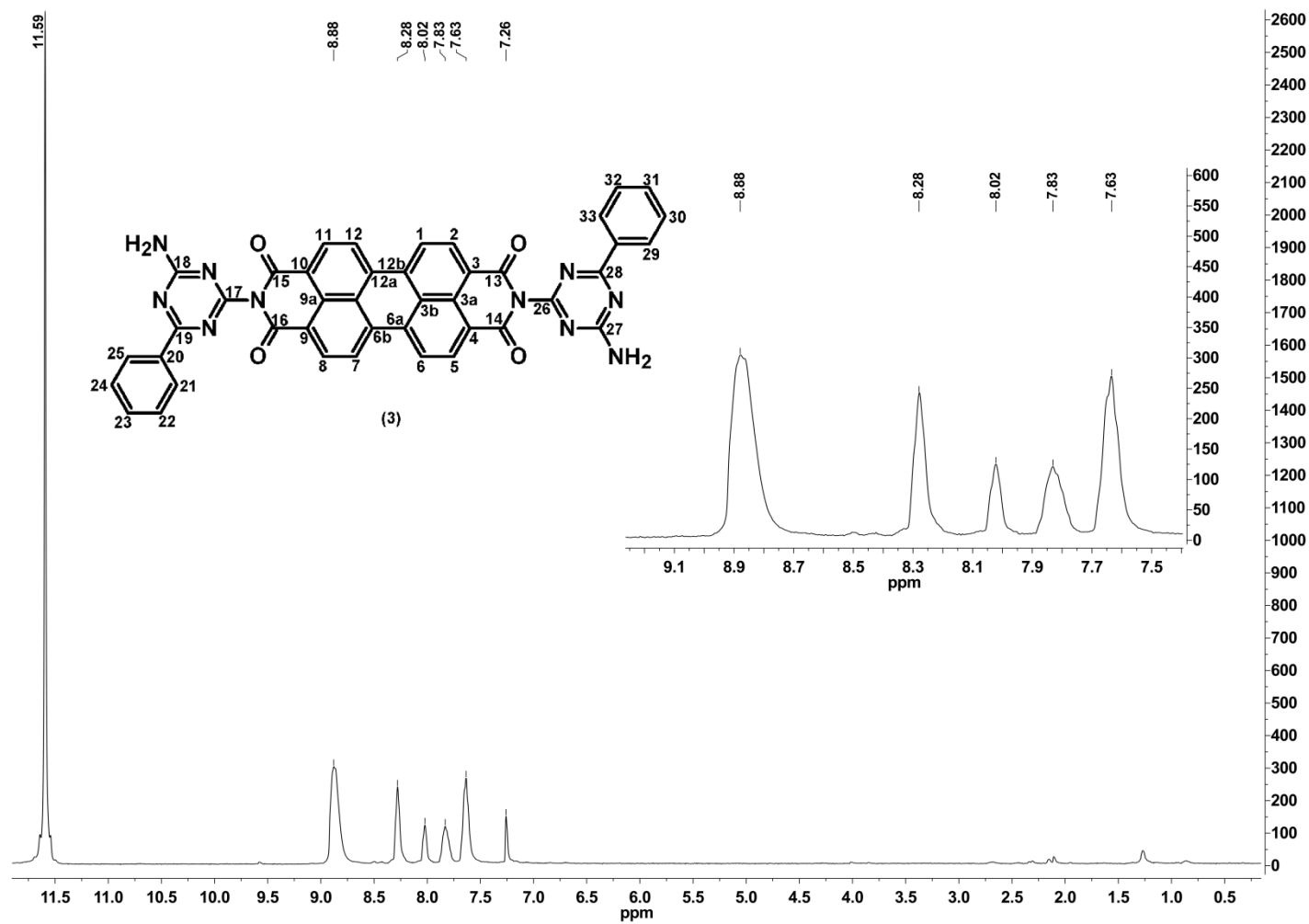
Figure 4.85: ^{1}H NMR of TAPDI
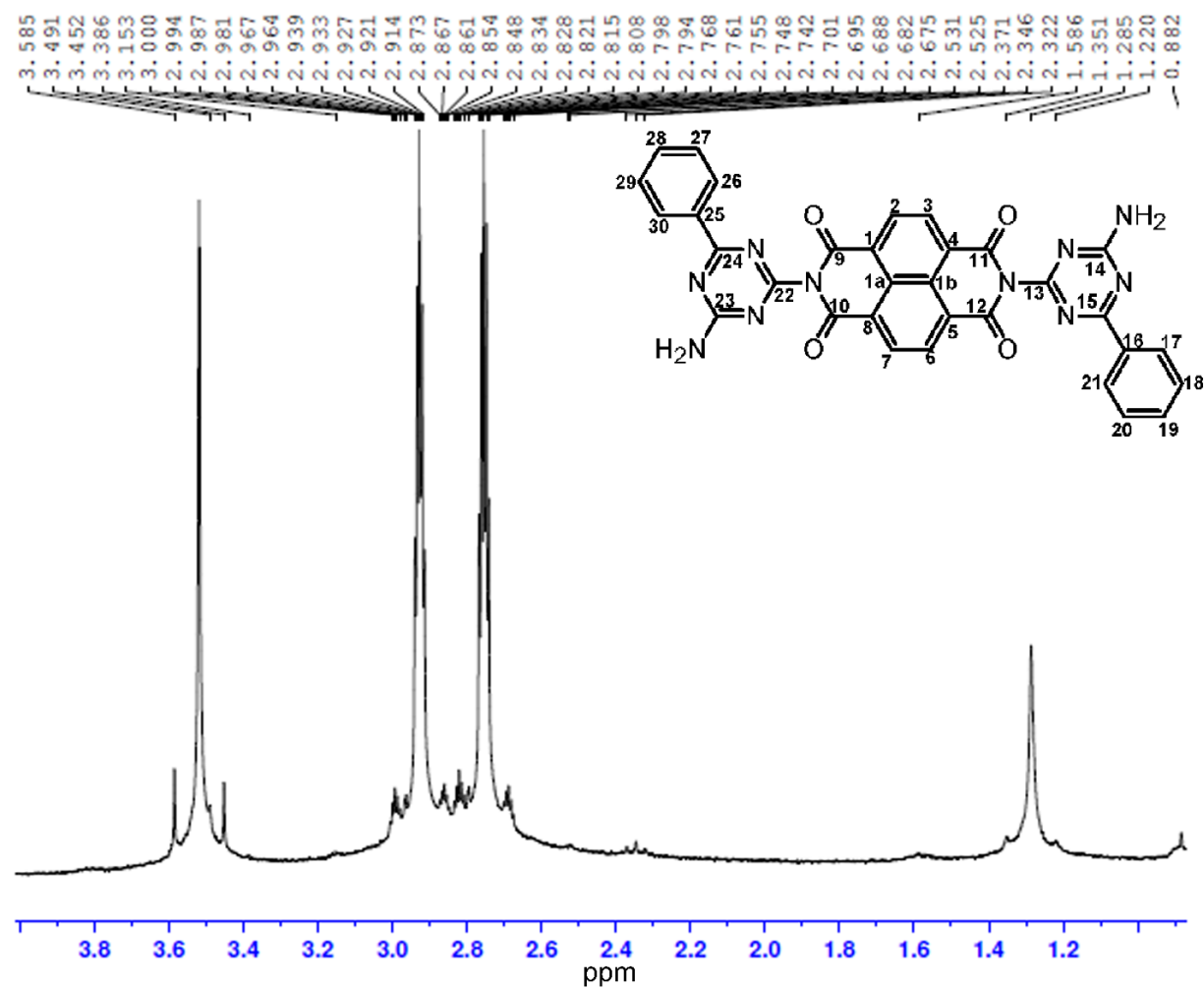
Figure 4.86: ^{1}H NMR of TANDI (0.5−4 ppm)
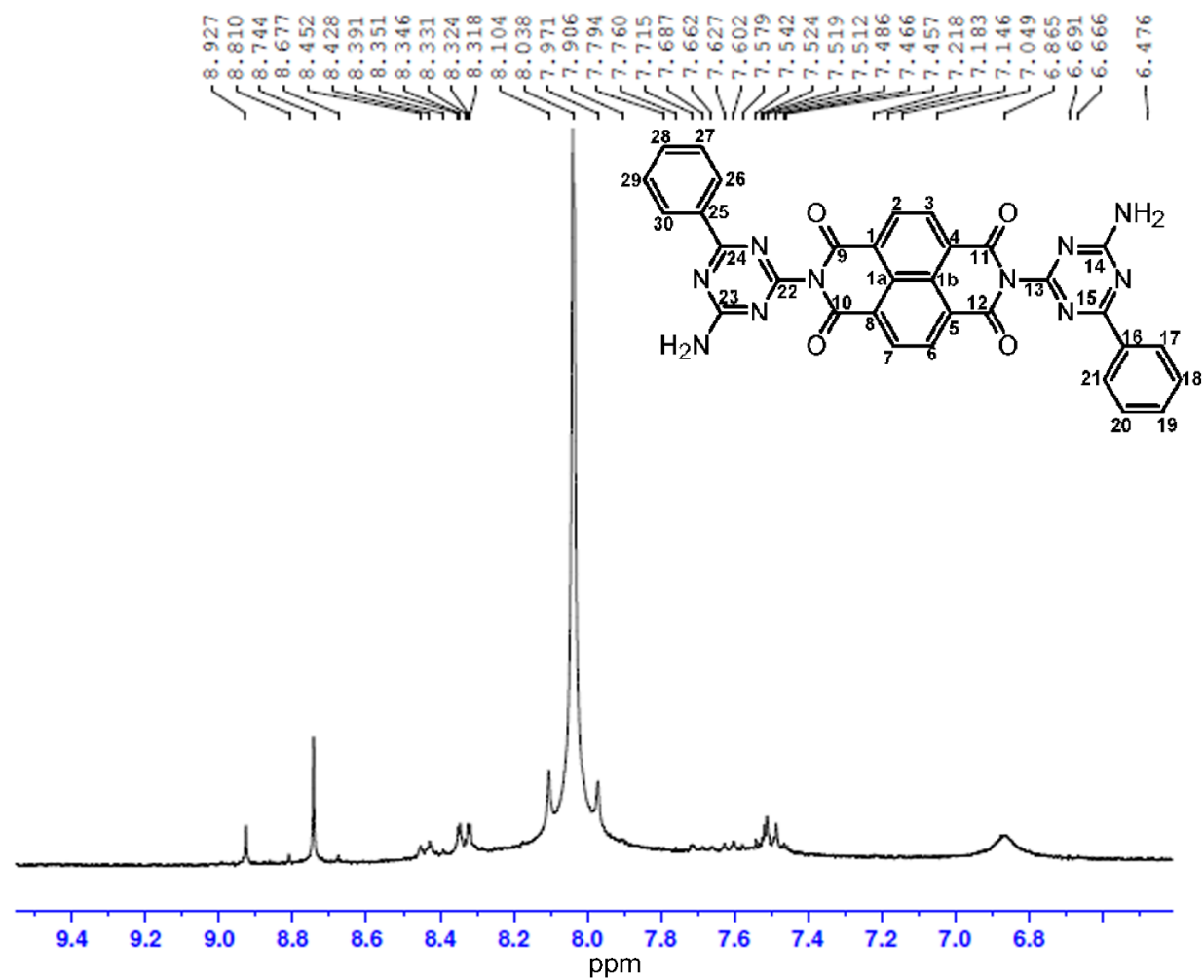
Figure 4.87: ^{1}H NMR of TANDI (6.4−9.6 ppm)
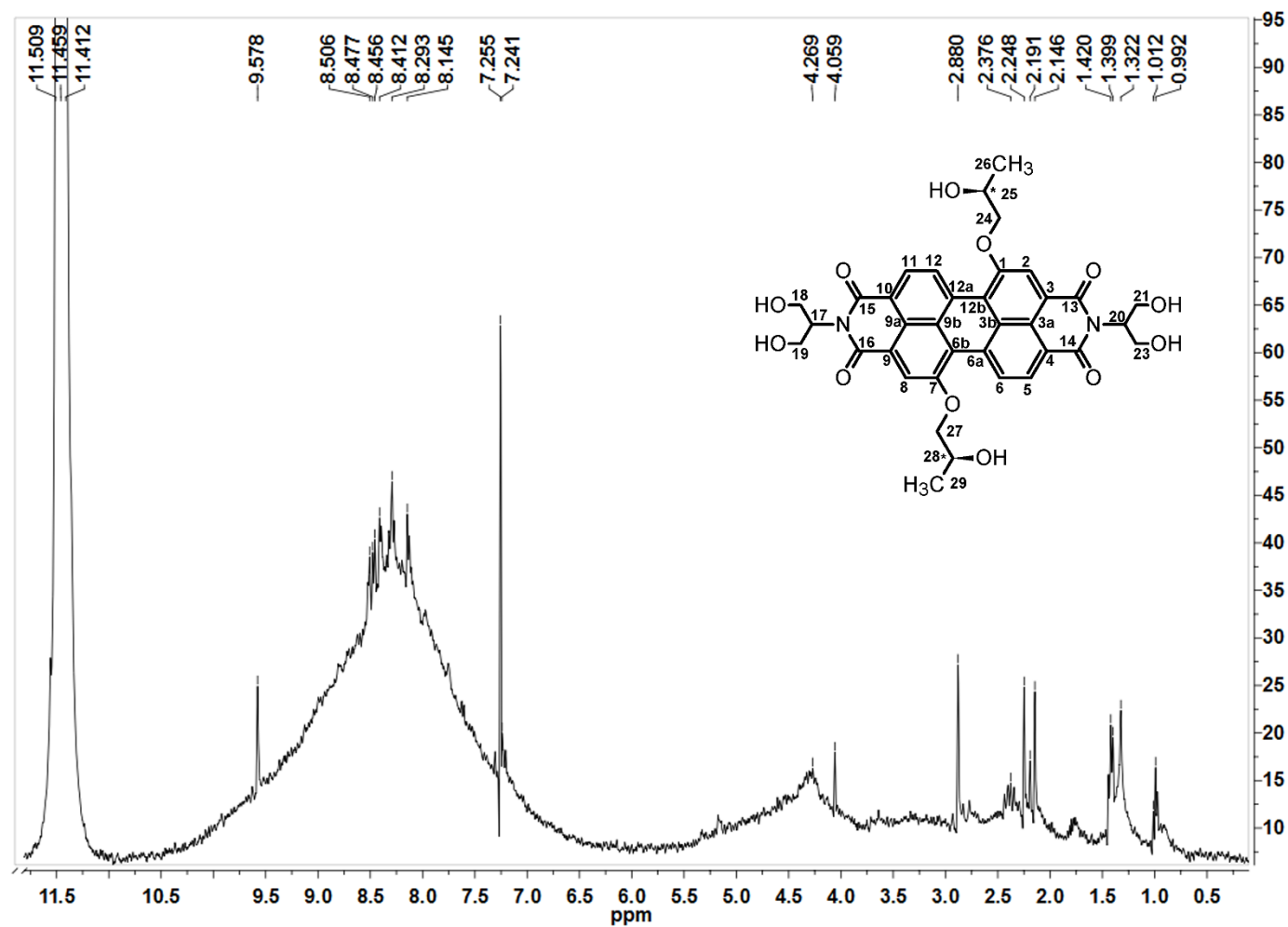
Figure 4.88: ¹H NMR of HP–HEPDI
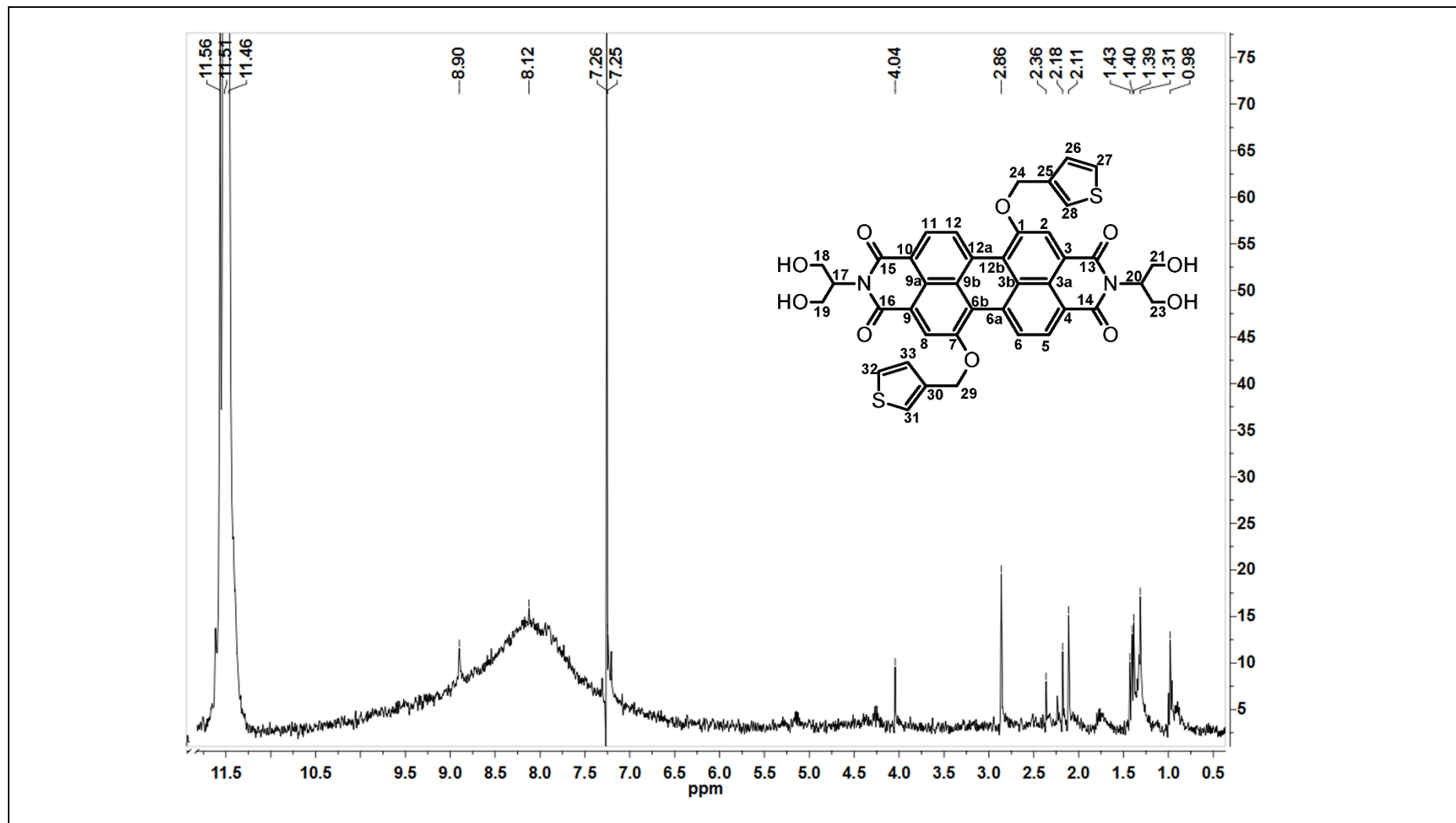
Figure 4.89: ¹H NMR of TM–HEPDI
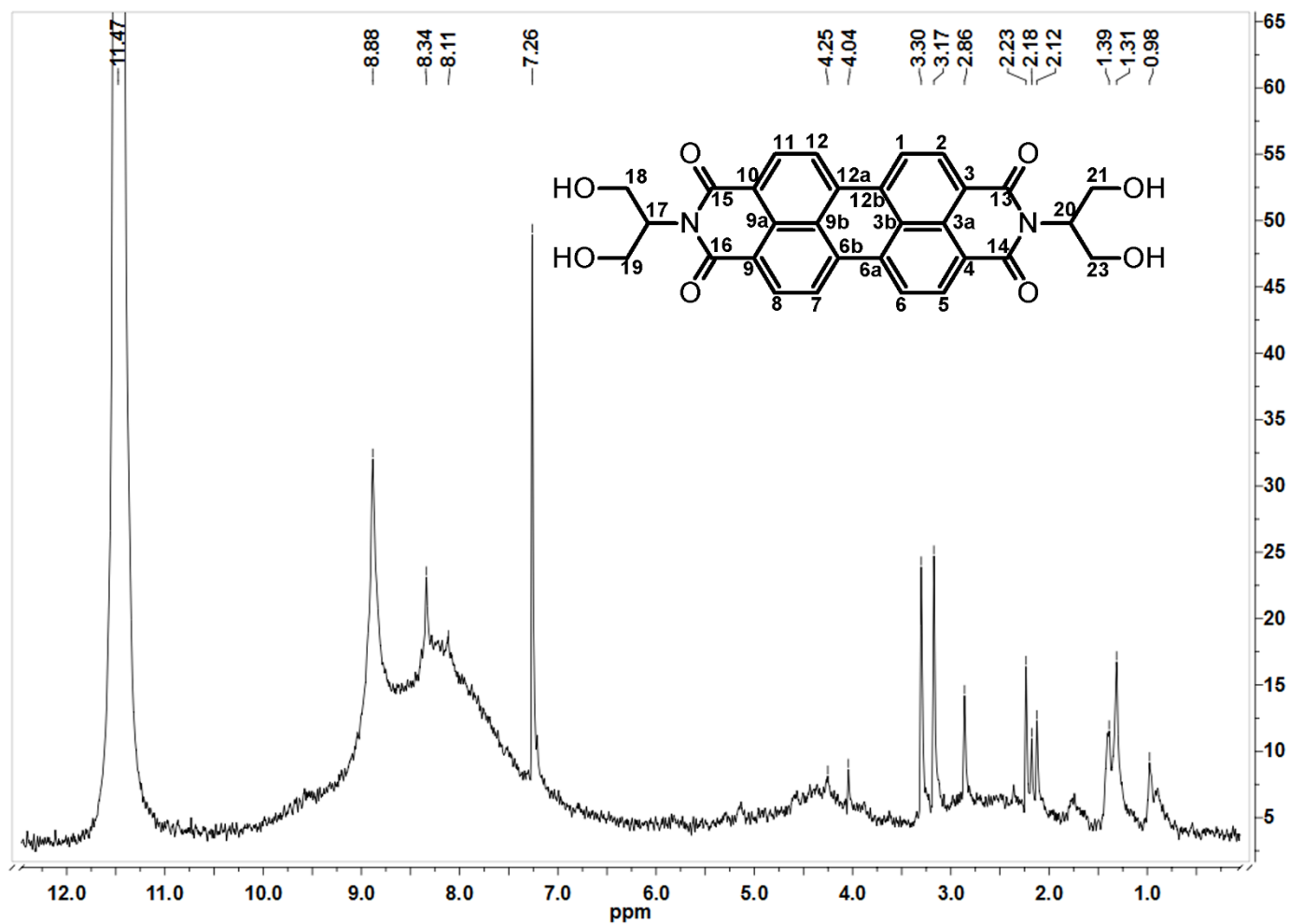
Figure 4.90: ¹H NMR of HEPDI

Chapter 5

RESULTS AND DISCUSSIONS

5.1 Syntheses of the Symmetrical Perylene and Naphtalene Diimides and Bay−Substituted Perylene Diimides

In the present work, two different symmetric perylene diimides (TAPDI and HEPDI) and naphthalene diimide (TANDI) were synthesized by a condensation reaction mechanism in high % yields. The synthetic routes of the compounds are shown in Scheme 3.5, Scheme 3.6 and Scheme 3.7, respectively.

To alter the photochemical and photophysical properties of the perylene diimide dyes, 1,7 (6)−symmetrically functionalized perylene diimides (TM−HEPDI, HP−HEPDI, HP−TCPDI) with electron donating and/or chiral groups have been prepared in three successful steps. To prepare these novel products, firstly brominated perylene dianhydride (Br−PDA) was synthesized in a good amount according to the given literature procedure [50] and then functionalization from bay position on perylene core have been completed with different alcoholic substituents. Finally, third step of synthetic procedure was completed with imidization in high boiling point solvents.

The structural chemical backbone of the novel compounds were analyzed in detail by using FT−IR spectroscopy, ^{1}HNMR spectroscopy, mass spectroscopy and elemental analyses. The physicochemical properties were identified by using cyclic

voltammetry. Moreover the thermal behaviors of the products are characterized by DSC and TGA.

5.2 Syntheses of the Coordinated Perylene Diimide Triads

In the present work, three metal complexes are synthesized as a sensitizer to increase η % of the fabricated DSSC device. The coordinated perylene diimide compounds were synthesized under a nitrogen atmosphere by one step complexation reaction of copper(II)perchlorate hexahydrate solution with perylene diimide dyes in 30 mL dried DMF solvent in high yields.

5.3 FT−IR Spectra Analyses

The numerous functional groups of synthesized dyes with assigned chemical structures have been depicted in the FT−IR spectra taken for all the synthetic products. The stretching and bending absorptions of functional groups are described in more detail below.

The FT−IR spectrum of TAPDI as depicted in the Figure 4.9. The characteristic peaks were as follow 3486, 3431, 3373 and 3326 cm^{-1} (N−H stretch), 3066 cm^{-1} (aromatic C−H stretch), 1710 and 1667 cm^{-1} (imide C=O stretch), 1594 cm^{-1} (aromatic C=C stretch), 1397, 1364 and 1344 cm^{-1} (imide C−N stretch), 811, 741 and 655 cm^{-1} (aromatic C−H bend). In the FT−IR spectrum of perylene dianhydride (Figure 4.8), the representative peaks of the anhydride carbonyl stretching band (1773) were exchanged by carbonyl stretching bands belonging to imide functional group (1710 and 1667 cm^{-1} for TAPDI). Likewise, the representative band of the stretching belonging to C−O−C (1020 cm^{-1}) have been disappear and was changed by C−N stretching band (1344 cm^{-1} for TAPDI).

The infrared spectrum of the TAPDI binded with TiO_2 has been showed in Figure 4.21. The stretching vibration peaks of N−H at 3486, 3431, 3373 and 3326 cm^{-1} observed in TAPDI (Figure 4.9) were disappeared in TAPDI/TiO_2, which may be indicative of the binding (such as Ti...O and Ti…N) between TAPDI and titanium. Besides, the stretching vibrations of imide C=O on TAPDI at 1710 and 1667 cm^{-1} are shifted to 1704 and 1637 cm^{-1} in TAPDI/TiO_2.

Figure 4.10 represents the infrared spectrum of TANDI. Characteristic vibrational bands were observed after imidization as follow: 3468 and 3341 cm^{-1} (N−H stretch), 3063 cm^{-1} (aromatic C−H stretch), 1713 and 1684 cm^{-1} (imide C=O stretch), 1556 cm^{-1} (aromatic C=C stretch) 1346 cm^{-1} (C−N stretch) and 761, 709 and 649 cm^{-1} aromatic C−H bend).

The FT−IR spectrum of the TANDI binded with TiO_2 has been represented in the Figure 4.22. The N−H stretching vibrations at 3468 and 3341 cm^{-1} investigated in infrared spectrum of TANDI (Figure 4.10) was shifted to 3338 cm^{-1} in TANDI/TiO_2, which may be indicative of the binding (such as Ti...N) between TANDI and titanium. Besides, the stretching vibrations of imide carbonyl (C=O) in the infrared spectrum of TANDI at 1713 and 1684 cm^{-1} shifted to 1704 and 1630 cm^{-1} in TANDI/TiO_2.

In the infrared spectrum of HEPDI (Figure 4.16), the specific vibration bands were observed as follow: 3429 cm^{-1} (O−H), 3054 cm^{-1} (aromatic C−H stretch), 2924 and 2851 cm^{-1} (aliphatic C−H stretch), 1687 cm^{-1} (imide C=O stretch), 1597 cm^{-1} (aromatic C=C stretch), 1360 cm^{-1} (imide C−N stretch), 809, 743 and 661 cm^{-1} (aromatic C−H bend). The specific vibration bands of the carbonyl group belonging to

anhydride stretching (C=O, 1773 cm^{-1}) in the infrared spectrum of perylene dianhydride have been lost and were exchanged by carbonyl (1687 cm^{-1} for HEPDI) stretching bands belonging to imide. Likewise, the C–O–C stretching (1020 cm^{-1}) band has been lost and was exchanged by C–N stretching band (1360 cm^{-1} for HEPDI).

The FT−IR measurement of the HEPDI binded with TiO$_2$ has been pictured in Figure 4.28. The O–H stretching vibration at 3429 cm^{-1} observed in HEPDI (Figure 4.16) was shifted to 3404 cm^{-1} in HEPDI/TiO$_2$, which may be indicative of the binding (such as Ti...O) between HEPDI and titanium. Moreover, the stretching vibration band of imide C=O on HEPDI at 1687 cm^{-1} shifted to 1680 cm^{-1} in HEPDI/TiO$_2$.

Br−PDA exhibits the characteristic infrared peaks in the FT−IR spectrum (Figure 4.11) as follow: 3059 cm^{-1} (aromatic C–H stretch), 1776 and 1719 cm^{-1} (anhydride C=O stretch), 1590 cm^{-1} (conjugated C=C stretch), 1036 cm^{-1} (anhydride C–O–C stretch), 807 and 753 cm^{-1} (C–H bend), 694 cm^{-1} (C–Br stretch).

The characteristic infrared peaks was observed in the infrared spectrum of TM−PDA (Figure 4.12) as follow: 3063 cm^{-1} (aromatic C–H stretch), 2923 and 2851 cm^{-1} (aliphatic C–H stretch), 1769 and 1719 cm^{-1} (anhydride C=O stretch), 1589 cm^{-1} (conjugated C=C stretch), 1232 cm^{-1} (ether C–O–C stretch), 1036 cm^{-1} (anhydride C–O–C stretch). The peak at 694 cm^{-1} belonging to C–Br stretch in the infrared spectrum of Br−PDA has been disappeared and the peak at 1232 cm^{-1} belonging to ether C–O–C stretch has been formed after substitution.

In Figure 4.26, the FT−IR spectrum of the TM−PDA binded with TiO_2 has been depicted. The stretching vibration band of anhydride carbonyl in the infrared spectrum of TM−PDA (Figure 4.12) at 1769 and 1719 cm^{-1} are shifted to 1766 cm^{-1} in TM−PDA/TiO_2 which may be indicative of the binding (such as Ti...O) between TM−PDA and Titanium.

The FT−IR spectrum of TM−HEPDI exhibits the featuristic absorption transitions in the Figure 4.15 as follow: 3355 cm^{-1} (O−H stretch), 3159 and 3039 cm^{-1} (aromatic C−H stretch), 2842 cm^{-1} (aliphatic C−H stretch), 1679 cm^{-1} (imide C=O stretch), 1582 cm^{-1} (aromatic C=C stretch), 1264 cm^{-1} (ether C−O−C stretch) and 743 cm^{-1} (aromatic C−H bend). Comparing the FT−IR spectra of TM−PDA and TM−HEPDI, the characteristic peaks of the carbonyl anhydride stretching band (1769 and 1719 cm^{-1}) have been lost and were exchanged by imide carbonyl stretching bands (1679 cm^{-1}) after imidization.

The FT−IR spectrum of the TM−HEPDI binded with TiO_2 has been represented in Figure 4.27. The O−H stretching vibrations at 3355 cm^{-1} observed in the infrared spectrum of TM−HEPDI (Figure 4.15) was shifted to 3404 cm^{-1} in the infrared spectrum of TM−HEPDI /TiO_2, which may be indicative of the binding (such as Ti...O) between TM−HEPDI and titanium. Also, the stretching vibration band of carbonyl group belonging to imide on TM−HEPDI at 1679 cm^{-1} shifted to 1671 cm^{-1} in TM−HEPDI/TiO_2.

Figure 4.13 has been depicted the infrared spectrum of the HP−PDA. Infrared spectrum of the compound shows following characteristic absorption peaks, 2924 cm^{-1} (aliphatic C−H stretch), 1760 cm^{-1} and 1719 cm^{-1} (anhydride C=O stretch), 1232 cm^{-1} (ether C−O−C stretch), 1590 cm^{-1} (aromatic C=C stretch) and 1012 cm^{-1} (ether C−O−C stretch). Comparing the FT−IR spectra of Br−PDA and HP−PDA, peak at 694 cm^{-1} belonging to C−Br stretch has been disappeared and the peak at 1232 cm^{-1} belonging to ether C−O−C stretch formed after substitution.

Figure 4.23 has been represented the infrared spectrum of the HP−PDA binded with TiO$_2$. The stretching vibration band of anhydride carbonyl (C=O) in infrared spectrum of HP−PDA (Figure 4.13) at 1760 cm^{-1} and 1719 cm^{-1} are combined into 1760cm^{-1} in HP−PDA/TiO$_2$ which may be indicative of the binding (such as Ti...O) between HP−PDA and Ti.

The FT−IR spectrum of bay substituted perylene diimide, HP−HEPDI (Figure 4.14) shows the characteristic peaks as follow: 3053 cm^{-1} (aromatic C−H stretch), 2924 and 2852 cm^{-1} (aliphatic C−H stretch), 1688 cm^{-1} (imide C=O stretch), 1590 cm^{-1} (aromatic C=C stretch), 1265 cm^{-1} (ether C−O−C stretch) and 752 cm^{-1} (aromatic C−H bend). Comparing the FT−IR spectra of HP−PDA and HP−HEPDI, the characteristic peaks of the carbonyl anhydride stretching band (1769 and 1719 cm^{-1}) have been lost and were exchanged by carbonyl stretching bands belonging to imide functional group (1688 cm^{-1}).

The FT−IR spectrum of the HP−HEPDI binded with TiO$_2$ has been presented in Figure 4.24. The stretching vibration band of imide carbonyl (C=O) in infrared spectrum of

HP–HEPDI (Figure 4.14) at 1688 cm^{-1} is moved to 1681 cm^{-1} in HP–HEPDI/TiO$_2$ which could be indicative of the binding between HP–HEPDI and titanium.

The FT–IR spectrum of HP–TCPDI (Figure 4.17) gives information about the characteristic vibrational bands as follow: 3397 cm^{-1} (O–H stretch), 3054 cm^{-1} (aromatic C–H stretch), 2924 and 2852 cm^{-1} (aliphatic C–H stretch), 1620 cm^{-1} (imide C=O stretch), 1589 cm^{-1} (aromatic C=C stretch) 1385 cm^{-1} (C–N stretch) and 1272 cm^{-1} (ether C–O–C stretch) 759 and 687 cm^{-1} aromatic C–H bend). Comparing the FT–IR spectra of HP–PDA and HP–TCPDI, the well–defined peaks of the carbonyl anhydride stretching band (1769 and 1719 cm^{-1}) have been disappeared and were exchanged by stretching bands belonging to imides carbonyl groups (1620 cm^{-1}) after imidization.

The FT–IR spectrum of complex 1 is depicted in Figure 4.18. The two vibration transitions at 3431 and 3228 cm^{-1} in the region of the amino (NH$_2$–) stretching vibrations of the diaminotriazine (Figure 4.9) in the infrared spectrum of metal free ligand are moved to 3429 and 3225 cm^{-1}, respectively, in the complex 1 (Figure 4.18). Moreover peaks at 3486 and 3373 cm^{-1} in FT–IR spectrum of TAPDI were disappeared. The imide carbonyl (C=O) stretching bands of the imide group at 1710 and 1667 cm^{-1} for the pure TAPDI are moved to 1704 and 1671 cm^{-1} in the coordinated perylene diimide dye (Complex 1). The aromatic C=C stretching and imide C–N stretching vibrations are shifted 4 cm^{-1} to lower frequencies.

The FT–IR spectrum of complex 2 has been pictured in the Figure 4.19. The FT–IR spectrum ensured wide statement respecting the coordination modes of the ligand in

the structural monad of the transition metal complex molecule. The FT−IR spectrum

of metal−free ligand (HP−HEPDI) show sharp peaks at 1688 and 1590 cm^{-1} belonging

to the C=O imide and aromatic C=C bands, respectively (Figure 4.14). When metal

ions are coordinated, the HP−HEPDI C=O imide and aromatic C=C stretching peaks

move to a higher frequency by 5 cm^{-1} and 8 cm^{-1}, respectively, showing that the lone

pair of nitrogen is donated to metal ions in the complexes. These shifts confirm the

involvement of the hydroxyl groups on imide position bonded with metal ion. Since

bonding is from imide position, the transition band at 1265 cm^{-1} in the range of the

ether stretching vibration of the ether functional group did not shift. The band is

determined at 3412 cm^{-1} in complex is preferable to the aliphatic −OH and coordinated

H$_2$O group present in the complex.

The FT−IR spectrum of complex 3 has been studied in the 4000–450 cm^{-1} range

(Figure 4.18). The infrared spectrum of ligand (TM−HEPDI) has been depicted clear

bands at 1679 and 1582 cm^{-1} belonging to the C=O imide and aromatic C=C groups,

respectively (Figure 4.15). The TM−HEPDI C=O imide and aromatic C=C stretching

peaks upon coordination with the metal ions shifted to 1687 and 1586 cm^{-1} by ~8 and

4 cm^{-1} to higher frequencies, showing contribution of the non−shared electron pairs of

nitrogen to metal ions in the complexes. These shifts confirm the involvement of the

hydroxyl groups on imide position bonded with metal ion. The vibration band at 1264

cm^{-1} in the range of the ether functional group stretching shifted to 1270 cm^{-1}.

5.4 Solubility of Symmetric Perylene and Naphtalene diimides

5.4.1 Solubility of *N,N'*–bis(5–amino–3–phenyl–2,4,6–triazinyl) perylene–3,4,9, 10–tetracarboxylic diimide (TAPDI)

Table 5.1 depicted the qualitative dissolution properties and colors of the TAPDI in distinct organic solvents. The synthetic compound was dissolved easily in aprotic solvents with high dielectric constants like DMSO, DMAc, NMP and DMF and in protic solvent such as TFAc. Complete solubility was also observed at 25°C in solvents which have lower dielectric constants like pyridine and *m*–cresol, but not in nonpolar solvents.

Table 5.1: Solubility of TAPDI in common organic solvents

	TAPDI
Solvent	Solubility[a] / color
m−cresol	(+) / violet
THF	(+) / pink
TFAc	(+ +) / fluorescence orange
Pyridine	(+) / fluorescence orange
Acetone	(− +) / orange
NMP	(+ +) / brown
Methanol	(− +) / purple
DMAc	(+ +) / orange
DMF	(+ +) / purple
DMSO	(+ +) / red

[a]Measured at a concentration of 1 mg mL^{-1} in solvents at 25 °C. (+ +): soluble at room temperature. (+): partial soluble at room temperature. (− +): slightly soluble on heating at 50 °C in sonicator. (−): insoluble.

5.4.2 Solubility of *N,N'*−bis(5−amino−3−phenyl−2,4,6−triazinyl) naphthalene−1,4 ,5,8−tetracarboxylic diimide (TANDI)

Table 5.2 represents the solubility features and colors of the solutions, TANDI in various organic solvents. The synthetic compound was dissolved in aprotic solvents like DMAc, DMF, NMP and DMSO which are highly polar, in protic solvent such as TFAc and also lower polarity solvent *m*−cresol and at 25ºC. But the TANDI is not soluble in nonpolar solvents.

Table 5.2: Solubility of TANDI in common organic solvents

Solvent	TANDI
	Solubility / color
m−cresol	(+ +) / yellow
THF	(−)
TFAc	(+ +) / yellow
Acetone	(−)
NMP	(+ +) / yellow
Methanol	(−)
DMAc	(+ +) / yellow
DMF	(+ +) / yellow
DMSO	(+ +) / yellow

5.4.3 Solubility of N,N'−Bis(2−hydroxy−1−(1−hydroxymethyl) ethyl)perylene −3,4,9,10−tetracarboxylic diimide (HEPDI)

Table 5.3 has been represented the qualitative solubility features and colors of the HEPDI in different organic solvents. The symmetrical perylene diimide was completely dissolved in polar protic solvent like TFAc at 25 ºC, in polar aprotic

solvents like DMAc, NMP, DMF and DMSO with dusty pink color at 50 ℃, as well as it is completely dissolve in less polar solvent *m*−cresol but not soluble in nonpolar solvents.

Table 5.3: Solubility of HEPDI in common organic solvents

Solvent	HEPDI
	Solubility / color
Chloroform	(− +) / purple color
m−cresol	(+ +) / dark brown
THF	(− +) / purple color
TFAc	(+ +) / cherry red
NMP	(+) / dusty pink
Methanol	(−)
DMAc	(+) / dusty pink
DMF	(+) / dusty pink
DMSO	(+) / dusty pink

5.5 Solubilities of Bay−Substituted Perylene Dianhydrides and Bay−Substituted Perylene Diimides

5.5.1 Solubilities of 1,7−di(3−thiophenemethoxy) perylene−3,4,9,10−tetracarboxy licdianhydride (TM−PDA) and N,N−Bis(2−hydroxy−1−(1−hydroxymethyl)ethyl)−1,7−di(3−thiophenemethoxy)perylene−3,4,9,10−tetracarboxylic diimide (TM−HEPDI)

Table 5.4 represents the comparative solubility properties and colors of the solutions for TM−PDA and TM−HEPDI in various organic solvents. The both compounds were

dissolved completely in solvents which are polar aprotic like DMAc, NMP, DMF and DMSO upon heating at 50 °C. The synthetic products were completely dissolve in less polar solvent *m*–cresol and in polar protic solvent such as TFAc at 25 °C. TM–HEPDI was not soluble in nonpolar solvents but TM–PDA was giving slightly soluble orange color solution.

Table 5.4: Solubility of TM–PDA and TM–HEPDI in common organic solvents

| Solvent | Solubility / color | |
	TM–PDA	TM–HEPDI
ChL	(− +) / orange	(−)
MC	(+) / pink	(+) / dark brown
TFAc	(+ +) / dark orange	(+ +) / cherry red
NMP	(+) / orange	(+) / dark brown
Methanol	(−)	(−)
DMAc	(+ +) / orange	(+) / dark brown
DMF	(+ +) / light orange	(+) / dark brown
DMSO	(+ +) / light orange	(+) / dark brown

5.5.2   Solubilities   of   1,7–di(2–hydroxypropoxy)perylene–3,4,9,10–tetracarboxylicdianhydride   (HP–PDA),   N,N'–Bis(2–hydroxy–1–(1–hydroxy methyl)ethyl)–1,7–di(2–hydroxypropoxy)   perylene–3,4,9,10–tetracarboxylic diimide   (HP–HEPDI)   and   *N,N'*–bis–[3–((2–methyl–5–pyrimidinyl)methyl) –5–(2–hydroxyethyl)–4–methylthiazolium]–1,7–di(2–hydroxy   propoxy) perylene–3,4,9,10–tetracarboxylic diimide (HP–TCPDI)

Table 5.5 represents the comparative solubility properties and colors of HP–PDA, HP–HEPDI and HP–HEPDI in various organic solvents. The HP–PDA was completely dissolved in solvents which are polar aprotic like DMAc, DMF, NMP and DMSO at 25 ^{o}C with reddish brown color. The other two compounds (HP–HEPDI and HP–HEPDI) were partially soluble in same polar aprotic solvents at 50 ^{o}C with brown color. All the compounds were soluble in polar protic solvent which is TFAc.

Table 5.5: Solubility of HP–PDA, HP–HEPDI and HP–HEPDI in common organic solvents

Solvent	Solubility / color		
	HP–PDA	HP–HEPDI	HP–TCPDI
MC	(− +) / purple	(−)	(+ +) / wine red
TFAc	(+ +) / cherry red	(− +) / brown	(+ +) / dark brown
NMP	(+ +) / reddish dark brown	(− +) / brown	(− +) / coffee brown
DMAc	(+ +) / reddish dark brown	(− +) / brown	(− +) / coffee brown
DMF	(+ +) / reddish dark brown	(− +) / brown	(− +) / coffee brown
DMSO	(+ +) / reddish dark brown	(− +) / brown	(− +) / coffee brown

5.6 UV−Vis Absorption and Emission Investigation

5.6.1 UV−Vis Absorption and Emission Spectra of TAPDI

Figure 4.29−4.31 have been represent the study on the UV−vis absorption and fluorescence (λ_{exc}= 485 nm) spectroscopic measurments of the TAPDI (1×10^{-5} M) in aprotic and protic polar solvents and also in the solid state at room temperature. In the low energy range (400−600 nm), absorption spectra of TAPDI (Figure 4.29.a) show three distinct vibronically well−structured transition bands in different organic solvents, with notably prominent ones in solution. The characteristic $\pi{\rightarrow}\pi^*$ transitions of perylene diimides could be ascribed to the absorption bands of TAPDI (DMF; 527, 491, and 461 nm). Obviously, the polar protic solvents like TFAc and m−cresol have been shown more stabilization violently the excited levels and bathochromically moved the $0{\rightarrow}0$ transition band. Consequently, the excited energy level of TAPDI has the broader dipole moment than the ground energy level (Figure 4.29). Particularly, in the strongly electron donating and the aprotic solvents which have high dielectric constant like NMP solvent, vibronically structured and broad absorption band is observed for compound TAPDI in the region 600−800 nm (794, 765, 712, 701, and 679 nm, Figure 4.29.a inset). The absorption bands around 700 nm indicates the presence of solvent related aggregation attitude and shows the effect of dielectric constant of solvents. The emission spectra of the compound in TFAc, pyridine, NMP, DMAc and DMF depict same structure with approximate mirror images of the absorption spectra (DMF, 545, 580 and 632 nm, Figure 4.29.b). Investigation reveal that fluorescence spectra of TAPDI show red shifted emission upon weaker aggregation as the polarity of solvent increase. It is important to note that, the maximum red shifted spectra were observed in the most polar solvent DMSO whereas very weak aggregation was observed. On the hand, the UV−vis absorption spectra

give an idea about aggregation behavior of TAPDI in solutions. The ratio $A^{0\to0}/A^{0\to1}$ is 1.47 for TAPDI in NMP solvent as it is shown in Table 5.6.

Table 5.6: Ratio of absorption intensities of TAPDI in various solvents

Solvent	$A^{0\to0}$	$A^{0\to1}$	$A^{0\to0}/A^{0\to1}$
TFAc	1.31	0.84	1.56
NMP	1.27	0.86	1.47
DMF	1.14	0.79	1.44
DMAC	1.40	0.99	1.45
DMSO	1.33	0.86	1.55

Figure 4.30 and 4.31 has been presented the differences in the absorption and fluorescence emission measurements (λ_{exc}=485 nm) of TAPDI in NMP at room temperature with freshly prepared five distinct concentrations from 7×10^{-5} M to 5×10^{-6} M together with the photographs of the solutions. As the concentrations of TAPDI raised both the intensity of transition bands raised parallel in absorption and emission spectra. Particularly, the maxima and the structure of the emission bands were investigated in Figure 4.31 strongly depend on the solvent used.

Importantly, structure of the spectrum (absorption up to 800 nm) and the position of peaks are not similar in the solid state absorption spectrum of TAPDI compare with the solution state. (Figure 4.49 red shift of the 0→1 transition; TAPDI: 31 nm). The absorption spectrum of the compound pictured the three wider and bathochromically shifted absorption bands in the solid state. These results have been proved to the presence of weak $\pi\to\pi$ stacking in the solid state. Figure 4.57 represents the solid state absorption spectrum of TAPDI binded with TiO_2. The absorption bands lost their fine vibronic structure and appeared to be broader when adsorbed on the TiO_2 films. A

bathochoromic shift was monitored in the solid state absorption spectrum of TAPDI binded with TiO_2 due to the electron withdrawing effect of the Ti^{4+} ions on binding of the compound to TiO_2 surface, relative to the photonated carboxylate precursor.

5.6.2 UV−Vis Absorption and Emission Spectra of TANDI

The absorption and emission (λ_{exc}= 360 nm) measurements of the TANDI (1×10^{-5} M) were studied in different organic solvents and in the solid state (Figure 4.32−4.34). The absorption spectra of naphthalene diimide in different solvents have shown three sharp vibronic transitions between 300 nm to 400 nm which are suited well with characteristic energy bands of NDI dyes and could be related to the $\pi-\pi^*$ transition (TFAc, 377, 357 and 339 nm, Figure 4.32.a). The fluorescence spectra of the triazine substituted naphthalene diimide in NMP, DMAc, DMF and DMSO show similar emission bands which could be attributed to charge transfer (DMSO, 424, 457 and 504 nm, Figure 4.34.b). The maximum value of red shifted spectrum has been observed in *m*−cresol. The aggregation behavior of TANDI in different solvents has been shown in the Table 5.7.

Table 5.7: Ratio of absorption intensities of TANDI in various solvents

Solvent	$A^{0 \rightarrow 0}$	$A^{0 \rightarrow 1}$	$A^{0 \rightarrow 0}/ A^{0 \rightarrow 1}$
m−Cresol	0.94	0.97	0.97
TFAc	1.18	1.02	1.16
NMP	0.88	0.78	1.13
DMF	0.88	0.77	1.14
DMAC	1.48	1.38	1.07
DMSO	0.64	0.60	1.07

As shown in the table given above, the calculated ratio ($A^{0 \rightarrow 0}/A^{0 \rightarrow 1}$) in most of the solvents are almost equal to 1.0 or a bit higher that could be a great demonstration of

slightly aggregated solutions. The presence of narrow absorption peaks is another sign of monomer structure of the compound.

More studies about photochemical properties of TANDI have been completed with the concentration dependent absorption and emission spectroscopic measurements of the compound in NMP, DMAc and DMF (Figure 4.33–4.34). In these absorption and emission spectra, transition bands were independent of altering the concentrations as can be seen from the figures.

Also, the absorption spectra of the TANDI in solid state is not similar compare with the solution state in terms of positions and structure transition bands as its shown in the Figure 4.51 (red shift of the $0 \rightarrow 1$ transition; TANDI: 22 nm). The three wider and bathochoromically shifted transition bands have been observed as in solution state for synthesized compound. These results have been proved to the presence of weak $\pi \rightarrow \pi$ stacking between the naphthalene chromophores in the solid state. Figure 4.58 gives the solid state absorption spectrum of TANDI binded with TiO_2. The absorption bands are lost their fine vibronic structure and appeared to be broader when adsorbed on the TiO_2 films. A bathochoromic shift was determined in the solid state absorption spectrum of TANDI binded TiO_2 with due to the electron withdrawing effect of the Ti^{4+} ions on binding of the compound to TiO_2 surface, relative to the photonated carboxylate precursor.

The result for ε_{max} of the compound in DMF and DMSO have been show inherently lower than those in NMP and DMAc owing to the solvent dependent aggregation attitude (NMP: 9037, DMSO: 5530, DMF: 6734 and DMAc: 17444).

5.6.3 UV−Vis Absorption and Emission Spectra of HP−PDA

The photochemical characteristics of bay modified perylene dianhydride which is HP−PDA have been analyzed by utilizing the absorption and emission spectroscopic measurements in polar protic and polar aprotic solvents (Figure 4.37−4.40). The UV−vis absorption spectra of compound have represented characteristic $\pi{-}\pi$ transition bands in polar aprotic solvents (NMP, 523, 494 and 419 nm, DMAc, DMF, DMSO, Figure 4.37.a). The broad absorption peaks between 650 nm to 800 nm could be based on charge transfer (CT) from donor moiety to acceptor moiety in the strongly electron donating solvents (NMP, 701 nm and 761 nm; DMAc, 683 nm and 749 nm). The absorption bands between 650 nm to 800 nm shows the effect of polarity of solvent used and the presence of solvent dependent aggregation behavior. The $0{\rightarrow}0$ transition bands have been red shifted in TFAc and *m*−cresol compared with other solutions, due to the protonation of hydroxyl groups in the substituent from bay position. The absorption spectra of HP−PDA have not shown the well separated $\pi{\rightarrow}\pi$ transition bands because of the indication of aggregation or intermolecular interaction like Hydrogen bonding interaction because of having free hydroxyl group in the substituent. The aggregation possibility of the compound in various solvents has been represented in the following table. The ratio between $0{\rightarrow}0$ transition band and $0{\rightarrow}1$ transition band is less than 1, this result shows that the compound is highly aggregated in the solutions.

Table 5.8: Ratio of absorption intensities of HP−PDA in various solvents

Solvent	$A^{0{\rightarrow}0}$	$A^{0{\rightarrow}1}$	$A^{0{\rightarrow}0}/ A^{0{\rightarrow}1}$
NMP	1.12	1.14	0.98
DMF	1.00	1.01	0.99
DMAc	1.19	1.21	0.98

The fluorescence property of the synthetic product has been characterized in different solvents at λ_{exc}=485, 420 and 315 nm as pictured in Figure 4.37.b, 4.39 and 4.40. The fluorescence spectra of HP−PDA at excitation wavelength 485 nm show excimer like emission bands in all the solvents (DMF, 539, 569). Red shifted emission bands are observed for HP−PDA in TFAc, DMAc and *m*−cresol solvents. In the excitation wavelength of 315 nm and 420 nm (Figure 4.40), the emission bands are more structureless and the excimer like emission bands have been detected along with broad charge−transfer complex emission bands between 600−800 nm in the acceptor region. The concentration dependent absorption and emission (λ_{exc}= 485 nm) spectroscopic studies of the compound have been presented in Figure 4.38–4.39. The absorption spectra were not dependent on molarity of freshly prepared solutions and no large distinction has been observed upon decreasing the molarity of solutions. But emission spectra shows that by decreasing the concentration, the intensity of 0→0 transition is increasing compared to the 0→1 transition.

In terms of the structure of the transition movements, the absorption spectra of the HP−PDA in solid state differ from the solution state absorption spectrum (in NMP solvent). The three broader and red shifted absorption bands were at 268, 509 and 548 nm. These results have been proved to the presence of $\pi\rightarrow\pi$ stacking interactions. Figure 4.53 presents UV−vis absorption spectrum of HP−PDA binded with TiO_2 in the solid state. The absorption bands lost their fine vibronic structure and appeared to be broader when adsorbed on the TiO_2 films. A bathochoromic shift was determined absorption spectrum in the solid state of HP−PDA binded with TiO_2 due to the electron withdrawing effect of the Ti^{4+} ions on binding of the compound to TiO_2 surface, relative to the photonated carboxylate precursor.

The fluorescence quantum yield in different organic solvents of the HP−PDA is figured out and the calculated data was given in Table 4.7. The results show that the fluorescence quantum yield values are quite low due to the aggregation in the solutions.

5.6.4 UV−Vis Absorption and Emission Spectra of HP−HEPDI

The photochemical behavior of bay substituted perylene diimide were studied by absorption and emission spectroscopic methods in polar protic, polar aprotic and nonpolar solvents (Figure 4.43−4.44). The solubility of bay substituted perylene diimide, HP−HEPDI is decreased compared with its bay substituted perylene dianhydride, HP−PDA as it is shown in Table 5.5. Due to the having more intermolecular interaction possibility at imide and bay position of perylene chromophore. In the absorption spectra of HP−HEPDI in different solvent, the $\pi \rightarrow \pi$ transition bands are more structureless and not separated well because of solubility and interaction issues (DMSO, 523 and 487 nm). Red shifted band was observed in TFAc solvent due the absorption bands are highly affected by polarity of solvents. On the hand, the UV−vis absorption spectra give an idea about aggregation behavior of HP−HEPDI in solutions. The ratio $A^{0 \rightarrow 0}/A^{0 \rightarrow 1}$ is around 1.00 which shows slightly aggregated solutions as it is shown in Table 5.9.

Table 5.9: Ratio of absorption intensities of HP−HEPDI in various solvents

Solvent	$A^{0 \rightarrow 0}$	$A^{0 \rightarrow 1}$	$A^{0 \rightarrow 0}/ A^{0 \rightarrow 1}$
TFAc	0.63	0.60	1.05
NMP	1.10	1.07	1.03
DMF	0.93	0.91	1.02
DMAc	1.14	1.13	1.02
DMSO	1.15	1.14	1.00

The fluorescence properties of the HP−HEPDI have been characterized in different solvents at excitation wavelengths of 485 nm and 420 nm as depicted in Figure 4.43.b−4.44, respectively. The emission spectra of the compound at excitation wavelength of 485 nm have been shown three characteristic emission bands (NMP, 535, 575 and 632 nm). The excimer like emission bands are observed in DMSO and TFAc. The fluorescence spectra of the compound at excitation wavelength of 420 nm have been represented almost similar emission bands which are not separated with the emission spectra of the compound at λ_{exc}= 485 nm. However the donor emission was detected around 400 nm at the λ_{exc}= 420 nm.

Spectral shapes of the compound, HP−HEPDI in the solid−state absorption spectrum have been changed compared to the transition bands observed in the NMP solvent. The one broad and red shifted absorption bands was at 559 nm. This result has been assigned to the presence of $\pi \rightarrow \pi$ stacking in the solid state (Figure 4.54). Focuses on the solid state UV−vis absorption spectrum of HP−HEPDI binded with TiO_2. The absorption bands lost their fine vibronic structure and appeared to be broader when adsorbed on the TiO_2 films. A hypsochormic shift was determined in the solid state absorption spectrum of HP−HEPDI binded with TiO_2.

The fluorescence quantum yield in different organic solvents of the HP−HEPDI is figured out and the results were tabulated in Table 4.7. The results show that the fluorescence quantum yield values are so low due to the aggregation and intermolecular interactions in the solutions.

5.6.5 UV−Vis Absorption and Emission Spectra of TM−PDA

The optical properties of TM−PDA were analyzed carefully by using absorption and emission spectroscopic measurements in polar aprotic solvents (Figure 4.35−4.36). The absorption spectra of compound in different polar aprotic solvents have represented characteristic $\pi \rightarrow \pi$ transition bands such as 517 nm and 492 nm in NMP solvents. The broad absorption peaks between 650 nm to 800 nm could be related to CT property from donor moiety to acceptor moiety in the used polar aprotic solvents (NMP, 686 nm and 739 nm; DMAc, 697 nm and 759 nm). The absorption peaks between 650 nm to 800 nm presents the effect of higher dielectric constant of solvents and indicates the presence of solvent dependent aggregation behavior. The $0 \rightarrow 0$ transition band has been slightly red shifted in DMSO solvent compared with other solutions. The absorption spectra of TM−PDA have not shown the well separated characteristic $\pi \rightarrow \pi$ transition bands due to the presence of aggregation. The aggregation possibility of the compound in different solvents has been tabulated in the Table 5.10. The ratio between $0 \rightarrow 0$ transition band and $0 \rightarrow 1$ transition band shows that the compound is slightly aggregated in different solvents.

Table 5.10: Ratio of absorption intensities of TM−PDA in various solvents

Solvent	$A^{0 \rightarrow 0}$	$A^{0 \rightarrow 1}$	$A^{0 \rightarrow 0} / A^{0 \rightarrow 1}$
NMP	0.94	0.83	1.13
DMF	0.77	0.62	1.24
DMAC	1.28	1.04	1.23
DMSO	1.34	1.13	1.19

The emission behavior of the TM−PDA has been studied in the same polar aprotic solvents at λ_{exc}= 485 nm as pictured in Figure 4.35.b The fluorescence spectra of

TM−PDA show the excimer like one emission band in all the used solvents (DMF, 549 and 578 nm). The concentration dependent UV−vis absorption measurements of the product have been presented in Figure 4.36. The absorption spectra were unaffected by concentration, and there was no obvious change when the concentration was reduced.

The solid state UV−vis absorption spectrum of the TM−PDA is not similar compare with the solution state UV−vis spectrum (in NMP solvent) in terms of structure of transition bands as shown in the Figure 4.52. The four broad and red shifted absorption bands were observed at 392, 468, 498 and 550 nm. These results have been assigned to the presence of $\pi \rightarrow \pi$ stacking in the solid state. Figure 4.62 depicted the solid state UV−vis absorption spectrum of TM−PDA binded with TiO_2. The absorption bands lost their fine vibronic structure and appeared to be broader when adsorbed on the TiO_2 films. A hypsochoromic shift was observed in the absorption spectrum TM−PDA binded with TiO_2. The hypsochoromic shift can be explained as ring opening of carbonyls of the anhydride groups on the perylene framework.

5.6.6 UV−Vis Absorption and Emission Spectra of TM−HEPDI

The optical features of bay substituted perylene diimide which is TM−HEPDI have been analyzed carefully by absorption and emission spectroscopic measurements in polar protic and polar aprotic (Figure 4.41−4.42). The UV−vis absorption spectra of synthetic product have been depicted different transition bands in polar aprotic solvents (DMSO, NMP, DMF, DMAc; 522 nm and 483 nm, Figure 4.41.a) compared with polar protic solvents (*m*−cresol; 544 nm and 504 nm and and TFAc). The broad absorption peaks between 650 nm to 800 nm can be attributed CT from donor (thiophene) to acceptor moieties in the polar protic solvents (NMP; 675 nm and 763

nm, DMF; 677 nm and 755 nm and DMAc; 671 nm). Due to the protonation of hydroxyl groups in the substituent from imide position of perylene skeleton, 0→0 transition bands have been red shifted in TFAc and *m*−cresol solvents compared with other solutions. The UV−vis absorption spectra of TM−HEPDI have not shown the well separated π→π transtition bands because of the indication of aggregation or intermolecular interaction like Hydrogen bonding interaction owing to the appearance of free hydroxyl functional moieties in the substituent. The aggregation behavior of the compound in different solvents has been tabulated in the following table. The ratio between 0→0 transition band and 0→1 transition band shows that the TM−HEPDI is highly aggregated in the solutions. The intensity of 0→0 transition is lower than 0→1 transition.

Table 5.11: Ratio of absorption intensities of TM−HEPDI in various solvents

Solvent	$A^{0\rightarrow0}$	$A^{0\rightarrow1}$	$A^{0\rightarrow0}/A^{0\rightarrow1}$
MC	1.26	1.36	0.93
TFAc	0.76	0.72	1.06
NMP	0.91	1.01	0.90
DMF	0.96	1.06	0.91
DMAc	1.07	1.19	0.89
DMSO	0.85	0.92	0.92

The emission properties of the TM−HEPDI have been characterized in different solvents at excitation wavelengths of 485 nm and 420 nm as shown in Figure 4.41.b−4.42. The fluorescence spectra of TM−HEPDI at λ_{exc}= 485 nm (Figure 4.41.b) show three characteristic emission bands in all the solvents (NMP, 534, 574 and 632 nm). Bathochoromically shifted emission bands are observed for TM−HEPDI in TFAc and *m*−cresol solvents. In the excitation wavelength of 420 nm (Figure 4.42), the

emission bands are more structureless and the excimer like emission bands have been detected along with broad charge−transfer complex emission bands between 600−800 nm in the acceptor region.

The absorption studies in the solid state were done for the thiophene substituted perylene dye (TM−HEPDI, Figure 4.55). The spectra of this measurement did not show similar structures of transition bands comparing to solution (in NMP solvent) state absorption spectrum. The red shifted and two broad absorption bands were at 511 and 558 nm. This result has been assigned to the existence of $\pi \rightarrow \pi$ stacking in the solid state. Figure 4.63 depicted the solid state UV−vis absorption spectrum of TM−HEPDI binded with TiO_2. The absorption bands are lost their fine vibronic structure and appeared to be broader when adsorbed on the TiO_2 films. A blue shift was seen in the solid state absorption spectrum of TM−HEPDI binded TiO_2.

The Φ_f of the TM−HEPDI is determined in different organic solvents and the results of calculation were given in Table 4.8. The results have been represented that the fluorescence quantum yield values are so low due to the aggregation and intermolecular interactions in the solutions.

5.6.7 UV−Vis Absorption and Emission Spectra of HEPDI

The optical characteristics of perylene diimide are analyzed by absorption and emission spectroscopic measurements in different solvents (Figure 4.45−4.47). In the absorption spectra of HEPDI in different solvent, three characteristic $\pi \rightarrow \pi$ transition bands (DMAc; 522, 487 and 459 nm, Figure 45.a) compared to the bay substituted perylene diimides which are TM−HEPDI and HP−HEPDI in same solvents. Red shifted absorption bands was observed in *m*−cresol and TFAc solvents due the

interactions between the solvents and compound which contain free four hydroxyl groups. On the hand, the UV−vis absorption spectra give an idea about aggregation behavior of HEPDI in solutions. The ratio $A^{0\to0}/A^{0\to1}$ is around 1.00 for compound as it is shown in Table 5.12.

Table 5.12: Ratio of absorption intensities of HEPDI in various solvents

Solvent	$A^{0\to0}$	$A^{0\to1}$	$A^{0\to0}/A^{0\to1}$
MC	1.49	1.40	1.07
TFAc	1.31	0.98	1.34
NMP	1.10	0.99	1.11
DMF	1.25	1.26	0.99
DMAc	0.98	0.96	1.02
DMSO	0.98	0.95	1.03

The fluorescence properties of the HEPDI have been characterized in distinct solvents at excitation wavelengths of 485 nm as depicted in Figure 4.45.b, respectively. The fluorescence spectra of the product at λ_{exc}=485 nm have been shown three characteristic and well separated emission bands (DMAc, 533, 573 and 622 nm). Bathochoromically shifted emission bands are observed for HEPDI in TFAc solvent. Figure 4.46–4.47 have been presented the UV−vis absorption and fluorescence emission spectra (excitation at λ_{max}=485 nm) of HEPDI in NMP, DMF, DMSO at room temperature with different concentrations from 9.08×10^{-5} M to 1.79×10^{-5} M. As the concentrations of HEPDI solutions raise the intensities of transition bands raise in the absorption and emission spectra. Specially, the structure of the emission bands and the maxima were determined in the Figure 4.47 strongly depend on solvents used to prepare the solutions.

The absorption spectra of the HEPDI in solid state (Figure 4.56) show different spectral shapes comparing with the solution state absorption spectrum. Highly broad and bathochorically shifted absorption bands was observed at 517 nm and 566nm. The reason of these broad absorption bands is the presence of strong $\pi\rightarrow\pi$ stacking between the perylene choromophore in the solid state. Figure 4.64 gives the solid state absorption spectrum of HEPDI binded with TiO_2. The absorption bands lost their fine vibronic shape and appeared to be broader than solid state absorption of HEPDI when adsorbed on the TiO_2 films. A hypsochormic shift from 566 nm to 552 nm was seen in the solid state absorption spectrum of HEPDI binded with TiO_2.

The fluorescence quantum yield of the symmetric perylene diimide HEPDI is determined in different organic solvents and the results were given in Table 4.9. The calculated data show that the fluorescence quantum yield values are so low because of the intermolecular H−bonding interactions in the prepared solutions.

5.6.8 UV−Vis and Emission Spectra of Complex 1

The photochemical characteristics of metal coordinated perylene diimide which named as complex 1 are analyzed by using absorption and emission spectroscopic studies in polar aprotic solvents (Figure 4.48) and compared with optical properties of TAPDI ligand (Figure 4.29). As it is shown in the figures, $0\rightarrow0$ transition band of TAPDI in the absorption spectra shifted from 527 nm to 531 nm and $0\rightarrow1$ transition band shifted by 2 nm to the longer wavelength. Emission spectra of the TAPDI and Complex 1 are compared and bathochromic shifts are observed. $0\rightarrow0$ transition band of emission spectra of dye shifted by 4 nm to the longer wavelength and $0\rightarrow1$ transition bands are shifted from 578 nm to 584 nm. These shifts have shown complex formation between the TAPDI and Cu(II) ion.

5.7 Electrochemical Properties of the Synthetic Products

5.7.1 Electrochemical Properties of TAPDI

The cyclic voltammetric experiments of TAPDI was conducted in dry dicholorometha ne containing 0.1 M TBAPF$_6$ to investigate the redox feautures and measure the HOMO and the LUMO energy states and band gap energy data as its shown in the Table 4.50 and Figure 4.83. Cyclic voltammogram of TAPDI has shown characteristic two reversible, one−electron reductions with E$_{1/2}$ at −0.960 and −1.165 V (vs. ferrocene/ferrocenium couple, scan rate: 100 mV s^{-1}) related to the production of the radical anion and dianion with peak potential separations ΔE_{p1} = 150 mV. Notably, an irreversible oxidation peak was observed in the cathodic region (onset, +1.44 V vs. Ag wire) which is based on the highly conjugated perylene chromophore linked to the electron accepting groups of the imide.

The HOMO and LUMO energy states for TAPDI in solution are predicted utilizing E$_{ox/red}$ onset potentials in dicholoromethane solvent considering the known level for reference level for Fc (4.80 eV under the vacuum level). The calculations were determined with the empirical relation E$_{LUMO}$ = [(E$_{red}$ − E$_{1/2(Fc)}$) + 4.8] eV or E$_{HOMO}$ = [(E$_{ox}$ − E$_{1/2(Fc)}$) + 4.8]. Fc was operated as external standard (E$_{1/2(Fc)}$= 0.41 V vs. Ag/AgCl). The HOMO/LUMO data, the calculated redox potentials and band gap energies were given in the Table 4.50. Depend on the CV measurement results of TAPDI (E$_{ox,onset}$ = 1.44 V) the HOMO energy data are estimated as E$_{HOMO}$= −5.83 eV from the equation E$_{HOMO}$ = [(E$_{ox, onset}$ − E$_{1/2(Fc)}$) + 4.8] eV. Similarly, the onset reduction potential value of the TAPDI is found as E$_{red, onset}$ = − 0.460 V which is making the LUMO data as E$_{LUMO}$ = −3.93 eV from the equation E$_{LUMO}$ = [(E$_{red,onset}$ − E$_{1/2(Fc)}$) + 4.8]

eV. Finally, the electrochemical band gap (Eg_{CV}) value of TAPDI was calculated from the equation given, $Eg_{CV} = E_{LUMO} - E_{HOMO}$ and found as 1.90 eV.

5.7.2 Electrochemical Properties of TAPPI

The typical two-step reductions of perylene dyes overlapped in the oligomer TAPPI cyclic voltammogram, most probably due to the disturbed planarity of the perylene core in the oligomer TAPPI ($E_{1/2}$,red1 = −1.15 V vs. Fc/Fc+ couple, Figure 4.82). Notably, the peak potential separations for the reductive processes for the oligomer clearly show the electrochemical reversibility (ΔE_p =140 mV).

Moreover, the potential reduction value of TAPPI is slightly more positive than that observed for compound TAPDI (Figure 4.83), indicating an easier reduction with a higher reduction rate. This property is attributed to the inductive effect of the increased imide nitrogens on the oligomer backbone compared to compound TAPDI. The irreversible oxidation peak of oligomer TAPPI was observed in the cathodic region at 1.84 V vs. Ag wire (onset) attributed to the extended conjugated perylene cores.

Based on the cyclic voltammetry result, TAPPI (Eox, onset =1.71 V) the HOMO energy value weas calculated as E_{HOMO}=−6.10 eV. Similarly, the onset reduction potential value of the TAPPI is observed as Ered,onset=−0.380 V, which makes the LUMO value as E_{LUMO} = −4.01 eV. Finally, the electrochemical bandgap, E_{gCV} value of TAPDI was calculated as 2.09 eV, respectively. The HOMO–LUMO energy gaps of oligomer TAPPI are higher than that of compound TAPDI.

Surprisingly, the electron-withdrawing moieties on TAPPI substantially decreased the HOMO and LUMO energy levels and caused to increase in the bandgap compared to that of diimide TAPDI. This result is attributed to reducing the intra− and

intermolecular interaction when the planar structure of the diimide TAPDI was converted to helical conformation in oligomer TAPPI through the polycondensation process.

5.8 Thermal Properties of the Synthetic Products

The thermal behavior of the synthetic products have been investigated by using DSC (differential scanning calorimetry, heating rate 10 K per minute) under nitrogen atmosphere and TGA (thermo gravimetric analysis, heating range 5 K per minute) under oxygen atmosphere.

Oligomer compound, TAPPI represents no melting point or glass transition temperature in the DSC run up to 440 ºC (Figure 4.65.a). TGA thermogram shows that TAPPI exhibited excellent thermal stability with 96% weight loss at a temperature above 504 ºC. Besides, a 4% char yield was observed at 571 ºC (Figure 4.65.b).

Figure 4.66 has depicted the DSC (a.) and TGA (b.) thermograms of TAPDI. TAPDI does not show melting point or glass transition temperature in the DSC run up to 440 ºC (Figure 4.66.a). The TGA curve of compound showed three stages of thermal decomposition. The first and second stages occurred within the temperature range 497 ºC−533 ºC and 533 ºC−614 ºC with a weight loss of 28% and 20% due to the loss of amine units from the perylene diimide. The third decomposition stage, in the temperature range 614 ºC−780 ºC was found with a mass loss of 50% and a 0% char yield.

Figure 4.67 has been represented the DSC (a.) and TGA (b.) thermograms of TANDI. The DSC thermogram of TANDI shows no melting point or glass transition up to 440 ºC (Figure 4.67.a). TGA thermogram in the Figure 4.67.b describes the thermal

stability of compound and shows four stages of thermal decomposition in the wide temperature range 0–700 ºC. The thermal decomposition initialized at 394 ºC and 99.84% weight loss was recorded up to 650 °C.

The DSC (a.) and TGA (b.) thermograms of TM−PDA are given in the Figure 4.71. The DSC thermogram of TM−PDA has shown no thermal transitions related to the physical state differences untill 300 °C (Figure 4.71.a). TGA curve of compound in the describes the thermal stability and shows three stages of thermal decomposition in the wide temperature range 0−960 ºC as its shown in Figure 4.71.b. Also, TGA thermogram shows that compound was stable up to 288 ºC and totally 92.35 % weight loss was recorded up to 960 °C.

Figure 4.69 has depicted the DSC (a.) and TGA (b.) thermograms of HP−PDA. The DSC thermogram of HP−PDA has shown no thermal transitions related to the physical state change up to 370 °C as it is shown in the Figure 4.69.a). The TGA thermogram (Figure 4.69.b) shows the decomposition of product was started almost at 354 °C and 62% weight loss was analyzed up to 900 °C.

The DSC (a.) and TGA (b.) curves of HP−HEPDI is given in the Figure 4.70. The DSC thermogram of the compound does not show any melting point or glass transition up to up to 440 °C (Figure 4.70.a). TGA thermogram shown in Figure 4.70.b describes the thermal stability and presents two thermal decomposition steps. The compound was stable up to 318 ºC and 94.70 % weight loss was recorded up to 600 °C. Compared to HP−PDA, thermal stability of the compound decreased after imidization.

The DSC (a.) and TGA (b.) thermograms of TM−HEPDI are shown in the Figure 4.72. The DSC thermogram of the compound gives no melting point or glass transition corresponding to the phase change until 440 °C (Figure 4.72.a). TGA thermogram in the Figure 4.72.b describes the thermal stability of the compound in the wide temperature range 0−1000 ºC. The decomposition of TM−HEPDI was started almost at 514 °C and 97.54% weight loss was determined up to 650 °C. Compared to TM−PDA, thermal stability of the compound decreased after imidization.

TGA curve of HEPDI has shown in Figure 4.68 describes the thermal stability and presents three thermal decomposition steps. Also, the thermal decomposition of product was started around 302 °C and 96 % weight loss is determined until 550 °C. The results show that bay substituted perylene diimide is thermally more stable than perylene diimide which is not substituted from bay position even though substituents are the same in the imide position.

5.9 I−V Characteristic of the Synthetic Products

Photovoltaic measurement results of solar cells which prepared with perylene dyes are given in Figure 4.73−4.81 and Table 5.13. According to results listed in the table, the highest power conversion efficiency was obtained by using complex 1 as a photosensitizer in construction of DSSC. Second one is bay substituted perylene diimide with free hydroxyl groups from bay and imide positions of the perylene core, HP−HEPDI as a photosensitizer with 0.028 %, followed by HP−TCPDI with 0.015 % efficiency, TM−PDA with 0.014 % efficiency, triazine substituted perylene diimide with free amino groups, TAPDI with 0.011 % efficiency, HP−PDA with 0.008 % efficiency, TM−HEPDI with 0.007 % efficiency and HEPDI with 0.0001 % efficiency.

Table 5.13: η of DSSC by using different compounds.

Compound	η
TAPDI	0.011
Complex 1	0.069
TANDI	0.023
TM−PDA	0.014
HP−PDA	0.008
HP−HEPDI	0.028
TM−HEPDI	0.007
HEPDI	0.0001
HP−TCPDI	0.015

TAPDI consist of triazine substituent as a donor group on the imide position of perylene core. TAPDI sensitized solar cell resulted a short current density (I_{sc}) of 0.4320 mA.cm^2, an open circuit voltage (V_{oc}) of 316 mV, leading to efficiency (η) of 0.011% under standard solar conditions (Figure 4.73). Solar to electricity efficiency value for DSSCs depend on triazine substituted dye TAPDI is lower than the complex 1 made of TAPDI and Cu^{2+} under the same conditions. Complex 1 sensitized solar cell gave I_{sc} of 1.9200 mA.cm^2, V_{oc} of 189 mV, leading to η of 0.069 % (Figure 4.81). This progress in DSSC efficiency might be related to long excited lifetime, effective metal−to−ligand CT spectra, and good electrochemical characteristics of metal complexes. Efficiency of the constructed cell was observed 0.023% when TANDI was used as photosensitizer where I_{sc} of 0.124 mA.cm^2 and V_{oc} of 348 mV (Figure 4.74).

Under standard solar conditions, dye HP−PDA, HP−HEPDI and HP−TCPDI sensitized solar cells gave I_{sc} of 0.0948, 0.1579 and 0.1750 mA.cm^2 (Figure 4.76), V_{oc} of 229, 348 and 377 mV (Figure 4.77), leading to η of 0.008%, 0.028%, and 0.015% (Figure 4.80), respectively. The highest cell efficiency is belonging to the HP−HEPDI due to the strong intermolecular H−bonding interaction and having freer hydroxyl groups than other two perylene derivatives to work as an anchoring group.

Under similar solar conditions, dye TM−PDA, TM−HEPDI and HEPDI sensitized solar cells resulted I_{sc} of 0.0997, 0.0713 and 0.0021 mA.cm^2 (Figure 4.75), V_{oc} of 276, 248 and 194 mV (Figure 4.78), leading to η of 0.014%, 0.007%, and 0.0001% (Figure 4.79), respectively. The lowest solar to light efficiency is found in the device which constructed by using HEPDI as photosensitizer. The reason is using dye which is not modified from bay position. If there is no substituent from bay position electron transfer is not being easy to TiO$_2$ conduction band.

5.10 GPC of the poly[bis−N,N'−(3−phenyl−2,4,6−triazinyl)−3,4,9,10−perylenebisdicarboximide]

A monomodal molar mass distribution was observed in the GPC chromatograms (Figure 4.7). The weight-average molecular mass (Mw) of 3500 g/mol was obtained from GPC measurements (Figure 4.7). This value corresponds to an average oligomer size containing seven repeating units. The Mn, Mw, and polydispersity obtained for compound TAPPI were 1200, 3500, and 2.96, respectively. The monomodal molar mass distributions are the characteristics of step-growth polymerization of perylene chromophoric units.

On the other hand, the low weight-average molecular mass indicated an abrupt polymerization termination, most probably due to the intra- and intermolecular interactions. It is important to note that we took great care in pre-drying reactants and solvents before completely removing any residual water. Undoubtedly, the reason for the abrupt termination of polymerization cannot be water.
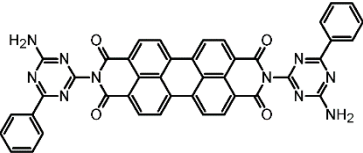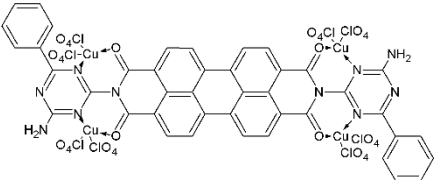
Chapter 6
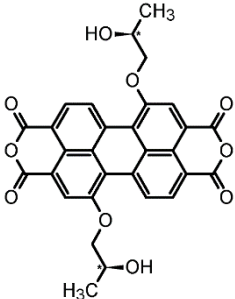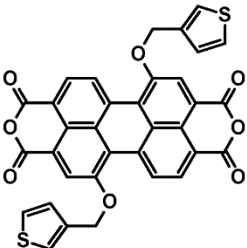
CONCLUSION

In the present research work, two novel chromogenic perylene diimides, TAPDI and HEPDI and one naphthalene diimide, TANDI have been synthesized with high yield. To enhance the optoelectronic and photochemical characteristics of perylene diimides dyes, three 1,7–symmetrically substituted perylene dyes, HP–HEPDI, TM–HEPDI and HP–TCPDI were produced in good amount. In order to reach this goal firstly Br–PDA was synthesized and then modification of perylene framework from bay position was done with the two different alcoholic substituents at the end two different bay substituted perylene dianhydrides, HP–PDA and TM–PDA were yielded. Also, in order of increasing the efficiency of the fabricated devices, dye molecules are modified to copper complexes. Complexation of TAPDI, HP–HEPDI and TM–HEPDI was done with copper (II) metal.

The photochemical features of the compound characterized widely by using absorption and emission spectroscopic methods. And distinct absorption and emission characteristics have been characterized in detail owing to differences in intermolecular interactions by using various organic solvents. The molecular structures of the synthetic products were approved with elemental analyzes, FT–IR, mass and NMR spectroscopic measurements. Thermal stabilities of the compounds were studied with TGA and DSC measurements. Redox characteristics of the synthetic products were characterized by cyclic voltammetry technic.

Additionally, the power conversion efficiencies of the constructed DSSC device by using synthetic products as photosensitizers were measured and tabulated carefully in Table 6.1. The binding studies of dye molecules with TiO_2 semiconductor material were done with solid−state UV−vis absorption and FT−IR spectroscopy methods and discussed in the previous chapter in detail.

Table 6.1: Chemical structures and optoelectronic properties of the synthetic products

Dye	Structure	λ_{max}	ε_{max}	η
TAPDI		527	124258	0.011
Complex 1		531	–	0.069
HP−PDA		523	15620	0.014
TM−PDA		517	89955	0.008

HP–HEPDI		522	–	0.028
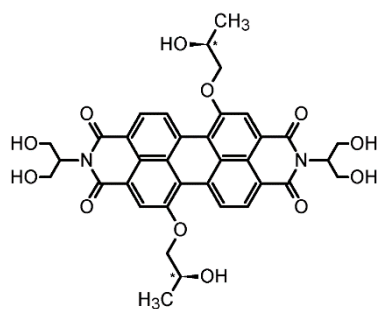
TM–HEPDI		523	–	0.007
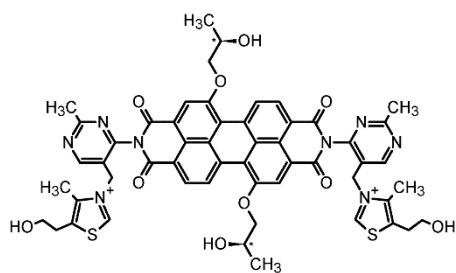
HEPDI		523	12735	0.0001
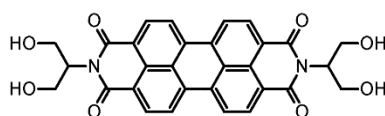
HP-TCPDI		–	–	0.015
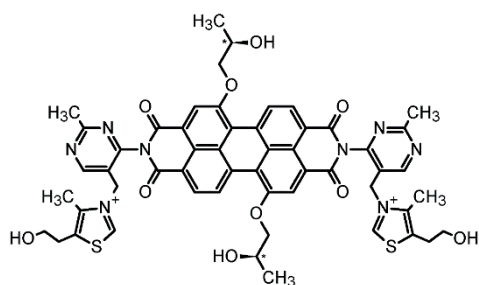
REFERENCES

[1] Dresselhaus, M. S., & Thomas, I. L. (2001). Alternative energy technologies. *Nature*, *414*(6861), 332-337.

[2] Ferroukhi, R., Khalid, A., Lopez-Peña, A., & Renner, M. (2017). Renewable energy and jobs: annual review 2015. *International Renewable Energy Agency (IRENA)*.

[3] Wagner, P. L. (1993). General energetics: energy in the biosphere and civilization.

[4] Lewis, N. S., & Nocera, D. G. (2006). Powering the planet: Chemical challenges in solar energy utilization. *Proceedings of the National Academy of Sciences*, *103*(43), 15729-15735.

[5] Lopez, A., Roberts, B., Heimiller, D., Blair, N., & Porro, G. (2012). *US Renewable Energy Technical Potentials. A GIS-Based Analysis* (No. NREL/TP-6A20-51946). National Renewable Energy Lab.(NREL), Golden, CO (United States).

[6] Wu, J., Lan, Z., Lin, J., Huang, M., Huang, Y., Fan, L., ... & Wei, Y. (2017). Counter electrodes in dye-sensitized solar cells. *Chemical Society Reviews*, *46*(19), 5975-6023.

[7] Williams, R. (1960). Becquerel photovoltaic effect in binary compounds. *The journal of Chemical physics*, *32*(5), 1505-1514.

[8] Fritts, C. E. (1883). On a new form of selenium cell, and some electrical discoveries made by its use. *American Journal of Science*, (156), 465-472.

[9] Planck, M. (1901). On the law of the energy distribution in the normal spectrum. *Ann. Phys*, *4*(553), 1-11.

[10] Newburgh, R., Peidle, J., & Rueckner, W. (2006). Einstein, Perrin, and the reality of atoms: 1905 revisited. *American journal of physics*, *74*(6), 478-481.

[11] Goldmann, A., & Brodsky, J. (1914). Zur Theorie des Becquereleffektes. I. Lichtelektrische Untersuchungen an oxydierten Kupferelektroden. *Annalen der Physik*, *349*(14), 849-900.

[12] Schottky, W. (1930). Ueber den entstehungsort der photoelektronen in kupfer-kupferoxydul-photozellen. *Phys. Z.*, *31*, 913-925.

[13] Perlin, J. (1999). *From space to earth: the story of solar electricity*. Earthscan.

[14] Easton, R. L., & Votaw, M. J. (1959). Vanguard I IGY satellite (1958 beta). *Review of Scientific Instruments*, *30*(2), 70-75.

[15] Chu, S., & Majumdar, A. (2012). Opportunities and challenges for a sustainable energy future. *nature*, *488*(7411), 294-303.

[16] Kelzenberg, M. D., Turner-Evans, D. B., Kayes, B. M., Filler, M. A., Putnam, M. C., Lewis, N. S., & Atwater, H. A. (2008). Photovoltaic measurements in single-nanowire silicon solar cells. *Nano letters*, *8*(2), 710-714.

[17] Conway, E. J., Walker, G. H., & Heinbockel, J. H. (1981). A thermochemical model of radiation damage and annealing applied to GaAs solar cells. In *15th Photovoltaic Specialists Conference* (pp. 38-44).

[18] Schnitzer, I., Yablonovitch, E., Caneau, C., Gmitter, T. J., & Scherer, A. (1993). 30% external quantum efficiency from surface textured, thin-film light-emitting diodes. *Applied Physics Letters*, *63*(16), 2174-2176.

[19] Green, M. A. (2001). Third generation photovoltaics: Ultra-high conversion efficiency at low cost. *Progress in Photovoltaics: Research and Applications*, *9*(2), 123-135.

[20] Conibeer, G. (2007). Third-generation photovoltaics. *Materials today*, *10*(11), 42-50.

[21] Wang, Q. H., Kalantar-Zadeh, K., Kis, A., Coleman, J. N., & Strano, M. S. (2012). Electronics and optoelectronics of two-dimensional transition metal dichalcogenides. *Nature nanotechnology*, *7*(11), 699-712.

[22] Green, M. A., Emery, K., Hishikawa, Y., Warta, W., Dunlop, E. D., Levi, D. H., & Ho-Baillie, A. W. (2017). Solar cell efficiency tables (version 49). *Progress in photovoltaics: research and applications*, *25*(1), 3-13.

[23] Badawy, W. A. (2015). A review on solar cells from Si-single crystals to porous materials and quantum dots. *Journal of advanced research*, *6*(2), 123-132.

[24] Sharma, G. D., Roy, M. S., & Singh, S. P. (2012). Improvement in the power conversion efficiency of thiocyanate-free Ru (II) based dye sensitized solar cells by cosensitization with a metal-free dye. *Journal of Materials Chemistry*, *22*(36), 18788-18792.

[25] Pallikkara, A., & Ramakrishnan, K. (2021). Efficient charge collection of photoanodes and light absorption of photosensitizers: A review. *International Journal of Energy Research*, *45*(2), 1425-1448.

[26] Marenich, A. V., Cramer, C. J., & Truhlar, D. G. (2009). Universal solvation model based on solute electron density and on a continuum model of the solvent defined by the bulk dielectric constant and atomic surface tensions. *The Journal of Physical Chemistry B*, *113*(18), 6378-6396.

[27] Calle-Vallejo, F., & Koper, M. T. (2012). First-principles computational electrochemistry: Achievements and challenges. *Electrochimica acta*, *84*, 3-11.

[28] Nyholm, R. S. (1957). The renaissance of inorganic chemistry. *Journal of Chemical Education*, *34*(4), 166.

[29] Ruch, E., & Fischer, E. O. (1952). Zur Frage der Bindung im Dicyclopentadienyl-eisen. *Zeitschrift für Naturforschung B*, *7*(12), 676-676.

[30] Dunitz, J. D., & Orgel, L. (1953). Bis-cyclo pentadienyl Iron: a Molecular Sandwich. *Nature*, *171*(4342), 121-122.

[31] Dunitz, J. D., Orgel, L. E., & Rich, A. (1956). The crystal structure of ferrocene. *Acta Crystallographica*, *9*(4), 373-375.

[32] Bohn, R. K., & Haaland, A. (1966). On the molecular structure of ferrocene, Fe (C5H5) 2. *Journal of Organometallic Chemistry*, *5*(5), 470-476.

[33] Coriani, S., Haaland, A., Helgaker, T., & Jorgensen, P. (2006). The equilibrium structure of ferrocene. *ChemPhysChem*, *7*(1), 245-249.

[34] Cotton, F. A., Wilkinson, G., Murillo, C. A., Bochmann, M., & Grimes, R. (1988). *Advanced inorganic chemistry* (Vol. 6, p. 1455). New York: Wiley.

[35] Dunitz, J. D., & Orgel, L. (1953). Bis-cyclo pentadienyl Iron: a Molecular Sandwich. *Nature*, *171*(4342), 121-122.

[36] Yoo, J. J., Seo, G., Chua, M. R., Park, T. G., Lu, Y., Rotermund, F., ... & Seo, J. (2021). Efficient perovskite solar cells via improved carrier management. *Nature*, *590*(7847), 587-593.

[37] Mehmood, U., Rahman, S. U., Harrabi, K., Hussein, I. A., & Reddy, B. V. S. (2014). Recent advances in dye sensitized solar cells. *Advances in Materials Science and Engineering*, *2014*.

[38] Grant, F. A. (1959). Properties of rutile (titanium dioxide). *Reviews of Modern Physics*, *31*(3), 646.

[39] Neale, N. R., Kopidakis, N., Van De Lagemaat, J., Grätzel, M., & Frank, A. J. (2005). Effect of a coadsorbent on the performance of dye-sensitized TiO2 solar cells: shielding versus band-edge movement. *The Journal of Physical Chemistry B*, *109*(49), 23183-23189.

[40] Wu, J., Lan, Z., Hao, S., Li, P., Lin, J., Huang, M., ... & Huang, Y. (2008). Progress on the electrolytes for dye-sensitized solar cells. *Pure and applied chemistry*, *80*(11), 2241-2258.

[41] Kay, A., & Grätzel, M. (1996). Low cost photovoltaic modules based on dye sensitized nanocrystalline titanium dioxide and carbon powder. *Solar Energy Materials and Solar Cells*, *44*(1), 99-117.

[42] Liu, J., Tang, Q., He, B., & Yu, L. (2015). Cost-effective, transparent iron selenide nanoporous alloy counter electrode for bifacial dye-sensitized solar cell. *Journal of Power Sources*, *282*, 79-86.

[43] Kusama, H., Orita, H., & Sugihara, H. (2008). TiO2 band shift by nitrogen-containing heterocycles in dye-sensitized solar cells: a periodic density functional theory study. *Langmuir*, *24*(8), 4411-4419.

[44] Amiralaei, S., Uzun, D., & Icil, H. (2008). Chiral substituent containing perylene monoanhydride monoimide and its highly soluble symmetrical diimide:

synthesis, photophysics and electrochemistry from dilute solution to solid state. *Photochemical & Photobiological Sciences*, *7*(8), 936-947.

[45] Asir, S., Demir, A. S., & Icil, H. (2010). The synthesis of novel, unsymmetrically substituted, chiral naphthalene and perylene diimides: Photophysical, electrochemical, chiroptical and intramolecular charge transfer properties. *Dyes and pigments*, *84*(1), 1-13.

[46] Bodapati, J. B., & Icil, H. (2008). Highly soluble perylene diimide and oligomeric diimide dyes combining perylene and hexa (ethylene glycol) units: Synthesis, characterization, optical and electrochemical properties. *Dyes and Pigments*, *79*(3), 224-235.

[47] Herbst, W., & Hunger, K. (2006). *Industrial organic pigments: production, properties, applications*. John Wiley & Sons.

[48] Würthner, F. (2004). Perylene bisimide dyes as versatile building blocks for functional supramolecular architectures. *Chemical communications*, (14), 1564-1579.

[49] Salbeck, J., Kunkely, H., Langhals, H., Saalfrank, R. W., & Daub, J. (1989). Electron-Transfer (Et) Behavior of Fluorescent Dyes-Studied in Perylenebisdicarboximides and Dioxaindenoindenedione Using Cyclovoltammetry and Uv/Vis-Spectroelectrochemistry. *Chimia*, *43*(1-2), 6-9.

[50] Al-Khateeb, B., Dinleyici, M., Abourajab, A., Kök, C., Bodapati, J. B., Uzun, D., Koyuncu, S. & Icil, H. (2020). Swallow tail bay-substituted novel perylene bisimides: Synthesis, characterization, photophysical and electrochemical properties and DFT studies. *Journal of Photochemistry and Photobiology A: Chemistry*, *393*, 112432.

[51] Li, C., & Wonneberger, H. (2012). Perylene imides for organic photovoltaics: yesterday, today, and tomorrow. *Advanced Materials*, *24*(5), 613-636.

[52] Savyasachi, A. J., Kotova, O., Shanmugaraju, S., Bradberry, S. J., Ó'Máille, G. M., & Gunnlaugsson, T. (2017). Supramolecular chemistry: a toolkit for soft functional materials and organic particles. *Chem*, *3*(5), 764-811.

[53] Weil, T., Vosch, T., Hofkens, J., Peneva, K., & Müllen, K. (2010). The rylene colorant family—tailored nanoemitters for photonics research and applications. *Angewandte Chemie International Edition*, *49*(48), 9068-9093.

[54] Spano, F. C. (2010). The spectral signatures of Frenkel polarons in H-and J-aggregates. *Accounts of chemical research*, *43*(3), 429-439.

[55] Gsänger, M., Oh, J. H., Könemann, M., Höffken, H. W., Krause, A. M., Bao, Z., & Würthner, F. (2010). A crystal-engineered hydrogen-bonded octachloroperylene diimide with a twisted core: an n-channel organic semiconductor. *Angewandte Chemie International Edition*, *49*(4), 740-743.

[56] O'regan, B., & Grätzel, M. (1991). A low-cost, high-efficiency solar cell based on dye-sensitized colloidal TiO 2 films. *nature*, *353*(6346), 737-740.

[57] Burfeindt, B., Hannappel, T., Storck, W., & Willig, F. (1996). Measurement of temperature-independent femtosecond interfacial electron transfer from an anchored molecular electron donor to a semiconductor as acceptor. *The Journal of Physical Chemistry*, *100*(41), 16463-16465.

[58] Ferrere, S., Zaban, A., & Gregg, B. A. (1997). Dye sensitization of nanocrystalline tin oxide by perylene derivatives. *The Journal of Physical Chemistry B*, *101*(23), 4490-4493.

[59] Wang, S., Li, Y., Du, C., Shi, Z., Xiao, S., Zhu, D., ... & Cai, S. (2002). Dye sensitization of nanocrystalline TiO2 by perylene derivatives. *Synthetic metals*, *128*(3), 299-304.

[60] Zafer, C., Kus, M., Turkmen, G., Dincalp, H., Demic, S., Kuban, B., ... & Icli, S. (2007). New perylene derivative dyes for dye-sensitized solar cells. *Solar energy materials and solar cells*, *91*(5), 427-431.

[61] Shibano, Y., Umeyama, T., Matano, Y., & Imahori, H. (2007). Electron-donating perylene tetracarboxylic acids for dye-sensitized solar cells. *Organic Letters*, *9*(10), 1971-1974.

[62] Fortage, J., Séverac, M., Houarner-Rassin, C., Pellegrin, Y., Blart, E., & Odobel, F. (2008). Synthesis of new perylene imide dyes and their photovoltaic

performances in nanocrystalline TiO2 dye-sensitized solar cells. *Journal of Photochemistry and Photobiology A: Chemistry*, *197*(2-3), 156-169.

[63] Li, C., & Wonneberger, H. (2012). Perylene imides for organic photovoltaics: yesterday, today, and tomorrow. *Advanced Materials*, *24*(5), 613-636.

[64] Polo, A. S., Itokazu, M. K., & Iha, N. Y. M. (2004). Metal complex sensitizers in dye-sensitized solar cells. *Coordination Chemistry Reviews*, *248*(13-14), 1343-1361.

[65] Yanagida, M., Singh, L. P., Sayama, K., Hara, K., Katoh, R., Islam, A., ... & Grätzel, M. (2000). A new efficient photosensitizer for nanocrystalline solar cells: synthesis and characterization of cis-bis (4, 7-dicarboxy-1, 10-phenanthroline) dithiocyanato ruthenium (II). *Journal of the Chemical Society, Dalton Transactions*, (16), 2817-2822.

[66] Çakar, S. (2019). 1, 10 phenanthroline 5, 6 diol metal complex (Cu, Fe) sensitized solar cells: A cocktail dye effect. *Journal of Power Sources*, *435*, 226825.

[67] Icil, H., & Icli, S. (1997). Synthesis and properties of a new photostable polymer: Perylene-3, 4, 9, 10-tetracarboxylic acid-bis-(N, N′-dodecylpolyimide). *Journal of Polymer Science Part A: Polymer Chemistry*, *35*(11), 2137-2142.

[68] Turro, N. J. (1965). *Molecular Photochemistry, Benjamin, London, 44-64*.